Revealing the Early Solar System through Small Body Spectroscopy and Dynamics

Thesis by
Matthew Belyakov

In Partial Fulfillment of the Requirements for the
degree of
Doctor of Philosophy

CALIFORNIA INSTITUTE OF TECHNOLOGY
Pasadena, California

2027
Defended June 10, 2026

Matthew Belyakov
ORCID: 0000-0003-4778-6170

ACKNOWLEDGEMENTS

Мы все учились понемногу
Чему-нибудь и как-нибудь,
Так воспитаньем, слава богу,
У нас немудрено блеснуть.

We've all received an education,
In something, somehow, have we not?
So thank the lord that in this nation,
A little learning means a lot.

—from Stanza V, Chapter I of *Eugene Onegin* by A. S. Pushkin

I'm indebted to my advisor, Mike Brown, for both his incredible patience with my sometimes stochastic approach to research, and the significant wisdom and advice in matters both minor and major that he has provided me over the course of the past five years. I am very appreciative of the freedom I have had to pursue topics that interest me and to conduct timely work when and where necessary. I know that after leaving Caltech, I will continue to treasure his spirit of *de omnibus dubitandum*, and uphold an independent scientific mindset in the course of my career.

I am incredibly grateful to Konstantin Batygin for his unending support and encouragement both in professional and personal questions. Of the dozens of anecdotes that come to mind when writing this brief section, I'll recall an academically relevant one. We wrote an outline for a JWST proposal idea on a scrunched up piece of printer paper about 3 drinks in at some bar in Old Town. A few weeks later, that page grew into a last-minute, (and, to Mike's surprise), successful JWST proposal.

I would also like to acknowledge other members of the Caltech Planetary Science faculty. To Geoff Blake, I am grateful for numerous insights into spectroscopy and cosmochemistry. To Katherine de Kleer, I am thankful for our many conversations on mineral spectroscopy, oolong tea, and of course, for the discounted 2000 Toyota Corolla, which has allowed me to explore some of the far-flung parts of this metropolitan area. To Dave Stevenson, for the many conversations we have had on every facet of planetary science, from exoplanets to asteroids. To the late Yuk Yung, I am grateful for wise and optimistic words regarding the present pessimism that is pervasive among early-career scientists.

To the many co-workers in planetary science at Caltech (an apt term, now that we are unionized) – it has been an incredible community, and I am glad to have been a part of it. I would like to in particular thank Ryleigh Davis – our scientific collaboration and friendship has been the highlight of my days working here at Caltech. To Zac Milby, I am grateful for our discussions of the finer things in life and for reminding me to take it easy at all the right times. I also want to acknowledge the other members of the 2021 Caltech planetary science crop of students: Yuyu Phua, Morgan Saidel, Abigail Keebler, Kimberly Paragas, and Samantha Baker. To some of my "elders": Maria Camarca, thank you for conversation, coffee runs, and confidence; Mike Greklek-McKeon, thank you for your humor and hospitality; Julie Inglis, thank you for all the office banter. To Audrey Martin – thank you for all the laboratory spectra and scientific discussion.

I am very grateful to the administrative staff here in South Mudd, specifically Ruth Loisel and Rachael Danyew who were the administrative support for Mike Brown's group during my time here. And to Julie Lee in Arms, who is a true shining beacon of optimism and infinite support.

Outside Caltech, many co-authors and senior colleagues have also left a lasting impact on my development as a scientist. To Ian Wong, thank you for the many discussions we have had, the ideas we have explored, and for showing me around Taiwan at TNO2024. I hope that we will continue to collaborate for many years to come. To Bryce Bolin, thank you for the observing runs we have shared, especially those in the 3I/ATLAS observing campaign. To Casey Lisse, thank you for teaching me the mysteries of the mid-infrared, and for reminding me of the broader astrophysical context. To Matt Hedman, for inducting me into the "Cult of Mab". To Imke de Pater, for being an academic grandmother and for your words of support. To my undergrad advisors and mentors: Masao Sako, Bhuv Jain, and Gary Bernstein – without you, I would not be doing research today. My deepest thanks to Pedro Bernardinelli, who, as a graduate student, mentored a clueless undergrad (me) and remained a good friend for almost a decade now. And I also would like to briefly acknowledge some academic peers who are friends and good colleagues: Benjamin Sharkey, Carl Ingebretsen, and Ivy Knudsen.

I would like to acknowledge my out-of-department friends at Caltech who have made my time here at Caltech at worst passable, at best a true joy. In particular, I would like to thank all the members of "Borscht Club" throughout these few years. Between Friday night dinners, our many excursions and adventures, and every moment in between, it's been a pleasure.

To friends from earlier stages in life, many of whom I saw on zoom during the defense, thanks for keeping our paths intersecting even as I have been charging headlong into scientific work. Lakshay and Jake, I think none of us will forget our UPenn years together. Ethan – I hope you'll make it to LA soon.

To my partner, and soon-to-be fiancee, Masha, thanks for the love, support, and direct words of encouragement these past two years, through all the ups and downs. There are still many chapters to write together.

To my family, there is too much to say and hard to express in words. First to my grandmother Galya, thank you for raising me, for your endless love and support, for all the books you bought me when I was little, and for always being there for me. To my parents, Lena and Sasha, thank you for allowing me the freedom to pursue my goals, for encouraging me where I needed it most, and for letting me be myself. None of this would have been possible without your counsel and guidance. I still have so much to learn from both of you. To my brother Eugene, you are my greatest friend. Thank you for both pointing out my mistakes and defending me in difficult moments. Я вас всех очень люблю и благодарю за то, что вы меня вырастили, сподвигли на научную карьеру, и поддерживали всеми силами на протяжении всех этих лет.

Finally, I would like to dedicate this thesis to the memory of my late great-grandmother, Anna Efimovna Zheleznyak, who passed away at the beginning of my graduate school journey. Born on May 8, 1928, she survived the horrors of the Great Patriotic War as a teenager, and went on to build a family and a career that lasted until she, her daughter, and granddaughter, immigrated to the US. Because my grandmother was working and my mother was in college, Anna was my primary caretaker during my early childhood. The values she instilled in me, and the specific love of learning she passed down, set me on the path to writing this thesis.

ABSTRACT

One key event is thought to have defined the early outer Solar System, a so-called "dynamical instability", which simultaneously excited the orbits of the giant planets, scattered planetesimals throughout the solar system, and shaped the dynamics of the nascent Kuiper belt. The goal of my thesis has been to constrain the nature of the early dynamical instability and the outer solar system's original architecture. My tools of choice are its many small bodies. These are remnant planetesimals whose compositions and dynamical histories encode the conditions of the early solar system, and include Kuiper belt objects, Jupiter and Neptune Trojans, irregular satellites and small inner moons of the giant planets. Through spectroscopic observations with James Webb, ground-based photometry, and dynamical modelling, I have contributed towards a more refined picture of the early Solar System. These contributions constitute the six research chapters of my thesis.

The second chapter of my thesis presents observational evidence for a key prediction of dynamical instability models: that Jupiter's Trojan asteroids and the Kuiper belt share a common source population in the outer planetesimal disk. By analyzing photometry obtained from our own survey on Keck and Palomar telescopes combined with archival surveys, I find that the low-perihelion Kuiper belt has a bimodal color distribution resembling that of the Jupiter Trojans. By simulating the dynamical evolution of a model Kuiper belt, I demonstrate that the observed colors of low-perihelion objects do not arise from thermal processing, but are instead inherited from the scattered disk, connecting the Kuiper belt and Jupiter Trojans.

The third chapter of my thesis develops analytic methods for characterizing the onset of chaos in the scattered disk, a population of Kuiper belt objects with both high-eccentricity and relatively planar orbits. I develop a perturbative treatment of the circular three-body problem to qualitatively understand the machinery underlying chaotic diffusion in the scattered disk. At distances where most known scattered disk objects reside, a complex network of resonances drives diffusion in two distinct regimes. One is a fully chaotic layer in which transport is rapid. The second is a zone of slower diffusion in which $1:n$ resonances with Neptune emerge as increasingly strong barriers to diffusion at low eccentricity. My analytic framework provides a predictive tool for future population studies.

Chapters four, five, and six use James Webb Space Telescope Near-Infrared Spectrograph (JWST NIRSpec) observations of the small and irregular moons of the giant planets to constrain the history of the satellite systems of these planets. Chapter four presents NIRCam spectrophotometry of the small inner satellites of Uranus and Neptune. I detect a prominent 3 μmabsorption feature on all observed satellites in both systems, consistent with water ice

or hydrated minerals and comparable to the water-type class of Kuiper belt objects. Chapter five presents JWST NIRSpec observations of the three largest Saturnian irregular satellites: Phoebe, Siarnaq, and Albiorix. Phoebe had already been observed by the *Cassini* spacecraft, but my study pinpoints Phoebe as related to water-rich Kuiper belt objects, linking irregular satellites to the Kuiper belt as predicted by dynamical instability models. Chapter six resolves a 77-year-old Neptunian mystery regarding Nereid, the planet's third largest moon and one of the most eccentric in the solar system. Leveraging JWST NIRSpec spectroscopy of Nereid, combined with dynamical simulations of the Neptunian system's early history, I propose that Nereid did not originate in the outer planetesimal disk, but is instead the sole surviving intact regular satellite of Neptune.

The final chapter of my thesis addresses a new class of small body, interstellar objects. I present the first ever mid-infrared spectroscopic observations of an interstellar comet. Using the James Webb Space Telescope's Mid-Infrared Instrument (MIRI), I measure production rates and map the outflows of H_2O, CO_2, CH_4, and atomic nickel on 3I/ATLAS across two observing epochs. Methane is detected for the first time in an interstellar object, and 3I's sudden jump in methane production post-perihelion evinces the activation of a pristine subsurface reservoir. This work closes the thesis with a perspective connecting the solar system to our galactic neighborhood.

PUBLISHED CONTENT AND CONTRIBUTIONS

Belyakov, Matthew and Konstantin Batygin (Jan. 2026). "The perturbation theory approach to stability in the scattered disk". In: *Icarus* 443, 116773, p. 116773. DOI: 10.1016/j.icarus.2025.116773

Contributions: I developed the analytical model, ran computations to verify the model, and wrote the manuscript.

Belyakov, Matthew, M. Ryleigh Davis, Ian Wong, et al. (2026). "Nereid as a regular satellite of Neptune". In: *Science Advances* 12.21, eaeb1429. DOI: 10.1126/sciadv.aeb1429. URL: https://doi.org/10.1126/sciadv.aeb1429

Contributions: I conceived the project, led the JWST Cycle 3 Program which acquired the data, conducted the data reduction and spectroscopic analysis, performed the dynamical simulations, and wrote the manuscript.

Belyakov, Matthew, Ian Wong, et al. (Apr. 2026). "The Volatile Inventory of 3I/ATLAS as Seen with JWST/MIRI". In: *The Astrophysical Journal* 1001.1, L11, p. L11. DOI: 10.3847/2041-8213/ae5700

Contributions: I conceived the project, led the JWST ToO which acquired the data, led the coma mapping, analysis of nickel production, and fitting of radial/azimuthal profiles. The text and fluorescence model were a joint effort with my second author on the publication, Ian Wong.

Belyakov, Matthew and Michael E. Brown (Apr. 2025). "Saturnian Irregular Satellites as a Probe of Kuiper Belt Surface Evolution". In: *The Planetary Science Journal* 6.4, 97, p. 97. DOI: 10.3847/PSJ/adc55d

Contributions: I analyzed the spectroscopic data, wrote the radiative transfer code to model the spectra of the irregular moons, and wrote the manuscript.

Belyakov, Matthew, Michael E. Brown, and Alya Al-Kibbi (Sept. 2024). "The Trojan-like Colors of Low-perihelion Kuiper Belt Objects". In: *The Planetary Science Journal* 5.9, 193, p. 193. DOI: 10.3847/PSJ/ad698a

Contributions: I observed one of the nights on Keck that provided the necessary data for the publication, wrote the code to reduce the images and extract photometry, led the statistical analysis. For the second half of the publication, I ran, analyzed, and interpreted the dynamical simulations. I wrote the manuscript (with significant assistance from my advisor).

Belyakov, Matthew, M. Ryleigh Davis, Zachariah Milby, et al. (May 2024). "JWST Spectrophotometry of the Small Satellites of Uranus and Neptune". In: *The Planetary Science Journal* 5.5, 119, p. 119. DOI: 10.3847/PSJ/ad3d55

Contributions: I conceived the project, reduced the data, extracted the photometry, and wrote the manuscript.

CONTENTS

LIST OF FIGURES

LIST OF TABLES

Chapter 1

INTRODUCTION

One of the primary goals of astronomy since inception has been to understand the history of the Solar System and the mechanisms which underpin that history. The notion that the Solar System was the way it had always been was questioned already by Newton, who, without yet having a notion of perturbation theory, was concerned that interactions between planets would cause “irregularities” to their orbits to increase over time. The next century saw French celestial mechanicians attempt to find regularity in the orbits of the planets, developing secular theory, but remaining concerned about the question of whether the Solar System is long-term stable (a detailed historical review, upon which this summary is based, is presented in Jacques Laskar, 2012). The modern dynamical understanding of the evolution of the Solar System required the invention of computational machines. Numerical integrations of planetary orbits demonstrated that the Solar System is chaotic on timescales much shorter than its lifetime (J. Laskar, 1989; Sussman and Wisdom, 1992), with subsequent work refining these estimates by pointing out the distinct modes of instability in the inner and outer Solar System (Batygin and Laughlin, 2008).

Simultaneously, an observational revolution had taken place. The first asteroid belt object discovered was Ceres (for which C.F. Gauss had invented his method of determining orbits Forbes 1971), followed by Pallas, Juno, Vesta, and Astraea, after which Neptune was discovered by Le Verrier and Galle (Galle, 1846; Airy, 1847). In the next 90 years, numerous asteroids were discovered, which were commonly hypothesized to be remnants of a destroyed planet often termed Phaeton (Safronov, 1979). Asteroids were seen as “vermin of the sky” (Gehrels, 1979) until their critical importance as remnant planetesimals, which are themselves the progenitors of planets, was established; this planetesimal view is the beginning of the modern paradigm on small bodies (Safronov, 1972). Discovery of thousands of asteroids by the 1970s allowed for the development of a nascent asteroid taxonomy, and the combined dynamical and chemical interpretation of the history of the asteroid belt.

In the outer Solar System, this revolution was two decades delayed. The discovery of Pluto in 1930 (described in Tombaugh, 1946) pushed the boundaries of the outer solar system further, though the reasons for the eccentric and inclined orbits of the giant planets, the origin of Jupiter’s Trojan asteroids (discovered decades earlier), remained uncertain. Theoretical work began to predict the existence of an asteroid belt outside of Neptune, such as by the seminal work of Fernandez and Ip, 1984, though it took the development and use of

CCD-based cameras to discover 1992 QB (15760 Albion) (Jewitt, Luu, and Marsden, 1992), the second object after Pluto to be discovered past Neptune. Soon after, many more objects in what became termed the Kuiper belt were found, with the discovery of several large Pluto-sized bodies, such as Eris (M. E. Brown, Trujillo, and Rabinowitz, 2005), precipitating the reclassification of Pluto and similar objects into "Dwarf Planets".

It is at the crossroads of these observational and theoretical considerations that the modern paradigm for the Solar System's early history emerged. The Nice Model, named after the city in the French Riviera where it was born, is the model for the dynamical evolution of the Solar System which seeks to simultaneously explain all of its key dynamical and chemical features. A set of three papers published in Nature laid out the core argument (Gomes et al., 2005; A. Morbidelli et al., 2005; Tsiganis et al., 2005). Where previous models of the early Solar System had insisted that the planets must have formed in very close proximity to their current locations, the Nice model suggests that the giant planets formed in a compact orbital configuration. Inspired by the discovery that even the present Solar System experiences chaotic behavior, developments in nonlinear dynamics or chaos theory, and the widespread availability of computational power, the Nice model team suggested that an early resonant encounter between Jupiter and Saturn caused Saturn's eccentricity to increase, leading to a rapid change in orbital elements. Mechanisms such as these are termed dynamical instability mechanisms. As a result of the resonant encounter, Saturn moved outwards, which caused it to jostle the orbits of Uranus and Neptune. The giant planets then began to interact with the primordial outer disk, scattering planetesimals, with the resulting dynamical friction resulting in the damping of the excited orbital elements of the planets. During this epoch of more gradual migration, Jupiter moves slightly inwards, as it is capable of efficiently ejecting planetesimals from the Solar System, while the other three giant planets move outwards, kicking planetesimals towards Jupiter (Alessandro Morbidelli, 2010; Nesvorný, 2018).

The Nice model proved to be a veritable success story. It simultaneously explained several key features of the Solar System, and over time, the confidence in its predictions has grown stronger. Here is a non-exhaustive list of Nice model successes:

1. The capture of the irregular satellites can be explained as a result of planet-planet interactions driving planetesimals near the giant planets into planetocentric orbits during the instability phase (Nesvorný, Vokrouhlický, and Alessandro Morbidelli, 2007; Nesvorný, Vokrouhlický, and Deienno, 2014).

2. The capture of the Jupiter Trojans can be explained as a result of planet-planet interactions causing Jupiter to suddenly jump during the instability phase (A. Morbidelli et al., 2005; Nesvorný, Vokrouhlický, and Alessandro Morbidelli, 2013).

3. The observed implantation of P and D-type asteroids in the main belt is reproduced by dynamical instability models (Vokrouhlický, Bottke, and Nesvorný, 2016).

4. Formation of the Oort cloud from scattering planetesimals during the dynamical instability (Brasser and A. Morbidelli, 2013).

5. The structure of the Kuiper belt, in that there exists a Cold Classical belt untouched by Neptune's migration, the proportion of resonant to non-resonant objects, and numerous other features (Nesvorný and Vokrouhlický, 2016).

These successes have been possible because the precise mechanism of the dynamical instability and other details of the Nice Model have evolved significantly since 2005. Thus, using the term "Nice model" should perhaps be reserved for the original set of three publications and a set of adjacent papers such as Alessandro Morbidelli et al., 2007 and LEVISON et al., 2008. Instead, the modern iterations can be generally termed as dynamical instability models.

In 2009, the next set of dynamical instability models emerged, driven by the need to preserve the terrestrial planets and other considerations relevant for the inner Solar System. This iteration of models involved a "jumping Jupiter", in which Jupiter and one of the ice giants suffer a close encounter. Soon after, it became evident that a simpler explanation is to add in a fifth ice giant, which can be ejected from the system. This became the five-planet Nice model (Nesvorný, 2011; Batygin, Michael E. Brown, and Betts, 2012; Nesvorný and Alessandro Morbidelli, 2012), and remains the present go-to dynamical instability model. It is worth mentioning here that an entirely different premise, an instability triggered by a stellar fly-by, is also an instability-based model (Raymond and Kaib, 2026).

Over the course of my thesis, the driver behind my science has been questioning and testing dynamical instability models using small bodies. In terms of impact, my work has provided significant observational evidence for a Nice model prediction regarding the Jupiter Trojans and Kuiper belt objects, which I discuss in Chapter 2. Chapter 3 derives an analytical boundary for chaos in the scattered disk, a population of objects with high eccentricities, whose dynamics are driven by scattering with Neptune. This boundary separates objects undergoing significant chaotic diffusion, from "detached objects", which are of great interest to those trying to search for a distant Ninth Planet in the outer Solar System.

Chapters 4–6 represent the beginning of my campaign to redefine the history of the satellite systems around the giant planets. Chapter 4 was the genesis of what became a successful JWST proposal to observe the satellites of the ice giants with JWST. I used images of Uranus and Neptune taken for public relations purposes in order to obtain photometry of the small inner moons around the two planets. The photometry indicated they may be similar to water-rich Kuiper belt objects, rather than ones dominated by organics. Chapter 5 was a brief, though relevant, detour to the irregular satellites of Saturn, finding that the smaller two satellites observed lacked signatures of water ice on their surface, in stark contrast to their larger sibling, Phoebe. This proved to be a valuable testing ground for surface evolution of Kuiper belt objects, finding that collisions may deplete volatiles. Chapter 6 is a culmination of decades of slow-burn investigation, a "Caltech story" of sorts. Nereid, Neptune's third largest moon, is defined as an irregular moon due to its highly eccentric orbit. However, among irregular moons, Nereid is an outlier in that it is the largest member of its class, and with the closest periapse. The JWST spectrum of Nereid firmly placed it as an outlier among Kuiper belt objects, suggesting it may have formed as a regular moon, and been perturbed outwards. This conclusion was first developed by Peter Goldreich in Goldreich et al., 1989, and was followed up on by my advisor in Michael E. Brown, Koresko, and Blake, 1998, but JWST's significant sample of Kuiper belt spectra and spectral coverage solidified the result. The truly novel component of the study was that I combined the compositional evidence with a robust dynamical investigation. Simulating the capture of Triton into a system of primordial satellites, I found that a regular satellite can be perturbed onto a Nereid-like orbit. In fact, the efficiency of this process proved far higher than Nice model-like capture for Nereid. This chapter therefore redefines Nereid as the only remaining intact regular satellite of Neptune.

Chapter 7 closes the thesis by looking to connect our Solar System with other systems through observations of interstellar objects, specifically 3I/ATLAS. This was a sudden addition to the thesis, as its discovery came less than a year before my defense date. In a few weeks in July of 2025, I published a short research note (not in the thesis), and successfully applied for JWST time to observe 3I/ATLAS in the mid-infrared, which was uniquely possible due to its significant brightness and close approach. The resulting data, obtained in December, resulted in the first published mid-infrared spectrum of an interstellar object, providing broad coverage of several volatile species. Our detection of methane was novel, and demonstrated that the comet had begun to release a previously untapped subsurface reservoir of fresh material post-perihelion.

References

Airy, G. B. (1847). "Account of some circumstances historically connected with the discovery of the Planet exterior to Uranus." In: *Astronomische Nachrichten* 25.10, pp. 131–148. DOI: https://doi.org/10.1002/asna.18470251002. eprint: https://onlinelibrary.wiley.com/doi/pdf/10.1002/asna.18470251002. URL: https://onlinelibrary.wiley.com/doi/abs/10.1002/asna.18470251002.

Batygin, Konstantin, Michael E. Brown, and Hayden Betts (Jan. 2012). "Instability-driven Dynamical Evolution Model of a Primordially Five-planet Outer Solar System". In: *The Astrophysical Journal* 744.1, L3, p. L3. DOI: 10.1088/2041-8205/744/1/L3. arXiv: 1111.3682 [astro-ph.EP].

Batygin, Konstantin and Gregory Laughlin (Aug. 2008). "On the Dynamical Stability of the Solar System". In: *The Astrophysical Journal* 683.2, pp. 1207–1216. DOI: 10.1086/589232. arXiv: 0804.1946 [astro-ph].

Brasser, R. and A. Morbidelli (2013). "Oort cloud and Scattered Disc formation during a late dynamical instability in the Solar System". In: *Icarus* 225.1, pp. 40–49. ISSN: 0019-1035. DOI: 10.1016/j.icarus.2013.03.012. URL: http://dx.doi.org/10.1016/j.icarus.2013.03.012.

Brown, M. E., C. A. Trujillo, and D. L. Rabinowitz (Dec. 2005). "Discovery of a Planetary-sized Object in the Scattered Kuiper Belt". In: *The Astrophysical Journal* 635.1, pp. L97–L100. DOI: 10.1086/499336. arXiv: astro-ph/0508633 [astro-ph].

Brown, Michael E., Christopher D. Koresko, and Geoffrey A. Blake (Dec. 1998). "Detection of Water Ice on Nereid". In: *ApJL* 508.2, pp. L175–L176. DOI: 10.1086/311741.

Fernandez, J. A. and W.-H. Ip (Apr. 1984). "Some dynamical aspects of the accretion of Uranus and Neptune: The exchange of orbital angular momentum with planetesimals". In: *Icarus* 58.1, pp. 109–120. DOI: 10.1016/0019-1035(84)90101-5.

Forbes, Eric G. (Jan. 1971). "Gauss and the Discovery of Ceres". In: *Journal for the History of Astronomy* 2, p. 195. DOI: 10.1177/002182867100200305.

Galle, J. G. (Nov. 1846). "Account of the discovery of Le Verrier's planet Neptune, at Berlin, Sept. 23, 1846". In: *Monthly Notices of the Royal Astronomical Society* 7, p. 153. DOI: 10.1093/mnras/7.9.153.

Gehrels, T. (1979). "The asteroids: history, survey, techniques, and future work." In: *Asteroids*. Ed. by Tom Gehrels and Mildred Shapley Matthews, pp. 3–24.

Goldreich, P. et al. (Aug. 1989). "Neptune's Story". In: *Science* 245.4917, pp. 500–504. DOI: 10.1126/science.245.4917.500.

Gomes, R. et al. (May 2005). "Origin of the cataclysmic Late Heavy Bombardment period of the terrestrial planets". In: *Nature* 435.7041, pp. 466–469. DOI: 10.1038/nature03676.

Jewitt, D., J. Luu, and B. G. Marsden (Sept. 1992). "1992 QB1". In: *IAUC* 5611, p. 1.

Laskar, J. (Mar. 1989). "A numerical experiment on the chaotic behaviour of the Solar System". In: *Nature* 338.6212, pp. 237–238. DOI: 10.1038/338237a0.

Laskar, Jacques (Sept. 2012). "Is the Solar System Stable ?" In: *arXiv e-prints*. arXiv: 1209.5996 [astro-ph.EP].

LEVISON, H et al. (2008). "Origin of the structure of the Kuiper belt during a dynamical instability in the orbits of Uranus and Neptune". In: *Icarus* 196.1, pp. 258–273. ISSN: 0019-1035. DOI: 10.1016/j.icarus.2007.11.035. URL: http://dx.doi.org/10.1016/j.icarus.2007.11.035.

Morbidelli, A. et al. (May 2005). “Chaotic capture of Jupiter’s Trojan asteroids in the early Solar System”. In: *Nature* 435.7041, pp. 462–465. DOI: 10.1038/nature03540.

Morbidelli, Alessandro (Nov. 2010). “A coherent and comprehensive model of the evolution of the outer Solar System”. In: *Comptes Rendus Physique* 11, pp. 651–659. DOI: 10.1016/j.crhy.2010.11.001. arXiv: 1010.6221 [astro-ph.EP].

Morbidelli, Alessandro et al. (Nov. 2007). “Dynamics of the Giant Planets of the Solar System in the Gaseous Protoplanetary Disk and Their Relationship to the Current Orbital Architecture”. In: *The Astronomical Journal* 134.5, pp. 1790–1798. DOI: 10.1086/521705. arXiv: 0706.1713 [astro-ph].

Nesvorný, David (Dec. 2011). “Young Solar System’s Fifth Giant Planet?” In: *The Astrophysical Journal* 742.2, L22, p. L22. DOI: 10.1088/2041-8205/742/2/L22. arXiv: 1109.2949 [astro-ph.EP].

— (Sept. 2018). “Dynamical Evolution of the Early Solar System”. In: *ARA&A* 56, pp. 137–174. DOI: 10.1146/annurev-astro-081817-052028. arXiv: 1807.06647 [astro-ph.EP].

Nesvorný, David and Alessandro Morbidelli (Oct. 2012). “Statistical Study of the Early Solar System’s Instability with Four, Five, and Six Giant Planets”. In: *The Astronomical Journal* 144.4, 117, p. 117. DOI: 10.1088/0004-6256/144/4/117. arXiv: 1208.2957 [astro-ph.EP].

Nesvorný, David and David Vokrouhlický (2016). “NEPTUNE’S ORBITAL MIGRATION WAS GRAINY, NOT SMOOTH”. In: *The Astrophysical Journal* 825.2, p. 94. ISSN: 1538-4357. DOI: 10.3847/0004-637x/825/2/94. URL: http://dx.doi.org/10.3847/0004-637X/825/2/94.

Nesvorný, David, David Vokrouhlický, and Rogerio Deienno (Mar. 2014). “Capture of Irregular Satellites at Jupiter”. In: *The Astrophysical Journal* 784.1, 22, p. 22. DOI: 10.1088/0004-637X/784/1/22. arXiv: 1401.0253 [astro-ph.EP].

Nesvorný, David, David Vokrouhlický, and Alessandro Morbidelli (May 2007). “Capture of Irregular Satellites during Planetary Encounters”. In: *The Astronomical Journal* 133.5, pp. 1962–1976. DOI: 10.1086/512850.

— (May 2013). “Capture of Trojans by Jumping Jupiter”. In: *ApJ* 768.1, 45, p. 45. DOI: 10.1088/0004-637X/768/1/45. arXiv: 1303.2900 [astro-ph.EP].

Raymond, Sean N. and Nathan A. Kaib (Mar. 2026). “Was the Solar System’s dynamical instability triggered by a (sub)stellar flyby?” In: *Icarus* 447, 116910, p. 116910. DOI: 10.1016/j.icarus.2025.116910. arXiv: 2512.07979 [astro-ph.EP].

Safronov, V. S. (1972). *Evolution of the protoplanetary cloud and formation of the earth and planets.*

— (1979). “On the origin of asteroids.” In: *Asteroids*. Ed. by Tom Gehrels and Mildred Shapley Matthews, pp. 975–991.

Sussman, Gerald J. and Jack Wisdom (July 1992). “Chaotic Evolution of the Solar System”. In: *Science* 257.5066, pp. 56–62. DOI: 10.1126/science.257.5066.56.

Tombaugh, Clyde W. (Jan. 1946). “The Search for the Ninth Planet, Pluto”. In: *Leaflet of the Astronomical Society of the Pacific* 5.209, p. 73.

Tsiganis, K. et al. (May 2005). “Origin of the orbital architecture of the giant planets of the Solar System”. In: *Nature* 435.7041, pp. 459–461. DOI: 10.1038/nature03539.

Vokrouhlický, David, William F. Bottke, and David Nesvorný (Aug. 2016). “Capture of Trans-Neptunian Planetesimals in the Main Asteroid Belt”. In: *The Astronomical Journal* 152.2, 39, p. 39. DOI: 10.3847/0004-6256/152/2/39.

Chapter 2

TROJAN-LIKE COLORS OF LOW-PERIHELION KUIPER BELT OBJECTS

Belyakov, Matthew, Michael E. Brown, and Alya Al-Kibbi (Sept. 2024). "The Trojan-like Colors of Low-perihelion Kuiper Belt Objects". In: *The Planetary Science Journal* 5.9, 193, p. 193. DOI: 10.3847/PSJ/ad698a. arXiv: 2407.21168 [astro-ph.EP].

The solar system's early large-scale dynamical instability described by the many iterations of the Nice model has had great success in providing a single resolution to many phenomena in the solar system, including the excited eccentricities of the giant planets (Tsiganis et al., 2005) and the structure of the Kuiper belt and asteroid belt (Levison, Alessandro Morbidelli, et al., 2008; Alessandro Morbidelli, Brasser, et al., 2010) among many other properties of the solar system (Nesvorný, 2018). Since the initial publication of the Nice model in 2005, the nature of its dynamical instability model has evolved significantly. The first three landmark Nice model papers relied on Jupiter and Saturn acquiring excited eccentricities by slowly migrating through their mutual 1:2 resonance (Tsiganis et al., 2005). Resonance crossing was abandoned owing to its inconsistency with the structure of the inner Solar System, as during the instability Saturn's secular resonances would sweep out material needed to form the inner planets. The current model for the early instability involves the ejection of a fifth (or potentially more) giant planet by Jupiter, which suddenly shifts Jupiter's orbit inward, avoiding the issues of granular migration and resonance crossing (Nesvorný and Alessandro Morbidelli, 2012; Batygin, Michael E. Brown, and Betts, 2012; Nesvorný, 2018).

One of the most robust predictions present in all versions of the Nice model is that the Jupiter Trojan asteroids at 5.2 AU share a source population with the more distant Kuiper belt (Tsiganis et al., 2005; A. Morbidelli et al., 2005; Alessandro Morbidelli, 2010; Nesvorný, 2018). In the current iteration of the Nice model, the giant planets undergo a series of dynamical instabilities, caused by the ejection of one or more planetary cores formed somewhere between Jupiter and Neptune (Levison, Alessandro Morbidelli, et al., 2008; Nesvorný and Alessandro Morbidelli, 2012). At the time of these instabilities, small bodies that are in the Trojan region of any of the giant planets would be thrown onto now chaotic orbits (A. Morbidelli et al., 2005). In this picture, the current Jupiter Trojans could only have been captured during Jupiter's final large-scale instability. Jupiter Trojans are thus simply the objects that happened to be at Jupiter's L4/L5 points during its final "jump", captured into librating orbits. Meanwhile, planetesimals originating in the primordial Kuiper belt disk would be scattering throughout the solar system, forming the dominant population of small bodies in the outer solar system. Consequently, the Nice model implies that progenitor objects for the Kuiper belt also became the Trojans we see today (A. Morbidelli et al., 2005; Nesvorný, Vokrouhlický, and Alessandro Morbidelli, 2013). This prediction gives a clear observational test for the Nice model: if Trojans and Kuiper belt objects (KBOs) indeed have a shared origin, these two populations should have common physical properties (A. Morbidelli et al., 2005; Alessandro Morbidelli, Levison, et al., 2009; Nesvorný, Vokrouhlický, and Alessandro Morbidelli, 2013; Jewitt, 2018). However, observational backing for a shared origin remains elusive, leaving a fundamental gap in the evidence for the Nice model's predictions regarding the evolution of the outer solar system.

One piece of evidence that supports the shared origin of KBOs and Jupiter Trojans is the similar size distribution of the excited component of the Kuiper belt and the Trojans (Alessandro Morbidelli, Levison, et al., 2009; Wesley C. Fraser et al., 2014). A similar size distribution is, however, only a necessary but not sufficient condition to prove that KBOs and Trojans have a common source. Complicating this prediction are the differences in the surface properties of KBOs and Trojans. Recent JWST spectroscopy has shown that KBOs have a rich surface chemistry, with water, carbon dioxide, methanol, and carbon monoxide ices frequently present (Michael E. Brown and Wesley C. Fraser, 2023; De Prá et al., 2024). By contrast, Jupiter Trojans are spectroscopically neutral in the 1-4 micron range, with only weak organic and hydration features at around 3.0 microns (J. P. Emery, Burr, and Cruikshank, 2011; M. E. Brown, 2016; Wong, Michael E. Brown, Blacksberg, et al., 2019; Wong, Michael E. Brown, Joshua P. Emery, et al., 2024). Resolving how two populations that ought to have the same origin have divergent spectral and photometric properties is necessary to prove the common origin of KBOs and Trojans – an essential component of the Nice Model for the formation of the solar system.

In this paper we find that the low-perihelion Kuiper belt objects (objects with $q < 30$ AU, $a > 30$ AU) have Trojan-like visible colors, and are a likely link between the Jupiter Trojans and the Kuiper belt. In section 2.1, we discuss the colors of the various populations of the outer solar system, demonstrating how observations of the low-perihelion Kuiper belt place it apart from the rest of the Kuiper belt and Centaurs and that its colors potentially bifurcate into those of the Jupiter Trojans. In section 2.2 we investigate the two possible reasons for the unique colors of the low-q Kuiper belt as opposed to the Centaurs: different heating histories, or different source populations. Both of these possibilities are examined through the lens of dynamical simulations, finding that the difference in source populations between Centaurs and low-q KBOs is the more likely reason for the more neutral colors of the low-q KBOs.

2.1 Colors of Outer Solar System Populations

Objects in the outer solar system generally have featureless visible reflectance spectra ranging from neutral to red colors. To good approximation, these colors can be defined by a single parameter referred to as the spectral slope. The spectral slope is defined as the slope of the reflectivity at each observed wavelength, expressed in units of the percent change in the reflectivity over 100 nm, typically normalized at V band (550 nm). The slope can be calculated from photometric observations in different colors and filter systems, though it is primarily useful in the regime where the spectrum of objects tends to be linear, between 400 and 800 nm (Jewitt and Meech, 1986; Hainaut, Boehnhardt, and Protopapa, 2012). In order to obtain a full picture of the variety of color distributions in the many dynamical sub-populations that exist in the outer solar system, we combine four data sets. The first is from the Minor Bodies of the Outer Solar System (MBOSS) set of colors (Hainaut, Boehnhardt, and Protopapa, 2012), the second is from the Colors of the Outer Solar System Origins Survey (Col-OSSOS) (Schwamb et al., 2019), the third is from the Dark Energy Survey (DES) (Bernardinelli, Bernstein, Sako, et al., 2022; Bernardinelli, Bernstein, Jindal, et al., 2023), and the fourth is our own small survey of the colors of low-perihelion Kuiper belt objects, the technical details of which we describe in section 2.4. We restrict ourselves to objects which have colors measured well enough that the uncertainty in the spectral slope is smaller than ±7%, equivalent to $g-i \pm 0.2$. We include only objects with absolute magnitude $H > 7$ in order to remove larger objects whose colors are significantly different from smaller objects, hypothetically due to the geologic processing from accretional heating of larger objects (M. E. Brown, Schaller, and W. C. Fraser, 2012). Moreover, since we are comparing the colors of the Kuiper belt with those of the Trojans, we should be selecting only those KBOs that match the size range of the Jupiter Trojans, the largest of which are at $H \sim 7$ (see figure 6 of Hainaut, Boehnhardt, and Protopapa 2012). In total, we include 12 low-q KBOs from OSSOS, 7 from MBOSS, 4 from DES, and 24 from our survey for a total of 47. For the Centaurs, 31 are taken from OSSOS, 38 from DES, none from MBOSS, and one from our survey.

Kuiper belt objects with semi-major axis greater than Neptune's orbit have long been known to have bifurcated colors, split into a "Very Red" (KBO VR) population with slope greater than 20% and a "Red" (KBO R) population with slope less than 20%, or $g-i = 1.15$ (Tegler and Romanishin, 1998; Doressoundiram et al., 2002; Hainaut, Boehnhardt, and Protopapa, 2012; Wong and Michael E. Brown, 2017a). The Jupiter Trojan asteroids are also bifurcated in color, but into a "Red" (JT R) population, with a mean spectral slope of

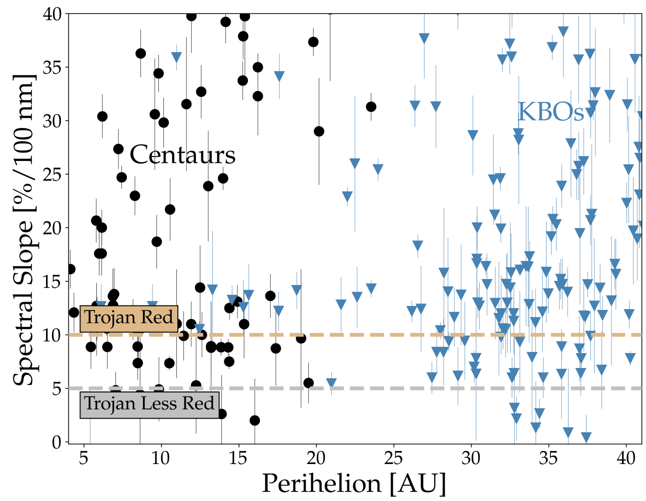

Figure 2.1: Colors and perihelia of the KBOs (blue; $a > 30$ AU) and Centaurs (black; $a < 30$ AU) taken from MBOSS and Col-OSSOS (Hainaut, Boehnhardt, and Protopapa, 2012; Schwamb et al., 2019). The colors of the two Jupiter Trojan sub-populations are shown as dashed lines. While KBO and Centaur colors are statistically indistinguishable and significantly different from Jupiter Trojan colors, the colors of KBOs at low perihelia appear Trojan-like for $q < 25$ AU.

around 10% or $g - i = 0.87$, and a "Less Red" (JT LR) population, with a mean spectral slope of around 5% or $g - i = 0.74$ (J. P. Emery, Burr, and Cruikshank, 2011; Wong and Michael E. Brown, 2016). In this classification scheme, the Kuiper belt's "Red" colors fully encompass the range of Jupiter Trojan colors.

Centaurs are former KBOs recently injected into the giant planet region and on unstable orbits with lifetimes typically between 100 kyr to 10 Myrs (Levison and Duncan, 1997; Alessandro Morbidelli, 1997; Tiscareno and Malhotra, 2003; di Sisto, Brunini, and de Elía, 2010). For the purposes of this paper, we define Centaurs as having both perihelia and semi-major axes less than 30 AU. This population represents a transition from the cold temperatures of the KBOs to the warmer environments of the Jupiter Trojans. Though Centaurs have been substantially heated for many millions of years, no evidence exists that Centaurs are developing the surface colors of Jupiter Trojans – their colors are statistically indistinguishable from those of the parent KBO population (see Figure 2.1).

Previous publications have suggested color changes in Centaurs with heating, but, in each case, as more data have appeared, the statistical evidence has gone away (see Melita and J. Licandro 2012; Peixinho et al. 2020). As an aside, KBO surfaces clearly do evolve if they are heated enough. Jupiter family comets that originate from the Kuiper belt have darker surfaces than those typically seen on KBOs and have spectra generally unlike most KBOs,

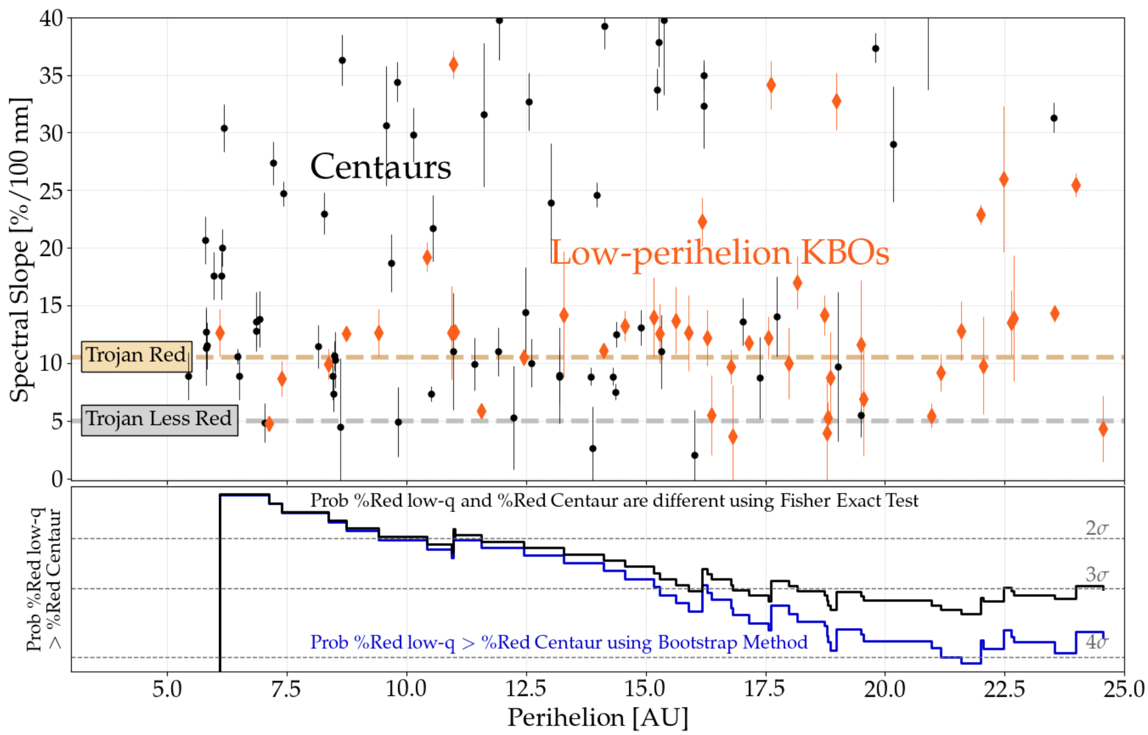

Figure 2.2: Statistical comparison of Centaur (black; $a < 30$ AU, $q < 30$ AU), and low-perihelion Kuiper belt (orange, $a > 30$ AU, $q < 30$ AU) colors, with Jupiter Trojan colors as dashed lines. The bottom panel shows the results of two tests of the difference in color of the Centaurs and low-perihelion KBOs: a one-sided Fisher exact test in black and a bootstrap method in blue. In both tests, objects are sequentially added to the analysis starting with the lowest perihelion objects. For any perihelion $15 < q < 25$ AU, the probability that the proportion of Red objects in the low-q KBOs is greater than that of the Centaurs is more than 3σ for the Fisher test, and nearly 4 σ for the bootstrap method, indicating that the low-perihelion Kuiper belt is potentially a Trojan-like population in the outer solar system.

presumably as a result of significant ice sublimation over many perihelion passages (Lisse et al., 2022; Pinto et al., 2023). Comet-like activity is seen in some of the closest Centaurs, though the correlation with surface colors remains unclear (Jewitt, 2009; Chandler et al., 2020). JWST spectroscopy of the active comet 39P/Oterma, which is on a Centaur-like orbit, shows active CO_2 outgassing and a surface that has muted absorption features compared to KBOs observed with JWST (Pinto et al., 2023). Additionally, JWST spectroscopy by Javier Licandro et al., 2024 has shown that the inactive Centaur Okyrhoe and Neptune co-orbital 2010 KR59 have spectra dissimilar to the larger KBO population, with broad 3.0 micron absorption features more similar to the Trojans shown in Wong, Michael E. Brown, Joshua P. Emery, et al., 2024 rather than to the KBOs. The lack of color changes in the Centaurs further obfuscates the link between Trojans and the Kuiper belt. For example, hypotheses such as Wong and Michael E. Brown, 2016 suggested heating as the mechanism for the change from KBO R/VR colors to Jupiter Trojan LR/R colors, yet this transition is not observed in the colors of the Centaur population.

A subpopulation within the Kuiper belt that does, however, appear to have distinct colors is the low-perihelion Kuiper belt ($q < 30$ AU, $a > 30$ AU). These objects are dynamically distinct from the Centaurs as they spend most of their orbits outside of Neptune, though both populations share similarly low perihelia. These low-q KBOs appear to have a distinct set of colors from the Red/Very Red KBO and Centaur-like colors to Jupiter Trojan-like Red colors for $q < 25$ AU, as shown in Figure 2.2. For perihelia between 25 and 30 AU, there are both low-perihelion KBOs and resonant objects with large eccentricities that cross Neptune's orbit, so we exclude this region from our analysis.

We can statistically compare the difference in the two populations by computing the fraction of KBO "Red" versus "Very Red" objects in each population. Of the 70 Centaurs with $q < 25$ AU in our sample, 28 are Very Red and 42 are Red, for a Red fraction of $f_r = 0.6 \pm 0.06$ (using the Wald interval for the binomial proportion confidence interval). Of the 47 low perihelion KBOs, 40 are Red, and only 7 are Very Red, for a Red fraction of $f_r = 0.85 \pm 0.05$. Drawing 10,000 samples from the Centaur proportion of Red and Very Red objects and asking whether the low-perihelion KBOs have a larger proportion of Red objects than the Centaurs gives a 99.94% confidence that the two populations have different proportions of each color for $q < 25$ AU. Using even the very conservative one-sided Fisher exact test, the probability of the low perihelion KBOs having fewer Red objects than the Centaurs is under $p = 0.003$, or over a 99.7% probability that their colors are different. In Figure 2.2, we iteratively repeat the Fisher test for each subset of the low-q population by successively adding objects from lowest to highest perihelion. We find a more than three sigma probability that the low-q KBOs have fewer Very Red objects than the Centaurs for any perihelion value above 17 AU. Moreover, our result for the Fisher exact test (or the more granular test in Figure 2.2) gives a confidence of over 99% even when spectral slopes of 15-25% are excluded, indicating that the difference in color between Centaurs and low-q KBOs is robust and does not rely on a finely tuned definition of the color bifurcation.

2.1.1 Testing the Trojan Bifurcation in Low-perihelion KBOs

We now test whether low-perihelion Kuiper belt objects have Trojan-like colors by analyzing the distribution of their colors in the Trojan-like 0-15% spectral slope range (KBO Red, or Jupiter Trojan LR/R colors). The upper end of this range was set to be 15% as that is the maximum spectral slope of Trojans reported in Wong and Michael E. Brown, 2016. First, we check whether the color distribution of Red low-q KBOs differs from that of similar

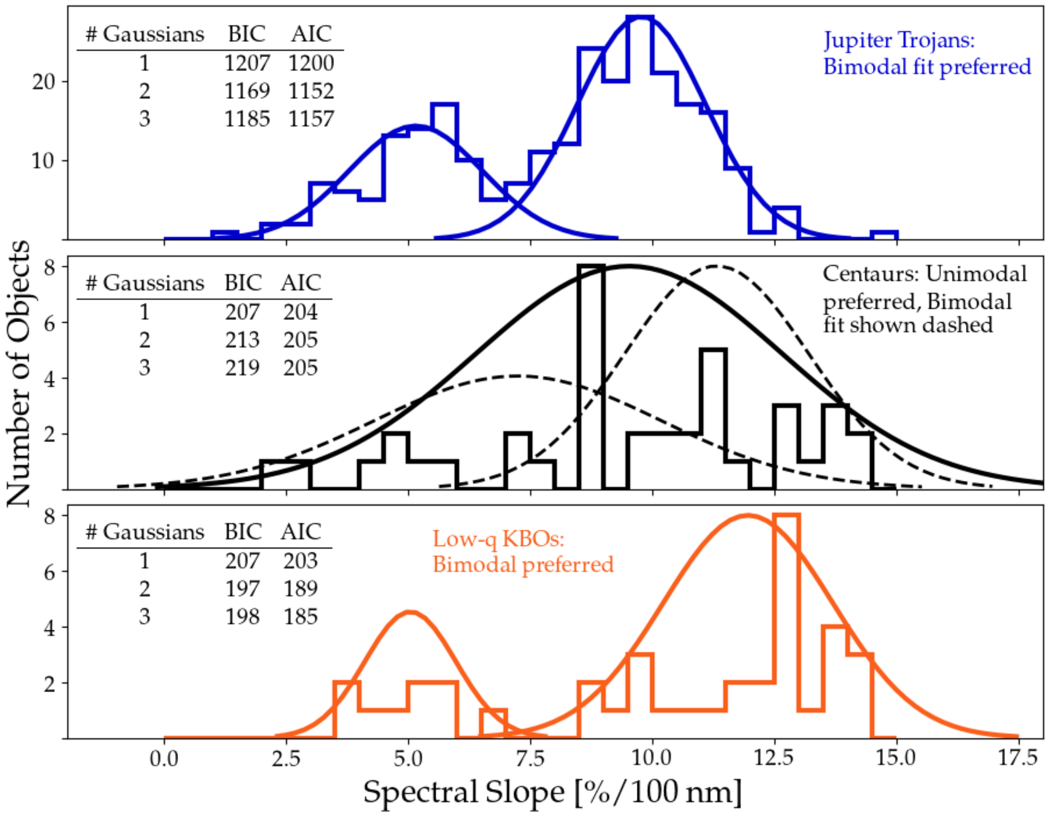

Figure 2.3: Gaussian mixture models for the spectral slopes of the Jupiter Trojans (top panel), Centaurs (middle panel), and low-perihelion Kuiper belt objects (bottom panel). Only objects with spectral slope < 15%, or those objects with Trojan-like slopes are included. For the Centaurs, a single Gaussian model is preferred to describe the data, with a double Gaussian fit shown with dotted lines for reference. By contrast, the spectral slopes of the low-q KBOs are best described by a bimodal model, with a Δ AIC = 14 between the unimodal and bimodal models.

spectral slope Centaurs. Selecting all Centaurs and low-q KBOs with spectral slope < 15% and comparing the slope distributions with a Kolmogorov-Smirnov test, we find that the probability of them being drawn from the same distribution is at $p = 0.058$. Although this result is just under a two-sigma significance, the 94% probability of the two populations having a different distribution in the range of Jupiter Trojan colors invites us to test whether the low-q KBOs or Centaurs are bifurcated similarly to the Jupiter Trojans. Using a Gaussian mixture model, we test how many Gaussians are preferred to describe the distribution of Centaur and low-q KBO colors. For the low-q KBOs, we find that a bifurcated model has a significantly lower Akaike Information criterion than a single Gaussian model, with Δ AIC = 14 (Akaike, 1974). For the Centaurs, the AIC is higher for any model with more than one Gaussian, indicating that a bifurcated model does not well-describe the slopes of the Centaurs. In Figure 2.3, we show the result of mixture models for the spectral slopes of the Centaurs and low-q KBOs along with the Jupiter Trojan colors from the Sloan Digital Sky Survey (Wong, Michael E. Brown, and Joshua P. Emery, 2014). We report both the AIC and BIC for the one, two, and three Gaussian mixture models for all three populations. The two means of the mixture model for the slopes $< 15\%$ low-q KBOs are close to the two colors of the Jupiter Trojan population, implying that the "Red" low-q KBOs have a similar color distribution to the Jupiter Trojans. A factor that also suggests the similarity between low-q KBOs and Trojans is that the ratio of objects with Trojan Red colors to Trojan Less Red colors seems to be replicated in the low-q KBO population. However, a notable inconsistency between the Trojan and low-q KBO colors is that the redder component of the two sub-populations in the low-q KBOs is slightly redder than the mean colors of the "Trojan Red" subpopulation, as seen in the right panel of Figure 2.3. A similar effect was found in Wong and Michael E. Brown, 2017b, who examine the Hilda asteroid population and find that their colors are bifurcated similarly to the Trojans, but with the mean colors shifted towards slightly more neutral values. The Hildas lie between the asteroid belt and Jupiter in the 3:2 mean motion resonance at 4 AU, and are thought to have a common origin story with the Trojans (Marsset et al., 2014; Wong and Michael E. Brown, 2017b). The successive shifts in the color bifurcation from the Trojan-like component of the low-q KBOs to the Jupiter Trojans to the Hildas indicates that spectral slopes could become slightly more neutral with decreasing heliocentric distances. Our evidence for the Trojan-like bifurcation among more neutrally-colored (Red, slope $< 15\%$) low-q KBOs suggests there exists a subset of objects in the Kuiper belt with Jupiter Trojan-like colors, giving an observational link between the two populations.

2.1.2 Highly Inclined Objects

An interesting subset of objects in the Centaurs and the low-perihelion KBOs are those that have high or retrograde inclinations. The dynamical origin of $i > 50°$ objects remains an open question (Batygin, Adams, et al., 2019). Simulations of the Nice model fail to produce the high-inclination ($i > 50°$) objects we observe in the Kuiper belt (Nesvorný, 2015), such as 2015 BP_{159} or any of the numerous $i > 90°$ Centaurs and low-perihelion KBOs (Gladman et al., 2009; Becker et al., 2018); simply put, the disk-like nature of a protoplanetary disk likely precludes the formation of any sizable reservoir of highly inclined objects. Moreover, starting from the currently observed Kuiper belt, there is no way to produce retrograde objects with $q > 5.2$ AU with the four giant planets (Nesvorný, 2015). All of the 14 low-q KBOs and 3 Centaurs with $i > 50°$ have remarkably similar colors, with spectral slopes between 5% and 20%. If we repeat our statistical comparison of the

Centaurs and low-q KBOs without these inclined objects, the significance of the difference between Centaurs and low-q KBOs lessens from more than 3σ to over 2σ, largely due to the decreased sample size. Similarly, evidence for the bifurcation in Figure 2.3 weakens, with a less significant ΔAIC ~ 7. However, these retrograde objects are a key feature of the low-q KBOs and the Centaurs – our current inability to assess the dynamical pathways of these $i > 60°$ objects does not reduce the significance of the difference in colors of the Centaurs and low-q KBOs. Therefore, our dynamical analysis in the remainder of this paper excludes the high inclination ($i > 50°$) objects from our sample, as these objects cannot be replicated in dynamical simulations of the Kuiper belt and the four gas giants (Batygin and Alessandro Morbidelli, 2017; Batygin, Adams, et al., 2019).

2.2 Origin of Trojan-like colors

We present two possible testable hypotheses for why the colors of the low-perihelion Kuiper belt are distinct from the Centaurs. The first hypothesis is that the average low-q KBO is heated longer than the average Centaur, causing their surfaces to undergo the chemical changes that produce Jupiter Trojan colors, resulting in the population-level color difference we observe. The second hypothesis is a purely dynamical one – the low-q KBOs and Centaurs have distinct source populations with distinct colors, which are then carried over to the two excited populations. To test these hypotheses, we need to obtain the distribution of possible Kuiper belt origins and dynamical lifetimes of our sample of Centaurs and low-q KBOs, and determine whether the populations have significantly different heating histories or source populations.

Dynamical histories of unstable objects are impossible to directly ascertain, as backward integration gives radically different results from infinitesimally small changes to initial conditions. Even starting with thousands of clones for each object and integrating backwards does not correctly link observed Centaurs and low-q KBOs with the Kuiper belt. This method starts with a problematic assumption that these clones are all equally likely to appear from the scattering of Kuiper belt objects. Instead, we create a forward model, integrating a sample Kuiper belt for four billion years to see what differences exist in the dynamical behavior of the bodies that produce Centaurs and low-q KBOs.

Our forward model begins with the Canada-France Ecliptic Plane Survey (CFEPS) L7 simulated Kuiper belt reference population (Petit et al., 2011). We first integrate the reference population with the four giant planets using the `MERCURY` integrator (Chambers, 1999). We exclude objects that are initially low-q KBOs (and thus have an uncertain source) to avoid contaminating our sample of the excited population. We use a hybrid changeover radius of 6 Hill radii, a timestep of 150 days, and an ejection distance of 10000 AU. Every 10 million

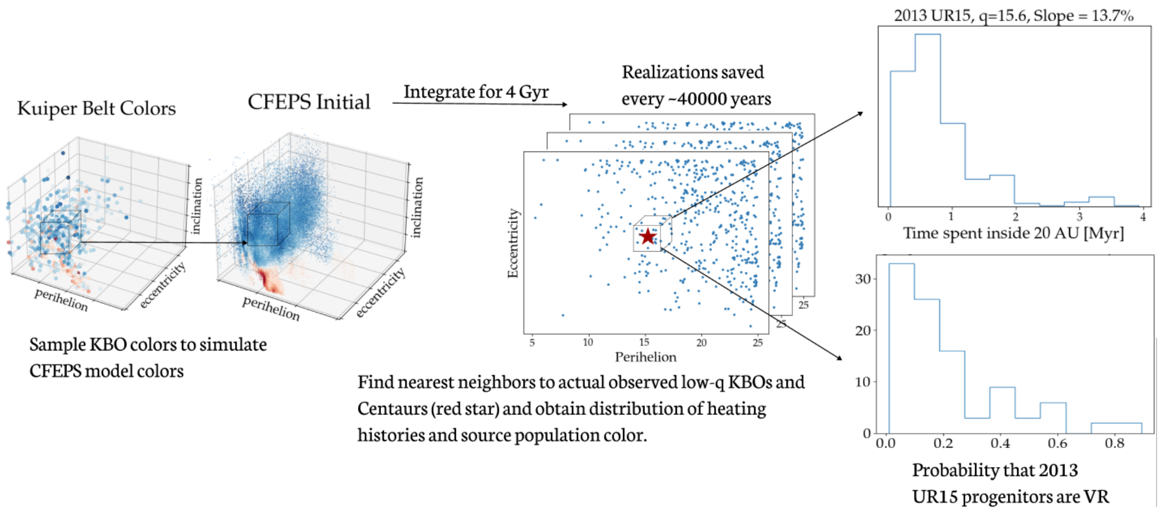

Figure 2.4: Schematic of the method used in section 2.2 for tracking the source and dynamical evolution of low-q KBOs and Centaurs. We begin with the Canada–France Ecliptic Plane Survey (CFEPS) L7 simulated Kuiper belt reference population (Petit et al., 2011), integrating it forward for 4 Gyr with the four giant planets. These integrations produce around 150,000 realizations of the $q < 25$ AU component of the Kuiper belt. Simultaneously, we find the color distribution for each CFEPS object based on the known colors of nearby Kuiper belt objects, using a K-nearest neighbor algorithm. During the integration, we also track the heating history (time spent within 20 AU) of all of the synthetic objects. Using all of these snapshots of synthetically generated low-q KBO and Centaur populations, we then compute statistics on real objects that we have colors for by drawing the closest objects from our simulations. As a result, we obtain distributions on both the possible heating histories and color as a function of original Kuiper belt source for the Centaurs and low-q KBOs from section 2.1.

days (around 25,000 years), we record instantaneously whether each object fits our definition of a Centaur or low-q KBO and its initial orbital elements. Over four billion years, we obtain 150,000 snapshots of our populations of interest, which contain 25.1 million synthetic low-q KBOs and 3.1 million Centaurs. With millions of simulated Centaurs and low-q KBOs each with a full dynamical history, we can begin to test whether a difference in heating or difference in source population is responsible for the distinct color distribution of the Centaurs and low-q KBOs.

We cannot, however, compare all simulated low-q KBOs to all simulated Centaurs to answer our hypotheses. To explain the colors we observe in the specific sample from section 2.1, we must select simulated low-q KBOs and Centaurs that are similarly distributed to the real low-q KBOs and Centaurs. For each low-q KBO and Centaur in the photometric data from section 2.1, we compute statistics on its 1000 nearest synthetic neighbors. Nearest neighbors are determined using the Euclidean distance in eccentricity/inclination/perihelion space, where we have normalized each parameter to be between zero and one. A schematic of this method is shown in Figure 2.4.

2.2.1 Heating Hypothesis

To test the heating hypothesis, we track how much insolation each synthetic object has experienced using a simple metric: time spent within 20 AU. Specifically, we track the time a given object is inside of 20 AU within its orbit, not the time an object has a perihelion of less than 20 AU. This specific threshold is an arbitrary one, and is not due to any sublimation line – repeating our analysis for other thresholds such as 10 or 15 AU produces similar results. By selecting the 1000 synthetic objects closest to each real Centaur and low-q KBO in our sample, we can obtain a statistical distribution of the time spent within 20 AU for each object we have colors for. The left panel of Figure 2.5 shows the median amount (with one sigma error bars) of time spent inside of $r < 20$ AU as a function of current perihelion distance for the Centaurs or low-q KBOs used in our photometric analysis in section 2.1. For Centaurs and low-q KBOs, the typical time spent within 20 AU is 1 to 10 million years, with the low-q KBOs past 15 AU spending more time within 20 AU than the average Centaur.

Having found the distribution of time spent within 20 au for each real Centaur and low-q KBO using the synthetic population generated from the CFEPS simulations, we can evaluate whether the heating histories of the two populations produce the observed distinct colors. In order to determine whether distinct heating histories can reproduce the colors of the two populations, we test whether there exists a critical threshold for time spent within 20 au for the change from Very Red to Red colors that would create a significantly different proportion of Red to Very Red objects in the low-q KBOs as opposed to Centaurs. For each real low-q KBO and Centaur in the left panel of Figure 2.5, we assign a base 50% chance of the object being Red. Starting from a threshold of 20 million years of heating to transition from Very Red to Red, we determine the probability of each object having transitioned to Red colors, given its distribution of time spent within 20 AU. In other words, for each real object, we determine its probability of being Red based on how many of its synthetic look-alikes have spent more time within 20 au within each given time threshold. We then simulate 10,000 draws for the colors of all the objects, thus producing 10,000 simulations of the colors of Centaur and low-q KBOs populations. We then get the median proportion of Red objects in each population as a function of heating threshold for transitioning between the two colors, which is shown in the right panel of Figure 2.5. Regardless of the choice of the minimum amount of time it takes for an object to change color, heating of low-q KBOs and Centaurs results in the low-q KBOs having only slightly fewer Very Red objects than the Centaurs, not distinct enough to match the real proportions. In the 10,000 simulations performed at

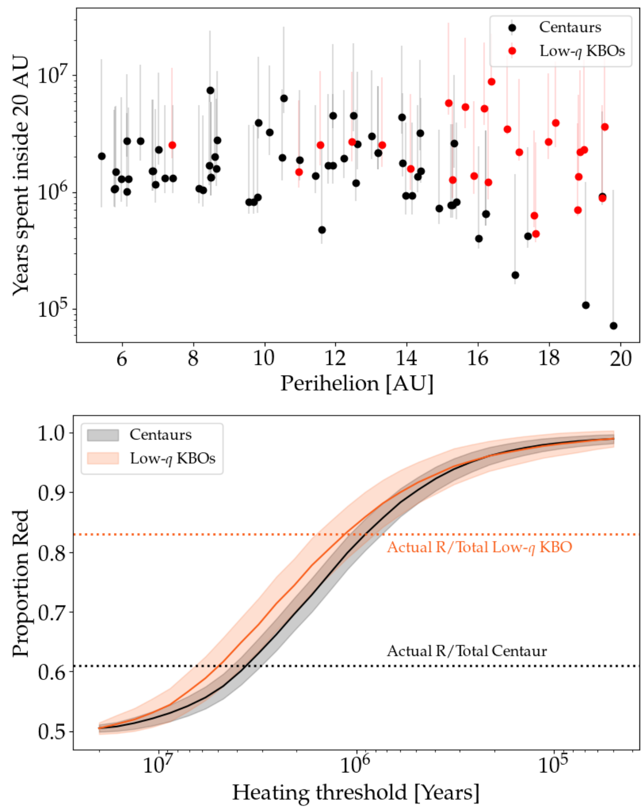

Figure 2.5: *Left panel*: The median total years spent within 20 AU of realizations of simulated objects with orbital elements similar to the observed low-q KBOs (in orange dots) and Centaurs (in black dots). The Centaurs spend a similar amount of time within 20 AU as the low-q KBOs.
Right panel: Simulation of the proportion of Red objects in the two populations (starting from around the KBO Red proportion), assuming heating is responsible for changing Very Red objects into Red ones. The difference between Centaurs and low-q objects in their Red/total ratio never approaches that of the photometric data. Heating is therefore not sufficient to create the observed difference between the two populations.

each heating threshold, at most 4% of the simulations yield a color difference between the two populations that is more than the observed one. All heating thresholds outside the 1-3 Myr range result in all of the simulations yielding a difference in the proportion of Red objects between the two populations that is less than the one observed. It is therefore unlikely that irradiation of surfaces results in the difference between the colors of low-q KBOs and Centaurs.

Heating and stability are a nontrivial result of dynamical interactions, but our modeling suggests that heating is insufficient as an explanation for the more neutral colors of low-q KBOs as compared to the Centaurs. Other, more physical means of modeling heating produce the same result. Computing the solar flux accumulated over the lifetimes of these

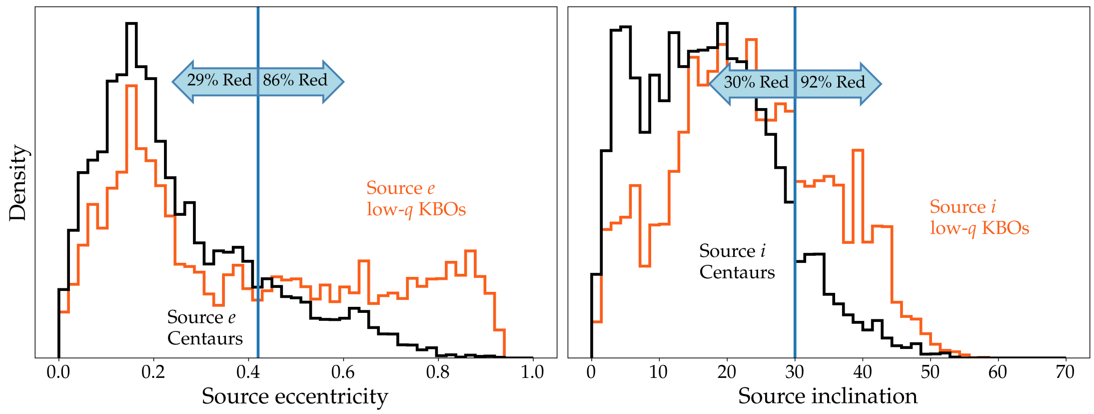

Figure 2.6: Distribution of the eccentricity and inclination of source objects that become dynamically similar to known low-q KBOs or Centaurs at any point in our 4 Gyr simulations. The low-q Kuiper belt has a unique source from objects with $e > 0.6$ or $i > 40°$. Objects with those dynamical characteristics in the Kuiper belt tend to not have very red colors, thus the origin of low-q KBOs in these dynamically hot populations causes the population to have significantly more Red (fewer Very Red) objects. A similar analysis of the rarity of VR objects in the scattered disk was presented in Ali-Dib et al., 2021.

objects after they cross inside of 30 AU produces a nearly identical result to time spent within 20 AU. We use time spent within 20 AU because it is the most conservative metric for heating given the question we are testing – Centaurs are on average at lower perihelia than low-q KBOs, thus, if they spend a similar amount of time within 20 AU, low-q KBOs are heated less. We note that there are indeed spectral changes in the infrared observed on comets that are a result of surface processing, such as those that occur to the 1.5, 2.0, 3.0 micron water features, or the CO_2 absorption feature (Pinto et al., 2023; Javier Licandro et al., 2024). Rather, we find evidence that surface processing on timescales equal to or less than the dynamical lifetimes of these excited objects cannot reproduce the color difference in the visible between Centaurs and the low-q KBOs. Thus, the origin of Jupiter Trojan-like spectral slopes in the visible in the low-q KBO population has to be addressed by comparing the dynamical sources of the two populations.

2.2.2 Source Population Hypothesis

Since heating is unlikely to be responsible for the difference in color between Centaurs and low-q KBOs, we test whether the color distribution in the $q > 30$ AU Kuiper belt, which is the source population for the Centaurs and low-q KBOs, can account for the distinct colors of the two populations. We test whether there are differences in source location of the low-q KBOs and Centaurs from which they inherit their distinct colors. We show the distribution of source eccentricities and inclinations for Centaurs and low-q KBOs in Figure 2.6. The source eccentricities and inclinations are determined by selecting synthetic low-q KBOs and Centaurs near the observed ones and tracing them back to their origin in CFEPS, recording the starting eccentricity and inclination. Despite objects commonly transitioning between these two dynamical classes, the two populations are unevenly sampling the same Kuiper belt source. Centaurs preferentially come from the low-e, low-i part of the Kuiper belt, while low-q KBOs are more likely than Centaurs to come from the high-eccentricity scattered disk or high-inclination populations, such as the most excited of the hot classicals and Plutinos. The more excited populations in the Kuiper belt are known to have fewer VR objects, as shown in Figure 2.6. For objects with eccentricity above 0.4, around 14% are VR, whereas 71% are VR for lower eccentricities. Similarly, among the objects with inclinations above 30°, only 8% are VR. Given that the Centaurs draw more frequently from the less excited population that has significantly more Very Red objects than the excited population, we can test whether these differences are enough to account for their different observed source colors.

Having found that low-q KBOs and Centaurs have differences in their source populations, we can test whether this difference is enough to reproduce the color difference of the two populations. First, we need to determine what is the probability of each synthetic object being Red or Very Red as a consequence of its Kuiper belt source in the CFEPS population. Since the CFEPS population is a model of the observed Kuiper belt, we can use observed colors from MBOSS, Col-OSSOS, and DES (Hainaut, Boehnhardt, and Protopapa, 2012; Schwamb et al., 2019; Bernardinelli, Bernstein, Sako, et al., 2022; Bernardinelli, Bernstein, Jindal, et al., 2023) to get a likelihood that a given CFEPS reference population object is R or VR. We exclude Neptune Trojans, $H < 7$, and Slope error < 7% objects from our Kuiper belt color sample. For each object in CFEPS, we determine its color using a K-nearest neighbors regression on the observed colors from the aforementioned sources. In other words, the color of each object in CFEPS is given by the distance-weighted average of nearby observed Kuiper belt colors. This distance is the Euclidean distance between the CFEPS object and any given object in the MBOSS/Col-OSSOS/DES sample, where inclination, eccentricity, and perihelion are normalized to be between 0 and 1, such that each dynamical parameter is equally weighted. For example, a synthetic low-q KBO that is sourced from the classical Kuiper belt is more likely to be Very Red than one coming from the Scattered disk.

Now that we have the likelihood of an object being R/VR for each synthetic object, we can determine the probability that our real objects are R/VR as described in the beginning of this section. We take the nearest 1000 simulated neighbors to each real low-q KBO and Centaur, and calculate a distance-weighted average of the R/VR probabilities of the synthetic objects. As a result, for each low-q KBO and Centaur in our photometric sample, we have the

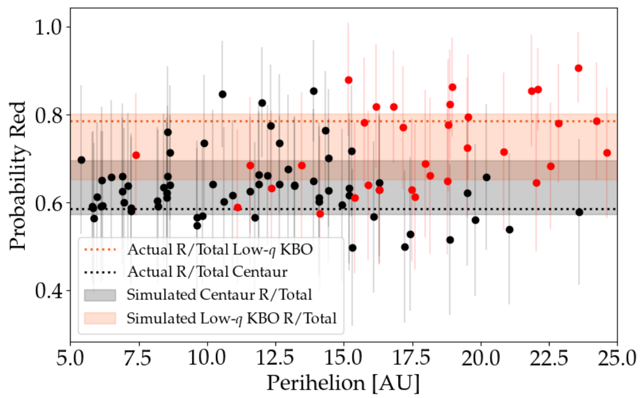

Figure 2.7: Scatterplot of the median probability that a low-q KBO (orange) or Centaur (black) from our photometric sample is Red given its dynamical origin in the Kuiper belt. This probability is determined using the method in Figure 2.4, wherein each real Centaur and low-q KBO is linked to possible Kuiper belt progenitors, whose colors are simulated using a combination of available photometric data. Dashed lines show the true proportions in observed Centaurs and low-q KBOs with $q < 25$ AU, while the shaded areas show the simulated proportion of Red objects with one sigma error. The simulated proportions are consistent with the data proportions for the number of Red objects in the Centaurs and low-q KBOs.

corresponding probability of any given object being R/VR based on its Kuiper belt source.

Finally, to test our hypothesis, we compute the proportion of the low-q KBOs and Centaurs that we expect to be Red, similarly to the statistic obtained in section 2.1, where $58 \pm 6\%$ of Centaurs and $78 \pm 7\%$ of low-q KBOs (now excluding the retrograde objects from the color sample) were found to be Red. Given that we have the probability of each real Centaur and low-q KBO being red, we can simulate 10,000 draws for the color of each object, thus producing 10,000 simulations of the colors of Centaur and low-q KBOs populations. In Figure 2.7, we show the probability that each Centaur and low-q KBO used in our photometric analysis has Red/Very Red colors based on its Kuiper belt source. The shaded regions show the one sigma range for the population proportion of Red objects for the two populations, while the dashed lines show the true proportions from section 2.1. We find that the proportion of Red low-q KBOs derived from propagating the colors of their source population is 0.73 ± 0.07 (where the observed value for the proportion of Red $q < 25$ AU low-q KBOs is 0.78 ± 0.07), while for Centaurs the Red proportion is 0.63 ± 0.06 (where the observed proportion is 0.58 ± 0.06).

While the data proportions of Red objects for both Centaurs and low-q KBOs are within one sigma error bars of the simulated proportions, there is overlap between the simulated proportions for both sets of objects. This indicates that while we can match the Centaur proportion of Red objects or the low-q KBO proportion of Red objects, we do not necessarily match the difference between the two populations of 20%. Of our 10,000 simulations of the Centaur and low-q KBO populations, just over 17% have a difference in Centaur and low-q KBO Red proportion of 20% or more. While this result indicates it is possible that source population differences explain color differences and that this hypothesis is a more likely one than the heating hypothesis, we cannot assert source population differences as the complete explanation without more evidence. One likely possibility for our model not explaining the full difference in colors of the Centaurs and low-q KBOs is that CFEPS does not include enough high eccentricity and high inclination objects. The scattered disk in the CFEPS model is known to be too small (Bernardinelli, Bernstein, Sako, et al., 2022), and more current models, such as those being developed from the OSSOS survey include notably more SDOs and higher-order resonant objects (Kavelaars, Personal communication, 2023). If we increase the number of both $e > 0.8$ and $i > 40°$ objects at the start of the CFEPS simulation by an order of magnitude (simply by duplicating them), we find that in over 35% of our simulations we match the observed difference between the two populations.

Stepping back to the bigger question, the link between colors in the scattered disk, the low-perihelion component of the Kuiper belt, and the Jupiter Trojans provides observational support for the Nice model. According to the Nice model, the scattered disk is sourced from the inner part of the outer planetesimal disk (24–30 AU) (Nesvorný, Vokrouhlický, Alexandersen, et al., 2020), similarly to the Jupiter Trojans, which are the inner disk planetesimals that are scattered and then captured by Jupiter during its final instability (Nesvorný, Vokrouhlický, and Alessandro Morbidelli, 2013). The scattered disk indeed has more neutral colors relative to the rest of the Kuiper belt, similar to the Jupiter Trojans. Our observations of the low-perihelion component of the Kuiper belt find it to have the same preferentially "Red" colors. Then from dynamical simulations, we find that the low-q KBOs preferentially originate from the scattered disk, selecting mostly those objects which were part of the inner part of the planetesimal disk, from which Jupiter Trojans originate. Thus, the Trojan-like colors of the low-q KBOs suggest that the scattered disk and Jupiter Trojans have a common initial Nice model origin in the component of the planetesimal disk closest to the Sun.

2.3 Discussion

Combining our photometric observations on Keck and Palomar with all available data from MBOSS (Hainaut, Boehnhardt, and Protopapa, 2012), Col-OSSOS (Schwamb et al., 2019), and DES (Bernardinelli, Bernstein, Sako, et al., 2022; Bernardinelli, Bernstein, Jindal, et al., 2023), we have isolated the low-perihelion Kuiper belt as a population with Jupiter Trojan-like colors in the outer solar system. The measured colors show that these KBOs with $q < 30$ AU and $a > 30$ AU have a proportion of Red to Very Red objects more than 3σ distinct from Centaurs, which have similar perihelion distances. Critically, we note that the low-perihelion KBOs display a similar bifurcation in colors to the Jupiter Trojans, with a slightly redder color, mimicking how the Hildas, interior to the Trojans, are also bifurcated, but with a slightly bluer set of colors.

More importantly, we have found observational evidence for the Nice model, by linking the Jupiter Trojans and Scattered Disk Objects, which according to the Nice model, have a common source in the inner disk. The low-q KBOs share the more neutral colors of the Scattered Disk and Jupiter Trojans, while having a distinct source in the scattered disk, unlike the Centaurs, which are sourced from the more stable parts of the Kuiper belt. We also demonstrate that these colors cannot have arisen from heating of the low-perihelion population, as similar-perihelion KBO-colored Centaurs and Trojan-colored low-q KBOs have heating histories which do not result in the drastic difference in color shown in Figure 2.2. Instead, we show that the difference in colors of Centaurs and low-q KBOs is plausibly explained by the two populations having different Kuiper belt progenitors. The low-q KBOs are more frequently sourced from the scattered disk and high-inclination population than the Centaurs. Our results indicate that the difference in source populations is preferable to heating as an explanation for the distinct proportions of Red objects in the low-q KBOs and Centaurs. Further improvements to both the simulated models of the Kuiper belt as well as our knowledge of its colors should help fully resolve the question of the origin of the difference in Centaur and low-q KBO colors.

2.4 Observational Details

In the course of our observing campaign, we obtained optical g/i photometry of 34 objects, 24 of which were $q < 25$ AU KBOs, with the P200 telescope at Palomar Observatory and the Keck I 10 meter telescope at Maunakea Observatory. Observations taken at Palomar observatory used the WaSP instrument (Wafer-Scale Imager for Prime) and were collected in three days spread over 2018-20. Observations taken at Maunakea observatory used the LRIS instrument (Low Resolution Imaging Spectrometer) and were collected in two days, one in 2021 and one in 2022. Observations were done in series pairs of g, i or i, g observations from which colors were derived, with at least two but typically four colors obtained for each object, with two sets done an hour apart to confirm object on-sky motion.

Reductions were performed using standard bias subtraction and flat fielding, followed by standard aperture photometry done using Pan-STARRS stars in the field of view of the images to calculate zero points. Apertures were selected to maximize the signal-to-noise, typically close to the FWHM seeing (typical values around 1.5” at Palomar and 1.0” at Keck).

Table 2.1: Palomar Observations for Chapter 2.

Name	Mean m_g^1	Mean m_i^2	Spec. Slope[3] (%/100 nm)	Obs. Date and UT[4]
2004 TE282	24.11 ± 0.11	22.98 ± 0.07	$(18.4 \pm 5.1)\%$	2018 Sep. 23 10:48
2009 MS9	22.19 ± 0.04	21.23 ± 0.04	$(12.7 \pm 0.3)\%$	2018 Sep. 23 09:14
2010 JG210	22.56 ± 0.01	21.62 ± 0.01	$(11.7 \pm 0.3)\%$	2019 July 27 05:37
2011 LZ28	22.17 ± 0.17	21.38 ± 0.14	$(6.9 \pm 4.4)\%$	2020 Sep. 18 07:10
2013 KZ18	21.98 ± 0.06	21.13 ± 0.15	$(8.8 \pm 4.1)\%$	2020 Sep. 18 07:32
2014 JF80	21.71 ± 0.09	21.01 ± 0.08	$(4.0 \pm 4.9)\%$	2020 Sep. 18 05:25
2014 LN28	21.04 ± 0.08	20.19 ± 0.04	$(8.7 \pm 3.3)\%$	2020 Sep. 18 04:42
2014 QV441	22.06 ± 0.06	21.31 ± 0.03	$(5.3 \pm 1.3)\%$	2020 Sep. 18 09:45
2014 SK349	22.92 ± 0.14	22.01 ± 0.12	$(11.3 \pm 0.5)\%$	2020 Sep. 18 10:31
2014 UG241	23.08 ± 0.11	22.12 ± 0.11	$(12.5 \pm 3.0)\%$	2020 Sep. 18 10:12
2014 UT114	21.96 ± 0.07	20.99 ± 0.08	$(12.6 \pm 3.3)\%$	2018 Sep. 23 10:31
2014 WD536	23.10 ± 0.08	22.17 ± 0.10	$(11.7 \pm 5.5)\%$	2020 Sep. 18 09:55
2014 WR509	22.66 ± 0.06	21.75 ± 0.13	$(10.6 \pm 3.4)\%$	2020 Sep. 18 10:50
2015 KZ120	20.52 ± 0.06	19.64 ± 0.02	$(9.9 \pm 1.3)\%$	2019 July 27 05:53
2017 RG16	21.61 ± 0.02	20.88 ± 0.01	$(4.8 \pm 0.2)\%$	2020 Sep. 18 07:22

1) Average apparent g-band magnitude. 2) Average apparent i-band magnitude. 3) Spectral slope is calculated from successive $g - i$ color measurements (where the slope is normalized to V-band following Hainaut, Boehnhardt, and Protopapa, 2012), and will not precisely match the slope calculated from the average magnitudes in each band. 4) Time is of the first observation in the set.

In our images, the average trailing of objects was sub-pixel for the Palomar observations and around one pixel for the Keck observations, with few objects trailing more than 2 pixels. Background photometric stars were characterized and selected using the `DAOfind` algorithm (Stetson, 1987) as implemented in the `Photutils` package (Bradley et al., 2023). Stars fainter than $m_g = 21$, with errors more than 0.03 mags, or with fewer than 5 observations per band were excluded from the zero-point calculations. Due to the differences between SDSS and Pan-STARRS filters, magnitudes were converted using the bandpass transformations given in Tonry et al., 2012. Background subtraction was performed with `SExtractor` (Bertin and Arnouts, 1996). A notable point in the reduction is that we only use one of the four available detectors in the P200 WaSP images, as bias drift over the night causes each detector to scale in a visibly different way even after biasing, flat fielding, and background subtraction. We summarize the results of our observations in Table 2.1 and Table 2.2. The errors provided for the observations are obtained by calculating the standard deviation from multiple measurements of the color of the object, rather than Poisson noise on the photometry, as the photometric error for a set of measurements in any one band is dwarfed by

Table 2.2: Keck Observations for Chapter 2.

Name	m_g^1	m_i^2	Spec. Slope[3] (%/100 nm)	Obs. Date
2005 ER318	23.44 ± 0.01	22.62 ± 0.03	(7.7 ± 0.8)%	2022 April 28 08:53
2007 BP102	23.97 ± 0.07	22.97 ± 0.09	(14.0 ± 3.5)%	2021 May 15 08:07
2008 KV42	23.47 ± 0.03	22.61 ± 0.03	(9.2 ± 1.6)%	2021 May 15 12:58
2011 FY9	23.16 ± 0.04	22.16 ± 0.10	(13.9 ± 3.5)%	2021 May 15 11:21
2012 GU11	23.80 ± 0.03	22.71 ± 0.05	(17.0 ± 2.3)%	2021 May 15 11:06
2012 GX17	23.57 ± 0.05	22.87 ± 0.14	(3.7 ± 4.4)%	2021 May 15 07:54
2013 FJ28	22.77 ± 0.16	21.84 ± 0.06	(11.6 ± 5.6)%	2021 May 15 07:37
2013 LU28	19.42 ± 0.01	18.46 ± 0.01	(12.6 ± 0.5)%	2022 April 28 07:55
2013 ME14	23.84 ± 0.05	22.34 ± 0.07	(32.7 ± 2.5)%	2021 May 15 13:38
2014 BF70	21.26 ± 0.03	20.49 ± 0.01	(5.8 ± 0.4)%	2022 April 28 08:51
2014 LM28	23.18 ± 0.07	22.30 ± 0.09	(9.7 ± 1.5)%	2022 April 28 12:56
2014 LN28	21.47 ± 0.06	20.52 ± 0.02	(12.2 ± 2.4)%	2021 May 15 14:18
2014 XO40	21.11 ± 0.04	19.88 ± 0.04	(22.3 ± 2.1)%	2022 April 28 09:59
2014 XQ40	22.31 ± 0.09	21.42 ± 0.04	(10.0 ± 3.1)%	2022 April 28 10:12
2015 BE568	22.91 ± 0.17	22.11 ± 0.07	(6.9 ± 4.9)%	2021 May 15 07:43
2017 CX33	23.23 ± 0.06	22.08 ± 0.02	(19.2 ± 1.3)%	2021 May 15 05:37
2017 FO161	23.50 ± 0.09	22.15 ± 0.10	(27.0 ± 2.3)%	2021 May 15 06:02
2017 KZ31	23.04 ± 0.12	22.08 ± 0.06	(12.6 ± 4.1)%	2022 April 28 05:27
2017 YG5	22.45 ± 0.06	21.61 ± 0.02	(8.6 ± 1.6)%	2022 April 28 08:48

1) Apparent *g*-band magnitude. 2) Apparent *i*-band magnitude. 3) Spectral slope calculated using the *g* and *i* measurements normalized to V-band following Hainaut, Boehnhardt, and Protopapa, 2012.

the variability of an object and observing conditions over the course of a night. We convert our $g - i$ colors to spectral slopes normalized to V band at 544.8 nm, following Hainaut, Boehnhardt, and Protopapa, 2012. Solar colors for g and i band are taken from Willmer, 2018.

References

Akaike, H. (Jan. 1974). "A New Look at the Statistical Model Identification". In: *IEEE Transactions on Automatic Control* 19, pp. 716–723.

Ali-Dib, Mohamad et al. (July 2021). "The Rarity of Very Red Trans-Neptunian Objects in the Scattered Disk". In: *AJ* 162.1, 19, p. 19. DOI: 10.3847/1538-3881/abf6ca. arXiv: 2104.04271 [astro-ph.EP].

Batygin, Konstantin, Fred C. Adams, et al. (May 2019). “The planet nine hypothesis”. In: *PhR* 805, pp. 1–53. DOI: 10.1016/j.physrep.2019.01.009. arXiv: 1902.10103 [astro-ph.EP].

Batygin, Konstantin, Michael E. Brown, and Hayden Betts (Jan. 2012). “Instability-driven Dynamical Evolution Model of a Primordially Five-planet Outer Solar System”. In: *ApJL* 744.1, L3, p. L3. DOI: 10.1088/2041-8205/744/1/L3. arXiv: 1111.3682 [astro-ph.EP].

Batygin, Konstantin and Alessandro Morbidelli (Dec. 2017). “Dynamical Evolution Induced by Planet Nine”. In: *AJ* 154.6, 229, p. 229. DOI: 10.3847/1538-3881/aa937c. arXiv: 1710.01804 [astro-ph.EP].

Becker, J. C. et al. (Aug. 2018). “Discovery and Dynamical Analysis of an Extreme Trans-Neptunian Object with a High Orbital Inclination”. In: *AJ* 156.2, 81, p. 81. DOI: 10.3847/1538-3881/aad042. arXiv: 1805.05355 [astro-ph.EP].

Bernardinelli, Pedro H., Gary M. Bernstein, Nicholas Jindal, et al. (Nov. 2023). “Photometry of Outer Solar System Objects from the Dark Energy Survey. I. Photometric Methods, Light-curve Distributions, and Trans-Neptunian Binaries”. In: *ApJS* 269.1, 18, p. 18. DOI: 10.3847/1538-4365/acf6bf. arXiv: 2304.03017 [astro-ph.EP].

Bernardinelli, Pedro H., Gary M. Bernstein, Masao Sako, et al. (Feb. 2022). “A Search of the Full Six Years of the Dark Energy Survey for Outer Solar System Objects”. In: *ApJS* 258.2, 41, p. 41. DOI: 10.3847/1538-4365/ac3914. arXiv: 2109.03758 [astro-ph.EP].

Bertin, E. and S. Arnouts (June 1996). “SExtractor: Software for source extraction.” In: *A&AS* 117, pp. 393–404. DOI: 10.1051/aas:1996164.

Bradley, Larry et al. (May 2023). *astropy/photutils: 1.8.0*. Version 1.8.0. DOI: 10.5281/zenodo.7946442. URL: https://doi.org/10.5281/zenodo.7946442.

Brown, M. E. (Dec. 2016). “The 3-4 μm Spectra of Jupiter Trojan Asteroids”. In: *AJ* 152.6, 159, p. 159. DOI: 10.3847/0004-6256/152/6/159. arXiv: 1606.03013 [astro-ph.EP].

Brown, M. E., E. L. Schaller, and W. C. Fraser (June 2012). “Water Ice in the Kuiper Belt”. In: *AJ* 143.6, 146, p. 146. DOI: 10.1088/0004-6256/143/6/146. arXiv: 1204.3638 [astro-ph.EP].

Brown, Michael E. and Wesley C. Fraser (July 2023). “The State of CO and CO_2 Ices in the Kuiper Belt as Seen by JWST”. In: *PSJ* 4.7, 130, p. 130. DOI: 10.3847/PSJ/ace2ba. arXiv: 2306.17051 [astro-ph.EP].

Chambers, J. E. (Apr. 1999). “A hybrid symplectic integrator that permits close encounters between massive bodies”. In: *MNRAS* 304.4, pp. 793–799. DOI: 10.1046/j.1365-8711.1999.02379.x.

Chandler, Colin Orion et al. (Apr. 2020). “Cometary Activity Discovered on a Distant Centaur: A Nonaqueous Sublimation Mechanism”. In: *ApJL* 892.2, L38, p. L38. DOI: 10.3847/2041-8213/ab7dc6. arXiv: 2003.04904 [astro-ph.EP].

De Prá, Mário N. et al. (May 2024). "Widespread CO_2 and CO ices in the trans-Neptunian population revealed by JWST/DiSCo-TNOs". In: *Nature Astronomy*. DOI: 10.1038/s41550-024-02276-x.

di Sisto, R. P., A. Brunini, and G. C. de Elía (Sept. 2010). "Dynamical evolution of escaped plutinos, another source of Centaurs". In: *A&A* 519, A112, A112. DOI: 10.1051/0004-6361/200913668. arXiv: 1005.3267 [astro-ph.EP].

Doressoundiram, A. et al. (Oct. 2002). "The Color Distribution in the Edgeworth-Kuiper Belt". In: *AJ* 124.4, pp. 2279–2296. DOI: 10.1086/342447. arXiv: astro-ph/0206468 [astro-ph].

Emery, J. P., D. M. Burr, and D. P. Cruikshank (Jan. 2011). "Near-infrared Spectroscopy of Trojan Asteroids: Evidence for Two Compositional Groups". In: *AJ* 141.1, 25, p. 25. DOI: 10.1088/0004-6256/141/1/25. arXiv: 1012.1284 [astro-ph.EP].

Fraser, Wesley C. et al. (Feb. 2014). "The Absolute Magnitude Distribution of Kuiper Belt Objects". In: *ApJ* 782.2, 100, p. 100. DOI: 10.1088/0004-637X/782/2/100. arXiv: 1401.2157 [astro-ph.EP].

Gladman, B. et al. (June 2009). "Discovery of the First Retrograde Transneptunian Object". In: *ApJL* 697.2, pp. L91–L94. DOI: 10.1088/0004-637X/697/2/L91.

Hainaut, O. R., H. Boehnhardt, and S. Protopapa (Oct. 2012). "Colours of minor bodies in the outer solar system. II. A statistical analysis revisited". In: *A&A* 546, A115, A115. DOI: 10.1051/0004-6361/201219566. arXiv: 1209.1896 [astro-ph.EP].

Jewitt, David (May 2009). "The Active Centaurs". In: *AJ* 137.5, pp. 4296–4312. DOI: 10.1088/0004-6256/137/5/4296. arXiv: 0902.4687 [astro-ph.EP].

— (Feb. 2018). "The Trojan Color Conundrum". In: *AJ* 155.2, 56, p. 56. DOI: 10.3847/1538-3881/aaa1a410.48550/arXiv.1712.04855. arXiv: 1712.04855 [astro-ph.EP].

Jewitt, David and Karen J. Meech (Nov. 1986). "Cometary Grain Scattering versus Wavelength, or, "What Color Is Comet Dust?"" In: *ApJ* 310, p. 937. DOI: 10.1086/164745.

Levison, Harold F. and Martin J. Duncan (May 1997). "From the Kuiper Belt to Jupiter-Family Comets: The Spatial Distribution of Ecliptic Comets". In: *Icarus* 127.1, pp. 13–32. DOI: 10.1006/icar.1996.5637.

Levison, Harold F., Alessandro Morbidelli, et al. (July 2008). "Origin of the structure of the Kuiper belt during a dynamical instability in the orbits of Uranus and Neptune". In: *Icarus* 196.1, pp. 258–273. DOI: 10.1016/j.icarus.2007.11.035. arXiv: 0712.0553 [astro-ph].

Licandro, Javier et al. (Dec. 2024). "Thermal evolution of trans-Neptunian objects through observations of Centaurs with JWST". In: *Nature Astronomy*. DOI: 10.1038/s41550-024-02417-2.

Lisse, C. M. et al. (Nov. 2022). "29P/Schwassmann-Wachmann 1: A Rosetta Stone for Amorphous Water Ice and CO to CO_2 Conversion in Centaurs and Comets?" In: *PSJ* 3.11, 251, p. 251. DOI: 10.3847/PSJ/ac9468. arXiv: 2209.09136 [astro-ph.EP].

Marsset, M. et al. (Aug. 2014). "Similar origin for low- and high-albedo Jovian Trojans and Hilda asteroids?" In: *Astronomy & Astrophysics* 568, p. L7. ISSN: 1432-0746. DOI: 10.1051/0004-6361/201424105. URL: http://dx.doi.org/10.1051/0004-6361/201424105.

Melita, M. D. and J. Licandro (Mar. 2012). "Links between the dynamical evolution and the surface color of the Centaurs". In: *A&A* 539, A144, A144. DOI: 10.1051/0004-6361/201117439.

Morbidelli, A. et al. (May 2005). "Chaotic capture of Jupiter's Trojan asteroids in the early Solar System". In: *Nature* 435.7041, pp. 462–465. DOI: 10.1038/nature03540.

Morbidelli, Alessandro (May 1997). "Chaotic Diffusion and the Origin of Comets from the 2/3 Resonance in the Kuiper Belt". In: *Icarus* 127.1, pp. 1–12. DOI: 10.1006/icar.1997.5681.

— (Nov. 2010). "A coherent and comprehensive model of the evolution of the outer Solar System". In: *Comptes Rendus Physique* 11, pp. 651–659. DOI: 10.1016/j.crhy.2010.11.001. arXiv: 1010.6221 [astro-ph.EP].

Morbidelli, Alessandro, Ramon Brasser, et al. (Nov. 2010). "Evidence from the Asteroid Belt for a Violent Past Evolution of Jupiter's Orbit". In: *AJ* 140.5, pp. 1391–1401. DOI: 10.1088/0004-6256/140/5/1391. arXiv: 1009.1521 [astro-ph.EP].

Morbidelli, Alessandro, Harold F. Levison, et al. (July 2009). "Considerations on the magnitude distributions of the Kuiper belt and of the Jupiter Trojans". In: *Icarus* 202.1, pp. 310–315. DOI: 10.1016/j.icarus.2009.02.033.

Nesvorný, David (Sept. 2015). "Evidence for Slow Migration of Neptune from the Inclination Distribution of Kuiper Belt Objects". In: *AJ* 150.3, 73, p. 73. DOI: 10.1088/0004-6256/150/3/73. arXiv: 1504.06021 [astro-ph.EP].

— (Sept. 2018). "Dynamical Evolution of the Early Solar System". In: *ARA&A* 56, pp. 137–174. DOI: 10.1146/annurev-astro-081817-052028. arXiv: 1807.06647 [astro-ph.EP].

Nesvorný, David and Alessandro Morbidelli (Oct. 2012). "Statistical Study of the Early Solar System's Instability with Four, Five, and Six Giant Planets". In: *AJ* 144.4, 117, p. 117. DOI: 10.1088/0004-6256/144/4/117. arXiv: 1208.2957 [astro-ph.EP].

Nesvorný, David, David Vokrouhlický, Mike Alexand ersen, et al. (July 2020). "OSSOS XX: The Meaning of Kuiper Belt Colors". In: *AJ* 160.1, 46, p. 46. DOI: 10.3847/1538-3881/ab98fb. arXiv: 2006.01806 [astro-ph.EP].

Nesvorný, David, David Vokrouhlický, and Alessandro Morbidelli (May 2013). "Capture of Trojans by Jumping Jupiter". In: *ApJ* 768.1, 45, p. 45. DOI: 10.1088/0004-637X/768/1/45. arXiv: 1303.2900 [astro-ph.EP].

Peixinho, Nuno et al. (2020). "From Centaurs to Comets - 40 years". In: *The Trans-Neptunian Solar System*. Ed. by Dina Prialnik, Maria Antoinetta Barucci, and Leslie Young, pp. 307–329. DOI: 10.1016/B978-0-12-816490-7.00014-X.

Petit, J. -M. et al. (Oct. 2011). "The Canada-France Ecliptic Plane Survey—Full Data Release: The Orbital Structure of the Kuiper Belt". In: *AJ* 142.4, 131, p. 131. DOI: 10.1088/0004-6256/142/4/13110.48550/arXiv.1108.4836. arXiv: 1108.4836 [astro-ph.EP].

Pinto, O. Harrington et al. (Nov. 2023). "First Detection of CO_2 Emission in a Centaur: JWST NIRSpec Observations of 39P/Oterma". In: *PSJ* 4.11, 208, p. 208. DOI: 10.3847/PSJ/acf928. arXiv: 2309.11486 [astro-ph.EP].

Schwamb, Megan E. et al. (July 2019). "Col-OSSOS: The Colors of the Outer Solar System Origins Survey". In: *ApJS* 243.1, 12, p. 12. DOI: 10.3847/1538-4365/ab2194. arXiv: 1809.08501 [astro-ph.EP].

Stetson, Peter B. (Mar. 1987). "DAOPHOT: A Computer Program for Crowded-Field Stellar Photometry". In: *PASP* 99, p. 191. DOI: 10.1086/131977.

Tegler, S. C. and W. Romanishin (Mar. 1998). "Two distinct populations of Kuiper-belt objects". In: *Nature* 392.6671, pp. 49–51. DOI: 10.1038/32108.

Tiscareno, Matthew S. and Renu Malhotra (Dec. 2003). "The Dynamics of Known Centaurs". In: *AJ* 126.6, pp. 3122–3131. DOI: 10.1086/379554. arXiv: astro-ph/0211076 [astro-ph].

Tonry, J. L. et al. (May 2012). "The Pan-STARRS1 Photometric System". In: *ApJ* 750.2, 99, p. 99. DOI: 10.1088/0004-637X/750/2/99. arXiv: 1203.0297 [astro-ph.IM].

Tsiganis, K. et al. (May 2005). "Origin of the orbital architecture of the giant planets of the Solar System". In: *Nature* 435.7041, pp. 459–461. DOI: 10.1038/nature03539.

Willmer, Christopher N. A. (June 2018). "The Absolute Magnitude of the Sun in Several Filters". In: *ApJS* 236.2, 47, p. 47. DOI: 10.3847/1538-4365/aabfdf. arXiv: 1804.07788 [astro-ph.SR].

Wong, Ian and Michael E. Brown (Oct. 2016). "A Hypothesis for the Color Bimodality of Jupiter Trojans". In: *AJ* 152.4, 90, p. 90. DOI: 10.3847/0004-6256/152/4/90. arXiv: 1607.04133 [astro-ph.EP].

— (Apr. 2017a). "The Bimodal Color Distribution of Small Kuiper Belt Objects". In: *AJ* 153.4, 145, p. 145. DOI: 10.3847/1538-3881/aa60c3. arXiv: 1702.02615 [astro-ph.EP].

— (Feb. 2017b). "The Color-Magnitude Distribution of Hilda Asteroids: Comparison with Jupiter Trojans". In: *AJ* 153.2, 69, p. 69. DOI: 10.3847/1538-3881/153/2/69. arXiv: 1701.00367 [astro-ph.EP].

Wong, Ian, Michael E. Brown, Jordana Blacksberg, et al. (Apr. 2019). "Hubble Ultraviolet Spectroscopy of Jupiter Trojans". In: *AJ* 157.4, 161, p. 161. DOI: 10.3847/1538-3881/ab0e00. arXiv: 1903.03576 [astro-ph.EP].

Wong, Ian, Michael E. Brown, and Joshua P. Emery (Dec. 2014). "The Differing Magnitude Distributions of the Two Jupiter Trojan Color Populations". In: *AJ* 148.6, 112, p. 112. DOI: 10.1088/0004-6256/148/6/112. arXiv: 1408.2485 [astro-ph.EP].

Wong, Ian, Michael E. Brown, Joshua P. Emery, et al. (Apr. 2024). "JWST Near-infrared Spectroscopy of the Lucy Jupiter Trojan Flyby Targets: Evidence for OH Absorption, Aliphatic Organics, and CO_2". In: *PSJ* 5.4, 87, p. 87. DOI: 10.3847/PSJ/ad2fc3. arXiv: 2311.11531 [astro-ph.EP].

Chapter 3

THE PERTURBATION THEORY APPROACH TO STABILITY IN THE SCATTERED DISK

Belyakov, Matthew and Konstantin Batygin (Jan. 2026). "The perturbation theory approach to stability in the scattered disk". In: *Icarus* 443, 116773, p. 116773. DOI: 10.1016/j.icarus.2025.116773. arXiv: 2508.10119 [astro-ph.EP].

Scattered disk objects (SDOs) are distant minor bodies that orbit the Sun on highly eccentric orbits, frequently with perihelia near Neptune's orbit. Gravitational perturbations due to Neptune frequently lead to chaotic dynamics, with the degree of chaotic diffusion set by an object's perihelion distance. Batygin, Mardling, and Nesvorný, 2021 developed a perturbative approach for scattered disk dynamics, finding that, to leading order in semi-major axis ratio, an infinite series of $2 : j$ resonances drives the dynamics of the distant scattered disk, with overlaps between resonances driving chaotic motion. In this work we extend this model by taking the spherical harmonic expansion for Neptune's gravitational potential to octupole order and beyond. In continuing the expansion out to smaller semi-major axis limits, we find that the $1 : j$ and $3 : j$ resonances that emerge in the octupole expansion do not individually set new limits on the stability boundary. Instead, we find that for increasingly Neptune-proximate orbits, resonances of progressively higher index are dominant in explaining the emergence of chaotic behavior. In this picture, the mutual intersections between series of $2 : j$, $3 : j$, $4 : j \ldots$, resonant chains explain local chaotic evolution of SDOs and shape the dynamical distribution of the population at large.

3.1 Introduction

Since the discovery of the first body past Pluto, 1992 QB1 (Jewitt, Luu, and Marsden, 1992), the taxonomy of the Kuiper belt has expanded to include numerous sub-populations, each one shedding light on the evolution of the outer solar system. The distinctions between sub-populations of the Kuiper belt are based on a few criteria: whether or not objects are trapped in a quasi-stable resonance, whether they experience largely secular evolution, or whether they scatter chaotically off of Neptune (Saillenfest, 2020). Within this broad and diverse census of Trans-Neptunian objects (TNOs), a particularly distinctive population is the scattered disk, which is composed of highly eccentric, distant, and relatively planar orbits ($q \gtrsim 30$ au, $a \gtrsim 50$ au, $i \lesssim 20°$). A by-product of the early outwards scattering of planetesimals by Neptune's migration (Gomes et al., 2008; Nesvorný, 2018), the scattered disk extends to hundreds of au away from the Sun, thus providing a testing ground for dynamical interactions in the outer solar system, as close encounters with Neptune shape the long-term evolution of scattered disk objects (SDOs).

The scattering dynamics themselves are principally facilitated by the interactions SDOs have with Neptune at perihelion. The strong perturbations from Neptune lead to chaotic evolution as a result of which SDOs are driven out of the solar system, either by diffusion to large enough semi-major axes for galactic effects to ensue, or by becoming centaurs or low-perihelion KBOs (objects with $q < 30$, with centaurs also having $a < 30$), and finally being ejected by Jupiter. The long-term instability of SDO orbits distinguishes the population from detached Kuiper belt objects, which reside at large enough perihelia to avoid short-period effects from Neptune. Understanding the chaotic dynamics of the scattered disk is an essential component of population studies in the outer solar system, such as those of KBO orbital clustering (Batygin, Adams, et al., 2019; Pichierri and Batygin, 2025; Siraj, Chyba, and Tremaine, 2025), or analyses based on surface composition (Sheppard, 2010; Nesvorný et al., 2020; Ali-Dib et al., 2021; Pike et al., 2023; Belyakov, Brown, and Al-Kibbi, 2024).

Presently, there are three broad approaches for studying the dynamics of the scattered disk. The simplest and most realistic approach is direct integration of test particles (examples include Fernández, Gallardo, and Brunini 2004; Volk and Malhotra 2008). Direct integration is useful for understanding population statistics and behavior at large scales across the scattered disk, but does not readily yield insight into how the celestial mechanics of the Sun-Neptune-SDO three body system lead to specific dynamical outcomes.

The second approach is the mapping approach, in which scattered disk dynamics are treated as a perturbed two-body problem with a periodic kick applied at perihelion. Historically, this approach has relied on the Kepler map to explain the evolution of long-period comets and can be applied to the most eccentric scattered disk objects (Malyshkin and Tremaine, 1999). Recent work by Hadden and Tremaine, 2024 uses a twist map to describe the evolution of a test particle subject to pericenter-passage kicks. In particular, Hadden and Tremaine, 2024 use this approach to derive resonant widths for mean-motion resonances (MMRs), and by computing a covering fraction of resonances in any given location of phase space are able to predict the onset of chaos in the scattered disk. This mapping approach applies a perturbative treatment to SDOs with long-period orbits, but converges to direct integration for shorter period orbits that are more affected by short-period terms from Neptune. Although the novel method of Hadden and Tremaine, 2024 is able to provide a single curve for the stability boundary of the scattered disk, it leaves open the question of which specific resonant terms are relevant to the dynamical evolution of any given SDO.

Finally, Batygin, Mardling, and Nesvorný, 2021 characterized the dynamics of the scattered disk using a fully analytic model, seeking to not only place the onset of chaos at a numerical boundary, but also qualitatively explain the underlying machinery of how scattered disk objects go unstable. Using the disturbing function expanded in semi-major axis ratio ($\alpha = a_{\mathrm{N}}/a$) for the circular, restricted, three-body problem, Batygin, Mardling, and Nesvorný, 2021 derived a functional form for the critical value of perihelion (q_{crit}) below which chaos ensues at a given semi-major axis. This result follows from the application of the Chirikov criterion (Chirikov, 1979) for resonance overlap to the infinite chain of $2 : j$ resonances, which in turn arises from the resonant argument of the quadrupole expansion of the disturbing function[1]. However, this quadrupole analytic approach breaks down at semi-major axis distances below ~400 au, as values of q_{crit} unphysically drop below 30 au. Therefore, a full analytic understanding of the emergence of chaotic dynamics and scattering in the restricted, circular, three-body problem, remains incomplete in the $a \sim 50 - 400$ AU region of the scattered disk that most known SDOs occupy.

In this work, we expand on the approach of Batygin, Mardling, and Nesvorný, 2021, seeking to construct a predictive theory that does not assume that the Neptune-SDO semi-major axis ratio is a small number. We begin by extending the expansion to the next order – octupole. This expansion generates two new classes of resonances, $1 : j$ and $3 : j$, but neither of them individually is able to account for the onset of scattering any better than the quadrupole theory. Quantitatively, this is because each additional term appears to scale in a similar way, meaning that no individual higher order term will define the behavior after the $2 : j$ resonant chain begins to break down. Instead, we find that the spacing of resonances of increasing index sets the boundary for chaos in the scattered disk.

This work is organized as follows. In section 3.2, we expand the disturbing function to octupole order and illustrate the inability of individual higher order terms to predict the onset of chaos within 400 au. In section 3.3, we show the results of our general expansion to higher order, and use this expansion to generate a stability boundary that matches orbital integrations of the scattered disk and measurements of the chaos indicator MEGNO. In subsection 3.3.1, we arrive at the critical insight that overlap between resonances of all orders at a given point in phase space contribute to chaotic diffusion, and use this notion to develop a modified version of the Chirikov criterion to generate a local boundary for the onset of chaotic diffusion. We then combine the local picture of resonance overlap to generate a single stability boundary in subsection 3.3.2. We summarize our results and look to future work in section 3.4.

[1]See equation 5 of Batygin, Mardling, and Nesvorný, 2021.

3.2 Octupole Theory

Expanding the disturbing function out to octupole order largely resembles the quadrupole expansion in Batygin, Mardling, and Nesvorný (2021). We begin by stating the assumptions made in the perturbative model for the circular restricted three-body problem, highlighting changes made from previous work. We treat objects in the scattered disk as test particles, however we no longer limit ourselves to the case where the semi-major axis of the SDO is much larger than that of Neptune ($\alpha = a_n/a < 1$ instead of $\alpha \ll 1$). This relaxed assumption necessitates expanding the disturbing function to progressively higher order as α approaches unity. Secondly, we neglect Neptune's eccentricity as the existence of the scattered disk is not contingent on the ellipticity of Neptune's orbit. Finally, we restrict Neptune and the SDO to a common plane, neglecting inclination dynamics.

The disturbing function for the co-planar three-body system with the Sun, Neptune, and an SDO (exterior massless test particle) is given by (Kaula, 1962; Mardling, 2013):

$$\begin{aligned}\mathcal{R} = \frac{\mathcal{G}m_N}{a} &\sum_{\ell=2}^{\infty} \sum_{m=m_{min}}^{\ell} \sum_{j'=-\infty}^{\infty} \sum_{j=-\infty}^{\infty} c_{\ell m}^2 \mathcal{M}_\ell \\ &\times \alpha^\ell X_{j'}^{\ell,m}(e_N) X_j^{-(\ell+1),m}(e) \\ &\times \cos(j' M_N - jM + m(\omega_N - \omega)).\end{aligned} \tag{3.1}$$

In this series expansion, ℓ sets the degree of the expansion, m determines the order of the resonance, and j is the resonant index. In this nomenclature, an $m : j$ resonance is a mean-motion resonance of order m and index j, where the SDO completes m orbits in the time Neptune completes j orbits. We expand the above expression to octupole order, setting $\ell_{\max} = 3$ (the dynamics of the $\ell = 2$ term are explored in Batygin, Mardling, and Nesvorný 2021). The following simplifications and substitutions can be made based on this restriction and the assumptions from above:

1. Mass factor $\mathcal{M}_3 = \left(m_\odot^2 - m_N^2\right) / \left(m_\odot + m_N\right)^2 \approx 1$.

2. Hansen coefficients that depend on the eccentricity of Neptune can be neglected: $X_{j'}^{\ell,m}(e_N) = 1$. This also sets $j' = m$, as for $j' \neq m$, $X_{j'}^{\ell,m}(e_N) = 0$.

3. Set ω_N to 0 without loss of generality, as $e_\mathrm{N} \to 0$.

From these assumptions, the disturbing function can be simplified to a more tractable form:

$$\begin{aligned}\mathcal{R}^{\text{octupole}} = \frac{\mathcal{G}m_N \alpha^3}{a} &\sum_{m=m_{min}}^{3} \sum_{j=-\infty}^{\infty} c_{3,m}^2 X_j^{-4,m} \\ &\times \cos(jM - m(M_N - \omega)),\end{aligned} \tag{3.2}$$

where the differences from the quadrupole expansion manifest as an additional factor of α, as well as a different set of Hansen coefficients and spherical harmonics. Substituting possible values of m into $c^2_{3,m}$, we have:

$$c^2_{3,m} = \tfrac{8\pi}{7}(Y_{3,m}(\pi/2,0))^2 = \begin{cases} 0 & m = 0,2 \\ 3/8 & m = 1 \\ 5/8 & m = 3 \end{cases}$$

Eliminating $m = 0$ and $m = 2$ allows us to isolate the two sets of resonant arguments that will be of interest in the octupole expansion: the $1 : j$ and $3 : j$ resonances. We can now write the disturbing function as:

$$\mathcal{R}^{\text{octupole}} = \frac{\mathcal{G}m_N\alpha^3}{8a} \sum_{j=-\infty}^{\infty}\left[3\underbrace{X_j^{-4,1}(e)\cos(jM-(M_N-\omega))}_{1:j\text{ resonances}} + 5\underbrace{X_j^{-4,3}(e)\cos(jM-3(M_N-\omega))}_{3:j\text{ resonances}}\right]. \tag{3.3}$$

Examining the harmonics, we have $\phi_{1:j} = jM - (\omega - M_N) = j(\lambda - \varpi) - 1(\lambda_N - \varpi)$ and $\phi_{3:j} = jM - 3(\omega - M_N) = j(\lambda - \varpi) - 3(\lambda_N - \varpi)$, which are the $1 : j$ and $3 : j$ MMRs with Neptune respectively. Since the octupole expansion is higher order in the semi-major axis ratio α, we would expect the $1 : j$ and $3 : j$ terms at octupole order to behave differently from the $2 : j$ term from the quadrupole expansion. However, as we will show, this is not the case due to the contribution from the Hansen coefficients that arise at octupole order.

The Hansen coefficient at quadrupole order for the $2 : j$ resonances is $X_j^{-3,2}$, which has been shown to scale linearly with the resonant index j over contours of constant perihelion or as eccentricity approaches unity (S. Yu. Sadov, 2006; Sergey Yu. Sadov, 2008). $X_j^{-4,1}$ and $X_j^{-4,3}$ have no known closed form approximations, and combinatorial expansions (see Aksenov 1986) do not offer any direct intuition on the behavior of the coefficient. We instead determine the scaling of $X_j^{-4,1}$ and $X_j^{-4,3}$ with j numerically by evaluating the coefficient along contours of constant perihelion, $q = a_{\text{SDO}}(1-e) = (j/m)^{2/3}a_N(1-e)$. We find that the j dependence of $X_j^{-4,1}$ goes as $j^{5/3}$ times a prefactor that depends only on perihelion, holding to less than 1% for the selected range of perihelion distances. The Hansen coefficient for the $3 : j$ resonance $X_j^{-4,3}$ also follows the same $j^{5/3}$ scaling, but with a different coefficient

order (ℓ)								Scaling of $X_j^{\ell,m}$
2	secular	-	**$2 : j$**					$\propto j$
3	-	**$1 : j$**	-	**$3 : j$**				$\propto j^{5/3}$
4	secular	-	$2 : j$	-	**$4 : j$**			$\propto j^{7/3}$
5	-	$1 : j$	-	$3 : j$	-	**$5 : j$**		$\propto j^{3}$
6	secular	-	$2 : j$	-	$4 : j$	-	**$6 : j$**	$\propto j^{11/3}$
	0	1	2	3	4	5	6	$X_j^{\ell,m} \propto j^{(2\ell-1)/3}$
	resonant orders m, resonant indices j							

Table 3.1: Schematic representation of the terms that appear in the expansion of the disturbing function. At each successive order ℓ in the expansion, a new resonant index appears. The same resonant index also appears at every other order (even indices appear at even orders), however we only include the term associated with a given resonant index's highest order appearance. Therefore, in all cases except that of the $1 : j$ resonance $m = \ell$.

than for $X_j^{-4,1}$. The coefficients at octupole order therefore pick up an extra factor of $j^{2/3}$ as compared to the linear scaling with j of $X_j^{-3,2}$ in the $2 : j$ resonance expansion. An analytic demonstration of this scaling of the Hansen coefficients is given in section 3.5.

Following the analysis from Batygin, Mardling, and Nesvorný, 2021 and writing down a pendulum-like Hamiltonian for the two resonant terms which follow from the octupole expansion, for which the full derivation can be found in section 3.6, we obtain expressions for the Chirikov criterion for the onset of chaotic motion as a function of resonant index, semi-major axis ratio, and the Hansen coefficient for the quadrupole $2 : j$ and octupole $1 : j$ and $3 : j$ terms:

$$\frac{\Delta a}{\delta a}(2 : j) = \frac{6}{\alpha^{1/2}}\sqrt{\frac{m_n}{M_\odot}X_j^{-3,2}}$$
$$\frac{\Delta a}{\delta a}(1 : j) = \sqrt{18\frac{m_n}{M_\odot}X_j^{-4,1}}$$
$$\frac{\Delta a}{\delta a}(3 : j) = \sqrt{270\frac{m_N}{M_\odot}X_j^{-4,3}}.$$

Since approximating the Hansen coefficients with a simple functional form becomes more difficult in the octupole expansion than in the quadrupole one, we do not replace the coefficients with a functional form in the expressions for the Chirikov criterion. The expressions for the Chirikov criterion for each resonant chain are similar, with the $1 : j$ and $3 : j$ expansions picking up a factor of $\alpha^{1/2}$. This factor of $\alpha^{1/2}$ is exactly equal to $j^{-1/3}$, which is canceled out since the Hansen coefficient at octupole order picks up an extra factor of $j^{2/3}$. Remarkably, this scaling will continue for arbitrarily high orders, as at each order, the additional factor in $\alpha^{1/2}$ will be canceled out by the scaling of the Hansen coefficient with $j^{2/3}$. Effectively, each order in the expansion of the disturbing function (assuming high-eccentricity, such that q_{SDO} is of order a_N) is the same up to a constant that does not depend on the resonant order, making the expansion of the disturbing function, in effect, a divergent series. Further discussion of the divergence (and, for low eccentricity, convergence) of the disturbing function can be found in Ferraz-Mello, 1994. Instead of working with individual terms (quadrupole, octupole, etc.) in a larger expansion, as is characteristic of expansions involving spherical harmonics, we now proceed to build up our theory by examining the intersections between multiple resonant chains. Just as the intersection between some $2 : j$ resonance and its neighboring $2 : j + 1$ resonance creates chaos, so will the intersection between a $2 : j$ resonance and an adjacent $3 : j$ resonance.

3.3 General Theory for $m : j$ resonances

As demonstrated in the previous section, each successive expansion of the disturbing function to higher order yields roughly similar results for the stability boundary each time. Therefore, to improve our resonance-overlap model for the scattered disk, intersection between any members of different resonant classes needs to be accounted for, as intersections between any two resonances will produce a narrow band of chaotic diffusion. To be able to work with arbitrarily high-order resonant chains, we develop a generalization of our theory that can compute the chaotic layer produced by the resonant overlap of any two given $m : j$ and $m' : j'$ resonances. The full derivation is given in section 3.7, but we summarize the key points below. For the generic $m : j$ resonant case, the disturbing function is given by:

$$\begin{aligned}\mathcal{R}_{\ell,m} = \frac{\mathcal{G} m_N \mathcal{M}_\ell \alpha^\ell c_{\ell m}^2}{a} \sum_{j=-\infty}^{\infty} X_j^{-(\ell+1),m} \\ \times \cos(jM - m(M_N - \omega)).\end{aligned} \tag{3.4}$$

This full expansion involves three nested infinite series – iteration over the order of the expansion, the possible resonant orders at that order in the expansion, and all the resonant indices j. We show a schematic for the full expansion of the disturbing function in Table 3.1. At quadrupole order, we only encounter a secular term and the $2 : j$ resonant series, at octupole order we encounter the $1 : j$ and $3 : j$ terms, but at fourth order, we see another set of $2 : j$ terms along with the new $4 : j$ term, and so on. At each successive order in the expansion of the disturbing function a new resonant term is introduced along with higher-order expansions of previous terms. In our model for resonance overlap, we only select terms where $m = \ell$ (except for the $1 : j$ resonances where $\ell = 3$ but $m = 1$) which is the first appearance of any given resonant term. These higher-degree terms, such as $\ell = 4, m = 2$ in Table 3.1 which also describes the behavior of $2 : j$ resonances, will contribute to chaotic

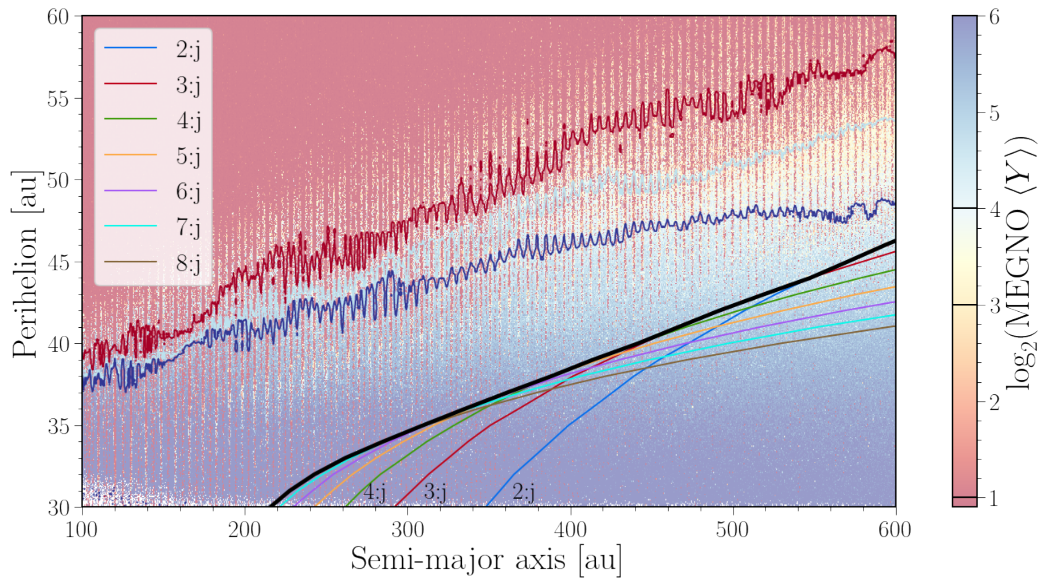

Figure 3.1: Perihelion stability criteria derived from individual networks of the quadrupole ($2 : j$ resonances), octupole ($3 : j$ resonances), and successively higher-order ($4 \rightarrow 8 : j$), expansions of the disturbing function. These boundaries do not take into account overlaps between, for example, the 2:7 and 3:10 resonances, but only interactions between same-order resonances. The black line is the result of selecting the best boundary of the individual resonant chains of resonances at each semi-major axis. We overlay these boundaries on the heat map of $\log_2$ of the Mean Exponential Growth of Nearby Orbits (MEGNO) chaos indicator $\langle Y \rangle$ computed in orbital simulations of the Sun, Neptune, and a test particle SDO using `rebound` (H. Rein and Liu, 2012). Three contours roughly show the transition between regular quasi-periodic ($\log_2$(MEGNO)< 1.01, red) and increasingly chaotic orbits (two contours: $1.01 < \log_2$(MEGNO)< 3, cyan; $4 < \log_2$(MEGNO), blue). The lines in the colorbar show the values set by the three contours. While the boundary set by the black line improves upon the single $2 : j$ boundary (blue line) determined by Batygin, Mardling, and Nesvorný, 2021 in the 200-400 au region, it still does not match the MEGNO stability map obtained from direct integration. Instead, we must look to the overlap of neighboring resonances of different orders.

diffusion around the separatrices of resonances, as described in Morbidelli and Giorgilli, 1997. However, the inclusion of higher-degree terms will not significantly widen associated resonances, and therefore can be neglected in our analysis.

As we show in section 3.7, the width of a given $m : \chi$ resonance is given by

$$\Delta a_{m:\chi} = \frac{8a}{\sqrt{3}}\sqrt{\frac{m_N}{M_\odot}} \cdot \sqrt{\alpha^m \mathcal{M}_m c_{m,m}^2 X_\chi^{-(m+1),m}}. \tag{3.5}$$

Equipped with the expression for the width of any resonance to arbitrary order and the distance between any two given resonances, we can now analytically determine whether any two resonances overlap for a given eccentricity/perihelion value. The Hansen coefficient is the only component of our expression that requires a numerical calculation, which we evaluate by numerical integration (see equation B19 in Appendix B4 of Mardling 2013).

Arguably the most naive approach to improving on the quadrupole boundary from Batygin, Mardling, and Nesvorný, 2021, we can simply find the resonant widths of successively higher index resonance chains and compute the stability boundary for each chain. Then, at every increment in semi-major axis we can select the chain that has resonance overlap at the highest perihelion, and use that as our boundary. In Figure 3.1, we show the result of generating stability boundaries from overlap of resonant chains from $2 : j \ldots 8 : j$, and then selecting at each semi-major axis the highest perihelion value out of the individual boundaries generated. There is clear improvement in the 200-400 au range, with the boundary taking on a more linear functional form, monotonically decreasing in perihelion below 600 au. However, as shown by direct integration of the three-body problem with the chaos indicator MEGNO (mean exponential growth factor of nearby orbits; Cincotta and Simó 2000)[2], the part of phase space in which chaotic diffusion is occurring extends to much higher perihelia than the boundary set by the overlap of individual resonant chains of the same order ℓ would suggest. As discussed in the previous section, we do not expect these successive expansions to arbitrary order in the disturbing function to result in a significant improvement – the Hansen coefficient scales similarly at all orders of the expansion of the disturbing function.

3.3.1 Overlap between different resonant orders

The more precise way of computing the stability boundary from resonance overlap is to include the overlap between all resonances near a given location in phase space. In developing their criterion for the onset of chaos through resonance overlap, Hadden and Tremaine, 2024 determine a local density of resonances based on work from Quillen, 2011 and Hadden and

[2]We describe these simulations and the MEGNO criterion, which are used throughout the paper, in section 3.8.

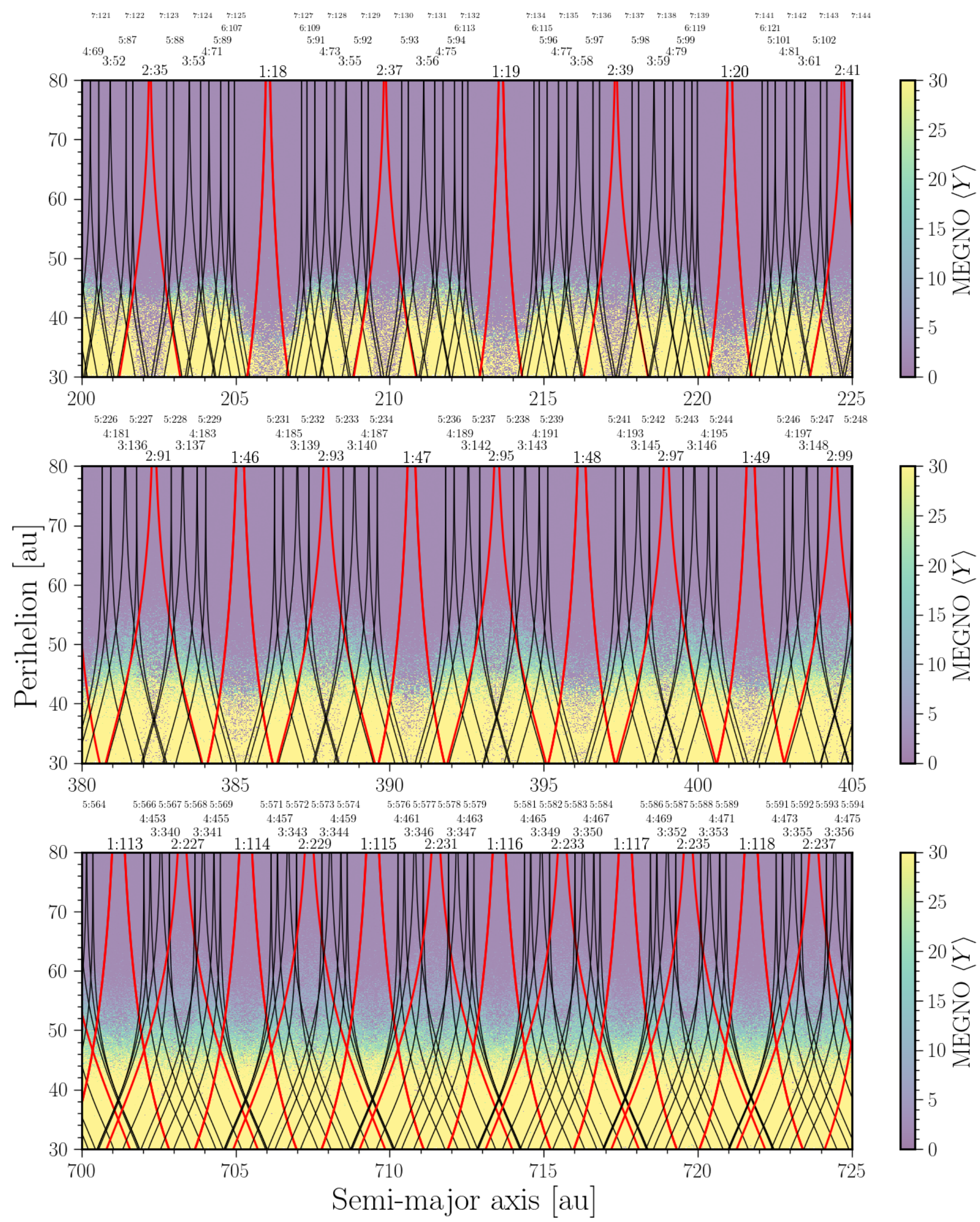

Figure 3.2: Three heat maps of the chaos indicator MEGNO ⟨Y⟩ on a semi-major axis versus perihelion plane, derived from simulations of the Sun, Neptune, and test particle scattered disk objects. Purple regions correspond to initial conditions that lead to regular motion, whereas particles initialized in yellow regions evolve chaotically. The nominal locations and widths of mean motion resonances are shown with red ($1 : j$, $2 : j$) and black ($3 : j$ and higher) lines and are labeled above the heatmaps.

Lithwick, 2018. Between any two given $1:j, 1:j+1$ resonances, Hadden and Tremaine, 2024 evaluate a "covering fraction of resonances" such that if the value is greater than or equal to one, overlaps between resonances cover the entire area between the adjacent $1:j$ resonances, thus chaotic diffusion ensues. This approach sets an upper bound on any possible chaotic diffusion in the three-body problem, but obscures the fine resonant structure that governs the dynamical evolution of the scattered disk.

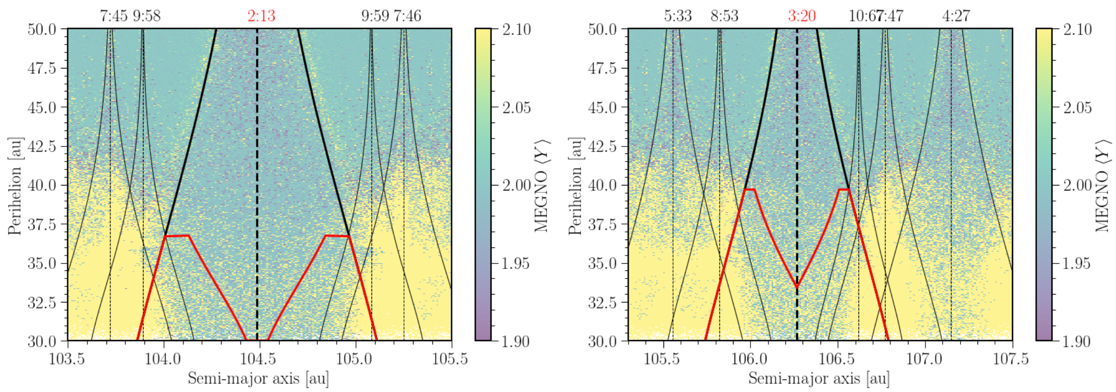

Figure 3.3: Top and bottom panels demonstrate graphically our modified Chirikov criterion (shown in red) based on the relative strength of resonances (individual resonances shown in black lines). In the top panel, the strong $2:13$ resonance overlaps only slightly with the much weaker $7:45$, $9:58$, $9:59$, and $7:46$ resonances. The modified stability criterion identifies that trajectories in the middle of the $2:13$ are more stable than those closer to the neighboring higher-order resonances. For the $3:20$ resonance in the bottom panel, the more stable area in the center of the resonance is smaller, as the ratio of the widths of nearby resonances is closer to unity. These individual boundaries obtained for every resonance out to arbitrary order can then be combined into a single boundary for stability in the scattered disk.

More specifically, the covering fraction approach does not account for the spacing between resonances. Resonances appear at integer ratios – rational numbers – consequently the relative spacing and local density between a pair of $1:j, 1:j+1$ resonances is given by the Farey sequence (Tomás, 2014; Hadden and Lithwick, 2018). The Farey sequence is the sequence of completely reduced fractions, e.g. $F_4 = \{\frac{0}{1}, \frac{1}{4}, \frac{1}{3}, \frac{1}{2}, \frac{2}{3}, \frac{3}{4}, \frac{1}{1}\}$. For sequences F_n with small n, there tend to be more terms that are closer to $1/2$ than to $0/1$ or $1/1$. In the first 20 sequences $F_1 \ldots F_{21}$, all sequences have the same number or more terms closer to $1/2$ than to $0/1$. Given our previous results on the widths of $1:j$ and $2:j$ resonances in section 3.2, we can hypothesize that the increased density of resonances around the $2:j$ resonances should cause an earlier onset of chaos with increasing eccentricity than in the neighborhood of $1:j$ resonances.

In Figure 3.2 we show three panels with the "forest" of resonances from $1 : j$ out to $7 : j$ around 200, 400, and 700 au in semi-major axis, overlaid on top of heat maps of the MEGNO chaos indicator. At $a \sim 200$ au, particles in the vicinities of both the $2 : j$ and $1 : j$ resonances tend to be less chaotic than between these resonances. At $a \sim 400$ au, individual $2 : j$ resonances begin to overlap as shown in Batygin, Mardling, and Nesvorný, 2021 and the chaotic layer starts to become more smooth, though $1 : j$ resonances still generate barriers that can locally slow down diffusive transport. Finally, at $a \sim 700$ au, resonances become so dense that the overlap between $2 : j$ resonances becomes a good approximation for the onset of chaos.

Given the structure of resonances shown in Figure 3.2, an improved boundary for stability based on resonance overlap needs to incorporate the onset and extent of resonance overlap with respect to perihelion and semi-major axis. In the typical formulation of the Chirikov criterion, if the sum of the half-widths of two adjacent resonances divided by the distance between their nominal locations is greater than unity, then motion of particles within their domains will be chaotic. This can be expressed as:

$$\text{chaos ensues when } \frac{\Delta a - \Delta a_{\text{adjacent}}}{[a] - [a]_{\text{adjacent}}} > 1, \tag{3.6}$$

where Δa is the resonance width and $[a]$ is the nominal location of the resonance. However, we are examining resonances of different widths, whereas in the Standard map resonance widths are assumed to be equal (Chirikov, 1979). For example, if a strong $2 : j$ resonance is just barely touching a much weaker $7 : j$ resonance, we do not expect trajectories close to the nominal center of the $2 : j$ resonance to be chaotic or strongly perturbed. However, as described in Section 4 of Chirikov, 1979, adjacent resonances will deform each other's separatrices, and resonances can be everywhere dense. We therefore modify the Chirikov criterion to account for the density of resonances and order of magnitude differences in resonance strength.

Let us take two resonances with widths $\Delta a_1(q)$ and $\Delta a_2(q)$ that are functions of perihelion, and nominal centers $[a]_1$ and $[a]_2$ such that $[a]_2 > [a]_1$. We first determine the perihelion q_{crit} for which the usual Chirikov criterion is met. For perihelia below q_{crit}, we determine the extent of resonance overlap by computing $\Delta a_1(q) + [a]_1$, the width of one resonance added to its nominal center, and evaluating whether it reaches the center of the adjacent resonance $[a]_2$. For values of q where $\Delta a_1(q) + [a]_1 \geq [a]_2$, all trajectories with $a \in [a]_2 \pm \Delta a_2(q)/2$ are chaotic, while for values of q where $\Delta a_1(q) + [a]_1 < [a]_2$, trajectories within the region $a_1(q) + [a]_1 < a < 2[a]_2 - (a_1(q) + [a]_1)$ are stable, but are unstable for all other $a \in [a]_2 \pm \Delta a_2(q)/2$. In plain language, when a weaker resonance overlaps a stronger one, we only allow the weaker resonance to interact with the stronger resonance up to the full-width extent of the weaker resonance. If the full width of the smaller resonance does not reach the vicinity of the nominal center of the stronger resonance, then particles in that vicinity fall outside of our boundary for chaos, reproducing the behavior of particles deep in the $1 : j$ and $2 : j$ resonances shown in the first and second panels of Figure 3.2. We show the process of computing our modified Chirikov criterion in Figure 3.3, with two examples of strong $2 : j$ and $3 : j$ resonances overlapping nearby weaker resonances producing a boundary that is at lower perihelion towards the middle of the wider resonance. Trajectories that begin close to the nominal center of the $2 : 13$ resonance in the left panel of Figure 3.3 are stable, while trajectories that begin closer to the separatrix will chaotically diffuse out.

3.3.2 The Stability Boundary

To derive our stability boundary, we begin by computing the local stability boundary at resonances of orders $1 : j$ to $10 : j$ in the 100-1000 au range using our modified Chirikov criterion as demonstrated in Figure 3.3. We then need to combine these locally computed boundaries into a single boundary. The first approach we can take is to select the maximum perihelion value at each semi-major axis from each resonant order, essentially tracing over the maxima of the local boundaries to obtain a single coherent boundary. This will correspond to the overall boundary for where chaotic diffusion begins in the scattered disk, and should be roughly equivalent to the semi-analytic result of Hadden and Tremaine, 2024. We show this boundary in Figure 3.4 plotted on top of the MEGNO map from previous figures. The resulting boundary is excellent at characterizing locally the behavior of particles in the circular restricted three-body problem out to 100 au, and predicts that at ~200 au, a secondary layer begins to form (shown by the thick black line), within which there are no long-term stable trajectories. This roughly corresponds to the boundary in Figure 3.2, inside which resonance overlap becomes dense enough that even near the centers of nominal resonances there is no stabilizing effect. The fine comb of resonances shown in Figure 3.4 creates a transition between the entirely chaotic region of phase space at very high eccentricity and relatively stable orbits at lower eccentricity. In this transitionary region, we should expect SDOs locked in resonances, or, alternatively, on chaotic orbits that have diffusion slowed by the interactions with strong resonances.

In order to better understand the fine chaos boundary and the transition between the fully chaotic layer and stable region in Figure 3.4, we can leverage that each local boundary is associated with a specific resonant order in order to then obtain multiple boundaries to more granularly characterize the dynamical behavior of SDOs. For example, the boundaries in Figure 3.3 can be converted to a single point at the center of the nominal resonance in semi-major axis and a perihelion value equal to either the maximum of the local boundary or

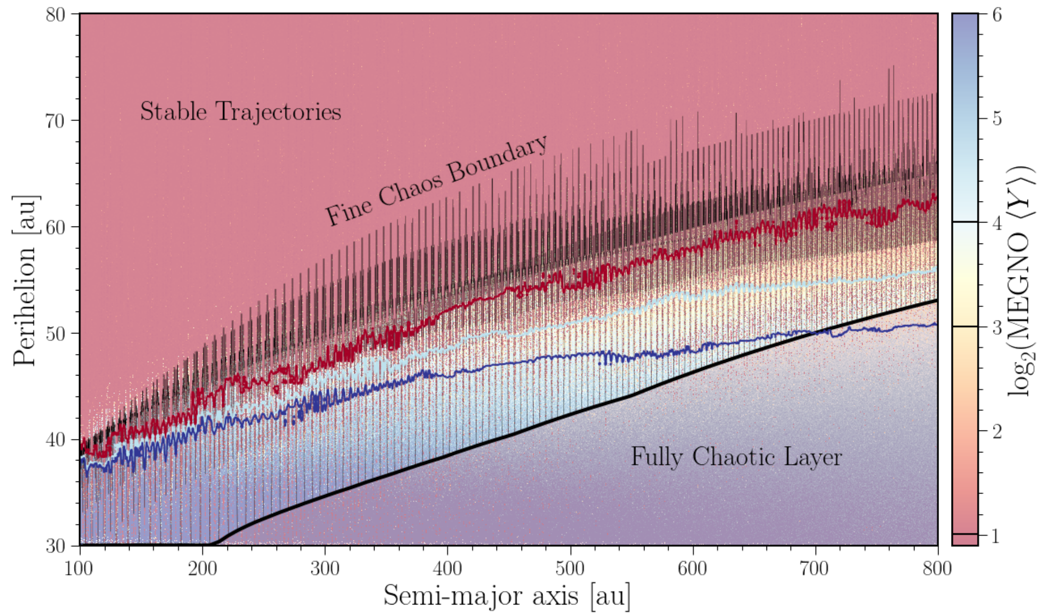

Figure 3.4: Our full stability boundary plotted on top of the MEGNO map for the circular restricted three-body problem. Due to the inclusion of resonances from $1 : j$ to $10 : j$, we see extremely fine comb-like structure appear due to the relative placement and strength of resonances. Selecting the minimum values of the chaos boundary, we get a secondary boundary below which there do not appear to be significant zones of stability.

the perihelion value at the center of the nominal resonance, thus generating a single boundary. These two options for selecting the perihelion of the boundary are physically meaningful. For example, a global boundary set using the value at the center of the nominal resonance of the local boundaries associated with the $1 : j$ resonances is the boundary below which no trajectory can be stabilized by librating around a $1 : j$ resonance. Alternatively, the boundary obtained from the maxima of the local $1 : j$ boundaries is the line above which SDOs are bounded in semi-major axis between adjacent $1 : j$ resonances, and will not pass outside of the adjacent $1 : j$ resonances unless they are transported along the separatrices of the $1 : j$ resonances, significantly limiting their diffusion.

In Figure 3.5 we show our schematic for the different regimes particles will experience in the scattered disk, plotting these against the boundaries derived in Hadden and Tremaine, 2024. Our stability boundary shown in blue is defined as the perihelion of the local boundary for $10 : j$ resonances at their nominal centers. This boundary closely follows the resonant overlap boundary from Hadden and Tremaine, 2024, but falls off at lower perihelia. Below this line and above the red line defined by the maximum value for the overlap criterion at $1 : j$ resonances is the zone in which diffusion is severely impeded at the locations of $1 : j$ resonances. A similar idea was suggested in Section 4.4 of Hadden and Tremaine, 2024,

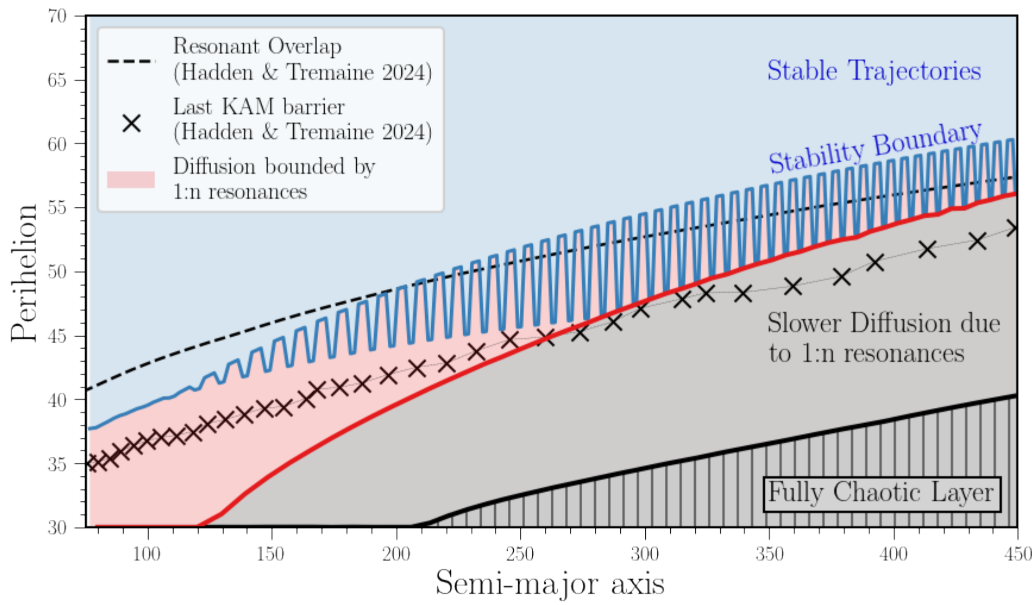

Figure 3.5: Schematic for the different scattering regimes in the circular restricted three-body problem as derived from resonance overlap. In the black dashed line is the resonant overlap criterion from Hadden and Tremaine, 2024, and the black crosses are the boundary for which motion is bounded by KAM tori again from Hadden and Tremaine, 2024. Our stability boundary in blue lies between these two boundaries, and shows that with increasing semi-major axis, stability as a function of (q, a) has significant local dependence. Below the blue line, trajectories diffuse more rapidly with lower perihelion, with $1 : j$ resonances serving as barriers to semi-major axis evolution. The red line is the maximum value for the overlap criterion computed at $1 : j$ resonances. Below this boundary, the black line and the barred region show the part of phase space where $1 : j$ resonances no longer act as barriers to diffusion, as the collection of resonances near them grow strong enough to have strong overlap.

who find that particles in the vicinity of $1 : j$ resonances are "sticky" and impede diffusion. Below the peak of the local $1 : j$ boundaries is the most chaotic region, which we split into two parts. One is the fully chaotic layer that matches the initial result in Figure 3.2 or the lower boundary in Figure 3.4, and above it is a layer where we expect slower diffusion from the stickiness of $1 : j$ resonances as particles that begin close to the centers of the $1 : j$ resonances can remain on librating orbits. We provide approximate functional fits to these boundaries in section 3.9. We also make the boundaries shown in Figure 3.5 and Figure 3.4 available online[3] (Belyakov and Batygin, 2025).

[3] https://doi.org/10.22002/men4e-m4a20

3.4 Discussion

With approximately 10^4 scattered disk objects predicted to be discovered by Vera Rubin Observatory in the coming decade (Kurlander et al., 2025), the striking complexity of this population will invigorate studies both of the orbital evolution of individual objects and the scattered disk as a whole. Previous theoretical characterizations of TNO scattering leveraged the detection of individual objects sticking to $1:j$ mean-motion resonances with Neptune to argue for the importance of $1:j$ resonances in sculpting the scattered disk (Pan and Sari, 2004; Lykawka and Mukai, 2007; Lan and Malhotra, 2019; Graham and Volk, 2024). These works, however, do not characterize the behavior of long-period SDOs, which Vera Rubin Observatory will excel at detecting. The approach of Hadden and Tremaine, 2024 determined the onset of chaos in the scattered disk using the mapping approach, providing a clear boundary in perihelion as a function of semi-major axis, below which SDO orbits undergo chaotic diffusion.

The goal of our perturbative treatment of the circular restricted three-body problem has been to uncover the machinery of the network of resonances that underlie the scattered disk. We expand on the theory of Batygin, Mardling, and Nesvorný, 2021, which leveraged the quadrupole expansion of the disturbing function (Kaula, 1962; Mardling, 2013) to determine that the overlap between $2:j$ resonances drives chaotic evolution in SDOs past 400 au. By taking the expansion of the disturbing function to octupole order and repeating the exercise of Batygin, Mardling, and Nesvorný, 2021 for $1:j$ and $3:j$ resonances, we find that in isolation, each order in the expansion of the disturbing function yields a similar stability boundary that does not significantly improve on the one derived from $2:j$ resonance overlap alone. Using the intuition obtained from the octupole expansion, we generalize our perturbative treatment of the three-body problem by determining the resonance widths and overlaps between mean-motion resonances out to arbitrary order. We find that chaotic transport is facilitated by the density of resonances, such that for lower semi-major axes, it is the mutual overlap between harmonics of ever-higher order that results in diffusive behavior. By modifying the Chirikov criterion to account for the lesser amount of diffusion from the overlap of strong and much weaker resonances, we are able to generate a stability boundary from the overlap of all $1:j$ to $10:j$ mean-motion resonances with Neptune as shown in Figure 3.4.

Our key result is the mapping of the geography of resonances that facilitate scattering (Figure 3.5). Past 400 au, a single network of resonances – the $2:j$ as shown by Batygin, Mardling, and Nesvorný, 2021 – are sufficient to explain the onset of chaos in the scattered disk. Closer in, the Farey sequence banded resonance structure drives diffusion in two distinct diffusive regimes. One is a zone of complete overlap in a fully chaotic layer, where no resonance provides a barrier to transport. The second is a zone of slower diffusion, in which $1:j$ resonances emerge as increasingly strong barriers to diffusion as eccentricity is lowered. This regime in which $1:j$ resonances act as a boundary for chaotic evolution, or in other words, are sticky, is a direct consequence of the Farey sequence being the representation of orbital commensurabilities.

Future work will address how the stability boundary for the scattered disk is altered by the introduction of inclination resonances. Scattered disk objects acquire their inclinations either through close encounters with Neptune, or by exchanging eccentricity for inclination through the von Zeipel-Lidov-Kozai mechanism when trapped in mean-motion resonances (Gomes et al., 2008). The inclination of the scattered disk has typically been characterized as low (90% of SDOs are below 40°), with the persistent caveat that observational bias favors detection of objects in the ecliptic plane. Recent efforts by Bernardinelli et al., 2022 in discovering Kuiper belt objects at high-ecliptic latitudes have not significantly changed the observed inclination distribution of SDOs. We anticipate that the addition of inclination-dependent terms in the disturbing function will cause diffusion to diminish at high eccentricity, in line with predictions by Gallardo, 2019.

3.5 Scaling of Hansen coefficients

We begin with the recurrence relation for the Hansen coefficients from Aksenov, 1986.

$$\begin{aligned}(1-e^2)X_j^{n,m} &= X_j^{n+1,m} + \frac{e}{2}\left(X_j^{n+1,m+1} + X_j^{n+1,m-1}\right)\\ X_j^{n,m} &= \frac{1}{(1-e^2)}X_j^{n+1,m} + \frac{e}{2(1-e^2)}\left(X_j^{n+1,m+1} + X_j^{n+1,m-1}\right).\end{aligned} \tag{3.7}$$

Using $e = 1 - q/a = 1 - q/(a_N \cdot j^{2/3})$, we can rewrite the above equation as:

$$X_j^{n,m} = \frac{a_N^2 \cdot j^{4/3}}{2q \cdot a_N \cdot j^{2/3} - q^2}X_j^{n+1,m} + \frac{1}{2}\frac{a_N^2 \cdot j^{4/3} - q \cdot a_N \cdot j^{2/3}}{2q \cdot a_N \cdot j^{2/3} - q^2}\left(X_j^{n+1,m+1} + X_j^{n+1,m-1}\right). \tag{3.8}$$

In the limit where q is not much larger than a_N (large j), this expression approaches:

$$X_j^{n,m} = \frac{j^{2/3}}{2}X_j^{n+1,m} + \frac{j^{2/3}}{2}\left(X_j^{n,m+1} + X_j^{n,m-1}\right). \tag{3.9}$$

Given that j is negative in our analysis for an internal perturber, we have recovered the $j^{2/3}$ scaling of the Hansen coefficient with increasing degree of the expansion. We also show this scaling numerically in Figure 3.6. For small j, the fit becomes poor for Hansen coefficients associated with very large ℓ, however it holds extremely well for large j at all orders.

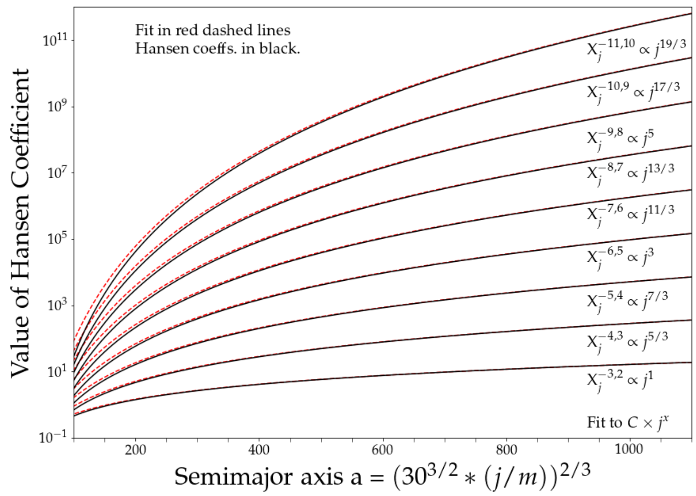

Figure 3.6: Numerically computed Hansen coefficients $X_j^{\ell,m}$ at $q = 40$ au in black, plotted at the nominal semi-major axis of each $m : j$ resonance.

3.6 Derivation of resonance width for $1 : j$ and $3 : j$ resonances

Starting with the octupole order disturbing function in Equation (3.3), we can write down two model Hamiltonians for an SDO interacting with the $1 : \chi$ and $3 : \chi$ resonances respectively. We only give the derivation for the special case of the resonance width of a $1 : \chi$ resonance while the widths of $3 : \chi$ resonances can be evaluated from the general case for $m : j$ resonant widths, given in a later section. The Hamiltonian for the $1 : j$ resonances using the pendulum model for resonances can be written as:

$$\mathcal{H} = -\frac{\mathcal{G}M_\odot}{2a} - \frac{3\mathcal{G}m_N\mathcal{M}_3\alpha^3}{8a}\sum_{j=-\infty}^{\infty} X_j^{-4,1}(e)\cos(jM - (M_N - \omega)) + \mathcal{T}. \tag{3.10}$$

We can use Delaunay Variables as given in ch. 2 of Murray and Dermott to rewrite the Keplerian term as:

$$-\frac{\mathcal{G}M_\odot}{2a} = -\frac{1}{2}\left(\frac{\mathcal{G}M_\odot}{L}\right)^2. \tag{3.11}$$

$$-\frac{1}{2}\left(\frac{\mathcal{G}M_\odot}{L}\right)^2 = -\frac{1}{2}\left(\frac{\mathcal{G}M_\odot}{[L]}\right)^2 + \underbrace{\left(\frac{\mathcal{G}M_\odot}{L}\right)^2\left(\frac{\delta L}{[L]}\right) - \frac{3}{2}\left(\frac{\mathcal{G}M_\odot}{L}\right)^2\left(\frac{\delta L}{[L]}\right)^2}_{[n]\left(\delta L - \frac{3}{2}\frac{\delta L^2}{[L]}\right)}. \tag{3.12}$$

We define a type-2 generating function:

$$\mathcal{F}_2 = \underbrace{(\chi l - (n_N t - g))}_{\phi}\Phi + \underbrace{(l)}_{\psi}\Psi + \underbrace{(t)}_{\xi}\Xi. \tag{3.13}$$

$$\delta L = \frac{\partial \mathcal{F}_2}{\partial l} = \chi\Phi + \Psi$$
$$\delta G = \frac{\partial \mathcal{F}_2}{\partial g} = \Phi \tag{3.14}$$
$$\delta \mathcal{T} = \frac{\partial \mathcal{F}_2}{\partial t} = \Xi - n_N\Phi.$$

We apply these transformations to our Hamiltonian, now isolating just one resonance $1 : \chi$:

$$\begin{aligned}\mathcal{H}_\chi = & -\frac{3\mathcal{G}m_N\mathcal{M}_3\alpha^3}{8a}X_\chi^{-4,1}\cos(\phi) + \Xi - n_N\Phi \\ & + [n]\left(\chi\Phi + \Psi - \frac{3}{2}\frac{(\chi\Phi+\Psi)^2}{[L]}\right) - \frac{1}{2}\left(\frac{\mathcal{G}M_\odot}{[L]}\right)^2.\end{aligned} \tag{3.15}$$

Simplifying and removing constant terms (those with only Ψ):

$$\mathcal{H}_\chi = -\frac{3\mathcal{G}m_N\mathcal{M}_3\alpha^3}{8a}X_\chi^{-4,1}\cos(\phi) - \frac{3n_N\chi}{2[L]}\Phi^2 - \frac{3n_N}{[L]}\Psi\Phi. \tag{3.16}$$

We can further simplify this by completing the square using the linear action term:

$$\mathcal{H}_\chi = -\frac{3\mathcal{G}m_N\mathcal{M}_3\alpha^3}{8a}X_\chi^{-4,1}\cos(\phi) - \frac{3n_N\chi}{2[L]}\underbrace{\left(\Phi + \frac{\Psi}{\chi}\right)^2}_{\tilde{\Phi}^2}. \tag{3.17}$$

where $\tilde{\Phi}$ is the new action conjugate to the angle ϕ. The resonance width of a pendulum is given by $\Delta\tilde{\Phi} = 4\sqrt{\gamma/\beta}$, where, $\Delta\delta L = \chi\Delta\tilde{\Phi}$. However, we want the width, Δa, which we can find using $\Delta\delta L = \Delta(L - [L]) = \Delta L$, where $[L]$ is constant, such that $\Delta[L] = 0$, which gives us

$$\Delta\delta L = \Delta(\sqrt{\mathcal{G}M_\odot a}) = \frac{\Delta a}{\sqrt{a}}\frac{\sqrt{\mathcal{G}M_\odot}}{2}$$
$$\Delta a = \frac{2\sqrt{a}\Delta\delta L}{\sqrt{\mathcal{G}M_\odot}} = \frac{8\chi\sqrt{a\cdot\gamma/\beta}}{\sqrt{\mathcal{G}M_\odot}}. \tag{3.18}$$

The width of a given $1 : \chi$ resonance is therefore:

$$\begin{aligned}\Delta a &= \frac{8\chi\sqrt{a}}{\sqrt{\mathcal{G}M}}\cdot\sqrt{\frac{\frac{3\mathcal{G}m_N\mathcal{M}_3\alpha^3}{8a}X_\chi^{-4,1}}{\frac{3n_N\chi}{[L]}}} \\ &= \sqrt{\frac{8m_n}{M_\odot}\underbrace{\mathcal{M}_3}_{\approx 1}}\cdot\sqrt{X_\chi^{-4,1}\alpha^3\cdot\underbrace{\frac{\chi[L]}{n_N}}_{a^2}} = \frac{a}{\chi}\sqrt{\frac{8m_n}{M_\odot}X_\chi^{-4,1}}.\end{aligned} \tag{3.19}$$

3.7 Derivation of resonance width for arbitrary $m : j$ resonances

For completeness, we give again the disturbing function for the co-planar three-body system with the Sun, Neptune, and an SDO (massless test particle):

$$\mathcal{R} = \frac{\mathcal{G}m_N}{a} \sum_{l=2}^{\infty} \sum_{m=m_{min}}^{l} \sum_{j'=-\infty}^{\infty} \sum_{j=-\infty}^{\infty} \zeta_m c_{lm}^2 \mathcal{M}_l \times \alpha^l X_{j'}^{l,m}(e_N) X_j^{-(l+1),m}(e) \times \cos(j' M_N - jM + m(\omega_N - \omega)). \tag{3.20}$$

For the generic $m : j$ case, we can still make certain simplifications relevant to the circular restricted three-body problem. We start by addressing only the innermost sum, by choosing an order ℓ, which fixes the order of the expansion. For example, $\ell = 2$ is the quadrupole expansion, $\ell = 3$ is the octupole expansion and so on. Then, we fix $m = \ell$, which sets the resonant index, such that the quadrupole expansion for $\ell = m = 2$ gives a $2 : j$ chain of resonances. Choosing an $m < \ell$ begins to include integer multiples of the resonance, essentially expanding the perturbative terms associated with the resonance at that location out to higher order, which we can neglect. With ℓ, m fixed, the disturbing function becomes:

$$\mathcal{R}_{\ell,m} = \frac{\mathcal{G}m_N \mathcal{M}_\ell \alpha^\ell c_{\ell m}^2}{a} \sum_{j=-\infty}^{\infty} X_j^{-(\ell+1),m}(e) \times \cos(jM - m(M_N - \omega)). \tag{3.21}$$

The $m : j$ Hamiltonian for an expansion out to order ℓ is given by:

$$\mathcal{H}_{m:j} = -\frac{\mathcal{G}M_\odot}{2a} - \frac{\mathcal{G}m_N \mathcal{M}_\ell \alpha^\ell c_{\ell m}^2}{a} \times \sum_{j=-\infty}^{\infty} X_j^{-(\ell+1),m}(e) \cos(jM - m(n_N t - \omega)) + \mathcal{T}, \tag{3.22}$$

where we have added a conjugate action $\mathcal{T}$ that will be useful for removing time dependence. For all terms except that of the $1 : j$ resonance, $m = l$. The $1 : j$ resonance first appears at octupole order, where $l = 3, m = 1$. We can use Delaunay Variables to rewrite the Keplerian term as:

$$-\frac{\mathcal{G}M_\odot}{2a} = -\frac{1}{2}\left(\frac{\mathcal{G}M_\odot}{L}\right)^2. \tag{3.23}$$

We then Taylor expand the Keplerian term around the resonance location through the nominal action $[L] = \sqrt{\mathcal{G}M_\odot a_N (j/m)^{2/3}}$

$$-\frac{1}{2}\left(\frac{\mathcal{G}M_\odot}{L}\right)^2 = -\frac{1}{2}\left(\frac{\mathcal{G}M_\odot}{[L]}\right)^2 + \underbrace{\left(\frac{\mathcal{G}M_\odot}{L}\right)^2 \left(\frac{\delta L}{[L]}\right) - \frac{3}{2}\left(\frac{\mathcal{G}M_\odot}{L}\right)^2 \left(\frac{\delta L}{[L]}\right)^2}_{[n]\left(\delta L - \frac{3}{2}\frac{\delta L^2}{[L]}\right)}, \tag{3.24}$$

where $[n] = n_{\rm N} \cdot m/\chi$. Here, χ fixes the index of the specific $m : \chi$ resonance of interest. We can now define a type-2 generating function:

$$\mathcal{F}_2 = \underbrace{(\chi l/m - (n_N t - g))}_{\phi}\Phi + \underbrace{(l)}_{\psi}\Psi + \underbrace{(t)}_{\xi}\Xi. \tag{3.25}$$

with transformation equations between the old and new actions defined as:

$$\begin{aligned} \delta L &= \frac{\partial \mathcal{F}_2}{\partial l} = \chi\Phi/m + \Psi \\ G &= \frac{\partial \mathcal{F}_2}{\partial g} = \Phi \\ \mathcal{T} &= \frac{\partial \mathcal{F}_2}{\partial t} = \Xi - n_N\Phi. \end{aligned} \tag{3.26}$$

We can now apply these transformations to our Hamiltonian, isolating just one resonance $m : \chi$ instead of the series of terms:

$$\begin{aligned} \mathcal{H}_\chi = &-\frac{\mathcal{G}m_N\mathcal{M}_\ell\alpha^\ell c_{\ell m}^2}{a}X_\chi^{-(\ell+1),m}\cos(m\phi) + \Xi - n_N\Phi + \\ &[n]\left(\chi\Phi/m + \Psi - \frac{3}{2}\frac{(\chi\Phi/m+\Psi)^2}{[L]}\right) - \frac{1}{2}\left(\frac{\mathcal{G}M_\odot}{[L]}\right)^2. \end{aligned} \tag{3.27}$$

Simplifying and removing constant terms (those without Φ or conjugate angle ϕ):

$$\mathcal{H}_\chi = -\frac{\mathcal{G}m_N\mathcal{M}_\ell\alpha^\ell c_{\ell m}^2}{a}X_\chi^{-(\ell+1),m}\cos(m\phi) - \frac{3n_N\chi}{2m[L]}\Phi^2 - \frac{3n_N}{[L]}\Psi\Phi. \tag{3.28}$$

We can further simplify this by completing the square using the linear action term:

$$\mathcal{H}_\chi = \underbrace{\frac{\mathcal{G}m_N\mathcal{M}_\ell\alpha^\ell c_{\ell m}^2}{a}X_\chi^{-(\ell+1),m}}_{\gamma}\cos(m\phi) - \underbrace{\frac{3n_N\chi}{m[L]}}_{\beta}\cdot\frac{1}{2}\underbrace{\left(\Phi + \frac{m\Psi}{\chi}\right)^2}_{\tilde{\Phi}^2} = \gamma\cos(m\phi) - \frac{\beta}{2}\tilde{\Phi}^2. \tag{3.29}$$

where $\tilde{\Phi}$ is the new action conjugate to the angle ϕ. We can now calculate the resonance width. For a mathematical pendulum, we have $\Delta\tilde{\Phi} = 4\sqrt{\gamma/\beta}$. Using our transformation equations for δL, $\Delta\delta L = \chi/m \cdot \Delta\tilde{\Phi}$. However, we want the width, Δa, which we can find from $\Delta\delta L = \Delta(L - [L]) = \Delta L$, where $[L]$ is constant, such that $\Delta[L] = 0$. Therefore,

$$\begin{aligned} \Delta\delta L &= \Delta(\sqrt{\mathcal{G}M_\odot a}) = \frac{\Delta a}{\sqrt{a}}\frac{\sqrt{\mathcal{G}M_\odot}}{2} \\ \Delta a &= \frac{2\sqrt{a}\Delta\delta L}{\sqrt{\mathcal{G}M_\odot}}. \end{aligned} \tag{3.30}$$

Combining with $\Delta\delta L = \Delta\tilde{\Phi}\chi/m$ and $\Delta\tilde{\Phi} = 4\sqrt{\gamma/\beta}$, we get:

$$\begin{aligned}\Delta a = \frac{8a^{1/2}\chi}{m\sqrt{\mathcal{G}M_\odot}}\sqrt{\gamma/\beta} &= \frac{8a^{1/2}\chi}{m\sqrt{\mathcal{G}M_\odot}}\sqrt{\frac{\mathcal{G}m_N\mathcal{M}_\ell\alpha^\ell c_{\ell m}^2 X_\chi^{-(\ell+1),m}/a}{3n_N\chi/(m[L])}} \\ &= \frac{8}{\sqrt{3}}\cdot\sqrt{\frac{\mathcal{M}_\ell\alpha^\ell c_{\ell m}^2 X_\chi^{-(\ell+1),m}\chi[L]}{m\cdot n_N}\cdot\frac{m_N}{M_\odot}} \\ &= \frac{8}{\sqrt{3}}\cdot\sqrt{\frac{m_N}{M_\odot}}\cdot\sqrt{\mathcal{M}_\ell\alpha^\ell c_{\ell m}^2 X_\chi^{-(\ell+1),m}}\cdot\sqrt{\frac{\chi[L]}{m\cdot n_N}} \\ &= \frac{8a}{\sqrt{3}}\cdot\sqrt{\frac{m_N}{M_\odot}}\cdot\sqrt{\alpha^\ell\mathcal{M}_\ell c_{\ell m}^2 X_\chi^{-(\ell+1),m}},\end{aligned} \tag{3.31}$$

the expression for resonance width in our paradigm for an arbitrary $m : j$ resonance. Following Chirikov, 1979, we can compare the resonance width to that of adjacent resonances (s.t. $\delta a \approx (2a_N/3m)(m/\chi)^{1/3} = (2a_N/3m)\times\alpha^{1/2}$):

$$\frac{\Delta a}{\delta a} = 4m\cdot\sqrt{\frac{m_N}{M_\odot}}\cdot\sqrt{3\alpha^{\ell-3}\mathcal{M}_\ell c_{\ell m}^2 X_\chi^{-(\ell+1),m}}. \tag{3.32}$$

This expression only holds for adjacent resonances of the same order, it does not apply for the $2:10$ and $4:21$ resonance overlap, for example. A more generalized expression can be written down:

$$\frac{\Delta(a,a')}{\delta(a,a')} = \frac{8\left(\sqrt{\alpha^\ell\mathcal{M}_\ell c_{\ell m}^2 X_\chi^{-(\ell+1),m}} + \sqrt{\alpha^{\ell'}\mathcal{M}_{\ell'} c_{\ell' m'}^2 X_{\chi'}^{-(\ell'+1),m'}}\right)}{\sqrt{3}\alpha\left((\chi/m)^{2/3} - (\chi'/m')^{2/3}\right)}. \tag{3.33}$$

3.8 Simulations

We carried out the simulations used for comparison to our analytic model using the `REBOUND` software package (H. Rein and Liu, 2012; Hanno Rein et al., 2019), utilizing the `TRACE` integration algorithm (Lu, Hernandez, and Hanno Rein, 2024). We initialize our simulations with the Sun, Neptune with $m = 5.15\cdot 10^{-5} M_\odot$, $a = 30$ au, and zero eccentricity, inclination, and mean anomaly, and a test particle SDO on a grid of a/q values with random mean anomaly and zero inclination. We use a timestep corresponding to $\delta t = P_{\text{Neptune}}/(2\pi\times 113)$, and integrate for $\Delta t = 2\pi\times 10^6$ code units.

These simulations were then used to derive the MEGNO chaos indicator (Y) (mean exponential growth of nearby orbits; Cincotta and Simó 2000). The MEGNO criterion converges to 2 for stable quasi-periodic motion, and increases with time for chaotic motion. Note here that chaotic motion with $Y > 2$ does not directly correspond to an orbit that is unstable on some given timescale. While larger values of MEGNO will correspond to more chaotic orbits which are likelier to lead to ejection of the SDO, the MEGNO criterion or Lyapunov time are distinct from the diffusion timescale and cannot be used to directly estimate the time until an SDO is ejected from the Solar System.

3.9 Approximations to Stability Boundaries

In order to facilitate the use of our theoretical results, we provide approximate functional fits to the curves shown in Figure 3.5. The boundary for the fully chaotic layer wherein objects pass unimpeded through $1 : n$ resonances can be approximated with a power-law:

$$q = 13.37 + 0.55 \times a^{0.64}. \tag{3.34}$$

The second curve (red in Figure 3.5) which sets the boundary for orbits which have their diffusion slowed by interacting with $1 : n$ resonances, can be approximated with a logarithmic function:

$$q = -63.1 + 19.4 \times \log(a). \tag{3.35}$$

Finally, the fine comb-like boundary shown in blue in Figure 3.5 is approximated by a power-law:

$$q = 10.28 + 6.01 \times a^{0.34}. \tag{3.36}$$

References

Aksenov, E. P. (1986). *Special functions in celestial mechanics.*

Ali-Dib, Mohamad et al. (July 2021). "The Rarity of Very Red Trans-Neptunian Objects in the Scattered Disk". In: *AJ* 162.1, 19, p. 19. DOI: 10.3847/1538-3881/abf6ca. arXiv: 2104.04271 [astro-ph.EP].

Batygin, Konstantin, Fred C. Adams, et al. (May 2019). "The planet nine hypothesis". In: *PhR* 805, pp. 1–53. DOI: 10.1016/j.physrep.2019.01.009. arXiv: 1902.10103 [astro-ph.EP].

Batygin, Konstantin, Rosemary A. Mardling, and David Nesvorný (Oct. 2021). "The Stability Boundary of the Distant Scattered Disk". In: *ApJ* 920.2, 148, p. 148. DOI: 10.3847/1538-4357/ac19a4. arXiv: 2111.00305 [astro-ph.EP].

Belyakov, Matthew and Konstantin Batygin (Aug. 2025). "Stability Boundary of the Scattered Disk". In: DOI: 10.22002/men4e-m4a20.

Belyakov, Matthew, Michael E. Brown, and Alya Al-Kibbi (Sept. 2024). "The Trojan-like Colors of Low-perihelion Kuiper Belt Objects". In: *PSJ* 5.9, 193, p. 193. DOI: 10.3847/PSJ/ad698a. arXiv: 2407.21168 [astro-ph.EP].

Bernardinelli, Pedro H. et al. (Feb. 2022). "A Search of the Full Six Years of the Dark Energy Survey for Outer Solar System Objects". In: *ApJS* 258.2, 41, p. 41. DOI: 10.3847/1538-4365/ac3914. arXiv: 2109.03758 [astro-ph.EP].

Chirikov, Boris V. (May 1979). “A universal instability of many-dimensional oscillator systems”. In: *PhR* 52.5, pp. 263–379. DOI: 10.1016/0370-1573(79)90023-1.

Cincotta, P. M. and C. Simó (Dec. 2000). “Simple tools to study global dynamics in non-axisymmetric galactic potentials - I”. In: *A&AS* 147, pp. 205–228. DOI: 10.1051/aas:2000108.

Fernández, Julio A., Tabaré Gallardo, and Adrián Brunini (Dec. 2004). “The scattered disk population as a source of Oort cloud comets: evaluation of its current and past role in populating the Oort cloud”. In: *Icarus* 172.2, pp. 372–381. DOI: 10.1016/j.icarus.2004.07.023.

Ferraz-Mello, S. (Jan. 1994). “The Convergence Domain of the Laplacian Expansion of the Disturbing Function”. In: *Celestial Mechanics and Dynamical Astronomy* 58.1, pp. 37–52. DOI: 10.1007/BF00692116.

Gallardo, Tabaré (Jan. 2019). “Strength, stability and three dimensional structure of mean motion resonances in the solar system”. In: *Icarus* 317, pp. 121–134. DOI: 10.1016/j.icarus.2018.07.002. arXiv: 1807.07956 [astro-ph.EP].

Gomes, R. S. et al. (2008). “The Scattered Disk: Origins, Dynamics, and End States”. In: *The Solar System Beyond Neptune*. Ed. by M. A. Barucci et al., p. 259.

Graham, Severance and Kathryn Volk (June 2024). “Uranus’s Influence on Neptune’s Exterior Mean-motion Resonances”. In: *PSJ* 5.6, 135, p. 135. DOI: 10.3847/PSJ/ad4707. arXiv: 2402.07824 [astro-ph.EP].

Hadden, Sam and Yoram Lithwick (Sept. 2018). “A Criterion for the Onset of Chaos in Systems of Two Eccentric Planets”. In: *AJ* 156.3, 95, p. 95. DOI: 10.3847/1538-3881/aad32c. arXiv: 1803.08510 [astro-ph.EP].

Hadden, Sam and Scott Tremaine (Jan. 2024). “Scattered disc dynamics: the mapping approach”. In: *MNRAS* 527.2, pp. 3054–3075. DOI: 10.1093/mnras/stad3478. arXiv: 2309.00684 [astro-ph.EP].

Jewitt, D., J. Luu, and B. G. Marsden (Sept. 1992). “1992 QB1”. In: *IAUC* 5611, p. 1.

Kaula, William M. (June 1962). “Development of the lunar and solar disturbing functions for a close satellite”. In: *AJ* 67, p. 300. DOI: 10.1086/108729.

Kurlander, Jacob A. et al. (Aug. 2025). “Predictions of the LSST Solar System Yield: Near-Earth Objects, Main Belt Asteroids, Jupiter Trojans, and Trans-Neptunian Objects”. In: *AJ* 170.2, 99, p. 99. DOI: 10.3847/1538-3881/add685. arXiv: 2506.02487 [astro-ph.EP].

Lan, Lei and Renu Malhotra (Aug. 2019). “Neptune’s resonances in the scattered disk”. In: *Celestial Mechanics and Dynamical Astronomy* 131.8, 39, p. 39. DOI: 10.1007/s10569-019-9917-1. arXiv: 1901.06040 [astro-ph.EP].

Lu, Tiger, David M. Hernandez, and Hanno Rein (Sept. 2024). “TRACE: a code for time-reversible astrophysical close encounters”. In: *MNRAS* 533.3, pp. 3708–3723. DOI: 10.1093/mnras/stae1982. arXiv: 2405.03800 [astro-ph.EP].

Lykawka, Patryk Sofia and Tadashi Mukai (Dec. 2007). “Resonance sticking in the scattered disk”. In: *Icarus* 192.1, pp. 238–247. DOI: 10.1016/j.icarus.2007.06.007. arXiv: 0707.4301 [astro-ph].

Malyshkin, Leonid and Scott Tremaine (Oct. 1999). “The Keplerian Map for the Planar Restricted Three-Body Problem as a Model of Comet Evolution”. In: *Icarus* 141.2, pp. 341–353. DOI: 10.1006/icar.1999.6174. arXiv: astro-ph/9808172 [astro-ph].

Mardling, Rosemary A. (Sept. 2013). “New developments for modern celestial mechanics – I. General coplanar three-body systems. Application to exoplanets”. In: *Monthly Notices of the Royal Astronomical Society* 435.3, pp. 2187–2226. ISSN: 0035-8711. DOI: 10.1093/mnras/stt1438. URL: http://dx.doi.org/10.1093/mnras/stt1438.

Morbidelli, Alessandro and Antonio Giorgilli (Feb. 1997). “On the role of high order resonances in normal forms and in separatrix splitting”. In: *Physica D Nonlinear Phenomena* 102.3-4, pp. 195–207. DOI: 10.1016/S0167-2789(96)00155-8.

Nesvorný, David (Sept. 2018). “Dynamical Evolution of the Early Solar System”. In: *ARA&A* 56, pp. 137–174. DOI: 10.1146/annurev-astro-081817-052028. arXiv: 1807.06647 [astro-ph.EP].

Nesvorný, David et al. (July 2020). “OSSOS XX: The Meaning of Kuiper Belt Colors”. In: *AJ* 160.1, 46, p. 46. DOI: 10.3847/1538-3881/ab98fb. arXiv: 2006.01806 [astro-ph.EP].

Pan, Margaret and Re’em Sari (Sept. 2004). “A Generalization of the Lagrangian Points: Studies of Resonance for Highly Eccentric Orbits”. In: *AJ* 128.3, pp. 1418–1429. DOI: 10.1086/423214. arXiv: astro-ph/0302135 [astro-ph].

Pichierri, Gabriele and Konstantin Batygin (Mar. 2025). “Measuring the degree of clustering and diffusion of trans-Neptunian objects”. In: *arXiv e-prints*, arXiv:2503.07146, arXiv:2503.07146. DOI: 10.48550/arXiv.2503.07146. arXiv: 2503.07146 [astro-ph.EP].

Pike, Rosemary E. et al. (Oct. 2023). “Col-OSSOS: The Distribution of Surface Classes in Neptune’s Resonances”. In: *PSJ* 4.10, 200, p. 200. DOI: 10.3847/PSJ/ace2c2.

Quillen, Alice C. (Dec. 2011). “Three-body resonance overlap in closely spaced multiple-planet systems”. In: *MNRAS* 418.2, pp. 1043–1054. DOI: 10.1111/j.1365-2966.2011.19555.x. arXiv: 1106.0156 [astro-ph.EP].

Rein, H. and S. -F. Liu (Jan. 2012). “REBOUND: an open-source multi-purpose N-body code for collisional dynamics”. In: *A&A* 537, A128, A128. DOI: 10.1051/0004-6361/201118085. arXiv: 1110.4876 [astro-ph.EP].

Rein, Hanno et al. (June 2019). “Hybrid symplectic integrators for planetary dynamics”. In: *MNRAS* 485.4, pp. 5490–5497. DOI: 10.1093/mnras/stz769. arXiv: 1903.04972 [astro-ph.EP].

Sadov, S. Yu. (Mar. 2006). “Stability of resonance rotation of a satellite with respect to its center of mass in the orbit plane”. In: *Cosmic Research* 44.2, pp. 160–171. DOI: 10.1134/S0010952506020080.

Sadov, Sergey Yu. (Apr. 2008). "Analytic properties of Hansen coefficients". In: *Celestial Mechanics and Dynamical Astronomy* 100.4, pp. 287–300. DOI: 10.1007/s10569-008-9123-z.

Saillenfest, Melaine (Feb. 2020). "Long-term orbital dynamics of trans-Neptunian objects". In: *Celestial Mechanics and Dynamical Astronomy* 132.2, 12, p. 12. DOI: 10.1007/s10569-020-9954-9. arXiv: 2001.07579 [astro-ph.EP].

Sheppard, Scott S. (Apr. 2010). "The Colors of Extreme Outer Solar System Objects". In: *AJ* 139.4, pp. 1394–1405. DOI: 10.1088/0004-6256/139/4/1394. arXiv: 1001.3674 [astro-ph.EP].

Siraj, Amir, Christopher F. Chyba, and Scott Tremaine (Jan. 2025). "Orbit of a Possible Planet X". In: *ApJ* 978.2, 139, p. 139. DOI: 10.3847/1538-4357/ad98f6. arXiv: 2410.18170 [astro-ph.EP].

Tomás, R. (Jan. 2014). "From Farey sequences to resonance diagrams". In: *Phys. Rev. ST Accel. Beams* 17 (1), p. 014001. DOI: 10.1103/PhysRevSTAB.17.014001. URL: https://link.aps.org/doi/10.1103/PhysRevSTAB.17.014001.

Volk, Kathryn and Renu Malhotra (Nov. 2008). "The Scattered Disk as the Source of the Jupiter Family Comets". In: *ApJ* 687.1, pp. 714–725. DOI: 10.1086/591839. arXiv: 0802.3913 [astro-ph].

Chapter 4

JWST SPECTROPHOTOMETRY OF THE SMALL SATELLITES OF URANUS AND NEPTUNE

Belyakov, Matthew et al. (May 2024). “JWST Spectrophotometry of the Small Satellites of Uranus and Neptune”. In: *The Planetary Science Journal* 5.5, 119, p. 119. DOI: 10.3847/PSJ/ad3d55. arXiv: 2404.06660 [astro-ph.EP].

4.1 Introduction

Thirty-five years after Voyager 2’s fly-by of Uranus and Neptune (B. A. Smith, L. A. Soderblom, Beebe, et al., 1986; B. A. Smith, L. A. Soderblom, Banfield, et al., 1989), the satellites of the ice giants remain understudied as compared to those of the gas giant systems. The lack of dedicated spacecraft exploration, combined with the difficulty of ground-based observations due to intense scattered light from the planets, has left the innermost satellites of the ice giants without spectral characterization of their surfaces. Much of what is known about these satellites comes from Voyager 2 images, along with HST and ground-based visible and near-IR photometry (B. A. Smith, L. A. Soderblom, Banfield, et al., 1989; Colas and Buil, 1992; Karkoschka, 2001; Dumas, Terrile, et al., 2002; Karkoschka, 2003a; Pascu et al., 2006).

Constant cycling of material from collisions and subsequent re-accretion on million year timescales is the dominant process shaping the small interior satellites of the ice giants (Colwell and Esposito, 1992; R. S. French and Mark R Showalter, 2012; Charnoz et al., 2018; Ćuk et al., 2022). Catastrophic collisions to these moons from Kuiper belt objects and Oort Cloud comets are less frequent, occurring on 2 Gyr timescales for the smallest moons, and on timescales significantly longer than the lifetime of the solar system for the larger interior satellites like Neptune’s Proteus or Uranus’ Puck (Zahnle et al., 2003; Ćuk et al., 2022). While the larger satellites of Uranus (Miranda, Ariel, Umbriel, Titania, Oberon) and Neptune (Triton) all present their own interesting geology (S. Croft and L. Soderblom, 1991; S. K. Croft et al., 1995; Richard J Cartwright et al., 2015; Schenk and Moore, 2020; Richard J. Cartwright et al., 2020; Hansen et al., 2021), the heavy endogenous modification of their surfaces makes them poor probes of the original composition of the ice giants and their subnebulae. Although the exact histories of the inner satellites of Uranus and Neptune are unknown, they are likely a combination of ice giant subnebulae material and interloping comets, with larger objects being close to the original subnebula material, and smaller

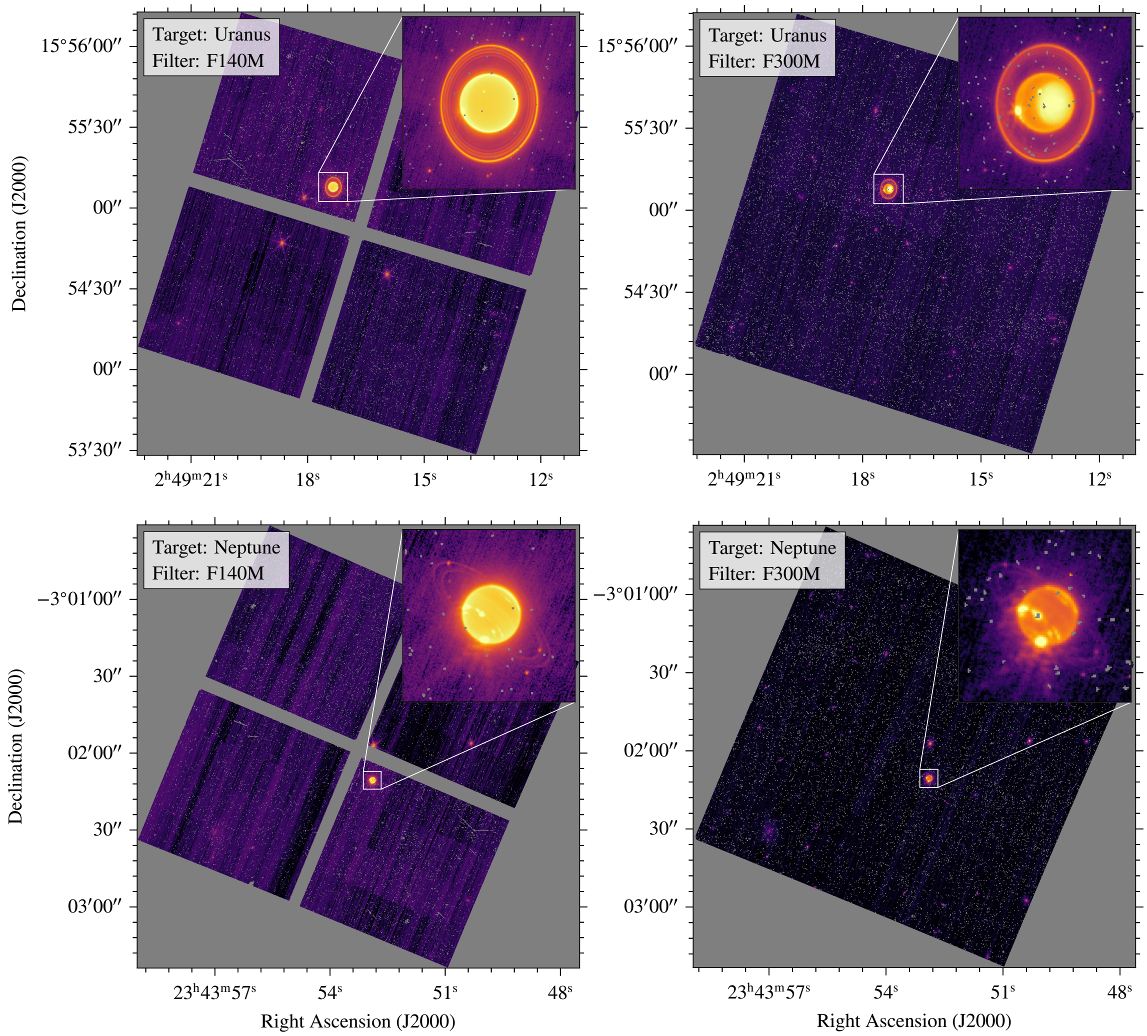

Figure 4.1: Representative JWST NIRCam images (brightness is square root scale) of the Neptunian and Uranian systems in the F140M and F300M filters.

satellites being of mixed composition (Colwell and Esposito, 1992; Szulágyi, Cilibrasi, and Mayer, 2018; Hesselbrock and Minton, 2019; Ćuk et al., 2022).

We briefly review the main properties of the thirteen inner moons of the Uranian system. Although Uranus has a larger and more varied set of rings than Neptune, it has fewer shepherd moons (at least known moons, see Chancia and Hedman, 2016 for a discussion of the possibility of new Uranian moons) for its rings, with the innermost Cordelia and Ophelia shepherding the ϵ and λ rings (Karkoschka, 2003b; Mark R Showalter and Lissauer, 2006). The next nine moons in the set (Bianca, Cressida, Desdemona, Juliet, Portia, Rosalind, Cupid, Belinda, Perdita) all share common albedos and spectral slopes with the second-largest moon, Portia, and are collectively described as the "Portia Group" (Karkoschka, 2003b). The largest

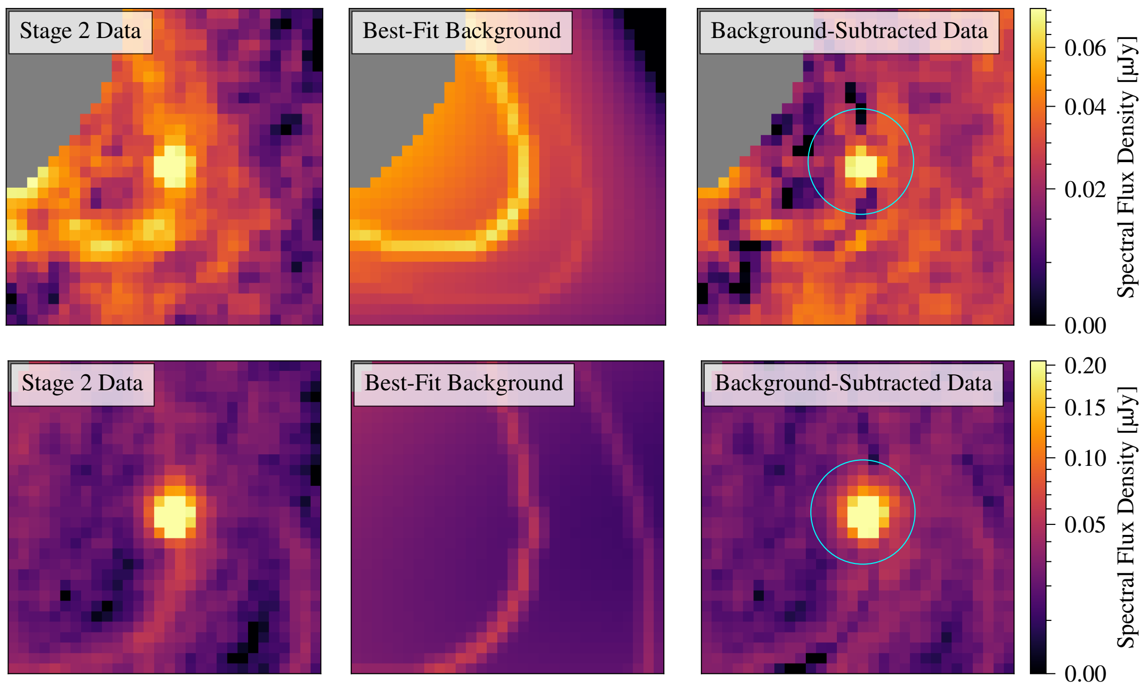

Figure 4.2: Background subtraction for an F140M (top) and an F300M (bottom) image of Neptune's moon Despina. Despina is situated adjacent to the Le Verrier ring, which has a significant contribution to the flux around the moon. The left panels show the data after stage 2 pipeline reduction which produces absolute flux-calibrated images. The middle panels show the composite background made by combining a model for the rings with a second-degree polynomial surface that characterizes the scattered light background from Neptune. The background-subtracted data is on the right, showing effective subtraction of the scattered light gradient and the ring contribution. Note that while each image is 30×30 pixels, the pixel scale in the F300M image is twice that of the F140M image, which accounts for the difference in the apparent shape of the rings and the masking of Neptune in the F300M data.

inner moon Puck has a slightly larger visual albedo, and has a distinct spectral slope in the visible from the closer-in satellites (Karkoschka, 2003b; Dumas, Bradford A. Smith, and Terrile, 2003). Given the large number of moons, the system is unstable on more than a hundred million years, with collisions and re-accretions expected (R. S. French and Mark R Showalter, 2012; Ćuk et al., 2022).

The inner component of the Neptunian system consists of seven moons, which we briefly review, starting from innermost Naiad and Thalassa. Naiad is locked into a 73:69 resonance with Thalassa (Brozović et al., 2020), and both moons are likely rubble piles based on their apparently low densities (B. A. Smith, L. A. Soderblom, Banfield, et al., 1989; Grundy and Fink, 1991; Karkoschka, 2003a). The next two moons are Despina and Galatea, which are shepherd moons of the Le Verrier and Adams rings respectively (C. C. Porco, 1991; Namouni and C. Porco, 2002). The rapid evolution of the ring arcs in the Adams ring on decade-long timescales suggest that the orbits of the inner Neptunian moons are still evolving (Renner et al., 2014). Larissa is slightly larger, at 200 km, and orbits just outside Neptune's rings (B. A. Smith, L. A. Soderblom, Banfield, et al., 1989). The next moon, Hippocamp, was only discovered in 2013, and is likely a small collisional product of the largest of the inner moons, Proteus (M. R. Showalter et al., 2019). Proteus has a notable leading/trailing brightness asymmetry in the visible, attributed to charged-particles from Neptune's magnetosphere bombarding Proteus' trailing hemisphere (Pascu et al., 2006). However, the source of the asymmetry is unclear, and details about Proteus' surface composition remain unclear. All of the inner moons have similarly low visual albedos at under 10% (Karkoschka, 2003a) and similar neutral colors (B. A. Smith, L. A. Soderblom, Banfield, et al., 1989).

In this paper we use JWST NIRCam four band (1.4, 2.1, 3.0, 4.6 μm) near-IR photometry of the inner moons of Uranus and Neptune obtained via images of the ice giants taken in Program 2739 (JWST Cycle 1 Outreach Campaign). We first discuss the observations and data reduction, focusing on the background subtraction which, due to the complexity of the scattered light from the planets and their rings, has to be handled separately from the standard JWST pipeline. With the resulting spectrophotometry, we compare the satellites with one another and to spectra of other solar system small bodies.

4.2 Observations

The Neptunian and Uranian systems were observed through JWST Program 2739 (JWST Cycle 1 Outreach Campaign) on three separate dates using the near-infrared imager NIRCam. The Neptunian observations were taken on 2022 July 12 when the planet was at a phase angle of 1.8°, and are in four filters: F140M, F210M, F300M, and F460M, which are correspondingly centered at 1.4, 2.1, 3.0, and 4.6 μm. The Uranian observations are split between two dates, one set of images taken only in F140M and F300M filters on 2023 February 6 (phase angle 2.9°), and a second group of images taken on 2023 September 4 (phase angle 2.8°) in the same four filters as the Neptune images. In total, there are 40 images for Neptune and 48 images for Uranus, split between the four filters used.

Images were taken using NIRCam's module B, which offers higher long-wavelength throughput than module A (NIRCam has two modules, offering slightly different performance; Rigby et al. 2023). Ten exposures were taken in each filter resulting from five dithers performed with two different exposure strategies. For the Neptune and second set of Uranus images, a first series of exposures was done with an 80 s exposure time (1 integrations, 8 groups, `RAPID` readout mode), and a second was taken with a 280 s effective exposure time (2 integrations, 7 groups, `Bright1` readout mode). The short wavelength images are split between four detectors with a 5″ gap, and the positioning of the planets on the detector frequently results in moons falling on the detector gap or too close to the detector edge in one or more dithers. The choice of dither put Neptune's moon Galatea in the detector gap for three out of five of the F140M and F210M images, while for Uranus, Juliet and Portia are off the detector in the final F210M image.

4.3 Data Reduction

For each image, we begin with the Level 2 "rate" data products, which have been bias- and dark-corrected and converted into units of counts/second by the ramp fitting step (JWST pipeline version 1.11.3, Bushouse et al., 2023). We then skip the background subtraction of stage two processing, as we apply our own background subtraction scheme later, and proceed with the `assign_wcs`, `flat_field`, and `photom` steps, the latter of which converts the ramp files to flux units of MJy/sr. The product of these steps can be seen in Figure 4.1.

At this step, we also discard all of the images taken with the `Bright1` readout pattern. Program 2739 was designed to provide images of the Neptunian and Uranian systems at large for public release, and thus JWST's tracking rate was set to match the planet's motion, not that of any given satellite. As the moons have an extra on-sky motion of 0.01-0.02 "/minute (just under the pixel scale of the short wavelength detector) relative to their host planets, they are smeared on the detector. However, the ramp-fitting step in the JWST pipeline encounters issues, especially with the Uranian satellites, as the brightness in the pixels changes as the moon moves over the course of one integration. The sudden drop or jump in counts prevents the ramp-fitting or jump detection steps from accurately fitting the count rate of the object in the longer exposure images. We therefore discard the longer 280 s observations for both the Neptunian and Uranian system, instead using only the 80s exposures, during which the motion of the satellites' PSFs on the detector is on a sub-pixel scale.

4.3.1 Astrometry

To simplify the analysis process and the mapping between sky coordinates and pixel coordinates, we re-projected each image into rectangular sky coordinates with right ascension increasing to the left along the horizontal axis and declination increasing upward along the vertical axis. For this reprojection, we used the Astropy-affiliated package `reproject`[1]. We first find the optimal WCS for our set of images using the Astropy-affiliated package `reproject`, then use its flux-conserving interpolation algorithm `reproject_adaptive` to create a composite image of all detectors (four detector images for the F140M and F300M data, one detector image for the F210M and F460M data) reprojected into rectangular right

[1] https://reproject.readthedocs.io/en/stable/

ascension and declination sky coordinates (see figure 4.1 for an example of these reprojections). For each satellite target, we calculated the position in RA/Dec at the time of the observation using JPL Horizons [2], which we then mapped to pixel positions using WCS transforms. However, the satellite positions were often different by up to 3 pixels along either axis. The calculated position of Neptune was always accurate, so we suspect the error is due to imprecision in the satellite ephemeris used by Horizons. To calculate the true position of the satellite, we extracted a 10-pixel-by-10-pixel image around the Horizons coordinates, then fit a two-dimensional Gaussian profile with a background constant, which provided us with refined pixel coordinates.

4.3.2 Background Subtraction

Given the proximity of the inner moons of Uranus and Neptune to the planet and the presence of multiple rings, the standard method of taking the median brightness value in an annulus around each satellite is not sufficient to account for the background. Instead, we create a background subtraction that accounts for the scattered light from the planet and any contribution from the rings.

Removing the contribution from the rings is especially important for the satellites of Neptune, where Galatea blends with the Adams ring and Despina blends with the Le Verrier ring. In order to remove the ring flux, we first mask out the targeted satellite, the two rings, and Neptune, then fit a second-degree two-dimensional polynomial surface to the scattered light background. After removing the scattered light contribution, we construct and fit a model of the rings projected into the viewing geometry of the individual observation and the pixel scale of the detector. We begin by constructing a weighted brightness map of the rings using the following procedure. First, for both of the rings, we generate 3,600 separate on-sky coordinates in RA/Dec, azimuthally equidistant in 0.1° increments. These RA/Dec positions on the ring are obtained by adding a radial offset in the ring plane of Neptune using the ring radii given in De Pater et al., 2018 to the position of Neptune in JPL Horizons. We then bin the coordinates into a 2D histogram with boundaries defined by the NIRCam pixel edges. This effectively adds up, for each detector pixel, the contribution of each 0.1∘ segment of the ring to the brightness in that pixel. This model therefore determines which pixels encompass a larger section of the ring; e.g., pixels next to the ring ansa are proportionally brighter than other pixels, as they contain more of the ring flux. As a result, we have a map for the relative flux of each pixel in the ring as compared to any other pixel in the ring. We then convolve the histogram with a 2D Gaussian kernel approximating the appropriate filter PSF. Having obtained the relative proportions for the brightness of each component of the ring, we now

[2] https://ssd.jpl.nasa.gov/horizons/

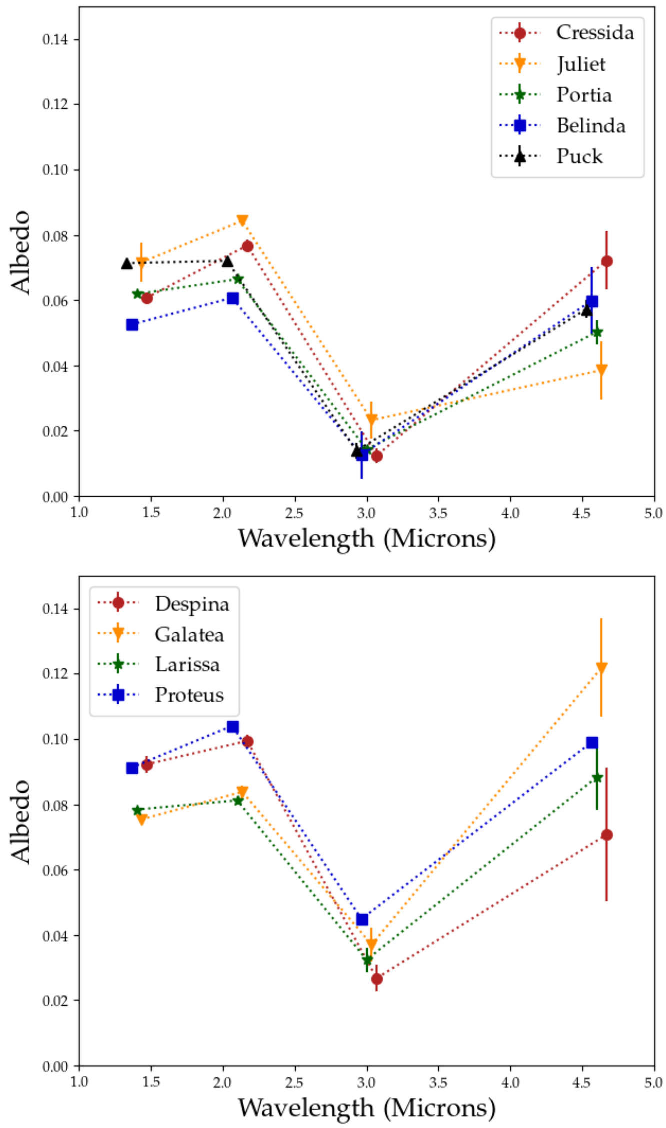

Figure 4.3: *Left panel:* Albedos of the $r > 40$ km satellites of Uranus (Cressida, Juliet, Portia, Belinda, and Puck). *Right panel:* Albedos of four inner Neptunian satellites (Despina, Galatea, Larissa, and Proteus) for the four wavelengths observed. Each moon's observations have a slight horizontal offset from the filter's central wavelength to assist readability. Both diagrams share the same vertical axis for easier comparison. All of the satellites show a clear 3 μmabsorption feature, and most have an upwards slope between 1.4 and 2.1 μm. The Uranian satellites are on average lower albedo than the Neptunian ones, and seem to have a somewhat smaller F300M-F460M slope.

fit the model ring image to the data for the ring using a simple linear fit using least-squares minimization: we find which coefficient times the ring model plus some constant offset best matches the data. In order to prevent the fit from being skewed by the brightest pixels next to Neptune, we only fit using those pixels in the ring which are 7-12 pixels away from our target of interest. We then subtract the best-fit final ring model from the science image.

Figure 4.2 shows an example of this method applied to Despina for both the higher spatial-resolution short wavelength mosaic data (top row) and lower spatial-resolution long wavelength single-detector data (bottom row). The first column shows the product of stage 2 pipeline-processed data in units of μJy(after the `photom` step of the JWST pipeline). The middle column shows the best fit background composed of the scattered light polynomial surface and the two rings. The right column shows the background-subtracted data, demonstrating the effective removal of the rings without significant residuals.

The background subtraction for Uranus is simpler as all satellites we analyze are exterior to the orbit of the bright ϵ ring, rather than coincident with it at the detector scale of NIRCam. However, because some satellites are still affected by scattered light from the bright ring, the rings must be removed before fitting for the scattered light background, and so we simply mask the ϵ ring completely for all stages of the background subtraction.

4.3.3 Photometry

In order to obtain accurate photometry, we empirically determine what fraction of light is captured by our chosen aperture radius of six pixels. First, we take the CALSPEC spectrum of solar analog P330E (which is a composite of HST spectra and stellar models) and convolve it with the four filter bandpasses we use in order to obtain synthetic photometry for the star (Bohlin, Gordon, and Tremblay, 2014; Bohlin and Landolt, 2015; Gordon et al., 2022). Then, using NIRCam images of the same star from Program 1538 (Absolute Flux Calibration (G Dwarfs)), we draw successively larger apertures, determining what portion of the flux we obtain from photometry relative to the synthetic flux from the spectrum[3]. At six pixels, this is approximately 83% of the light for F140M, F210M, and F460M, and around 86% of the light for F300M (with less than 1% error). We also compare these values to the theoretical PSFs, finding that the curves for the percent of captured light as a function of aperture size closely match those from WebbPSF [4] (STSCI, 2016). All of our photometric measurements are divided by the proportion of captured flux in the corresponding filter at six pixels to

[3]We note that comparing to the NIRSpec spectrum is a necessary step, as the internal flux calibration used to generate the counts/s to MJy/sr conversion in the `photom` step is based off specific choices of aperture size, and it is such that the true flux is not obtained with an infinite aperture in the NIRCam images.

[4]See figures 8/9 of the JDox for JWST NIRCam for an example of encircled energy diagrams https://jwst-docs.stsci.edu/jwst-near-infrared-camera/nircam-performance/nircam-point-spread-functions

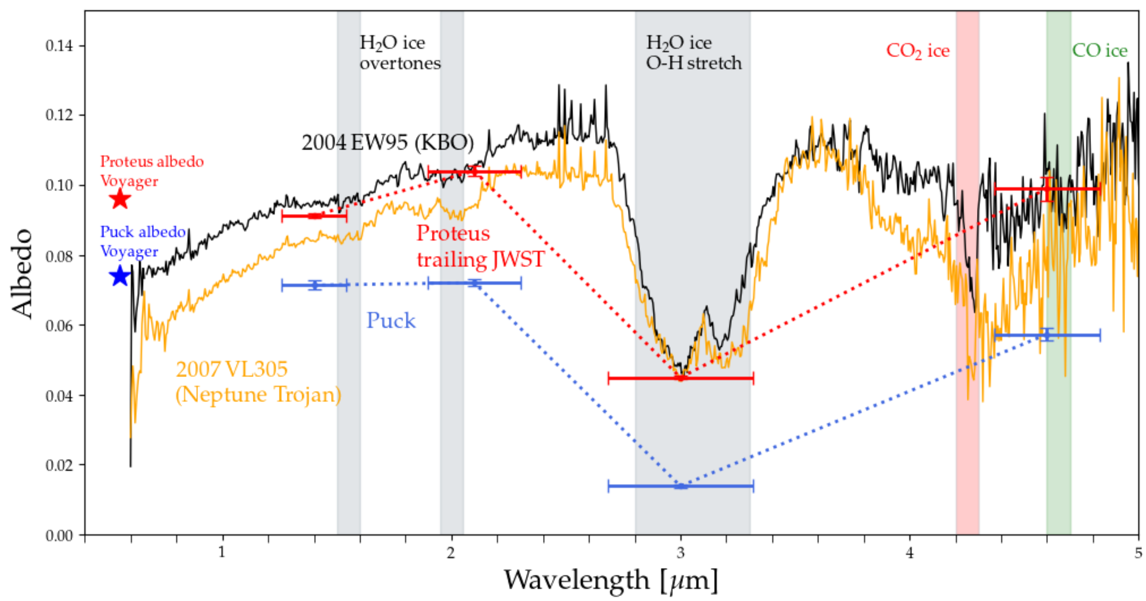

Figure 4.4: JWST NIRCam albedos of Proteus and Puck compared to the spectra of 2004 EW95 (Plutino) and 2007 VL305 (Neptune Trojan) from JWST Programs 2418 and 2550 respectively. Also shown are Voyager-derived visual geometric albedos, with the Puck albedo selected to be at the same phase angle as the JWST observations (see Figure 6 of Karkoschka, 2001 and Table 2 of Karkoschka, 2003b). The spectrophotometry for Proteus and Puck closely matches the shape and albedo for the selected objects, both of which have less red/neutral spectral slopes, and perihelia also near 30 AU. Higher resolution spectra for Puck and Proteus are needed to reveal surface composition.

obtain the true value for the flux.

We convert the intensities obtained from the photometry into geometric albedos using the measured solar flux in the NIRCam filters as given in Willmer, 2018 along with sizes for the moons obtained by Voyager 2 (B. A. Smith, L. A. Soderblom, Beebe, et al., 1986; B. A. Smith, L. A. Soderblom, Banfield, et al., 1989; Karkoschka, 2001; Karkoschka, 2003b). We report our photometry in both flux units and as albedos in every band in Table 4.1. To obtain an estimate for the error on each flux measurement, we calculate the flux in eight equidistant apertures centered ten pixels from the target, and take the standard deviation of their flux as an estimation of the systematic error present in the image after background subtraction. As there is significant local variation in the background of the images, both due to detector issues and structure from the rings and the planet, calculating the standard deviation of flux in nearby apertures provides a good estimate of the true uncertainty on the measurement. The albedo and flux for each target is then reported as the mean measurement, with the errors from all the images in a given filter added in quadrature, shown in Figure 4.3.

4.4 Discussion

Results from JWST have given extensive insight into the compositions of small bodies in the outer solar system, with CO_2, CO, H_2O, and CH_3OH ices being commonplace on Kuiper belt objects (Michael E. Brown and Wesley C. Fraser, 2023; Markwardt et al., 2023; Licandro et al., 2024). By comparison, little is known about the composition of the inner satellites of the ice giants. In the case of Neptune, the violent capture of Triton (Agnor and Hamilton, 2006) leaves open the question of what composes the collisional debris that went on to form the satellites interior to Triton (Goldreich et al., 1989; Nogueira, Brasser, and Gomes, 2011; Brozović et al., 2020). For the Uranian satellites, the reason for the stark difference between the very dark surfaces of Puck and Portia group satellites as compared to the brighter regular satellites (Karkoschka, 2001) remains unclear.

Our results for the photometry of the inner Uranian and Neptunian satellites (as shown in Figure 4.3) demonstrate that to first order, the small interior moons seem to all have similar spectral behavior in the infrared. Comparing between the two systems, we find that the Neptunian satellites have notably higher albedos than the Uranian satellites. The colors (ratio in albedo between any two filters) of the two sets of satellites are similar, but the Uranian moons generally have a higher 1.4-2.1 µmslope, a deeper 3.0 µmfeature, and a slightly smaller 3.0-4.6 µmslope than the Neptunian satellites. Notably, Uranus' Puck has nearly the same reflectance at 1.4 µmas at 2.1 µm.

We note that our measured near-infrared albedos are lower than the HST visible albedos from (Karkoschka, 2001; Karkoschka, 2003a). Yet other values from previous observations of the satellites, such as from Dumas, Bradford A. Smith, and Terrile, 2003, obtain near-IR photometry for Proteus with a distinctly lower albedo of near 7% in the 1.0-2.0 µmrange, and find Puck to be higher albedo than Proteus, inverting our results. The HST albedos from Dumas, Bradford A. Smith, and Terrile, 2003 were obtained for the leading hemisphere of Proteus, and the opposite (southern) hemisphere for Puck. Similarly, the old Voyager and Karkoschka, 2001; Karkoschka, 2003a HST observations were taken of different orientations of the satellites. Recent ground-based observations by Paradis, Moeckel, and de Pater, 2023 find H-band reflectivities of the Uranian satellites which are comparable to our results when looking at similar phase angles. Paradis, Moeckel, and de Pater, 2023 also find that Belinda and Portia have notably lower reflectivities than Puck in the near-IR, which is a good match to our results. Given the many decades between observations, varying phase angles, and very distinct orientations of these irregularly-shaped objects observed, we do not offer further comparison between our JWST spectrophotometry and past data obtained for the satellites. Future time-series observations of these satellites are necessary to constrain their photometric properties as a function of phase angle and orientation and may help to resolve discrepancies

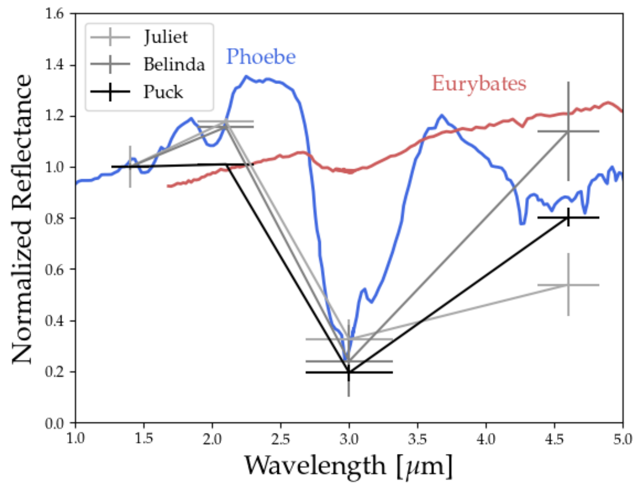

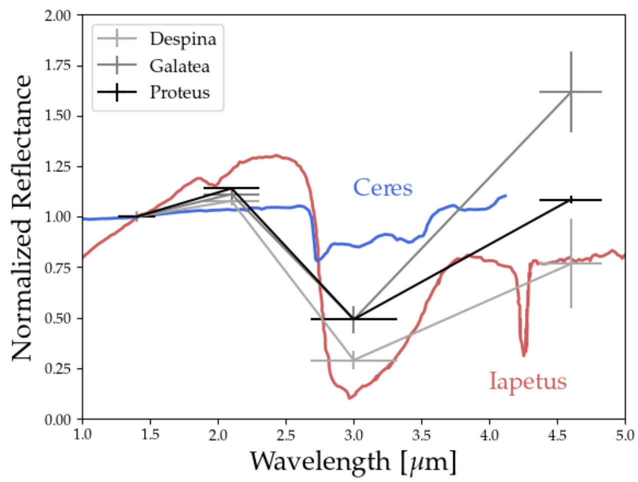

Figure 4.5: *Left panel:* Comparison of the normalized reflectance of Phoebe from Cassini VIMS data (Clark, R. H. Brown, et al., 2019), and Jupiter Trojan Eurybates (Wong et al., 2023), to Uranian inner satellites Juliet, Belinda, and Puck. Eurybates, while having a similarly low albedo to the Uranian inner satellites, has a significantly different infrared spectrum, with a much weaker 3.0 µmfeature. Phoebe's albedo is similar to the very dark Uranian satellites, and seems to have a similarly deep 3.0 µmfeature, with a similar upturn between 1.4 and 2.1 µm. *Right panel:* Comparison of the normalized reflectance of Ceres (from Raponi et al. 2021) and Iapetus from VIMS to Neptunian inner satellites Despina, Galatea, and Proteus. Ceres' 3.0 µmammonia feature is shallow, and does not match any ice giant inner satellite. The dark part of Iapetus has a spectrum that is compatible with that of Despina, but not Proteus or Galatea.

in photometric measurements accumulated over four decades of sparse observations.

The most prominent feature on the observed satellites is a 3.0 μmabsorption that could be attributed to multiple possible materials. Possible matches for this feature include: water ice or hydrated minerals from the O-H stretch at 3.0 μm(Janice L. Bishop, 1994; R. H. Brown and Cruikshank, 1997; Schmitt et al., 1998), clays containing ammonia salts such as NH_4^+ that has a 3.07 μmfeature (J. L. Bishop, Banin, et al., 2002), or complex aliphatic and aromatic organics that have a set of C-H stretches just past 3.0 μm(Hand and Carlson, 2012; Ricca et al., 2012). Combinations of these compounds are possible, similar to Kuiper belt objects that have both water ice and hydrocarbons. Most of the satellites show a slight upwards slope between 1.4 and 2.1 μm, a near-IR upturn that is characteristic of less red, dynamically excited KBOs (M. E. Brown, Schaller, and W. C. Fraser, 2012; Hainaut, Boehnhardt, and Protopapa, 2012; Wesley C. Fraser et al., 2023).

Without complete 1-5 μmspectra for the inner satellites, we cannot directly infer their surface composition and determine which of the above hypotheses for surface composition holds. However, we can draw comparisons to known spectra of the gas giant satellites and JWST NIRSpec data of other small outer solar system bodies, in particular KBOs and Neptune Trojans. In Figure 4.4, we overlay our JWST NIRCam photometry for the two largest of the inner satellites, Puck and Proteus against the spectrum of Kuiper belt object 2004 EW95 (JWST Program 2418) and Neptune Trojan 2007 VL305 (Markwardt et al., 2023). Both 2004 EW95 and 2007 VL305 have a 3.0 μmfeature with a Fresnel peak due to water ice, and a CO_2 ice feature at 4.25 μm. 2004 EW95 has a notably low albedo and, as a Plutino with a perihelion of 26 AU, experiences similar levels of peak insolation to Proteus. Similarly, the Neptune Trojan 2007 VL305 has likely been at Neptune's L4 point for 4.5 Gyr, thus providing an excellent comparison to Proteus in terms of amount of solar radiation received (the radius and thus albedo for 2007 VL305 is unknown, so we scale the albedo to match that of Proteus). We find that Proteus matches both of these spectra, with a deep 3.0 μmabsorption, and similar spectral slopes between 1.4/2.1 μmand 3.0/4.6 μm. However, there are numerous KBOs and Neptune Trojans that do not share these spectral features. Many KBOs with $q < 30$ AU have significantly higher albedos than the ones measured for Proteus (Lellouch et al., 2013), as well as clearly redder spectral slopes in the visible and near-infrared. Additionally, Neptune Trojans with "very red" visible spectral slopes, such as 2013 VX30, do not exhibit the 3.0-4.6 μmupturn that Proteus and Puck do (see figure 1 of Markwardt et al. 2023).

The Saturnian satellites also offer an important comparison point for our spectrophotometry. Many of the Saturnian satellites have high albedos (Enceladus, Tethys, Iapetus trailing) that are very distinct from the set of Uranian and Neptunian satellites observed, but the darker Phoebe or the leading side of Iapetus are a better point of comparison (see figure 2 of Filacchione et al., 2012, also data from Clark, Cruikshank, et al. 2012; Hedman et al. 2024). We show data from Cassini VIMS on the Saturnian system from Clark, R. H. Brown, et al., 2019 in Figure 4.5. Phoebe and Iapetus both have spectra similar to some of the Neptunian and Uranian moons, largely matching the depth of the 3.0 µmfeature and the 1.4-2.1 µmand 3.0-4.6 µmspectral slopes.

Our search for spectral analogues of the small satellites of the ice giants has returned two possible classes of bodies: dark, icy Kuiper belt objects, and two of the Saturnian satellites, Phoebe and Iapetus. However, the 3.0 µmabsorption on all the inner satellites is of uncertain provenance, and thus the formation history of moons like Proteus and Puck remains unclear. Although all of the solar system analogues that fit the data for the small satellites have clear water ice absorption features, the low resolution nature of our data precludes us from ruling out ammonia, organics, and hydrated minerals as the drivers of the 3.0 µmfeature in our spectrophotometry.

If the inner satellites are similar to KBOs with a 3.0 µmfeature due to water ice, it could indicate either that water ice was stable in the ice giant subnebulae at the formation radius of Puck and Proteus (Batygin and Morbidelli, 2020), or that the inner satellites are a mix of collisional material from comets, KBOs, and the primordial inner satellites (Colwell and Esposito, 1992). While water ice could be present on these objects, it cannot be the dominant component composing all of the small Uranian and Neptunian moons, specifically not the innermost ones. Recent work by R. G. French et al., 2024 has found that the density of Uranian inner satellites increases closer to the planet, consistent with the Roche critical density (see figure 38 of R. G. French et al. 2024). The innermost of the inner satellites must be composed of some material with density greater than that of ice, potentially consistent with silicates or organics (B. A. Smith, L. A. Soderblom, Beebe, et al., 1986; B. A. Smith, L. A. Soderblom, Banfield, et al., 1989; Karkoschka, 2001; Tiscareno et al., 2013). Reconciling these varying densities with the consistent 3.0 µmband depth we observe in both systems will require future observations.

Other possibilities for the 3.0 µmabsorption appear less likely. The O-H stretch due to hydrated minerals produces a smaller band depth than seen in our spectrophotometry (Janice L. Bishop, 1994; J. L. Bishop, Lane, et al., 2008; Takir et al., 2019). Ammonia is found in the ice giants' atmospheres and on the regular satellites of the Uranian system (Richard J. Cartwright et al., 2020), and its presence on the inner satellites would suggest they consist of subnebular material, as ammonia is not common throughout the Kuiper belt. Ceres has a prominent 3.0 µmfeature attributed to ammonia as shown in Figure 4.5 (Raponi et al., 2021), but has a much smaller band depth than the small Neptunian and Uranian satellites. The Jupiter Trojan Eurybates is an example of a solar system body with a similar albedo to the inner Uranian moons and a 3.0 μmfeature attributed to the O-H stretch mixed with organics (Wong et al., 2023). Organics also seem to be a poor match, as the depth of the 3.0 μmabsorption on Eurybates is significantly weaker than in our observations.

In order to resolve key questions on formation of satellites around ice giants, new observations that have spectral coverage from 0.6-5.0 μm(with JWST NIRSpec) for the inner satellites of Neptune and Uranus are necessary to pinpoint the surface compositions of these objects. With possible upcoming spacecraft exploration of Uranus in the next several decades, these data prove valuable in target selection and determining the capabilities needed to fully uncover the compositions of the ice giant systems.

4.5 Data

We report the fluxes and albedos for the spectrophotometry of the ice giant satellites below. Albedo is calculated as follows:

$$p = \left(\frac{\text{target flux}}{\text{solar flux}}\right) \div \left(\frac{1\text{AU}^2}{d_{pj}^2} * \frac{r_{\text{moon}}^2}{d_{ps}^2}\right), \tag{4.1}$$

where d_{ps} is the planet-sun distance and d_{pj} is the planet-JWST distance. Radii for objects are from B. A. Smith, L. A. Soderblom, Beebe, et al., 1986; B. A. Smith, L. A. Soderblom, Banfield, et al., 1989; Karkoschka, 2001; Karkoschka, 2003b, with mean radii used due to the non-sphericity of the satellites.

References

Agnor, Craig B and Douglas P Hamilton (2006). "Neptune's capture of its moon Triton in a binary–planet gravitational encounter". In: *Nature* 441.7090, pp. 192–194.

Batygin, Konstantin and Alessandro Morbidelli (May 2020). "Formation of Giant Planet Satellites". In: *ApJ* 894.2, 143, p. 143. DOI: 10.3847/1538-4357/ab8937. arXiv: 2005.08330 [astro-ph.EP].

Bishop, J. L., A. Banin, et al. (Jan. 2002). "Detection of soluble and fixed NH_4^+ in clay minerals by DTA and IR reflectance spectroscopy: a potential tool for planetary surface exploration". In: *Planet. Space Sci.* 50.1, pp. 11–19. DOI: 10.1016/S0032-0633(01)00077-0.

Bishop, J. L., M. D. Lane, et al. (Mar. 2008). "Reflectance and emission spectroscopy study of four groups of phyllosilicates: smectites, kaolinite-serpentines, chlorites and micas". In: *Clay Minerals* 43.1, pp. 35–54. DOI: 10.1180/claymin.2008.043.1.03.

Bishop, Janice L. (Jan. 1994). "Infrared Spectroscopic Analyses on the Nature of Water in Montmorillonite". In: *Clays and Clay Minerals* 42.6, pp. 702–716. DOI: 10.1346/CCMN.1994.0420606.

Table 4.1: JWST NIRCam Photometry of Neptunian and Uranian Inner Satellites

	F140M	F210M	F300M	F460M
Despina				
Flux (μJy)	7.5 ± 0.2	5.19 ± 0.10	0.76 ± 0.12	0.9 ± 0.3
Albedo	0.092 ± 0.003	0.100 ± 0.002	0.027 ± 0.004	0.07 ± 0.02
Galatea				
Flux (μJy)	7.68 ± 0.16	5.49 ± 0.13	1.32 ± 0.19	1.9 ± 0.2
Albedo	0.075 ± 0.002	0.084 ± 0.002	0.037 ± 0.005	0.122 ± 0.015
Larissa				
Flux (μJy)	9.84 ± 0.09	6.55 ± 0.10	1.42 ± 0.17	1.68 ± 0.19
Albedo	0.0784 ± 0.0007	0.0812 ± 0.0012	0.032 ± 0.004	0.088 ± 0.010
Proteus				
Flux (μJy)	53.68 ± 0.10	39.34 ± 0.10	9.24 ± 0.07	8.82 ± 0.13
Albedo	0.0913 ± 0.0002	0.1041 ± 0.0003	0.0449 ± 0.0003	0.0990 ± 0.0015
Cressida				
Flux (μJy)	6.86 ± 0.17	5.57 ± 0.13	0.49 ± 0.09	1.23 ± 0.15
Albedo	0.0607 ± 0.0015	0.0768 ± 0.0019	0.012 ± 0.002	0.072 ± 0.009
Juliet				
Flux (μJy)	11.2 ± 0.9	8.45 ± 0.10	1.27 ± 0.31	0.9 ± 0.2
Albedo	0.072 ± 0.006	0.0843 ± 0.0010	0.023 ± 0.006	0.039 ± 0.009
Portia				
Flux (μJy)	20.20 ± 0.12	13.93 ± 0.08	1.63 ± 0.11	2.48 ± 0.18
Albedo	0.0619 ± 0.0004	0.0664 ± 0.0004	0.0143 ± 0.0009	0.050 ± 0.004
Belinda				
Flux (μJy)	7.51 ± 0.10	5.58 ± 0.07	0.63 ± 0.37	1.3 ± 0.2
Albedo	0.0526 ± 0.0007	0.0607 ± 0.0007	0.013 ± 0.007	0.060 ± 0.010
Puck				
Flux (μJy)	33.03 ± 0.11	21.44 ± 0.10	2.2 ± 0.4	4.02 ± 0.19
Albedo	0.0713 ± 0.0002	0.0721 ± 0.0004	0.014 ± 0.002	0.057 ± 0.003

Bohlin, Ralph C., Karl D. Gordon, and P. -E. Tremblay (Aug. 2014). “Techniques and Review of Absolute Flux Calibration from the Ultraviolet to the Mid-Infrared”. In: *PASP* 126.942, p. 711. DOI: 10.1086/677655. arXiv: 1406.1707 [astro-ph.IM].

Bohlin, Ralph C. and Arlo U. Landolt (Apr. 2015). “The CALSPEC Stars P177D and P330E”. In: *AJ* 149.4, 122, p. 122. DOI: 10.1088/0004-6256/149/4/122. arXiv: 1502.01754 [astro-ph.IM].

Brown, M. E., E. L. Schaller, and W. C. Fraser (June 2012). “Water Ice in the Kuiper Belt”. In: *AJ* 143.6, 146, p. 146. DOI: 10.1088/0004-6256/143/6/146. arXiv: 1204.3638 [astro-ph.EP].

Brown, Michael E. and Wesley C. Fraser (July 2023). “The State of CO and CO_2 Ices in the Kuiper Belt as Seen by JWST”. In: *PSJ* 4.7, 130, p. 130. DOI: 10.3847/PSJ/ace2ba. arXiv: 2306.17051 [astro-ph.EP].

Brown, Robert H. and Dale P. Cruikshank (Jan. 1997). “Determination of the Composition and State of Icy Surfaces in the Outer Solar System”. In: *Annual Review of Earth and Planetary Sciences* 25, p. 243. DOI: 10.1146/annurev.earth.25.1.243.

Brozović, Marina et al. (Mar. 2020). "Orbits and resonances of the regular moons of Neptune". In: *Icarus* 338, 113462, p. 113462. DOI: 10.1016/j.icarus.2019.113462. arXiv: 1910.13612 [astro-ph.EP].

Bushouse, Howard et al. (July 2023). *JWST Calibration Pipeline*. Version 1.11.3. DOI: 10.5281/zenodo.8157276. URL: https://doi.org/10.5281/zenodo.8157276.

Cartwright, Richard J et al. (2015). "Distribution of CO2 ice on the large moons of Uranus and evidence for compositional stratification of their near-surfaces". In: *Icarus* 257, pp. 428–456.

Cartwright, Richard J. et al. (July 2020). "Evidence for Ammonia-bearing Species on the Uranian Satellite Ariel Supports Recent Geologic Activity". In: *ApJL* 898.1, L22, p. L22. DOI: 10.3847/2041-8213/aba27f. arXiv: 2007.02826 [astro-ph.EP].

Chancia, R. O. and M. M. Hedman (Dec. 2016). "Are There Moonlets Near the Uranian α and β Rings?" In: *AJ* 152.6, 211, p. 211. DOI: 10.3847/0004-6256/152/6/211. arXiv: 1610.02376 [astro-ph.EP].

Charnoz, S. et al. (2018). "The Origin of Planetary Ring Systems". In: *Planetary Ring Systems. Properties, Structure, and Evolution*. Ed. by M. S. Tiscareno and C. D. Murray, pp. 517–538. DOI: 10.1017/9781316286791.018.

Clark, Roger N., Robert H. Brown, et al. (Mar. 2019). "Isotopic ratios of Saturn's rings and satellites: Implications for the origin of water and Phoebe". In: *Icarus* 321, pp. 791–802. DOI: 10.1016/j.icarus.2018.11.029.

Clark, Roger N., Dale P. Cruikshank, et al. (Apr. 2012). "The surface composition of Iapetus: Mapping results from Cassini VIMS". In: *Icarus* 218.2, pp. 831–860. DOI: 10.1016/j.icarus.2012.01.008.

Colas, F. and C. Buil (Aug. 1992). "First Earth-based observations of Neptune's satellite Proteus". In: *A&A* 262.1, p. L13.

Colwell, Joshua E. and Larry W. Esposito (June 1992). "Origins of the rings of Uranus and Neptune 1. Statistics of satellite disruptions". In: *J. Geophys. Res.* 97.E6, pp. 10227–10241. DOI: 10.1029/92JE00788.

Croft, S. K. et al. (Jan. 1995). "The geology of Triton." In: *Neptune and Triton*, pp. 879–947.

Croft, SK and LA Soderblom (1991). "Geology of the Uranian satellites." In: *Uranus*, pp. 561–628.

Ćuk, Matija et al. (Aug. 2022). "Cupid is not Doomed Yet: On the Stability of the Inner Moons of Uranus". In: *AJ* 164.2, 38, p. 38. DOI: 10.3847/1538-3881/ac745d. arXiv: 2205.14272 [astro-ph.EP].

De Pater, I. et al. (2018). "The Rings of Neptune". In: *Planetary Ring Systems. Properties, Structure, and Evolution*. Ed. by M. S. Tiscareno and C. D. Murray, pp. 112–124. DOI: 10.1017/9781316286791.005.

Dumas, Christophe, Bradford A. Smith, and Richard J. Terrile (Aug. 2003). "Hubble Space Telescope NICMOS Multiband Photometry of Proteus and Puck". In: *AJ* 126.2, pp. 1080–1085. DOI: 10.1086/375909.

Dumas, Christophe, Richard J. Terrile, et al. (Mar. 2002). "Astrometry and Near-Infrared Photometry of Neptune's Inner Satellites and Ring Arcs". In: *AJ* 123.3, pp. 1776–1783. DOI: 10.1086/339022.

Filacchione, G. et al. (Aug. 2012). "Saturn's icy satellites and rings investigated by Cassini-VIMS: III - Radial compositional variability". In: *Icarus* 220.2, pp. 1064–1096. DOI: 10.1016/j.icarus.2012.06.040. arXiv: 1203.6230 [astro-ph.EP].

Fraser, Wesley C. et al. (May 2023). "Col-OSSOS: The Two Types of Kuiper Belt Surfaces". In: *PSJ* 4.5, 80, p. 80. DOI: 10.3847/PSJ/acc844. arXiv: 2206.04068 [astro-ph.EP].

French, Richard G. et al. (Mar. 2024). "The Uranus system from occultation observations (1977-2006): Rings, pole direction, gravity field, and masses of Cressida, Cordelia, and Ophelia". In: *Icarus* 411, 115957, p. 115957. DOI: 10.1016/j.icarus.2024.115957. arXiv: 2401.04634 [astro-ph.EP].

French, Robert S and Mark R Showalter (2012). "Cupid is doomed: An analysis of the stability of the inner uranian satellites". In: *Icarus* 220.2, pp. 911–921.

Goldreich, Peter et al. (1989). "Neptune's story". In: *Science* 245.4917, pp. 500–504.

Gordon, Karl D. et al. (May 2022). "The James Webb Space Telescope Absolute Flux Calibration. I. Program Design and Calibrator Stars". In: *The Astronomical Journal* 163.6, p. 267. DOI: 10.3847/1538-3881/ac66dc. URL: https://dx.doi.org/10.3847/1538-3881/ac66dc.

Grundy, William M. and Uwe Fink (Oct. 1991). "A new spectrum of Triton near the time of the Voyager encounter". In: *Icarus* 93.2, pp. 379–385. DOI: 10.1016/0019-1035(91)90220-N.

Hainaut, O. R., H. Boehnhardt, and S. Protopapa (Oct. 2012). "Colours of minor bodies in the outer solar system. II. A statistical analysis revisited". In: *A&A* 546, A115, A115. DOI: 10.1051/0004-6361/201219566. arXiv: 1209.1896 [astro-ph.EP].

Hand, K. P. and R. W. Carlson (Mar. 2012). "Laboratory spectroscopic analyses of electron irradiated alkanes and alkenes in solar system ices". In: *Journal of Geophysical Research (Planets)* 117.E3, E03008, E03008. DOI: 10.1029/2011JE003888.

Hansen, Candice J. et al. (Aug. 2021). "Triton: Fascinating Moon, Likely Ocean World, Compelling Destination!" In: *PSJ* 2.4, 137, p. 137. DOI: 10.3847/PSJ/abffd2.

Hedman, M. M. et al. (Feb. 2024). "Water-Ice Dominated Spectra of Saturn's Rings and Small Moons from JWST". In: *arXiv e-prints*, arXiv:2402.15698, arXiv:2402.15698. DOI: 10.48550/arXiv.2402.15698. arXiv: 2402.15698 [astro-ph.EP].

Hesselbrock, Andrew J. and David A. Minton (Jan. 2019). "Three Dynamical Evolution Regimes for Coupled Ring-satellite Systems and Implications for the Formation of the

Uranian Satellite Miranda”. In: *AJ* 157.1, 30, p. 30. DOI: 10.3847/1538-3881/aaf23a. arXiv: 1811.11884 [astro-ph.EP].

Karkoschka, Erich (May 2001). “Comprehensive Photometry of the Rings and 16 Satellites of Uranus with the Hubble Space Telescope”. In: *Icarus* 151.1, pp. 51–68. DOI: 10.1006/icar.2001.6596.

— (Apr. 2003a). “Sizes, shapes, and albedos of the inner satellites of Neptune”. In: *Icarus* 162.2, pp. 400–407. DOI: 10.1016/S0019-1035(03)00002-2.

— (2003b). “Sizes, shapes, and albedos of the inner satellites of Neptune”. In: *Icarus* 162.2, pp. 400–407.

Lellouch, E. et al. (Sept. 2013). ““TNOs are Cool”: A survey of the trans-Neptunian region. IX. Thermal properties of Kuiper belt objects and Centaurs from combined Herschel and Spitzer observations”. In: *A&A* 557, A60, A60. DOI: 10.1051/0004-6361/201322047.

Licandro, Javier et al. (Dec. 2024). “Thermal evolution of trans-Neptunian objects through observations of Centaurs with JWST”. In: *Nature Astronomy*. DOI: 10.1038/s41550-024-02417-2.

Markwardt, Larissa et al. (Oct. 2023). “First Near-IR Spectroscopic Survey of Neptune Trojans with JWST: Distinct Surface Compositions of Red vs Ultra-Red Neptune Trojans”. In: *arXiv e-prints*, arXiv:2310.03998, arXiv:2310.03998. DOI: 10.48550/arXiv.2310.03998. arXiv: 2310.03998 [astro-ph.EP].

Namouni, Fathi and Carolyn Porco (May 2002). “The confinement of Neptune’s ring arcs by the moon Galatea”. In: *Nature* 417.6884, pp. 45–47. DOI: 10.1038/417045a.

Nogueira, E., R. Brasser, and R. Gomes (July 2011). “Reassessing the origin of Triton”. In: *Icarus* 214.1, pp. 113–130. DOI: 10.1016/j.icarus.2011.05.003. arXiv: 1105.1179 [astro-ph.EP].

Paradis, Samuel, Chris Moeckel, and Imke de Pater (Feb. 2023). “Near-IR photometry of the small Uranian satellites with Keck at phase angles 0-2°”. In: *Icarus* 391, 115331, p. 115331. DOI: 10.1016/j.icarus.2022.115331.

Pascu, Dan et al. (2006). “HST BVI photometry of Triton and Proteus”. In: *Icarus* 185.2, pp. 487–491.

Porco, Carolyn C. (Aug. 1991). “An Explanation for Neptune’s Ring Arcs”. In: *Science* 253.5023, pp. 995–1001. DOI: 10.1126/science.253.5023.995.

Raponi, Andrea et al. (2021). “Organic Material on Ceres: Insights from Visible and Infrared Space Observations”. In: *Life* 11.1. ISSN: 2075-1729. DOI: 10.3390/life11010009. URL: https://www.mdpi.com/2075-1729/11/1/9.

Renner, S. et al. (Mar. 2014). “Neptune’s ring arcs: VLT/NACO near-infrared observations and a model to explain their stability”. In: *A&A* 563, A133, A133. DOI: 10.1051/0004-6361/201321910.

Ricca, Alessandra et al. (July 2012). "The Infrared Spectroscopy of Compact Polycyclic Aromatic Hydrocarbons Containing up to 384 Carbons". In: *ApJ* 754.1, 75, p. 75. DOI: 10.1088/0004-637X/754/1/75.

Rigby, Jane et al. (Apr. 2023). "The Science Performance of JWST as Characterized in Commissioning". In: *PASP* 135.1046, 048001, p. 048001. DOI: 10.1088/1538-3873/acb293. arXiv: 2207.05632 [astro-ph.IM].

Schenk, Paul M. and Jeffrey M. Moore (Dec. 2020). "Topography and geology of Uranian mid-sized icy satellites in comparison with Saturnian and Plutonian satellites". In: *Philosophical Transactions of the Royal Society of London Series A* 378.2187, 20200102, p. 20200102. DOI: 10.1098/rsta.2020.0102.

Schmitt, B. et al. (Jan. 1998). "Optical Properties of Ices from UV to Infrared". In: *Solar System Ices*. Ed. by B. Schmitt, C. de Bergh, and M. Festou. Vol. 227. Astrophysics and Space Science Library, p. 199. DOI: 10.1007/978-94-011-5252-5_9.

Showalter, M. R. et al. (Feb. 2019). "The seventh inner moon of Neptune". In: *Nature* 566.7744, pp. 350–353. DOI: 10.1038/s41586-019-0909-9.

Showalter, Mark R and Jack J Lissauer (2006). "The second ring-moon system of Uranus: discovery and dynamics". In: *Science* 311.5763, pp. 973–977.

Smith, B. A., L. A. Soderblom, D. Banfield, et al. (Dec. 1989). "Voyager 2 at Neptune: Imaging Science Results". In: *Science* 246.4936, pp. 1422–1449. DOI: 10.1126/science.246.4936.1422.

Smith, B. A., L. A. Soderblom, R. Beebe, et al. (July 1986). "Voyager 2 in the Uranian System: Imaging Science Results". In: *Science* 233.4759, pp. 43–64. DOI: 10.1126/science.233.4759.43.

STSCI (Jan. 2016). *JWST User Documentation (JDox)*. JWST User Documentation Website. URL: https://jwst-docs.stsci.edu/jwst-near-infrared-camera/nircam-performance/nircam-point-spread-functions.

Szulágyi, Judit, Marco Cilibrasi, and Lucio Mayer (2018). "In situ formation of icy moons of Uranus and Neptune". In: *The Astrophysical Journal Letters* 868.1, p. L13.

Takir, Driss et al. (Nov. 2019). "3-μm reflectance spectroscopy of carbonaceous chondrites under asteroid-like conditions". In: *Icarus* 333, pp. 243–251. DOI: 10.1016/j.icarus.2019.05.012. arXiv: 1904.09453 [astro-ph.EP].

Tiscareno, Matthew S. et al. (Mar. 2013). "Compositions and Origins of Outer Planet Systems: Insights from the Roche Critical Density". In: *ApJL* 765.2, L28, p. L28. DOI: 10.1088/2041-8205/765/2/L28. arXiv: 1302.1253 [astro-ph.EP].

Willmer, Christopher N. A. (June 2018). "The Absolute Magnitude of the Sun in Several Filters". In: *ApJS* 236.2, 47, p. 47. DOI: 10.3847/1538-4365/aabfdf. arXiv: 1804.07788 [astro-ph.SR].

Wong, Ian et al. (Nov. 2023). "JWST near-infrared spectroscopy of the Lucy Jupiter Trojan flyby targets: Evidence for OH absorption, aliphatic organics, and CO_2". In: *arXiv e-*

prints, arXiv:2311.11531, arXiv:2311.11531. DOI: 10.48550/arXiv.2311.11531. arXiv: 2311.11531 [astro-ph.EP].

Zahnle, Kevin et al. (2003). “Cratering rates in the outer Solar System”. In: *Icarus* 163.2, pp. 263–289.

Chapter 5

SATURNIAN IRREGULAR SATELLITES AS A PROBE OF KUIPER BELT SURFACE EVOLUTION

Belyakov, Matthew and Michael E. Brown (Apr. 2025). “Saturnian Irregular Satellites as a Probe of Kuiper Belt Surface Evolution”. In: *The Planetary Science Journal* 6.4, 97, p. 97. DOI: 10.3847/PSJ/adc55d. arXiv: 2503.20046 [astro-ph.EP].

We present the JWST NIRSpec PRISM 0.7–5.3 μmspectra of Albiorix and Siarnaq and the NIRSpec G235H/G395M 1.7–5.3 μmspectra of Phoebe, the three largest Saturnian irregular satellites. The irregular satellites of the giant planets are thought to be captured planetesimals from the same population as Kuiper belt objects. They are emplaced inside Saturn’s Hill sphere during the giant-planet instability described by the Nice Model, and are thus valuable tracers of Kuiper belt surface evolution. Phoebe’s JWST spectrum matches the global average from Cassini VIMS, and by comparing the spectrum to the library of Kuiper belt object spectra from JWST, we demonstrate Phoebe’s compositional similarity to water-rich KBOs. On the smaller Albiorix and Siarnaq, we observe a broad 3 μmO-H band but do not see a Fresnel peak or the 1.5/2.0 μmfeatures characteristic of H_2O ice. We posit that after capture, the frequent high-velocity collisions between smaller irregular satellites sublimate the water ice, while the much larger Phoebe is resistant to disruption and retains its water ice. We suggest that the presence of CO_2 on the smaller satellites, despite the lack of water ice, indicates later formation of CO_2 on these surfaces through irradiation of organic compounds.

5.1 Introduction

The irregular satellites of the giant planets are a population of small bodies on distant, eccentric, and highly-inclined or retrograde orbits that preclude in situ formation as a possible origin (Kuiper, 1956). Multiple capture mechanisms from initially heliocentric orbits have been proposed in the past, such as capture by drag from the gas surrounding circumplanetary disks (Pollack, Burns, and Tauber, 1979), capture from rapid mass accretion by giant planets in their early stages of growth (Heppenheimer and C. Porco, 1977), and collisions between asteroids (Colombo and Franklin, 1971). The modern mechanism for irregular satellite capture was proposed by Nesvorný, Vokrouhlický, and Morbidelli, 2007, who demonstrate that during giant planet migration in the early solar system (Morbidelli, 2010; Nesvorný, 2018), close encounters between planetary-sized bodies perturb planetesimals that happen to

Table 5.1: JWST NIRSpec Observations of the Saturnian Irregular Moons

Target	Date and Time	r (au)	R (au)	α (deg)	mag	t_{exp} (s)
Albiorix	2023 November 22, 01:20–03:00	9.86	9.79	5.81	21.1	2393
Phoebe	2023 November 20, 22:00–23:39	9.78	9.68	5.85	16.7	1109
Siarnaq	2023 November 22, 03:01–04:05	9.78	9.73	5.85	20.5	1517

[1] Heliocentric distance r, distance from JWST R, phase angle α, and V-band magnitude of Phoebe at time of observation, ground-based r-mag for Albiorix and Siarnaq from Peña and Fuentes, 2022.

[2] Total exposure times; Albiorix and Siarnaq are observed in PRISM mode, while Phoebe is observed in G235H/F170LP and G395M/F290LP, with the same exposure time in both dither settings.

be near the Hill spheres of the giant planets onto planet-bound orbits. Capture through third-body assist reproduces the observed size-frequency and orbital distributions of the irregular satellites (Bottke et al., 2010; Nesvorný, Vokrouhlický, and Deienno, 2014). This version of the capture mechanism implies that the irregular satellites share the same source population with the Kuiper belt and the Jupiter Trojans (Morbidelli, 2010). While three-body capture from binary asteroids as demonstrated in Agnor and Hamilton, 2006 could occur from a source region of planetesimals local to the giant planets (Jewitt and Haghighipour, 2007), irregular satellites captured pre-dynamical instability will be lost (Nesvorný, Vokrouhlický, and Morbidelli, 2007).

While the dynamical link between irregular satellites and Kuiper belt objects (KBOs) is well-established, the compositional connection remains incomplete. KBOs in the size range of irregular satellites have bifurcated visible spectral slopes split into two modes at 10 and 30 %/100 nm, sometimes termed "red" and "very red" (Tegler and Romanishin, 1998; Doressoundiram et al., 2002; Hainaut, Boehnhardt, and Protopapa, 2012; Ian Wong and Michael E. Brown, 2017). By contrast, the colors of the irregular satellites are more similar to those of the Jupiter Trojans, with typical spectral slopes between 0-15 %/100 nm (Tommy Grav and Bauer, 2007; Maris, Carraro, and Parisi, 2007; Graykowski and Jewitt, 2018; Peña and Fuentes, 2022). Spectroscopic studies of the Jupiter irregular satellites have shown them to be distinct from KBOs, with featureless spectra similar, though not identical, to the Jupiter Trojans (M. E. Brown and Rhoden, 2014; Sharkey et al., 2023). Spectroscopy of the Uranian irregular satellites has not found conclusive evidence for surface ices and volatiles (Romon et al., 2001; Vilas et al., 2006; Sharkey et al., 2023), though water ice has been detected on Nereid, the largest of the Neptunian irregular satellites (Michael E. Brown, Koresko, and Blake, 1998; R. H. Brown et al., 1999).

JWST NIRSpec has uncovered a wide range of outer solar system surface compositions, showing that KBOs commonly have H_2O, CO_2, CO, and organic ices on their surfaces (Michael E. Brown and Fraser, 2023; De Prá et al., 2024; Souza-Feliciano et al., 2024;

Licandro et al., 2024; Pinilla-Alonso et al., 2024), while the Jupiter Trojans have weak 3 and 3.4 µmabsorptions attributed to hydrated minerals and organics respectively, with a notable single detection of CO_2 (Ian Wong, Michael E. Brown, et al., 2024). This enhanced picture of the surfaces of outer solar system small bodies allows us to begin drawing comparisons between KBOs, Centaurs, Trojans, and irregular satellites, which are predicted by dynamical instability models to be part of the same initial source population. In this work we present the JWST NIRSpec 0.7-5.0 µmspectra of the three largest Saturnian irregular satellites: Phoebe, Siarnaq, and Albiorix. We briefly summarize their known properties.

Phoebe is the largest of the Saturnian irregular satellites with a diameter of 212 km and a retrograde orbit. It is the parent body for the material in its eponymous ring (Verbiscer, Skrutskie, and Hamilton, 2009), whose particles darken Iapetus's leading side. The 2004 *Cassini* fly-by estimated Phoebe's density to be 1.6 g cm^{-3}, which, combined with a low albedo of 0.1 (T. Grav et al., 2015a), indicates capture from the primordial planetesimal disk (Carolyn C. Porco et al., 2004; Johnson and Lunine, 2005). Spectral imaging of the surface found varying amounts of spatially anti-correlated water ice and CO_2 (Hansen et al., 2012), along with other potential absorption features (Clark, R. H. Brown, Jaumann, et al., 2005; Coradini et al., 2008). Later work by Fraser and Michael E. Brown, 2018 confirmed that water ice is ubiquitous on Phoebe's surface and is richest near impact basins, suggesting collisions are exposing subsurface ice. Prior to JWST, there did not exist KBO spectra with similar wavelength coverage as those of Phoebe, but photometrically, Phoebe's color is distinctly blue (g-i = 0.33) as opposed to the red KBOs (Tommy Grav and Bauer, 2007; Peña and Fuentes, 2022). However, colors of its different surface types span the full extent of the KBO color range from solar-like to very red (Fraser and Michael E. Brown, 2018).

Siarnaq (39 km) and Albiorix (29 km) are the largest members of the prograde Gallic and Inuit groups of Saturnian irregular satellites, respectively (T. Grav et al., 2015b; Denk et al., 2018). Both have darker albedos than Phoebe, at 5-6%, but have significantly redder colors (g-i = 0.77), similar to those of the Jupiter Trojans (Tommy Grav and Bauer, 2007; T. Grav et al., 2015a; Graykowski and Jewitt, 2018; Peña and Fuentes, 2022).

We begin by presenting the reduction of the JWST NIRSpec observations of Phoebe, Siarnaq, and Albiorix in section 5.2. In section 5.3 we show three key spectral features on the Saturnian irregular satellites in the context of available JWST Kuiper belt and Centaur data: H_2O, organics, and CO_2. Finally, in section 5.4 we discuss the possible reasons for the differences between Phoebe and the smaller Albiorix and Siarnaq, particularly in the lack of water ice on the smaller satellites.

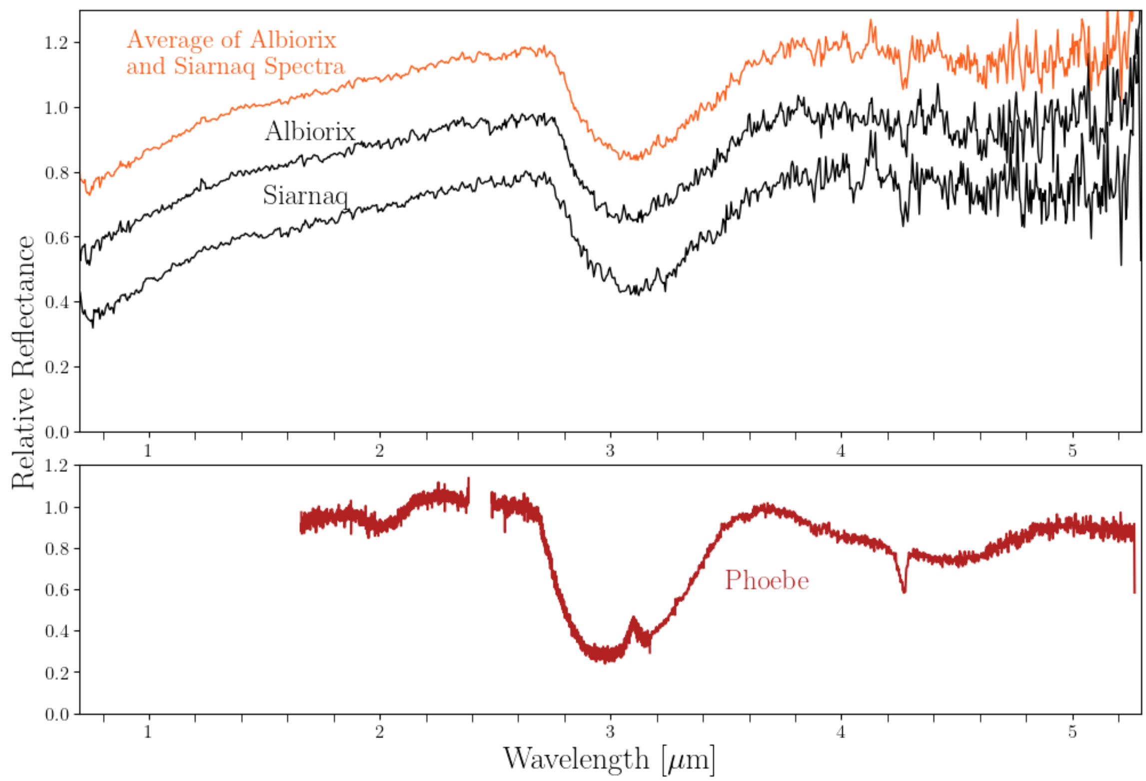

Figure 5.1: Relative reflectance spectra of the three largest Saturnian irregular satellites, Siarnaq, Albiorix, and Phoebe. Top panel shows the individual spectra of Albiorix and Siarnaq and their averaged spectrum, with Albiorix and Siarnaq offset down by 0.2 and 0.4 respectively. These two smaller irregular satellites show a broad 3 µmabsorption, a weak organic feature at 3.4 µm, and CO_2 at 4.27 µm. The bottom panel shows the spectrum of Phoebe, combining the G235H and G395M exposures and binning the G235H resolution down by a factor of 3 to match the G395M resolution. Our spectrum matches results from Cassini VIMS with clear water ice and CO_2 absorptions (Clark, R. H. Brown, Jaumann, et al., 2005; Fraser and Michael E. Brown, 2018). The lack of evidence for water ice on the smaller Albiorix and Siarnaq distinguishes them from the water-rich Phoebe, indicating either the smaller irregular satellites were initially depleted of their water ice, or that post-capture evolution removed the ice.

5.2 Observations

The observations of the three largest irregular satellites of Saturn – Phoebe, Siarnaq, and Albiorix – were taken using JWST NIRSpec as part of JWST Cycle 2 Program #3716 (PI: M. Brown). The smaller Siarnaq and Albiorix were obtained in PRISM mode, which observes in the 0.6-5.3 μmrange, with an R ∼ 30-300 resolution. Phoebe's spectrum was taken using two different gratings, at high resolution in G235H/F170LP mode which covers 1.66–3.05 μmat an R ∼ 2700 resolution, and at medium resolution in G395M/F290LP mode which covers 2.87–5.10 μmat resolution of R ∼ 1000. The observations used the NRSIRS2RAPID readout method, which reads additional non-science reference pixels to reduce the correlated noise caused during detector readout. Each satellite's ephemerides were sufficiently accurate to blindly acquire the targets into the 3×3 arcsecond aperture. Each integration was performed using a four-point dither to ameliorate the effects of bad pixels. Observational details are summarized in Table 5.1.

The raw "uncal.fits" image cubes are processed with version 1.15.1 of the official JWST calibration pipeline and calibration files (Bushouse et al., 2024). We proceed with the standard Step 1 and 2 pipelines, with a custom noise removal routine performed after the rate step, as described in Michael E. Brown and Fraser, 2023. The spectra are extracted from the Step 2 "s3d.fits" image cubes using a custom PSF-fitting algorithm that mitigates the wavelength-dependent features of the PSF, similarly to reductions described in Michael E. Brown and Fraser, 2023 and Ian Wong, Michael E. Brown, et al., 2024. First, the background is subtracted by taking the median of spatial pixels in a region outside a 10×10 pixel box centered on the target. Then, at each wavelength slice of the data cube, we model the PSF by taking a two-dimensional median over a 7×7 pixel area around the target across all wavelength slices within ± 50 wavelength bins in PRISM mode and ± 30 wavelength bins in the higher resolution mode, and normalizing the resulting template to sum to unity. The irradiance is then the best-fit parameter to the ratio of the data in each wavelength bin to the template empirical PSF, found by using a median weighted on the amplitude of the empirical PSF in each pixel. We then median-average the four dithers to obtain the final 1-D spectra, though we drop the final dither for Albiorix as there is a background source within the extraction aperture. The spectra are divided by a solar analog obtained from Program 1128 (PI: N. Luetzgendorf) to obtain the relative reflectance (Gordon et al., 2022).

5.3 Spectral features

The relative reflectance spectra of Albiorix, Siarnaq, and Phoebe are shown in Figure 5.1. Upon inspection, Albiorix and Siarnaq look distinct from Phoebe in the 1.5 to 5.0 μmrange. While Phoebe has significant water ice and a deep 3 μmO-H band, Albiorix and Siarnaq do not have apparent signatures of water ice as they do not have a Fresnel peak at 3.1 μm, the 1.5 overtone ($2\nu_3$) or 2.0 μmcombination feature ($\nu_1 + \nu_3$), or the broad 4.5 μmfeature ($\nu_2 + \nu_r$) (Mastrapa, Bernstein, et al., 2008; Mastrapa, Sandford, et al., 2009). All three objects have visible absorptions from CO_2 at 4.27 μm.

5.3.1 O-H Stretch and Water Ice

The broad 3 μmband associated with the O-H stretch is a common feature of the infrared spectra of outer solar system small bodies. The Jupiter Trojans observed with JWST (Ian Wong, Michael E. Brown, et al., 2024) show very shallow and broad 3 μmO-H bands that are distinct from those in the asteroid belt associated with hydrated silicates (Takir and Joshua P. Emery, 2012; Usui et al., 2019), but are also much less deep than on Centaurs and KBOs, possibly a result of the significant thermal processing at 5.2 au which removes water ice from their surfaces (Aurélie Guilbert-Lepoutre, 2014). Centaurs and KBOs have a greater variety of 3 μmbands, with some indicating the presence of water ice through the presence of the Fresnel peak at 3.1 μm, as well as features at 1.5 and 2.0 μm(Pinilla-Alonso et al., 2024).

In Figure 5.2 we show the 3 μmfeature of the Saturnian irregular satellites against representative small body spectra: water ice-rich KBOs and Centaurs from JWST programs 1191 (PI: J. Stansberry) and 2418 (PI: N. Pinilla-Alonso) reduced using the pipeline described here, the main belt Themis from Rivkin and Joshua P. Emery, 2010 and Usui et al., 2019, the Jupiter Trojan Eurybates from Ian Wong, Michael E. Brown, et al., 2024, and the Neptune Trojan 2006 RJ103 from Markwardt et al., 2023. Phoebe's 3 μmfeature has a 75% band depth and a sharp Fresnel peak at 3.1 μm, similar to most water-rich KBOs. Phoebe also shows a downwards slope in the spectrum past 3.6 μm, attributable to the broad 4.5 μmcombination band seen in Figure 5.1 (Mastrapa, Sandford, et al., 2009). By contrast, Albiorix and Siarnaq have a 3 μmfeature with 25% band depth, and no evidence for either the Fresnel peak or the 4.5 μmcombination band. Phoebe is similar to the most water-rich KBOs, while Albiorix and Siarnaq most resemble centaurs such as Okyrhoe and 2013 XZ8 which have muted 3 μmfeatures (Licandro et al., 2024). The two small Saturnian irregular satellites are both distinct from the Jupiter Trojans or main belt asteroids, owing to their much larger 3 μmband depths.

To confirm that the smaller irregular satellites lack pure water ice on their surface, we also look at the 1.5 μmwater ice overtone and 2.0 μmwater ice combination band. For the 2.0 μmfeature, we find a best-fit linear continuum between 1.7 and 2.3 μm, ignoring the band between 1.9 and 2.15 μm, then fit a simple Gaussian to the continuum-subtracted band. In Figure 5.3, we show the continuum-subtracted 2.0 μmfeature on Phoebe, the two smaller

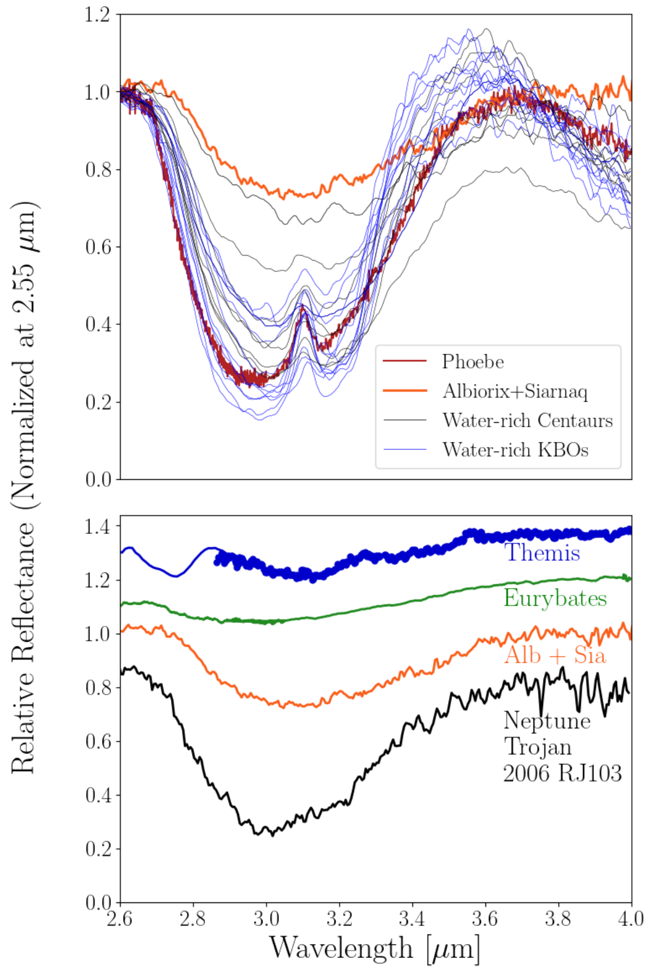

Figure 5.2: Top Panel: Comparison of the 3 µmfeature on Phoebe (red), Siarnaq and Albiorix (orange), and water-rich Centaurs (grey) and KBOs (blue) from Program 2418 (PI: N. Pinilla-Alonso). Phoebe's 3 µmfeature is similar to that of other water-rich KBO spectra, while Albiorix and Siarnaq are more similar to the most processed Centaurs, such as Okyrhoe. Bottom panel: Comparison of the 3.0 micron feature across representative small bodies, Eurybates (green, +0.3 offset, from Ian Wong, Michael E. Brown, et al. 2024), Themis (blue, +0.15 offset, from Rivkin and Joshua P. Emery, 2010 and Usui et al. 2019), Siarnaq and Albiorix (orange), and the Neptune Trojan 2006 RJ103 (black, -0.2 offset, from Markwardt et al. 2023). The Jupiter Trojans and asteroid belt objects are distinct from the Saturnian irregulars, with significantly weaker 3.1 µmabsorptions. The Neptune Trojan 2006 RJ103 has a deeper 3.0 µmband than the small Saturnian irregulars, but also lacks water ice features at other wavelengths.

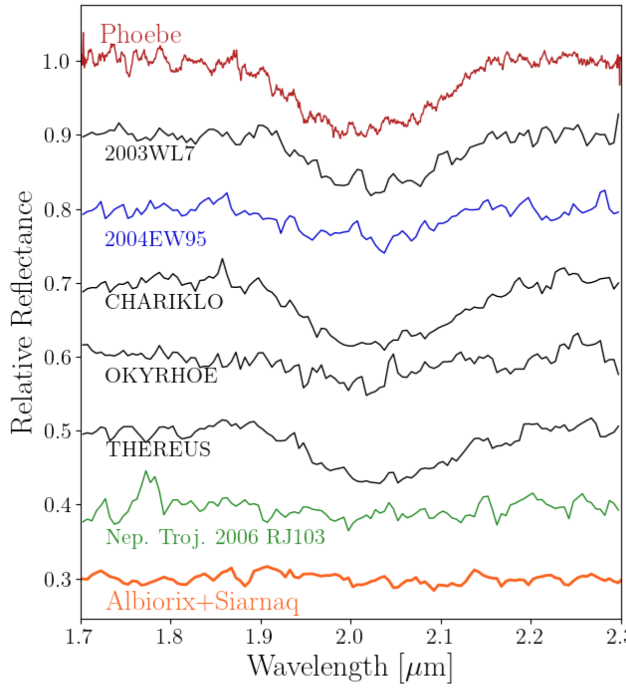

Figure 5.3: Comparison of the continuum-removed 2.0 μmfeature on Phoebe (red), Siarnaq and Albiorix (orange), selected Centaurs and Pluto 2004 EW95 from Licandro et al. 2024; Pinilla-Alonso et al. 2024, and the Neptune Trojan 2006 RJ103 from Markwardt et al. 2023. Each spectrum below Phoebe is successively offset by 0.1 down in relative reflectance. All of the KBOs and Phoebe show 2.0 μmabsorptions, ranging from 3.5% band depth on Okyrhoe to 9% on Chariklo. By contrast, Siarnaq and Albiorix, as well as 2006 RJ103, show no evidence for a 2.0 μmband, suggesting a lack of exposed water ice.

irregular satellites, and five KBOs and Centaurs. Siarnaq and Albiorix show no evidence for the 2.0 μmband. We find a 1.0% upper limit on the feature's band depth for Albiorix and Siarnaq, which we estimate by first determining the noise level surrounding the band, then adding Gaussian signal with the same band width and center as on the other KBOs until our fitting routine detects a band depth that is 3σ above the noise level. We avoid translating an upper limit on the band depth to a fraction of water ice as modeling using the available 1-5 μmrange will produce degeneracies between grain size and abundance. While the differences in the appearance of the 3 μmfeature between the KBOs, Centaurs, and Trojans could plausibly be explained by their different thermal histories, Albiorix, Siarnaq, and Phoebe have experienced the same level of solar insolation since capture, so some other mechanism must have led to the difference between them. The removal of water ice from the smaller irregular satellites is either a result of some other feature of post-capture evolution such as collisions, or a primordial lack of water ice for the smaller objects. We discuss these possible explanations for the lack of water ice on the smaller irregular satellites in section 5.4.

5.3.1.1 Compositional attribution of the 3 µmband

The distinct shape of the 3 µmfeature on Albiorix and Siarnaq combined with the lack of other typical signatures of water ice in the 1-5 µmrange makes suggesting a plausible composition challenging. The main belt asteroid Themis, whose spectrum is shown in the bottom panel of Figure 5.2, has a 3.0 µmband without the typical 1.5 or 2.0 µmfeatures. The 3.0 µmfeature on Themis has been attributed to silicate grains coated with sub-micron sized water ice grains (Rivkin and Joshua P. Emery, 2010), though this model has received several observational challenges in the form of non-detections of water-ice sublimation (Jewitt and Aurelie Guilbert-Lepoutre, 2012; McKay, Bodewits, and Li, 2017; O'Rourke et al., 2020). The band depth and shape of the feature is significantly different on Siarnaq and Albiorix than on Themis, and Themis has a 2.7 µmphyllosilicate band which does not appear on Siarnaq or Albiorix (Usui et al., 2019). Moreover, replicating the Shkuratov model of Rivkin and Joshua P. Emery, 2010 or M. E. Brown, 2016 for the small silicate grains covered in water but at a higher abundance does not reproduce the shape of the broad feature seen on the smaller Saturnian irregular satellites. We therefore argue against significant quantities of water ice on Siarnaq and Albiorix.

A hint to a possible compositional attribution of the 3 µmband on Albiorix and Siarnaq lies in their resemblance to the Neptune Trojan 2006 RJ103, which also does not show evidence for significant surface water ice (Markwardt et al., 2023). Ground-based visible spectroscopy of 2006 RJ103 shows a strong 600-700 nm feature associated with the Fe^{2+}/Fe^{3+} charge transfer (Sharkey et al., 2023), which combined with its 3.0 µmO-H feature shown in Figure 5.2 is indicative of the presence of iron-bearing hydrated minerals. It is therefore plausible that the deep 3.0 µmbands on Albiorix and Siarnaq (relative to the Jupiter Trojans and main belt objects) are a consequence of abundant hydrated minerals. Phoebe also has a clear 1.0 µmabsorption (Clark, R. H. Brown, Jaumann, et al., 2005; Coradini et al., 2008) that is deepest in the least water-rich areas (Fraser and Michael E. Brown, 2018), attributed to some unidentified iron-bearing mineral, possibly hydrated (Clark, R. H. Brown, Jaumann, et al., 2005; Clark, Dale P. Cruikshank, et al., 2012). While we do not see an identical feature on Albiorix and Siarnaq, there is a slope change at 1.15 µmin Figure 5.1, consistent with an absorber in the 0.7-1.0 µmrange. One issue with invoking hydrated minerals is that most show a narrow 2.7 µmabsorption, such as the one on Themis in Figure 5.2. However, there are hydrated minerals and meteorite samples without this band, such as the Murchison meteorite and the minerals cronstedtite and goethite (Bates et al., 2020); goethite has been suggested to be responsible for the 3.1 µmfeature in main belt asteroids (Beck et al., 2011).

5.3.2 Organic material

The albedos of Phoebe, Siarnaq, and Albiorix are significantly darker than those of the regular Saturnian satellites and are more similar to those typical of Kuiper belt objects (Lellouch et al., 2013). The dark material from Phoebe coats Hyperion and the leading side of Iapetus and is an important feature of the surface material in the Saturnian system (D. P. Cruikshank, Bell, et al., 1983; Verbiscer, Skrutskie, and Hamilton, 2009; Clark, Dale P. Cruikshank, et al., 2012; Dale P. Cruikshank et al., 2014), but a specific identification of the composition of the dark material remains elusive. We examine the 3.2-3.6 micron region of the irregular satellite spectra for potential absorptions by the C-H stretch typical of aromatic and aliphatic hydrocarbons.

One common explanation for the low albedos of outer solar system small bodies is the presence of an organic darkening agent (D. P. Cruikshank, Roush, et al., 1998; Khare et al., 2001; Barucci et al., 2011). In the infrared, organic compounds and their irradiation products have absorption features through the 3-4 µmregion that are observed throughout the outer solar system: large KBOs like Eris or Pluto have simpler organics (Grundy, Binzel, et al., 2016; J. P. Emery et al., 2024), comets show emission features attributed to aliphatic compounds (Raponi et al., 2020; Kelley et al., 2023), and KBOs have broad 3.4-3.6 µmabsorptions (Figure 1 of Michael E. Brown and Fraser 2023). Irradiation and sublimation destroy and remove the simplest organics from the surface, with the terminal stage of such processing resulting in amorphous, largely dehydrogenated, carbon (Moore and Hudson, 1998; Lyuba Moroz et al., 2004; Clark, Curchin, et al., 2009; Hand and Carlson, 2012). We expect the Saturnian irregular satellites to show organic bands similar to the Jupiter Trojans, which have broad 3.4 µmabsorptions.

To characterize the organics on the irregular satellites we isolate the 3.3-3.6 µmarea that could potentially host organic absorptions and try to see if there is an excess absorption, following the method laid out in Ian Wong, Michael E. Brown, et al., 2024. We perform a continuum fit to the area between 3.0 and 4.0 µmusing a fifth degree polynomial, excluding the 3.25-3.57 µmarea that potentially has organic absorption features. Repeating the exercise with a third-degree polynomial using the same region or a linear fit over a smaller range results in a qualitatively similar answer, with a less consistent result for the center of the band on Albiorix. A shorter wavelength range is used for Phoebe as the water feature Fresnel peak at 3.1 µmimpedes the continuum fit. In Figure 5.4 we show the continuum fits to the Jupiter Trojan Orus, Albiorix, Siarnaq, and Phoebe, and their average in the left set of panels, and the continuum-subtracted feature with Gaussian band fits in the right set of panels. We use a Monte Carlo procedure for fitting the band. Using the errors on each data point, we resample the spectra into 10,000 simulated spectra. To each continuum-subtracted spectrum,

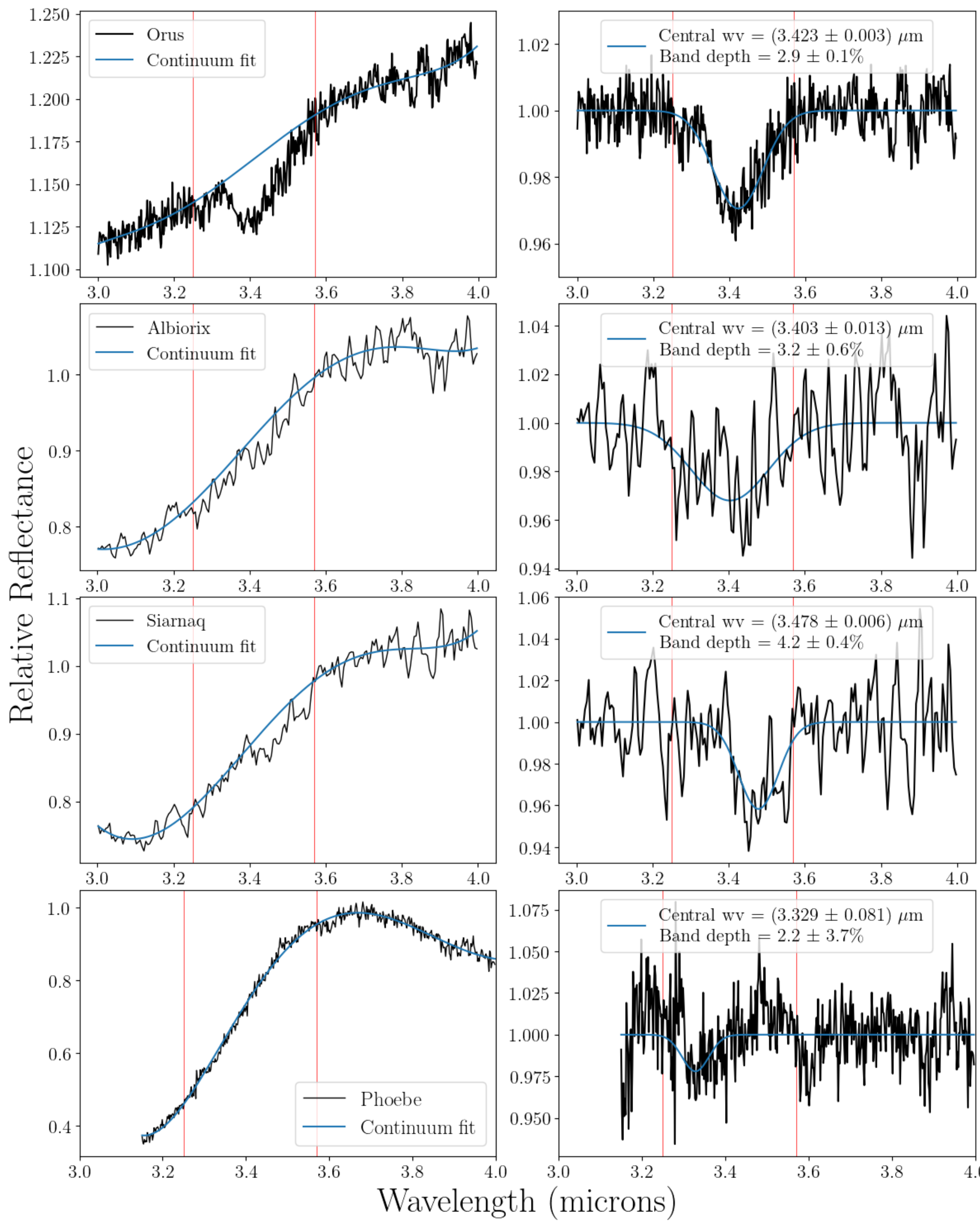

Figure 5.4: Left panels show the 3–4 μmspectra and polynomial continuum fits of Orus, Albiorix, Siarnaq, and Phoebe (from top to bottom). The red lines show the area ignored by the continuum fit, which is the same area used by Ian Wong, Michael E. Brown, et al., 2024. Right panels show the continuum-subtracted spectrum, with Gaussian fits to the organic band. Both individually and in their average, the small Saturnian irregular satellites show organic bands that are consistent with what is seen on the Trojans, but at slightly longer wavelengths. Phoebe does not show strong evidence for an absorption in the 3.25–3.6 μmrange, obscured by the water ice 3 μmfeature which makes determining a continuum difficult.

we fit a Gaussian using a least squares algorithm. The means and standard deviations of the resulting parameter distributions are the reported values and uncertainties for the band centers and depths in Figure 5.4.

The parameters of the 3.4 μmfeature on the smaller Saturnian irregular satellites are similar to Orus, which, of the five Trojans observed in Ian Wong, Michael E. Brown, et al., 2024, has the deepest 3.4 μmabsorption. The organic absorption on Albiorix has a band center and band depth within the margin of error of the fits for Orus from both our work and Ian Wong, Michael E. Brown, et al., 2024. Siarnaq has a slightly longer-wavelength and narrower band, though by eye the absorption is visible as a plateau at 3.45 μmeven without continuum subtraction. The organic band at 3.4 μmwe observe on the small irregular satellites is consistent with the C-H stretch, but the position is sensitive to the parent molecule the C-H group is attached to (c.f. Tables 112 and 115 in Herzberg 1945). Laboratory experiments by Hand and Carlson, 2012 show that the asymmetric mode of the -CH_2- band and the asymmetric and symmetric modes of the -CH_3- band in 70–100 K water ice/long-chain aliphatic mixtures are centered in the 3.38-3.49 area that our bands cover, and are stable not only to irradiation, but also to warming to 300 K.

Phoebe shows a potential absorption at 3.3 μmthat is short of the other irregular satellites. Whether the feature appears is extremely sensitive to the choice of anchor points for the continuum subtraction and the subset of dithers used to build the spectrum. In addition to the analysis we present in Figure 5.4, we repeat the spline continuum removal done by Dalle Ore, Dale P. Cruikshank, and Clark, 2012 and Dale P. Cruikshank et al., 2014 for the *Cassini* VIMS data of Phoebe on our data, but do not find evidence for any of the same aliphatic organic absorptions previously claimed on Phoebe. To fully extract the signatures of organic compounds, continuum removal is insufficient, as the water ice feature has complex behavior in the 3.0-3.6 μmrange with subtle changes in slope at 3.3-3.5 μmthat obscure the signatures of organic molecules.

5.3.3 4.27 μm CO_2 Feature

JWST spectroscopy has demonstrated that CO_2 is common on outer solar system small bodies, even on those that experience temperatures above 80K, at which pure CO_2 ice sublimates (Michael E. Brown and Fraser, 2023; Ian Wong, Michael E. Brown, et al., 2024; De Prá et al., 2024). On KBO surfaces, the CO_2 band has a wide range of appearances. The spectra of the most distant and organic-rich objects show evidence for Mie scattering caused by micron thick layers of small CO_2 grains on their surfaces (Michael E. Brown and Fraser, 2023). By contrast, the water-rich KBOs and Centaurs have what is likely CO_2 trapped in the water ice, organics, or silicates that are possibly present on their surfaces (De Prá et al., 2024).

The band centers of the CO_2 features range between 4.250-4.275 μm, with the water-ice rich KBOs tending to have longer-wavelength band centers than the organic-rich KBOs (see figure 4 of De Prá et al. 2024). On the Jupiter Trojans observed thus far, only Eurybates has shown evidence for a CO_2 feature, with a band center of 4.258 ± 0.002, more similar to the central wavelength of the organic rich KBOs than the water-rich ones (Ian Wong, Michael E. Brown, et al., 2024).

CO_2 was previously detected in the Cassini VIMS spectrum of Phoebe (Clark, R. H. Brown, Jaumann, et al., 2005), with Hansen et al., 2012 finding that the spatial distribution of the CO_2 on Phoebe has a slight inverse correlation with water ice and has a globally averaged band depth of approximately 20%. Improved abundance maps of water ice from Fraser and Michael E. Brown, 2018 also suggest the same inverse correlation between CO_2 and surface water ice (comparing the maps in Fig. 4 of Fraser and Michael E. Brown 2018 and Fig. 10 of Hansen et al. 2012). Further analysis by Clark, R. H. Brown, Dale P. Cruikshank, et al., 2019 also claims a detection of $^{13}CO_2$ on Phoebe, at 5% of the equivalent width or 10% of the band depth of the 4.27 μmCO_2 feature.

In Figure 5.5, we show the continuum removed CO_2 bands of Phoebe, Siarnaq and Albiorix averaged, Eurybates, and the median of all $q < 25$ au KBOs and Centaurs. We remove the continuum by fitting a line between 4.0 and 4.5 μm, excluding points between 4.20 and 4.33 μm. We then repeat the fitting procedure described above. Fitting a single Gaussian to the CO_2 band of the small irregular satellites, we find that Siarnaq has a CO_2 band center of 4.272 ± 0.002 μm, Albiorix's band is at 4.275 ± 0.004 μm, their average has a band center of 4.272 ± 0.001 μmand a band depth of 13.1 ± 0.6%. Phoebe's band minimum is at 4.271 μm, but the feature appears to be best modeled by the sum of two Gaussians, centered at 4.258 μmand 4.272 μmrespectively. The Centaur median CO_2 band is similar to Phoebe, with a similar, though slightly longer band minimum, suggesting a common mechanism for formation and trapping of CO_2 inside its sublimation line on KBO surfaces. Contrary to Clark, R. H. Brown, Dale P. Cruikshank, et al., 2019, we do not see evidence above the local noise level for the $^{13}CO_2$ feature on Phoebe (noise at the wings of the feature is 1.7%), ruling out the Clark, R. H. Brown, Dale P. Cruikshank, et al., 2019 claimed 0.053 band depth at 3 σ. Recent work has shown that the $^{13}C/^{12}C$ ratio in the methane on Eris and Makemake, as well as comet 67/P is similar to terrestrial values (Müller et al., 2022; Grundy, I. Wong, et al., 2024), and individual water-rich KBOs do not show clear evidence of the 4.36 μmfeature (De Prá et al., 2024). The absence of the $^{13}CO_2$ feature in the JWST spectrum of Phoebe combined with a set of similar results for the isotopic ratios of other bodies of outer solar system origin suggests that the $^{13}C/^{12}C$ ratio on Phoebe is likely more similar to that of Iapetus or terrestrial values, than the one determined in Clark, R. H. Brown,

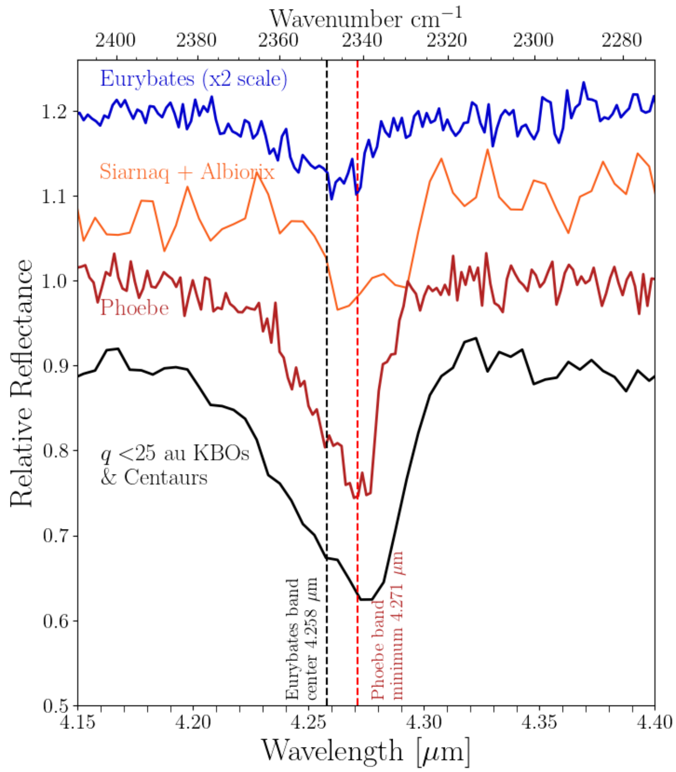

Figure 5.5: Continuum-removed CO_2 feature on, from top to bottom, Jupiter Trojan Eurybates, Albiorix and Siarnaq, Phoebe, and the average spectrum of $q < 25$ au KBOs and Centaurs. The band center of the CO_2 feature on Phoebe is similar to that of the Centaurs, indicating a common trapping mechanism, as pure CO_2 ice is not stable at Saturnian temperatures. Both Phoebe and the KBOs have a shallower short-wavelength slope that is not present on the CO_2 on the smaller irregular satellites. CO_2 on Eurybates has a distinct 4.258 μmband center (Ian Wong, Michael E. Brown, et al., 2024), possibly indicating that a different medium is trapping the CO_2 on Eurybates or that the wavelengths are temperature dependent.

Dale P. Cruikshank, et al., 2019.

CO_2 on the Saturnian irregular satellites is at temperatures well above its sublimation temperature, raising the question of what is trapping the CO_2. Michael E. Brown, Trumbo, et al. (2025) find that on all the outer Saturnian satellites (Hyperion, Iapetus, and Phoebe), the 4.271 μmCO_2 absorption is linked to the dark material derived from Phoebe. Organic compounds are a common explanation invoked for the low-albedo material both on Phoebe and on KBOs in general (D. P. Cruikshank, Roush, et al., 1998; Khare et al., 2001; Michael E. Brown, 2012; Dale P. Cruikshank et al., 2014). Irradiation of organics such as asphaltite layered with water ice in laboratory experiments from Strazzulla and L. Moroz, 2005 and Gomis and Strazzulla, 2005 result in a 4.270-4.272 μmfeature consistent with the band center of CO_2 on all three Saturnian irregular satellites. Albiorix and Siarnaq have evidence for a C-H feature at 3.4 μm, which strengthens the claim that organics are the source of the CO_2. Phoebe lacks an obvious detection of organics, but the iron oxides detected by Cassini VIMS (Clark, Dale P. Cruikshank, et al., 2012) could also efficiently trap CO_2 (Russell et al., 1975).

5.4 Discussion

The three Saturnian irregular satellites have spectra that are most similar to those of the water-rich Centaurs and KBOs observed thus far, (Licandro et al., 2024; Pinilla-Alonso et al., 2024), as is expected from the dynamical picture of irregular satellite capture. Less clear is why Albiorix and Siarnaq lack water ice, while Phoebe has ubiquitous surface water ice (Clark, R. H. Brown, Jaumann, et al., 2005; Fraser and Michael E. Brown, 2018).

We hypothesize that the smaller irregular satellites once had water ice like Phoebe and many of the Centaurs, but that this water ice has been removed by sublimation during catastrophic collisions. This mechanism is a unique consequence of the specific environment of the irregular satellite cloud. Unlike the Kuiper belt, collisional velocities among irregular satellites are very high – collisions between a prograde and retrograde object can reach 5 km/s relative speeds. Moreover, irregular satellites have notably high collisional probabilities post-capture, at least seven orders of magnitude higher than in the Kuiper belt (compare Bottke et al. 2010 and Abedin et al. 2021).

We can compare the energy of an impact between irregular satellites to the latent heat of ice, which is a first-order check for plausibility of collisional removal of the water ice. Assuming a temperature of 110K, and using the temperature-dependent expression for the latent heat of vaporization of water ice from Murphy and Koop, 2005, we find that the water ice will have a heat of vaporization of just under 2.8 MJ/kg, while if we assume Siarnaq and Albiorix have a head-on collision near perihelion (a combined relative velocity of 5 km/s) with equal mass, their collision will have a $v_{imp}^2/8 = 3.1$ MJ/kg specific impact energy over the total mass of the two bodies. Even though much of the impact energy will go to excavation and removal of mass to infinity rather than thermal processes, significant vaporization seems likely. An additional argument in favor of the water being fully processed by collisions is the high pressure at the point of contact, which is approximately $\rho \times v_{imp}^2$ (Melosh, 1989; Barr and Schwamb, 2016), resulting in significantly higher than 1 GPa pressures for these catastrophic collisions, more than enough to melt significant amounts of water ice. Shock wave experiments by Stewart and Ahrens, 2005 show that at 100K, bodies impacting with 4 GPa pressures will be completely melted. Simulations from Jutzi and Michel, 2020 predict that for two equal-sized bodies, a 5 km/s relative impact velocity will result in enough of a temperature increase to melt all water ice present, and sublimate around 10% of the ice.

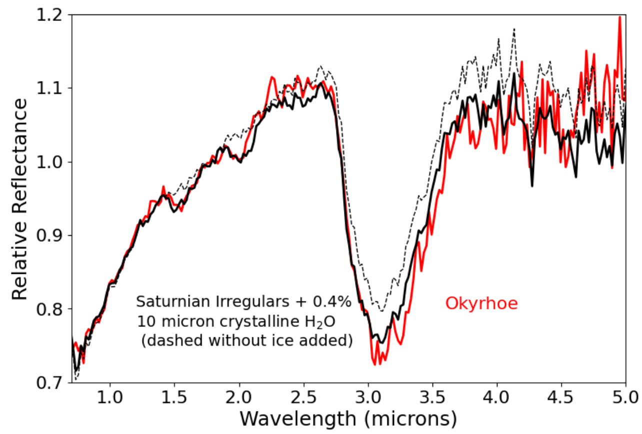

Figure 5.6: Average of Siarnaq and Albiorix spectra with a layer of 10 µmgrain size crystalline water ice added using Hapke modelling (original dashed, with water in black). Adding water ice as a singular component to the irregular satellites in an areal mixture results in a spectrum that matches Okyrhoe (red), indicating the irregular satellites are consistent with having once had a water-ice rich spectrum.

This melting would leave behind hydrated minerals that are a likely explanation for the deep O-H feature on the smaller irregular satellites as compared to the Jupiter Trojans.

We can visualize how the spectra of Siarnaq and Albiorix originally might have appeared by combining their spectra with a modeled water ice spectrum. We model the ice using Hapke theory from B. Hapke, 1981; Bruce Hapke, 1993 and optical constants for water ice from Clark, Dale P. Cruikshank, et al., 2012; Clark, R. H. Brown, Dale P. Cruikshank, et al., 2019. We use the Python package `miepython` (Prahl, 2023) to find the single-scattering albedo of a spherical water particle of a given diameter using the Clark, R. H. Brown, Dale P. Cruikshank, et al., 2019 optical constants. Then, using Equation (9.9) of Bruce Hapke, 1993 we obtain the diffusive reflectance which we then convert to geometric albedo using the approximation given in Equation (10.39). By adding 10 micron water ice grains at a 0.4 % abundance in a linear combination with the original spectrum of the small irregulars, we obtain a spectrum for the small irregular satellites with surface patches of water ice. An areal mixture is sensible in this case, as collisions are known to expose water ice on Phoebe (Fraser and Michael E. Brown, 2018). This spectrum, shown in Figure 5.6, closely matches the spectrum of the Centaur Okyrhoe, demonstrating the spectral similarity of the non-ice component of these objects. Reversing this operation, if we were to remove the water ice signature from Okyrhoe, its spectrum would resemble that of the small Saturnian irregulars. If water ice were present on Albiorix and Siarnaq, collisions would expose it in patches, which would then match the model in Figure 5.6. As a Centaur, Okyrhoe has not experienced the significant collisional history of an irregular satellite yet has retained its water ice, consistent with our hypothesis of collisions then removing water ice from Albiorix and Siarnaq.

Unlike the smaller irregular satellites, Phoebe retains its water ice. At 200 km in diameter, Phoebe is significantly larger than that of any other Saturnian irregular satellite, and plausibly an intact planetesimal. By contrast, Siarnaq and Albiorix are at ~40 km in diameter and parent members of the Gallic and Inuit satellite families, indicating past disruption of a parent body (Denk et al., 2018). Images of Phoebe show a highly-cratered surface with the largest craters nearing the catastrophic disruption limit (C. C. Porco et al., 2005; Bottke et al., 2010). Impactors that cause craters of that size would fully disrupt the smaller Albiorix and Siarnaq. Disrupting Phoebe would require a body of at least 20 km diameter (computed using equation 4 and figure 7 of Bottke et al. 2010), and an order of magnitude fewer such objects are captured than the 4 km diameter objects required to disrupt Siarnaq or Albiorix (Nesvorný, Vokrouhlický, and Morbidelli, 2007). Phoebe retains its water ice because it has not experienced a catastrophic collision, as evidenced by its near-spherical shape, high density, low bulk porosity, and evidence of structure and geology from images (C. C. Porco et al., 2005; Johnson and Lunine, 2005; Jacobson et al., 2006; Thomas, 2010). Melt from the collisions on Phoebe possibly accumulates at crater bottoms, explaining the observed higher abundance of water ice at the bottom of craters (Fraser and Michael E. Brown, 2018).

We posit that post-capture sublimation is not a plausible explanation for the differences between Phoebe and the smaller irregular satellites, as they have been at the same heliocentric distance since capture. On Phoebe, even the darkest locations have water ice (Fraser and Michael E. Brown, 2018) and have 3.0 μmband depths significantly exceeding Albiorix and Siarnaq. Finally, water ice is stable at temperatures in the Saturnian system. While Jeans escape will deplete some amount of water ice from the surface, even the low albedo leading side of Iapetus and dark parts of Phoebe have clear signs of water ice.

An alternative explanation for the spectra of the Saturnian irregular satellites is a different natal environment for Phoebe than Siarnaq and Albiorix, which would presumably then be formed in a less water-rich region of the protoplanetary disk. Our comparison of Siarnaq and Albiorix to Okyrhoe suggests that a distinct natal environment for observed water-poor bodies is a less plausible explanation than collisional processing, but to completely disfavor this hypothesis would require observation of a significant sample of similar-sized KBOs ($H \sim 11$) to demonstrate they retain their water ice.

The final piece of the spectroscopic puzzle is the presence of CO_2 on the smaller irregular satellites despite their potentially extreme past thermal and collisional history. The implication here is that CO_2 is formed in situ from solar irradiation of available materials. As we demonstrate in Figure 5.4, organics at 3.4 μm are a possible component of the spectra of the smaller irregular satellites, providing the necessary material to form CO_2. The presence of CO_2 on these heavily processed bodies suggests that radiolytic formation and subsequent trapping of CO_2 is a common process in the outer solar system when organics are found in conjunction with an O-H bearing material that can supply the oxygen necessary to form CO_2, such as the one causing the 3 micron band on the smaller irregular satellites.

5.4.1 The Trojan-Irregular-KBO Connection

While the spectral similarity of Phoebe to water-rich KBOs argues strongly in favor of a common origin for the irregular satellites and present-day Kuiper belt objects, there remains a tension between the difference between the observed distribution of visible colors in the redder Kuiper belt and the bluer captured populations: the giant planet irregular satellites and the Jupiter and Neptune Trojans (Ian Wong and Michael E. Brown, 2016; Graykowski and Jewitt, 2018; Jewitt, 2018; Bolin et al., 2023; Sharkey et al., 2023). For Jupiter's Trojans and Irregulars, thermal insolation is commonly invoked to explain the change from Kuiper belt colors to the present-day relatively neutral visible colors (Ian Wong and Michael E. Brown, 2016; Sharkey et al., 2023). The depletion of water from the smaller Saturnian irregular satellites is evidence that collisions can induce significant change in the surface properties of irregular satellites at large, which could potentially explain why at Saturn and Uranus the irregular satellites are notably bluer than the Kuiper belt. Finally, JWST spectroscopy of the Neptune Trojans by Markwardt et al., 2023 found that the Neptune Trojans span the same range of spectral types as the Kuiper belt objects presented in Pinilla-Alonso et al., 2024, though perhaps in different proportions of organic-rich to water-rich types as evidenced by statistics on their visible colors (Bolin et al., 2023). Thus far, the published JWST NIRSpec small body data suggests that each of the captured populations linked by dynamical instability theories to the Kuiper belt is either spectrally analogous to the larger Kuiper belt population or one of its subsets, or has a population-specific explanation for its difference from observed Kuiper belt object spectra.

References

Abedin, Abedin Y. et al. (Apr. 2021). "OSSOS. XXI. Collision Probabilities in the Edgeworth"=Kuiper Belt". In: *AJ* 161.4, 195, p. 195. DOI: 10.3847/1538-3881/abe418. arXiv: 2104.14039 [astro-ph.EP].

Agnor, Craig B. and Douglas P. Hamilton (May 2006). "Neptune's capture of its moon Triton in a binary-planet gravitational encounter". In: *Nature* 441.7090, pp. 192–194. DOI: 10.1038/nature04792.

Barr, Amy C. and Megan E. Schwamb (Aug. 2016). "Interpreting the densities of the Kuiper belt's dwarf planets". In: *MNRAS* 460.2, pp. 1542–1548. DOI: 10.1093/mnras/stw1052. arXiv: 1603.06224 [astro-ph.EP].

Barucci, M. A. et al. (July 2011). "New insights on ices in Centaur and Transneptunian populations". In: *Icarus* 214.1, pp. 297–307. DOI: 10.1016/j.icarus.2011.04.019.

Bates, H. C. et al. (Jan. 2020). "Linking mineralogy and spectroscopy of highly aqueously altered CM and CI carbonaceous chondrites in preparation for primitive asteroid sample return". In: *M&PS* 55.1, pp. 77–101. DOI: 10.1111/maps.13411.

Beck, P. et al. (Feb. 2011). "Goethite as an alternative origin of the 3.1 μm band on dark asteroids". In: *A&A* 526, A85, A85. DOI: 10.1051/0004-6361/201015851.

Bolin, B. T. et al. (May 2023). "Keck, gemini, and palomar 200-inch visible photometry of red and very-red neptunian trojans". In: *MNRAS* 521.1, pp. L29–L33. DOI: 10.1093/mnrasl/slad018. arXiv: 2302.04280 [astro-ph.EP].

Bottke, William F. et al. (Mar. 2010). "The Irregular Satellites: The Most Collisionally Evolved Populations in the Solar System". In: *AJ* 139.3, pp. 994–1014. DOI: 10.1088/0004-6256/139/3/994.

Brown, M. E. (Dec. 2016). "The 3-4 μm Spectra of Jupiter Trojan Asteroids". In: *AJ* 152.6, 159, p. 159. DOI: 10.3847/0004-6256/152/6/159. arXiv: 1606.03013 [astro-ph.EP].

Brown, M. E. and A. R. Rhoden (Oct. 2014). "The 3 μm Spectrum of Jupiter's Irregular Satellite Himalia". In: *ApJL* 793.2, L44, p. L44. DOI: 10.1088/2041-8205/793/2/L44. arXiv: 1409.1261 [astro-ph.EP].

Brown, Michael E. (May 2012). "The Compositions of Kuiper Belt Objects". In: *Annual Review of Earth and Planetary Sciences* 40.1, pp. 467–494. DOI: 10.1146/annurev-earth-042711-105352. arXiv: 1112.2764 [astro-ph.EP].

Brown, Michael E. and Wesley C. Fraser (July 2023). "The State of CO and CO_2 Ices in the Kuiper Belt as Seen by JWST". In: *PSJ* 4.7, 130, p. 130. DOI: 10.3847/PSJ/ace2ba. arXiv: 2306.17051 [astro-ph.EP].

Brown, Michael E., Christopher D. Koresko, and Geoffrey A. Blake (Dec. 1998). "Detection of Water Ice on Nereid". In: *ApJL* 508.2, pp. L175–L176. DOI: 10.1086/311741.

Brown, Michael E., Samantha K. Trumbo, et al. (July 2025). "A JWST Study of CO_2 on the Satellites of Saturn". In: *The Planetary Science Journal* 6.7, 180, p. 180. DOI: 10.3847/PSJ/ade807. arXiv: 2506.19921 [astro-ph.EP].

Brown, Robert H. et al. (June 1999). "NOTE: Water Ice on Nereid". In: *Icarus* 139.2, pp. 374–378. DOI: 10.1006/icar.1999.6109.

Bushouse, Howard et al. (July 2024). *JWST Calibration Pipeline*. Version 1.15.1. DOI: 10.5281/zenodo.12692459. URL: https://doi.org/10.5281/zenodo.12692459.

Clark, Roger N., Robert H. Brown, Dale P. Cruikshank, et al. (Mar. 2019). "Isotopic ratios of Saturn's rings and satellites: Implications for the origin of water and Phoebe". In: *Icarus* 321, pp. 791–802. DOI: 10.1016/j.icarus.2018.11.029.

Clark, Roger N., Robert H. Brown, Ralf Jaumann, et al. (May 2005). "Compositional maps of Saturn's moon Phoebe from imaging spectroscopy". In: *Nature* 435.7038, pp. 66–69. DOI: 10.1038/nature03558.

Clark, Roger N., Dale P. Cruikshank, et al. (Apr. 2012). "The surface composition of Iapetus: Mapping results from Cassini VIMS". In: *Icarus* 218.2, pp. 831–860. DOI: 10.1016/j.icarus.2012.01.008.

Clark, Roger N., John M. Curchin, et al. (Mar. 2009). "Reflectance spectroscopy of organic compounds: 1. Alkanes". In: *Journal of Geophysical Research (Planets)* 114.E3, E03001, E03001. DOI: 10.1029/2008JE003150.

Colombo, G. and F. A. Franklin (Oct. 1971). "On the formation of the outer satellite groups of Jupiter". In: *Icarus* 15.2, pp. 186–189. DOI: 10.1016/0019-1035(71)90073-X.

Coradini, A. et al. (Jan. 2008). "Identification of spectral units on Phoebe". In: *Icarus* 193.1, pp. 233–251. DOI: 10.1016/j.icarus.2007.07.023.

Cruikshank, D. P., J. F. Bell, et al. (Jan. 1983). "The dark side of Iapetus". In: *Icarus* 53.1, pp. 90–104. DOI: 10.1016/0019-1035(83)90023-4.

Cruikshank, D. P., T. L. Roush, et al. (Oct. 1998). "The Composition of Centaur 5145 Pholus". In: *Icarus* 135.2, pp. 389–407. DOI: 10.1006/icar.1998.5997.

Cruikshank, Dale P. et al. (May 2014). "Aromatic and aliphatic organic materials on Iapetus: Analysis of Cassini VIMS data". In: *Icarus* 233, pp. 306–315. DOI: 10.1016/j.icarus.2014.02.011.

Dalle Ore, Cristina Morea, Dale P. Cruikshank, and Roger N. Clark (Nov. 2012). "Infrared spectroscopic characterization of the low-albedo materials on Iapetus". In: *Icarus* 221.2, pp. 735–743. DOI: 10.1016/j.icarus.2012.09.010.

De Prá, Mário N. et al. (May 2024). "Widespread CO_2 and CO ices in the trans-Neptunian population revealed by JWST/DiSCo-TNOs". In: *Nature Astronomy*. DOI: 10.1038/s41550-024-02276-x.

Denk, T. et al. (2018). "The Irregular Satellites of Saturn". In: *Enceladus and the Icy Moons of Saturn*. Ed. by Paul M. Schenk et al. University of Arizona Press, p. 409. DOI: 10.2458/azu_uapress_9780816537075-ch020.

Doressoundiram, A. et al. (Oct. 2002). "The Color Distribution in the Edgeworth-Kuiper Belt". In: *AJ* 124.4, pp. 2279–2296. DOI: 10.1086/342447. arXiv: astro-ph/0206468 [astro-ph].

Emery, J. P. et al. (May 2024). "A tale of 3 dwarf planets: Ices and organics on Sedna, Gonggong, and Quaoar from JWST spectroscopy". In: *Icarus* 414, 116017, p. 116017. DOI: 10.1016/j.icarus.2024.116017. arXiv: 2309.15230 [astro-ph.EP].

Fraser, Wesley C. and Michael E. Brown (July 2018). “Phoebe: A Surface Dominated by Water”. In: *AJ* 156.1, 23, p. 23. DOI: 10.3847/1538-3881/aac213. arXiv: 1803.04979 [astro-ph.EP].

Gomis, O. and G. Strazzulla (Oct. 2005). “CO_2 production by ion irradiation of H_2O ice on top of carbonaceous materials and its relevance to the Galilean satellites”. In: *Icarus* 177.2, pp. 570–576. DOI: 10.1016/j.icarus.2005.04.003.

Gordon, Karl D. et al. (June 2022). “The James Webb Space Telescope Absolute Flux Calibration. I. Program Design and Calibrator Stars”. In: *AJ* 163.6, 267, p. 267. DOI: 10.3847/1538-3881/ac66dc. arXiv: 2204.06500 [astro-ph.IM].

Grav, T. et al. (Aug. 2015a). “NEOWISE: Observations of the Irregular Satellites of Jupiter and Saturn”. In: *ApJ* 809.1, 3, p. 3. DOI: 10.1088/0004-637X/809/1/3. arXiv: 1505.07820 [astro-ph.EP].

— (Aug. 2015b). “NEOWISE: Observations of the Irregular Satellites of Jupiter and Saturn”. In: *ApJ* 809.1, 3, p. 3. DOI: 10.1088/0004-637X/809/1/3. arXiv: 1505.07820 [astro-ph.EP].

Grav, Tommy and James Bauer (Nov. 2007). “A deeper look at the colors of the saturnian irregular satellites”. In: *Icarus* 191.1, pp. 267–285. DOI: 10.1016/j.icarus.2007.04.020. arXiv: astro-ph/0611590 [astro-ph].

Graykowski, Ariel and David Jewitt (Apr. 2018). “Colors and Shapes of the Irregular Planetary Satellites”. In: *AJ* 155.4, 184, p. 184. DOI: 10.3847/1538-3881/aab49b. arXiv: 1803.01907 [astro-ph.EP].

Grundy, W. M., R. P. Binzel, et al. (Mar. 2016). “Surface compositions across Pluto and Charon”. In: *Science* 351.6279, aad9189, aad9189. DOI: 10.1126/science.aad9189. arXiv: 1604.05368 [astro-ph.EP].

Grundy, W. M., I. Wong, et al. (Mar. 2024). “Measurement of D/H and $^{13}C/^{12}C$ ratios in methane ice on Eris and Makemake: Evidence for internal activity”. In: *Icarus* 411, 115923, p. 115923. DOI: 10.1016/j.icarus.2023.115923. arXiv: 2309.05085 [astro-ph.EP].

Guilbert-Lepoutre, Aurélie (Mar. 2014). “Survival of water ice in Jupiter Trojans”. In: *Icarus* 231, pp. 232–238. DOI: 10.1016/j.icarus.2013.12.014. arXiv: 1401.5196 [astro-ph.EP].

Hainaut, O. R., H. Boehnhardt, and S. Protopapa (Oct. 2012). “Colours of minor bodies in the outer solar system. II. A statistical analysis revisited”. In: *A&A* 546, A115, A115. DOI: 10.1051/0004-6361/201219566. arXiv: 1209.1896 [astro-ph.EP].

Hand, K. P. and R. W. Carlson (Mar. 2012). “Laboratory spectroscopic analyses of electron irradiated alkanes and alkenes in solar system ices”. In: *Journal of Geophysical Research (Planets)* 117.E3, E03008, E03008. DOI: 10.1029/2011JE003888.

Hansen, Gary B. et al. (Aug. 2012). “Water ice abundance and CO_2 band strength on the saturnian satellite Phoebe from Cassini/VIMS observations”. In: *Icarus* 220.2, pp. 331–338. DOI: 10.1016/j.icarus.2012.05.004.

Hapke, B. (Apr. 1981). “Bidirectional reflectance spectroscopy. I - Theory”. In: *J. Geophys. Res.* 86, pp. 3039–3054. DOI: 10.1029/JB086iB04p03039.

Hapke, Bruce (1993). *Theory of reflectance and emittance spectroscopy*.

Heppenheimer, T. A. and C. Porco (Feb. 1977). “New Contributions to the Problem of Capture”. In: *Icarus* 30.2, pp. 385–401. DOI: 10.1016/0019-1035(77)90173-7.

Herzberg, Gerhard (1945). *Molecular spectra and molecular structure. Vol.2: Infrared and Raman spectra of polyatomic molecules*. Van Nostrand Reinhold Company.

Jacobson, R. A. et al. (Dec. 2006). “The Gravity Field of the Saturnian System from Satellite Observations and Spacecraft Tracking Data”. In: *AJ* 132.6, pp. 2520–2526. DOI: 10.1086/508812.

Jewitt, David (Feb. 2018). “The Trojan Color Conundrum”. In: *AJ* 155.2, 56, p. 56. DOI: 10.3847/1538-3881/aaa1a4. arXiv: 1712.04855 [astro-ph.EP].

Jewitt, David and Aurelie Guilbert-Lepoutre (Jan. 2012). “Limits to Ice on Asteroids (24) Themis and (65) Cybele”. In: *AJ* 143.1, 21, p. 21. DOI: 10.1088/0004-6256/143/1/21. arXiv: 1111.3292 [astro-ph.EP].

Jewitt, David and Nader Haghighipour (Sept. 2007). “Irregular Satellites of the Planets: Products of Capture in the Early Solar System”. In: *ARA&A* 45.1, pp. 261–295. DOI: 10.1146/annurev.astro.44.051905.092459. arXiv: astro-ph/0703059 [astro-ph].

Johnson, Torrence V. and Jonathan I. Lunine (May 2005). “Saturn’s moon Phoebe as a captured body from the outer Solar System”. In: *Nature* 435.7038, pp. 69–71. DOI: 10.1038/nature03384.

Jutzi, Martin and Patrick Michel (Nov. 2020). “Collisional heating and compaction of small bodies: Constraints for their origin and evolution”. In: *Icarus* 350, 113867, p. 113867. DOI: 10.1016/j.icarus.2020.113867. arXiv: 2005.12785 [astro-ph.EP].

Kelley, Michael S. P. et al. (July 2023). “Spectroscopic identification of water emission from a main-belt comet”. In: *Nature* 619.7971, pp. 720–723. DOI: 10.1038/s41586-023-06152-y.

Khare, B. N. et al. (Jan. 2001). “Solid organic matter in the atmosphere and on the surface of outer solar system bodies”. In: *Advances in Space Research* 27.2, pp. 299–307. DOI: 10.1016/S0273-1177(01)00061-8.

Kuiper, Gerard P. (Jan. 1956). “On the origin of the satellites and the Trojans”. In: *Vistas in Astronomy* 2.1, pp. 1631–1666. DOI: 10.1016/0083-6656(56)90090-3.

Lellouch, E. et al. (Sept. 2013). ““TNOs are Cool”: A survey of the trans-Neptunian region. IX. Thermal properties of Kuiper belt objects and Centaurs from combined Herschel and Spitzer observations”. In: *A&A* 557, A60, A60. DOI: 10.1051/0004-6361/201322047.

Licandro, Javier et al. (Dec. 2024). “Thermal evolution of trans-Neptunian objects through observations of Centaurs with JWST”. In: *Nature Astronomy*. DOI: 10.1038/s41550-024-02417-2.

Maris, M., G. Carraro, and M. G. Parisi (Sept. 2007). "Light curves and colours of the faint Uranian irregular satellites Sycorax, Prospero, Stephano, Setebos, and Trinculo". In: *A&A* 472.1, pp. 311–319. DOI: 10.1051/0004-6361:20066927. arXiv: 0704.2187 [astro-ph].

Markwardt, Larissa et al. (Oct. 2023). "First Near-IR Spectroscopic Survey of Neptune Trojans with JWST: Distinct Surface Compositions of Red vs Ultra-Red Neptune Trojans". In: *arXiv e-prints*, arXiv:2310.03998, arXiv:2310.03998. DOI: 10.48550/arXiv.2310.03998. arXiv: 2310.03998 [astro-ph.EP].

Mastrapa, R. M., M. P. Bernstein, et al. (Sept. 2008). "Optical constants of amorphous and crystalline H $_2$O-ice in the near infrared from 1.1 to 2.6 μm". In: *Icarus* 197.1, pp. 307–320. DOI: 10.1016/j.icarus.2008.04.008.

Mastrapa, R. M., S. A. Sandford, et al. (Aug. 2009). "Optical Constants of Amorphous and Crystalline H_2O-ice: 2.5-22 μm (4000-455 cm^{-1}) Optical Constants of H_2O-ice". In: *ApJ* 701.2, pp. 1347–1356. DOI: 10.1088/0004-637X/701/2/1347.

McKay, Adam J., Dennis Bodewits, and Jian-Yang Li (Apr. 2017). "Observational constraints on water sublimation from 24 Themis and 1 Ceres". In: *Icarus* 286, pp. 308–313. DOI: 10.1016/j.icarus.2016.09.032. arXiv: 1609.07156 [astro-ph.EP].

Melosh, H. J. (1989). *Impact cratering : a geologic process*. Oxford University Press.

Moore, M. H. and R. L. Hudson (Oct. 1998). "Infrared Study of Ion-Irradiated Water-Ice Mixtures with Hydrocarbons Relevant to Comets". In: *Icarus* 135.2, pp. 518–527. DOI: 10.1006/icar.1998.5996.

Morbidelli, Alessandro (Nov. 2010). "A coherent and comprehensive model of the evolution of the outer Solar System". In: *Comptes Rendus Physique* 11, pp. 651–659. DOI: 10.1016/j.crhy.2010.11.001. arXiv: 1010.6221 [astro-ph.EP].

Moroz, Lyuba et al. (July 2004). "Optical alteration of complex organics induced by ion irradiation:. 1. Laboratory experiments suggest unusual space weathering trend". In: *Icarus* 170.1, pp. 214–228. DOI: 10.1016/j.icarus.2004.02.003.

Müller, D. R. et al. (June 2022). "High D/H ratios in water and alkanes in comet 67P/Churyumov"=Gerasimenko measured with Rosetta/ROSINA DFMS". In: *A&A* 662, A69, A69. DOI: 10.1051/0004-6361/202142922. arXiv: 2202.03521 [astro-ph.EP].

Murphy, D. M. and T. Koop (Apr. 2005). "Review of the vapour pressures of ice and supercooled water for atmospheric applications". In: *Quarterly Journal of the Royal Meteorological Society* 131.608, pp. 1539–1565. DOI: 10.1256/qj.04.94.

Nesvorný, David (Sept. 2018). "Dynamical Evolution of the Early Solar System". In: *ARA&A* 56, pp. 137–174. DOI: 10.1146/annurev-astro-081817-052028. arXiv: 1807.06647 [astro-ph.EP].

Nesvorný, David, David Vokrouhlický, and Rogerio Deienno (Mar. 2014). "Capture of Irregular Satellites at Jupiter". In: *ApJ* 784.1, 22, p. 22. DOI: 10.1088/0004-637X/784/1/22. arXiv: 1401.0253 [astro-ph.EP].

Nesvorný, David, David Vokrouhlický, and Alessandro Morbidelli (May 2007). "Capture of Irregular Satellites during Planetary Encounters". In: *AJ* 133.5, pp. 1962–1976. DOI: 10.1086/512850.

O'Rourke, L. et al. (Aug. 2020). "Low Water Outgassing from (24) Themis and (65) Cybele: 3.1 μm Near-IR Spectral Implications". In: *ApJL* 898.2, L45, p. L45. DOI: 10.3847/2041-8213/aba62b.

Peña, José and Cesar Fuentes (June 2022). "Colors of Irregular Satellites of Saturn with the Dark Energy Camera". In: *AJ* 163.6, 274, p. 274. DOI: 10.3847/1538-3881/ac6258. arXiv: 2204.08391 [astro-ph.EP].

Pinilla-Alonso, Noemí et al. (Dec. 2024). "A JWST/DiSCo-TNOs portrait of the primordial Solar System through its trans-Neptunian objects". In: *Nature Astronomy*. DOI: 10.1038/s41550-024-02433-2.

Pollack, J. B., J. A. Burns, and M. E. Tauber (Mar. 1979). "Gas drag in primordial circumplanetary envelopes: A mechanism for satellite capture". In: *Icarus* 37.3, pp. 587–611. DOI: 10.1016/0019-1035(79)90016-2.

Porco, C. C. et al. (Feb. 2005). "Cassini Imaging Science: Initial Results on Phoebe and Iapetus". In: *Science* 307.5713, pp. 1237–1242. DOI: 10.1126/science.1107981.

Porco, Carolyn C. et al. (Dec. 2004). "Cassini Imaging Science: Instrument Characteristics And Anticipated Scientific Investigations At Saturn". In: *SSRv* 115.1-4, pp. 363–497. DOI: 10.1007/s11214-004-1456-7.

Prahl, Scott (May 2023). *miepython*. Version v2.3.2. DOI: 10.5281/zenodo.7949403. URL: https://doi.org/10.5281/zenodo.7949403.

Raponi, A. et al. (Jan. 2020). "Infrared detection of aliphatic organics on a cometary nucleus". In: *Nature Astronomy* 4, pp. 500–505. DOI: 10.1038/s41550-019-0992-8. arXiv: 2009.14476 [astro-ph.EP].

Rivkin, Andrew S. and Joshua P. Emery (Apr. 2010). "Detection of ice and organics on an asteroidal surface". In: *Nature* 464.7293, pp. 1322–1323. DOI: 10.1038/nature09028.

Romon, J. et al. (Sept. 2001). "Photometric and spectroscopic observations of Sycorax, satellite of Uranus". In: *A&A* 376, pp. 310–315. DOI: 10.1051/0004-6361:20010934.

Russell, J. D. et al. (1975). "Adsorption of carbon dioxide on goethite (alpha-FeOOH) surfaces, and its implications for anion adsorption". In: *J. Chem. Soc., Faraday Trans. 1* 71 (0), pp. 1623–1630. DOI: 10.1039/F19757101623. URL: http://dx.doi.org/10.1039/F19757101623.

Sharkey, Benjamin N. L. et al. (Nov. 2023). "Spectroscopic Links among Giant Planet Irregular Satellites and Trojans". In: *PSJ* 4.11, 223, p. 223. DOI: 10.3847/PSJ/ad0845. arXiv: 2310.19934 [astro-ph.EP].

Souza-Feliciano, A. C. et al. (Jan. 2024). "Spectroscopy of the binary TNO Mors-Somnus with the JWST and its relationship to the cold classical and plutino subpopulations observed in the DiSCo-TNO project". In: *A&A* 681, L17, p. L17. DOI: 10.1051/0004-6361/202348222.

Stewart, Sarah T. and Thomas J. Ahrens (Mar. 2005). "Shock properties of H_2O ice". In: *Journal of Geophysical Research E* 110.E3, Art. No. E03005. ISSN: 0148-0227. DOI: 10.1029/2004JE002305.

Strazzulla, G. and L. Moroz (May 2005). "Ion irradiation of asphaltite as an analogue of solid hydrocarbons in the interstellar medium". In: *A&A* 434.2, pp. 593–598. DOI: 10.1051/0004-6361:20042468.

Takir, Driss and Joshua P. Emery (June 2012). "Outer Main Belt asteroids: Identification and distribution of four 3-μm spectral groups". In: *Icarus* 219.2, pp. 641–654. DOI: 10.1016/j.icarus.2012.02.022.

Tegler, S. C. and W. Romanishin (Mar. 1998). "Two distinct populations of Kuiper-belt objects". In: *Nature* 392.6671, pp. 49–51. DOI: 10.1038/32108.

Thomas, P. C. (July 2010). "Sizes, shapes, and derived properties of the saturnian satellites after the Cassini nominal mission". In: *Icarus* 208.1, pp. 395–401. DOI: 10.1016/j.icarus.2010.01.025.

Usui, Fumihiko et al. (Jan. 2019). "AKARI/IRC near-infrared asteroid spectroscopic survey: AcuA-spec". In: *PASJ* 71.1, 1, p. 1. DOI: 10.1093/pasj/psy125. arXiv: 1810.03828 [astro-ph.EP].

Verbiscer, Anne J., Michael F. Skrutskie, and Douglas P. Hamilton (Oct. 2009). "Saturn's largest ring". In: *Nature* 461.7267, pp. 1098–1100. DOI: 10.1038/nature08515.

Vilas, Faith et al. (Feb. 2006). "Aqueous alteration affecting the irregular outer planets satellites: Evidence from spectral reflectance". In: *Icarus* 180.2, pp. 453–463. DOI: 10.1016/j.icarus.2005.10.004.

Wong, Ian and Michael E. Brown (Oct. 2016). "A Hypothesis for the Color Bimodality of Jupiter Trojans". In: *AJ* 152.4, 90, p. 90. DOI: 10.3847/0004-6256/152/4/90. arXiv: 1607.04133 [astro-ph.EP].

— (Apr. 2017). "The Bimodal Color Distribution of Small Kuiper Belt Objects". In: *AJ* 153.4, 145, p. 145. DOI: 10.3847/1538-3881/aa60c3. arXiv: 1702.02615 [astro-ph.EP].

Wong, Ian, Michael E. Brown, et al. (Apr. 2024). "JWST Near-infrared Spectroscopy of the Lucy Jupiter Trojan Flyby Targets: Evidence for OH Absorption, Aliphatic Organics, and CO_2". In: *PSJ* 5.4, 87, p. 87. DOI: 10.3847/PSJ/ad2fc3. arXiv: 2311.11531 [astro-ph.EP].

Chapter 6

NEREID AS A REGULAR SATELLITE OF NEPTUNE

Belyakov, Matthew et al. (2026). "Nereid as a regular satellite of Neptune". In: *Science Advances* 12.21, eaeb1429. DOI: 10.1126/sciadv.aeb1429. eprint: https://www.science.org/doi/pdf/10.1126/sciadv.aeb1429. URL: https://www.science.org/doi/abs/10.1126/sciadv.aeb1429.

Nereid, Neptune's third largest moon, is considered to be a captured irregular satellite due to its highly eccentric orbit. However, among irregular satellites, Nereid is an outlier: it is the largest, the closest to its host planet, and the most eccentric. We present James Webb Space Telescope near-infrared spectroscopy of Nereid that demonstrates that its composition is inconsistent with its suggested captured origin. We then simulate Nereid's early orbital history subsequent to Triton's capture to demonstrate a plausible dynamical pathway for a regular satellite formed in situ around Neptune to evolve to Nereid's present-day orbit. Based upon the available spectroscopic and dynamical evidence, we propose that Nereid is not a body captured from the Kuiper belt, but rather the sole surviving intact regular satellite of Neptune.

6.1 Introduction

Neptune is the only giant planet that lacks an intact regular satellite system. The planet's largest moon, Triton, constitutes over 99% of the satellite system's mass and follows a 157 degree retrograde, synchronous orbit, at 14 Neptune radii. Triton's unique dynamical state among Solar System moons suggests the satellite was captured from the protoplanetary disk, with its orbit subsequently circularized through tidal dissipation or collisions Goldreich et al., 1989; Tsui, 2002; Agnor and Hamilton, 2006; Nogueira, Brasser, and Gomes, 2011. The conclusion that Triton was captured is further supported by notable similarities between Pluto and Triton McKinnon, 1984; Mousis et al., 2025.

Neptune also hosts a set of seven inner moons often referred to as ring-moons. As suggested by their name, ring-moons share material and an origin with the planet's rings. Neptune's ring-moons are likely the collisionally disrupted remnants of the proto-Neptunian disk Goldreich et al., 1989; Banfield and Murray, 1992; Ćuk and Gladman, 2005. Voyager imaging of Proteus, Neptune's second largest moon and the largest ring-moon, revealed a rough surface and a shape inconsistent with hydrostatic equilibrium, indicating Proteus may be a rubble pile Croft, 1992. Therefore, the ring-moons do not qualify as intact and original Neptunian satellites.

Nereid is the third largest Neptunian satellite, and is typically classified as an irregular satellite due to its highly eccentric orbit Gerald P. Kuiper, 1949. Irregular satellites are thought to be captured from planetesimals in the protoplanetary disk Gerard P. Kuiper, 1956; David Nesvorný, Vokrouhlický, and Morbidelli, 2007a. Among the irregular satellites of the giant planets, Nereid has the lowest pericenter (0.012 Hill radii or 56 Neptune radii) and semi-major axis (0.048 Hill radii or 224 Neptune radii), while typical irregular satellites have orbits outside 0.1 Hill radii of their host planets. Nereid also has the highest mean eccentricity ($e \simeq 0.75$) and the largest radius at 175 km – twice the size of Saturn's Phoebe Thomas, Veverka, and Helfenstein, 1991; Kiss et al., 2016. Compositionally, Nereid also stands out: it has a notably higher albedo (0.24) than typical similarly-sized Kuiper belt objects (KBOs) Kiss et al., 2016, and has a bluer spectral slope than Neptune's other irregular satellites Graykowski and Jewitt, 2018. Past ground-based near-infrared spectroscopy found deep water ice absorption features on Nereid Michael E. Brown, Koresko, and Blake, 1998; R. H. Brown et al., 1999; Sharkey et al., 2021, however these early studies had a limited compositional picture of outer solar system bodies and could not definitively determine Nereid's origin. Here, we use James Webb Space Telescope observations of Nereid coupled with dynamical simulations to ascertain the origin and evolution of this unique moon.

6.2 Results

6.2.1 JWST Spectroscopy

We observed Nereid using the James Webb Space Telescope (JWST) Near-Infrared Spectrograph (NIRSpec) integral field unit (IFU) in Prism mode, which covers 0.6-5.3 µmwith an R$\sim 30-300$ resolving power n.d. Nereid's reflectance spectrum (Figure 6.2) is dominated by water ice, with a negative, or blue slope between 1.0 and 2.5 µm. The 1.65 µmabsorption inset on the 1.5 µmband, along with the 3.1 µmnarrow Fresnel peak evidence crystalline water ice Mastrapa et al., 2009. JWST's expanded wavelength coverage also reveals the deep 4.5 µmH_2O combination band. Despite abundant water ice, the continuum across the large H_2O band at 3.0 µmis flat (dotted line in Figure 6.2), unlike both laboratory studies of water ice and outer solar system icy surfaces which have very low reflectances longwards of the 3.0 µmwater band R. N. Clark, 1980; Mastrapa et al., 2009; Roger N. Clark, R. H. Brown, et al., 2019.

To examine the possibility that Nereid is a former member of the Kuiper belt that was subsequently captured into an irregular orbit around Neptune, we compare it to the JWST sample of KBO spectra. JWST has revealed three distinct spectral types in the Kuiper belt: water-rich, CO_2-rich, and methanol-rich, in order of hypothesized formation distance Pinilla-Alonso et al., 2025. The methanol and CO_2-rich KBOs are substantially different from Nereid; these two spectral types have very red visible slopes, large aliphatic organic absorptions at 3.4 μm, and CO ice. Nereid is better matched by water-rich KBOs (Figure 6.1), which are defined by a deep 3.0 μmabsorption accompanied by water ice bands at 1.5, 2.0, and 4.5 μm, while lacking the numerous other volatiles seen on their CO_2 and methanol-rich counterparts. However, Nereid's H_2O ice spectral features are deeper than those on any observed water-rich KBO, while Nereid's 1.0 to 2.5 μmslope is bluer than that of any KBO in the JWST sample.

Nereid sees a higher impactor flux than KBOs David Nesvorný, Alvarellos, et al., 2003; Bottke et al., 2010, thus a better comparison to Nereid might be Phoebe, Saturn's heavily cratered irregular satellite thought to be a captured water-rich KBO Porco et al., 2005; Fraser and Michael E. Brown, 2018; Belyakov and Michael E. Brown, 2025. Comparing Nereid with Phoebe's JWST global spectrum (Figure 6.1), Phoebe has a redder NIR slope and lower overall water ice abundance. Water-rich pixels in cratered regions of Phoebe from *Cassini* VIMS fly-by data have a 2.0 μmabsorption band depth exceeding Nereid's (Figure 6.1), but have a lower albedo Porco et al., 2005; Fraser and Michael E. Brown, 2018, redder 1.0 to 2.5 μmslope, bluer 2.2 to 3.5 μmslope, and a shallower 4.5 μmwater ice absorption band than Nereid (Figure 6.1). Therefore, even when a water-rich KBO surface is processed to reveal deep water-ice absorptions, its spectrum does not become more Nereid-like, as demonstrated by the cratered regions on Phoebe being spectrally distinct from Nereid. Therefore, Nereid does not appear to be captured from the most common spectral type of dynamically excited KBOs.

Nereid's visible albedo is 0.24, higher than the 0.05-0.10 albedos of water-rich KBOs Pinilla-Alonso et al., 2025, but similar to the least icy Saturnian or Uranian icy satellites, such as Hyperion or Umbriel Buratti, Mosher, and Johnson, 1990; Karkoschka, 2001. The closest match to Nereid's visible color and albedo is Hyperion Kiss et al., 2016, yet Hyperion has a spectrum even icier than the water-rich parts of Phoebe Roger N. Clark, Cruikshank, et al., 2012; Brad Dalton, Cruikshank, and Roger N. Clark, 2012; Michael E. Brown, Trumbo, et al., 2025, with a more negative slope in the continuum across the 3.0 μmwater ice band. Water ice has a negative sloping continuum in the infrared Mastrapa et al., 2009, therefore the darkening agent on Nereid's surface must be red in the 2.0 to 5.0 μmregion to set Nereid's flat continuum between 2.2 and 3.5 μm. Organics and tholin-like materials are notably red in the visible and blue in the infrared unlike Nereid, while amorphous carbon is too dark with a flat 1–5 μmslope Roger N. Clark, Cruikshank, et al., 2012. Nano-phase hematite and iron have the Nereid-like blue visible and red infrared slope, however these silicate-derived materials usually display 1.0 μmabsorptions that are clearly seen on Phoebe or Hyperion Roger N. Clark, Cruikshank, et al., 2012 but are absent on Nereid.

Another relevant parameter to our comparisons is Nereid's size. In the sample of KBOs observed with JWST, there are a dozen similarly-sized objects, including 1996 TL_{66} and 2001 FP_{185}, both of which are water-rich KBOs that appear distinct from Nereid Pinilla-Alonso et al., 2025. Meanwhile, Haumea and its eponymous collisional family M. E. Brown, Trujillo, and Rabinowitz, 2005 show much higher albedos than Nereid, and do not match its spectrum (Figure 6.1). While we cannot, of course, rule out the possibility of some Nereid-like object lurking unobserved within the Kuiper belt, the sample of observed KBOs cover objects from all major dynamical classes as well as an albedo, size, and color range that includes Nereid. For example, in the hot classical Kuiper belt, there are under a hundred objects in the absolute magnitude of Nereid (H$\sim$ 3.5 − 5.5, Nereid is 4.4) Petit et al., 2023, of which JWST has sampled 10.

Nereid's unique spectrum among outer solar system bodies is not consistent with a scenario where Nereid is captured during the early solar system's dynamical instability David Nesvorný, Vokrouhlický, and Morbidelli, 2007b. The combination of a bright, water icy surface, with a unique dark material renders Nereid unlike KBOs or other irregular satellites like Phoebe, suggesting that Nereid did not form in the outer planetesimal disk alongside KBOs.

6.2.2 Nereid's dynamical origin

As Nereid does not appear to be compositionally related to KBOs, two possibilities emerge for its origin. The first is capture from dynamically cold planetesimals local to Neptune, most of which were scattered or incorporated into the planet, and are therefore not well-represented in the present-day Kuiper belt Jewitt and Haghighipour, 2007. This hypothesis presents multiple issues. Mechanisms of early, pre-instability capture are not efficient at the ice giants. Gas drag and capture by mass accretion of the host planet require large masses and extensive gas envelopes for which Neptune is too small David Nesvorný, Vokrouhlický, and Morbidelli, 2007b. Binary capture provides an alternative mechanism Agnor and Hamilton, 2006; Jewitt and Haghighipour, 2007, however, objects captured too early have a high risk of disruption as large planetesimals and planetary bodies cross the giant planet region prior to and during the Solar System's early dynamical instability David Nesvorný, Vokrouhlický, and Morbidelli, 2007b. Conversely, a post-instability capture is too late for the existence of a sizable reservoir of local planetesimals, and binary capture will then occur from more distant sources.

Nereid's dynamical peculiarities raise the question of whether it originated as a regular

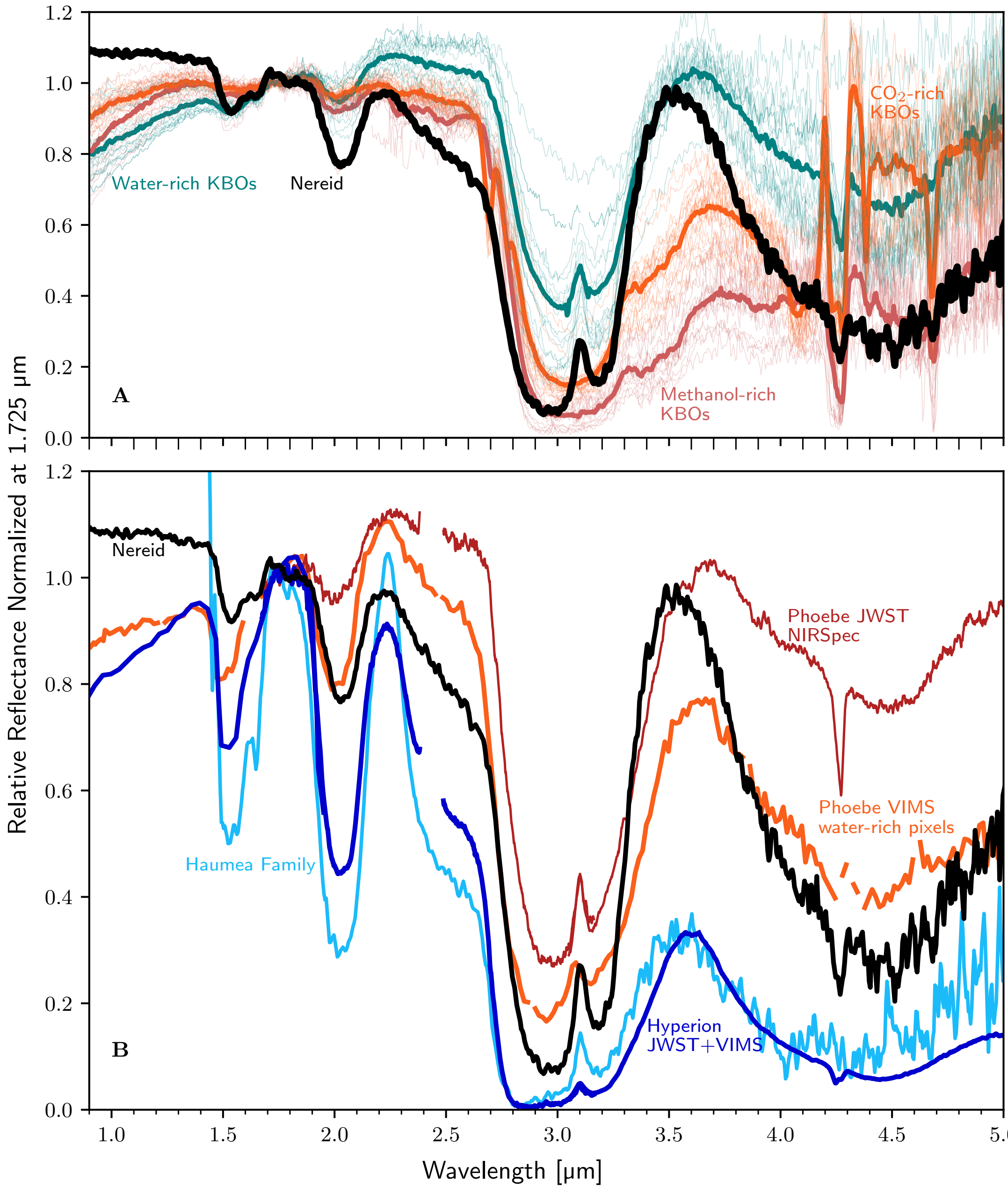

Figure 6.1: **Comparison of Nereid to outer solar system bodies.** (A) Spectrum of Nereid (black) plotted against the three classes of KBOs observed by JWST Pinilla-Alonso et al., 2025. (B) Nereid's spectrum compared to Phoebe, Hyperion, and Haumea-family members (see text).

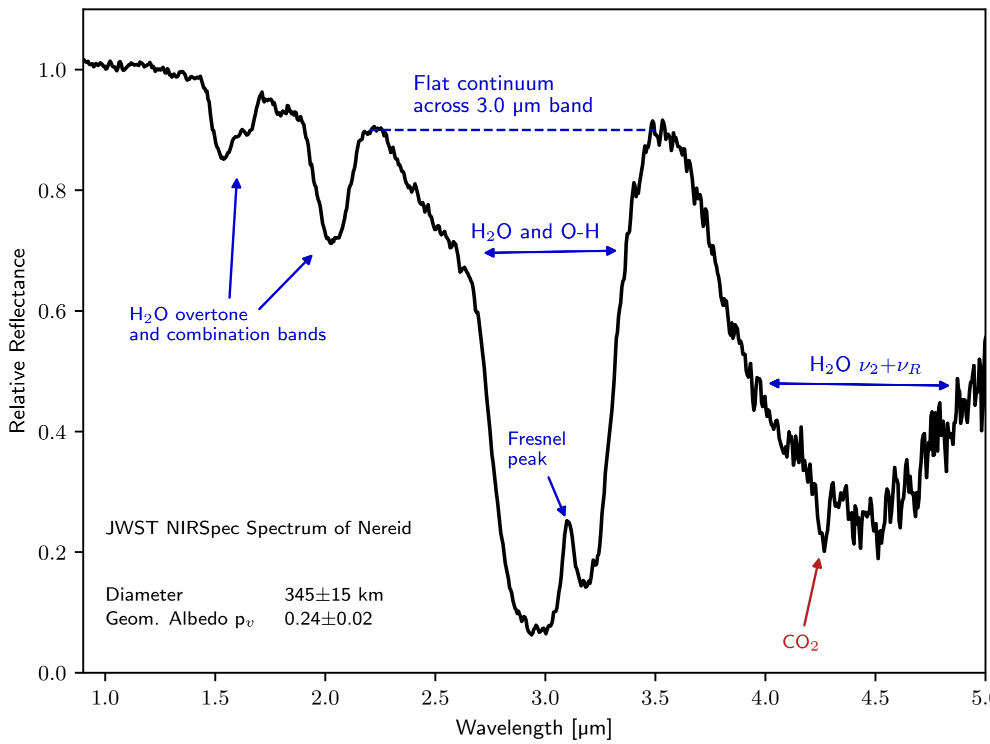

Figure 6.2: **JWST/NIRSpec spectrum of Nereid.** Relative reflectance spectrum of Nereid with key features highlighted. The near-infrared slope is distinctly negative. Features at 1.5, 2.0, 3.0, and 4.5 μmare due to abundant H_2O ice, while CO_2 produces the 4.27 μmband. Past the CO_2 absorption feature, high frequency variation in the signal appears owing to lower detector sensitivity, decreasing signal, and increased thermal background.

satellite, perturbed by Triton to its current orbit Goldreich et al., 1989. We explore whether Nereid, starting as an initially regular satellite formed around Neptune, could have acquired its present orbit following the key event in the Neptunian system's history: Triton's capture and orbital evolution. Triton likely originated as a Pluto-like body with a large satellite, evinced by the similar compositions of Pluto and Triton McKinnon, 1984. During a close encounter with Neptune, the binary pair of Triton and its satellite was dissociated, thus capturing Triton on a highly-eccentric, retrograde orbit Agnor and Hamilton, 2006. From this initial state, Triton's orbit circularized to evolve onto its current tidally-locked orbit, maintaining its retrograde inclination. The paucity of information on the initial satellite system and the exact conditions of Triton's capture limits us to demonstrating the plausibility of Triton perturbing Nereid to an irregular satellite-like orbit, rather than determining a pathway and set of conditions that give an exact orbital match to present-day Nereid.

Models of Triton's capture show that the dissociation of Triton from its binary initially produces a highly eccentric orbit, since the change in energy from a heliocentric to planetocentric orbit tends to leave Triton on a tenuous orbit around Neptune Agnor and Hamilton, 2006; Nogueira, Brasser, and Gomes, 2011. For Triton to remain bound to Neptune, it must rapidly lose orbital energy and circularize. While tides were originally suggested as the mechanism to bring Triton to its current orbit Nogueira, Brasser, and Gomes, 2011, recent work has demonstrated that tidal evolution may be too slow to preserve Triton as it interacts with a disk of pre-existing satellites. Instead, circularization via dissipative collisions can proceed over an order of magnitude more rapidly than high-eccentricity tidal migration Ćuk and Gladman, 2005; Rufu and Canup, 2017.

We simulate collisional circularization in order to determine the feasibility of transferring one of the pre-existing satellites to an irregular orbit as Triton disrupts the original Neptunian system. Our simulations include the Sun, Neptune, an eccentric and inclined Triton, and a satellite system with a Uranus-like mass at an evolved, but not final stage of satellite accretion. Evolving this system for a million years, we demonstrate that Triton is able to perturb initially regular satellites to an orbit within 10% of Nereid's present semi-major axis and periapse, while clearing out most of the system and circularizing in the process (Figure 6.3). In the simulation shown, the final Nereid-like satellite has a ~ 40 degree mean inclination relative to Neptune's equatorial plane and a mean eccentricity of 0.705. Nereid has a 28.4 degree inclination relative to Neptune's equator and an eccentricity of 0.75, thus our simulation can roughly reproduce Nereid's present-day orbit.

Characterizing our entire suite of simulations, we see three kinds of outcomes. The most frequent result is the ejection or destruction of Triton, representing 60% of runs, consistent with past work Rufu and Canup, 2017. Among simulations which do not leave Triton intact, nearly all produce one or more Nereid-like bodies. Considering the abundance of Triton-mass objects in our early Solar System Morbidelli et al., 2009, a plausible history for the Neptunian system and Nereid is that an early encounter with a Triton-sized body destroyed many of the original satellites while leaving Nereid on an irregular orbit. Present-day Triton is then a product of a second capture event, circularizing rapidly enough to preserve Nereid even if most of the system is gone. In fact, such a scenario is favorable for Triton's capture, as previous work indicates that a system mass that is 20% smaller than that of the Uranian moons is more likely to capture Triton than a Uranian-like system Rufu and Canup, 2017. The second outcome of our simulations, at 20% of runs, is one where Triton removes all the satellites except a set of inner moons, leaving the system much like the present-day one, but without Nereid. Finally, we have 20% of strictly successful simulations, in which Triton circularizes and leaves one or more satellites on irregular orbits. We define any object with semi-major axis greater than $R_N > 50$, and either an inclination greater than 10 degrees or eccentricity more than 0.2 as irregular satellite like. Were a satellite with such characteristics

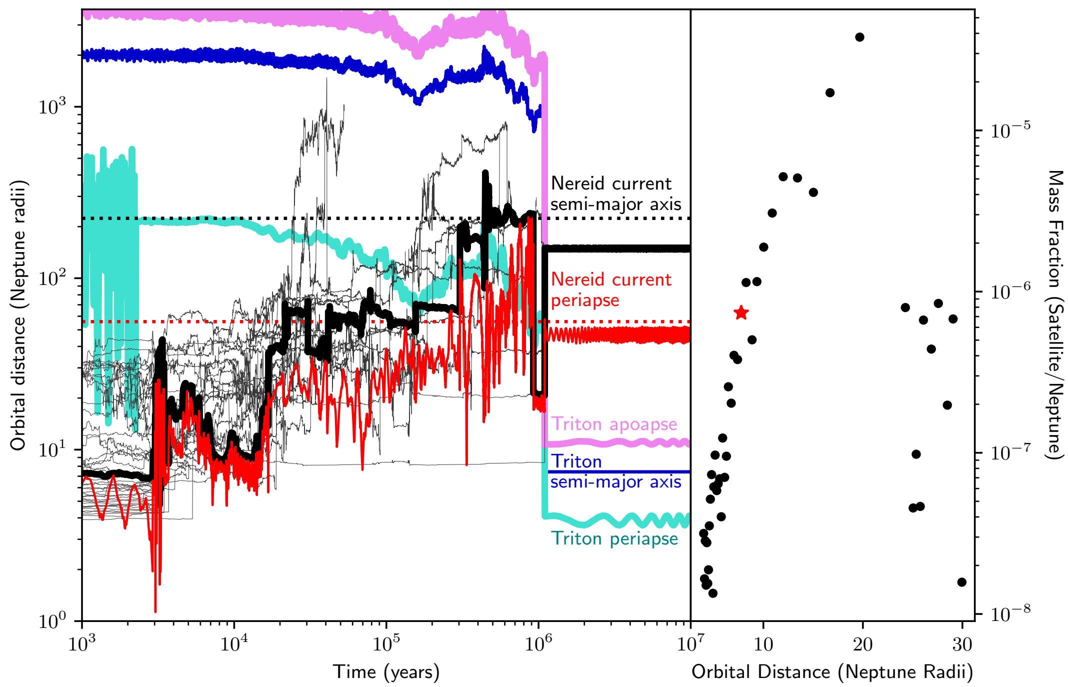

Figure 6.3: **Evolution of Triton into a disk of satellites.** Left: Triton's semi-major axis, periapse, and apoapse (blue, cyan, violet); the satellite perturbed to a Nereid-like orbit (black and red). Right: Initial proto-Neptunian satellite configuration Ida et al., 2020.

observed, it would evoke the same questions raised by Nereid. The probability of Triton both surviving an encounter with a Uranus-like system and kicking a regular satellite to a dynamically stable irregular orbit is thus approximately 20%. We show the range of outcomes described above in the supplementary material n.d.

6.3 Discussion

Nearly 70 years after Nereid's discovery by Kuiper and 40 years after the brief Voyager 2 fly-by, we have demonstrated that Nereid's spectroscopic characteristics do not appear to be consistent with irregular satellite capture David Nesvorný, Vokrouhlický, and Morbidelli, 2007b, as its near-infrared spectrum does not resemble that of any KBO or irregular satellite observed with JWST to date. Our proposed regular satellite genesis story for the moon leaves Nereid as the singular intact original satellite of Neptune — Neptune's innermost moons, such as Proteus, are re-accreted pieces of satellites destroyed by Triton's capture Banfield and Murray, 1992; Rufu and Canup, 2017. Further details in Nereid's spectrum not revealed by our study, such as the deuterium-to-hydrogen ratio, carbon isotope ratios, or precise CO_2 band center could unlock answers to key questions regarding the evolution of Neptune and the characteristics of its original satellite system. Future spacecraft exploration of the Neptunian system should search for signs of an early geologic history on Nereid consistent with formation as a regular satellite, as tidal evolution of Triton over billions of years has erased its collisional past Mousis et al., 2025. Additionally, finding evidence for the collisional capture of Triton through observations of inner moons such as Proteus and Larissa would help confirm our dynamical story for the Neptunian system.

The destruction of the initial Neptunian satellite system precludes us from definitively tracing Nereid's history from grains to accretion to transfer to an irregular orbit. Reliable inferences of the probability of the dynamical events described occurring would require knowledge of the mass of Nereid, the exact configuration of satellites in Neptune's primordial system, and a constraint on the timing of Triton's capture. Our outlined scenario for Nereid favors a mass for the original Neptunian satellite system that was either smaller than that of the Uranian system, or that the mass became smaller through interactions with large interlopers prior to Triton's capture. Such a system would both facilitate Triton's capture and have more mid-sized satellites than the present Uranian system, increasing the number of Nereid-like bodies that could be perturbed. Additionally, the collisional model for Triton's capture prefers a capture for Triton shortly after the formation of the Neptunian satellites, before they had time to evolve into a version of the present Uranian system. Perturbing a regular satellite to a Nereid-like orbit or a more distant one depends on the circularization timescale, where a longer circularization for Triton leaves more time for satellites to diffuse outwards, causing them to be kicked to yet more distant orbits. The possible parameter space for the initial configuration of the Neptunian system and Triton's capture is effectively unconstrained and is far larger than can be explored through simulations. As such, our simulations are merely illustrative of the process wherein a smaller body undergoing scattering is stabilized by interactions with a massive external perturber, demonstrating that a transfer of Nereid from a circular to eccentric and inclined orbit in the context of Triton's circularization is plausible. We note that the process we have outlined, though on much grander scales, has recently been shown to deliver planets to distant, yet bound orbits during dynamical instabilities in the early Solar System Izidoro et al., 2025.

We note that there exists another mechanism for exciting regular satellites to Nereid-like orbits that has been proposed in the literature on giant planet migration, supporting the dynamical scenario we have outlined. The early Solar System contained hundreds of Triton-sized bodies which were ejected by scattering off of the giant planets; this process is partially responsible for the migration of the giant planets Fernandez and Ip, 1984; Tsiganis et al., 2005. Simulations of close encounters between Neptune and > 1000km bodies demonstrate that regular satellites past 12 Neptune radii are readily excited to Nereid-like orbits Beaugé, Roig, and D. Nesvorný, 2002. More severe planet-planet close encounters can produce similar results, although planet-planet scattering events require fine-tuned initial conditions to produce Nereid without removing the entire proto-Neptunian system Li and Christou, 2020.

Finally, we discuss the effectiveness of dynamical models for capture of irregular satellites from the Kuiper belt, as applied to Nereid. Irregular satellite capture that proceeds from planet-planet interactions perturbing KBOs onto planetocentric orbits appears to be rather inefficient at delivering Nereid from the Kuiper belt to its present orbit David Nesvorný, Vokrouhlický, and Morbidelli, 2007b; David Nesvorný, Vokrouhlický, and Deienno, 2014. The original number of Nereid-sized objects in the proto-Kuiper belt is at most of order 10^5 bodies Morbidelli et al., 2009; Schlichting and Sari, 2011; Kenyon and Bromley, 2012. Capture efficiency for irregular satellites at Neptune is around 10^{-8} David Nesvorný, Vokrouhlický, and Deienno, 2014. Thus, the probability of capturing a single Nereid-like body from the proto-Kuiper belt is close to 0.1%, far lower than in our regular satellite origin story. An alternative capture regime is binary capture, as discussed for Triton. Capturing Nereid as the primary member of a binary is rather unlikely, as shown in three-body capture simulations Philpott, Hamilton, and Agnor, 2010; Gaspar, Winter, and Vieira Neto, 2013. If Nereid were instead the smaller member of a binary, capture is possible only for wide binary separations, at least as wide as Pluto/Hydra Agnor and Hamilton, 2006; Kobayashi et al., 2012. While we cannot rule out that Nereid was captured from a binary KBO, the numerous Pluto-mass objects of the early Solar System would have had their moons dispersed into the Kuiper belt, and would appear in the present-day record of 400km-sized bodies David Nesvorný and Vokrouhlický, 2019. A regular satellite origin for Nereid as proposed in our work and hinted at in previous studies Beaugé, Roig, and D. Nesvorný, 2002; Li and Christou, 2020 appears more likely than a rare capture of an object with no known spectral analogues in the present-day Kuiper belt.

6.4 Materials and Methods

6.4.1 JWST data reduction

Nereid was observed with JWST NIRSpec on November 23, 2024 between 03:28:53 UT and 05:24:45 UT as part of the Cycle 3 GO Program #4645. The observations were obtained using the Integral field unit (IFU) in PRISM mode with a nominal R∼30-300 resolving power over a 0.6-5.3 μmwavelength range. We used a four point dither configuration with a 160.5 second exposure time per dither. All other JWST spectra presented in this study were obtained from the Mikulski Archive for Space Telescope (MAST), and can be found at https://doi.org/10.17909/2bj1-h545. The spectrum of Nereid and all other objects shown were reduced using the PSF template fitting method that has been applied to numerous studies with JWST Michael E. Brown and Fraser, 2023; Wong et al., 2024. The reduction code, jwstspec, can be found online on Zenodo Wong, 2025.

6.4.2 Dynamical simulations

All of our simulations use the REBOUND N-body integrator Rein and Liu, 2012, and the code used to initialize all of our simulation runs is available for download at CaltechData (https://doi.org/10.22002/gf82m-rzz66) Belyakov, Davis, et al., 2025. Our simulations include the Sun, Neptune, Triton, and a disk of massive satellites. We use the adaptive timestep IAS15 integrator to ensure high precision during close encounters. We initialize Triton at a periapse of 14 or 21 Neptune radii, and vary semi-major axis distance from 1300 to 2300 R_N. Triton starts with its present-day inclination and randomized longitudes. We model the satellite system of Neptune to mimic the distribution of satellite masses and semi-major axes produced by the vapor disk model for Uranian satellite formation Ida et al., 2020. We generate moons between 3 and 20 Neptune radii following the isolation mass for oligarchic growth Ida et al., 2020, which is given by:

$$m_{\text{isolation}} = 0.74 \times 10^{-4} \left(\frac{r}{20 r_{\text{Nep}}} \right)^{21/4} M_{\text{Nep}}. \tag{6.1}$$

This distribution of satellitesimals would be replicated by other models of satellite formation, such as those from tidal disruption of comets Charnoz, Salmon, and Crida, 2010; Hyodo et al., 2017. We set the total mass of the disk to $10^{-4} \times M_{\text{Nep}}$, generating a system similar in mass to the Uranian system. We also run simulations with a smaller system mass, at $2 \cdot 10^{-5} \times M_{\text{Nep}}$. We cap the largest generated satellites at $1 \times 10^{-5}\ M_{\text{Neptune}}$, and multiply their masses by a random factor between 0.25 and 4. Past the cut-off of 20 r_{Nep}, we use a log-normal distribution centered at $10^{-7}\ M_{\text{Nep}}$ to generate satellites out to 30 r_{Nep} or until we reach our mass cap. Our resulting model satellite disk represents an intermediate stage of oligarchic growth of satellites at Neptune. A key point in our simulations is that we handle collisions by merging particles while conserving mass, momentum, and energy, and track these collisions in order to precisely ascertain which original moons survive the encounter.

References

Agnor, Craig B. and Douglas P. Hamilton (May 2006). “Neptune’s capture of its moon Triton in a binary-planet gravitational encounter”. In: *Nature* 441.7090, pp. 192–194. DOI: 10.1038/nature04792.

Banfield, Don and Norm Murray (Oct. 1992). "A dynamical history of the inner Neptunian satellites". In: *Icarus* 99.2, pp. 390–401. DOI: 10.1016/0019-1035(92)90155-Z.

Beaugé, C., F. Roig, and D. Nesvorný (Aug. 2002). "Effects of Planetary Migration on Natural Satellites of the Outer Planets". In: *Icarus* 158.2, pp. 483–498. DOI: 10.1006/icar.2002.6888.

Belyakov, Matthew and Michael E. Brown (Apr. 2025). "Saturnian Irregular Satellites as a Probe of Kuiper Belt Surface Evolution". In: *The Planetary Science Journal* 6.4, 97, p. 97. DOI: 10.3847/PSJ/adc55d. arXiv: 2503.20046 [astro-ph.EP].

Belyakov, Matthew, M. Ryleigh Davis, et al. (2025). *Code for Nereid as a Regular Satellite of Neptune*. DOI: https://doi.org/10.22002/gf82m-rzz66.

Bottke, William F. et al. (Mar. 2010). "The Irregular Satellites: The Most Collisionally Evolved Populations in the Solar System". In: *AJ* 139.3, pp. 994–1014. DOI: 10.1088/0004-6256/139/3/994.

Brad Dalton, J., Dale P. Cruikshank, and Roger N. Clark (Aug. 2012). "Compositional analysis of Hyperion with the Cassini Visual and Infrared Mapping Spectrometer". In: *Icarus* 220.2, pp. 752–776. DOI: 10.1016/j.icarus.2012.05.003.

Brown, M. E., C. A. Trujillo, and D. L. Rabinowitz (Dec. 2005). "Discovery of a Planetary-sized Object in the Scattered Kuiper Belt". In: *The Astrophysical Journal* 635.1, pp. L97–L100. DOI: 10.1086/499336. arXiv: astro-ph/0508633 [astro-ph].

Brown, Michael E. and Wesley C. Fraser (July 2023). "The State of CO and CO_2 Ices in the Kuiper Belt as Seen by JWST". In: *PSJ* 4.7, 130, p. 130. DOI: 10.3847/PSJ/ace2ba. arXiv: 2306.17051 [astro-ph.EP].

Brown, Michael E., Christopher D. Koresko, and Geoffrey A. Blake (Dec. 1998). "Detection of Water Ice on Nereid". In: *ApJL* 508.2, pp. L175–L176. DOI: 10.1086/311741.

Brown, Michael E., Samantha K. Trumbo, et al. (July 2025). "A JWST Study of CO_2 on the Satellites of Saturn". In: *The Planetary Science Journal* 6.7, 180, p. 180. DOI: 10.3847/PSJ/ade807. arXiv: 2506.19921 [astro-ph.EP].

Brown, Robert H. et al. (June 1999). "NOTE: Water Ice on Nereid". In: *Icarus* 139.2, pp. 374–378. DOI: 10.1006/icar.1999.6109.

Buratti, Bonnie J., Joel A. Mosher, and Torrence V. Johnson (Oct. 1990). "Albedo and color maps of the Saturnian satellites". In: *Icarus* 87.2, pp. 339–357. DOI: 10.1016/0019-1035(90)90138-Y.

Charnoz, Sébastien, Julien Salmon, and Aurélien Crida (June 2010). "The recent formation of Saturn's moonlets from viscous spreading of the main rings". In: *Nature* 465.7299, pp. 752–754. DOI: 10.1038/nature09096.

Clark, R. N. (Nov. 1980). "Ganymede, Europa, Callisto, and Saturn's rings: Compositional analysis from reflectance spectroscopy". In: *Icarus* 44.2, pp. 388–409. DOI: 10.1016/0019-1035(80)90033-0.

Clark, Roger N., Robert H. Brown, et al. (Mar. 2019). "Isotopic ratios of Saturn's rings and satellites: Implications for the origin of water and Phoebe". In: *Icarus* 321, pp. 791–802. DOI: 10.1016/j.icarus.2018.11.029.

Clark, Roger N., Dale P. Cruikshank, et al. (Apr. 2012). "The surface composition of Iapetus: Mapping results from Cassini VIMS". In: *Icarus* 218.2, pp. 831–860. DOI: 10.1016/j.icarus.2012.01.008.

Croft, Steven K. (Oct. 1992). "Proteus: Geology, shape, and catastrophic destruction". In: *Icarus* 99.2, pp. 402–419. DOI: 10.1016/0019-1035(92)90156-2.

Ćuk, Matija and Brett J. Gladman (June 2005). "Constraints on the Orbital Evolution of Triton". In: *The Astrophysical Journal Letters* 626.2, pp. L113–L116. DOI: 10.1086/431743. arXiv: astro-ph/0505235 [astro-ph].

Fernandez, J. A. and W.-H. Ip (Apr. 1984). "Some dynamical aspects of the accretion of Uranus and Neptune: The exchange of orbital angular momentum with planetesimals". In: *Icarus* 58.1, pp. 109–120. DOI: 10.1016/0019-1035(84)90101-5.

Fraser, Wesley C. and Michael E. Brown (July 2018). "Phoebe: A Surface Dominated by Water". In: *AJ* 156.1, 23, p. 23. DOI: 10.3847/1538-3881/aac213. arXiv: 1803.04979 [astro-ph.EP].

Gaspar, H. S., O. C. Winter, and E. Vieira Neto (July 2013). "Irregular satellites of Jupiter: three-dimensional study of binary-asteroid captures". In: *Monthly Notices of the Royal Astronomical Society* 433.1, pp. 36–46. DOI: 10.1093/mnras/stt648.

Goldreich, P. et al. (Aug. 1989). "Neptune's Story". In: *Science* 245.4917, pp. 500–504. DOI: 10.1126/science.245.4917.500.

Graykowski, Ariel and David Jewitt (Apr. 2018). "Colors and Shapes of the Irregular Planetary Satellites". In: *AJ* 155.4, 184, p. 184. DOI: 10.3847/1538-3881/aab49b. arXiv: 1803.01907 [astro-ph.EP].

Hyodo, Ryuki et al. (Jan. 2017). "Ring formation around giant planets by tidal disruption of a single passing large Kuiper belt object". In: *Icarus* 282, pp. 195–213. DOI: 10.1016/j.icarus.2016.09.012. arXiv: 1609.02396 [astro-ph.EP].

Ida, Shigeru et al. (Mar. 2020). "Uranian satellite formation by evolution of a water vapour disk generated by a giant impact". In: *Nature Astronomy* 4, pp. 880–885. DOI: 10.1038/s41550-020-1049-8. arXiv: 2003.13582 [astro-ph.EP].

Izidoro, André et al. (July 2025). "Very-wide-orbit planets from dynamical instabilities during the stellar birth cluster phase". In: *Nature Astronomy* 9, pp. 982–994. DOI: 10.1038/s41550-025-02556-0. arXiv: 2505.24093 [astro-ph.EP].

Jewitt, David and Nader Haghighipour (Sept. 2007). "Irregular Satellites of the Planets: Products of Capture in the Early Solar System". In: *ARA&A* 45.1, pp. 261–295. DOI: 10.1146/annurev.astro.44.051905.092459. arXiv: astro-ph/0703059 [astro-ph].

Karkoschka, Erich (May 2001). “Comprehensive Photometry of the Rings and 16 Satellites of Uranus with the Hubble Space Telescope”. In: *Icarus* 151.1, pp. 51–68. DOI: 10.1006/icar.2001.6596.

Kenyon, Scott J. and Benjamin C. Bromley (Mar. 2012). “Coagulation Calculations of Icy Planet Formation at 15-150 AU: A Correlation between the Maximum Radius and the Slope of the Size Distribution for Trans-Neptunian Objects”. In: *The Astronomical Journal* 143.3, 63, p. 63. DOI: 10.1088/0004-6256/143/3/63. arXiv: 1201.4395 [astro-ph.SR].

Kiss, C. et al. (Apr. 2016). “Nereid from space: rotation, size and shape analysis from K2, Herschel and Spitzer observations”. In: *Monthly Notices of the Royal Astronomical Society* 457.3, pp. 2908–2917. DOI: 10.1093/mnras/stw081. arXiv: 1601.02395 [astro-ph.EP].

Kobayashi, Shiho et al. (Apr. 2012). “Ejection and Capture Dynamics in Restricted Three-body Encounters”. In: *The Astrophysical Journal* 748.2, 105, p. 105. DOI: 10.1088/0004-637X/748/2/105. arXiv: 1201.4794 [astro-ph.HE].

Kuiper, Gerald P. (Aug. 1949). “The Second Satellite of Neptune”. In: *Publications of the Astronomical Society of the Pacific* 61.361, p. 175. DOI: 10.1086/126166.

Kuiper, Gerard P. (Jan. 1956). “On the origin of the satellites and the Trojans”. In: *Vistas in Astronomy* 2.1, pp. 1631–1666. DOI: 10.1016/0083-6656(56)90090-3.

Li, Daohai and Apostolos A. Christou (Apr. 2020). “The Origin of Neptune’s Unusual Satellites from a Planetary Encounter”. In: *The Astronomical Journal* 159.4, 184, p. 184. DOI: 10.3847/1538-3881/ab7cd5. arXiv: 2004.02512 [astro-ph.EP].

Mastrapa, R. M. et al. (Aug. 2009). “Optical Constants of Amorphous and Crystalline H_2O-ice: 2.5-22 μm (4000-455 cm^{-1}) Optical Constants of H_2O-ice”. In: *ApJ* 701.2, pp. 1347–1356. DOI: 10.1088/0004-637X/701/2/1347.

(N.d.). Materials and methods are available as supplementary materials.

McKinnon, W. B. (Sept. 1984). “On the origin of Triton and Pluto”. In: *Nature* 311.5984, pp. 355–358. DOI: 10.1038/311355a0.

Morbidelli, Alessandro et al. (July 2009). “Considerations on the magnitude distributions of the Kuiper belt and of the Jupiter Trojans”. In: *Icarus* 202.1, pp. 310–315. DOI: 10.1016/j.icarus.2009.02.033.

Mousis, Olivier et al. (2025). “Triton and Pluto: Same Origin but Separated at Birth”. In: *Triton and Pluto*. 2514-3433. IOP Publishing, 1-1 to 1–17. ISBN: 978-0-7503-5618-3. DOI: 10.1088/2514-3433/ad5278ch1. URL: https://doi.org/10.1088/2514-3433/ad5278ch1.

Nesvorný, David, Jose L. A. Alvarellos, et al. (July 2003). “Orbital and Collisional Evolution of the Irregular Satellites”. In: *The Astronomical Journal* 126.1, pp. 398–429. DOI: 10.1086/375461.

Nesvorný, David and David Vokrouhlický (Oct. 2019). "Binary survival in the outer solar system". In: *Icarus* 331, pp. 49–61. DOI: 10.1016/j.icarus.2019.04.030. arXiv: 1905.02282 [astro-ph.EP].

Nesvorný, David, David Vokrouhlický, and Rogerio Deienno (Mar. 2014). "Capture of Irregular Satellites at Jupiter". In: *The Astrophysical Journal* 784.1, 22, p. 22. DOI: 10.1088/0004-637X/784/1/22. arXiv: 1401.0253 [astro-ph.EP].

Nesvorný, David, David Vokrouhlický, and Alessandro Morbidelli (May 2007a). "Capture of Irregular Satellites during Planetary Encounters". In: *AJ* 133.5, pp. 1962–1976. DOI: 10.1086/512850.

— (May 2007b). "Capture of Irregular Satellites during Planetary Encounters". In: *The Astronomical Journal* 133.5, pp. 1962–1976. DOI: 10.1086/512850.

Nogueira, E., R. Brasser, and R. Gomes (July 2011). "Reassessing the origin of Triton". In: *Icarus* 214.1, pp. 113–130. DOI: 10.1016/j.icarus.2011.05.003. arXiv: 1105.1179 [astro-ph.EP].

Petit, Jean-Marc et al. (Apr. 2023). "The Hot Main Kuiper Belt Size Distribution from OSSOS". In: *The Astrophysical Journal Letters* 947.1, L4, p. L4. DOI: 10.3847/2041-8213/acc525. arXiv: 2309.01530 [astro-ph.EP].

Philpott, Catherine M., Douglas P. Hamilton, and Craig B. Agnor (Aug. 2010). "Three-body capture of irregular satellites: Application to Jupiter". In: *Icarus* 208.2, pp. 824–836. DOI: 10.1016/j.icarus.2010.03.026. arXiv: 0911.1369 [astro-ph.EP].

Pinilla-Alonso, Noemí et al. (Feb. 2025). "A JWST/DiSCo-TNOs portrait of the primordial Solar System through its trans-Neptunian objects". In: *Nature Astronomy* 9, pp. 230–244. DOI: 10.1038/s41550-024-02433-2.

Porco, C. C. et al. (Feb. 2005). "Cassini Imaging Science: Initial Results on Phoebe and Iapetus". In: *Science* 307.5713, pp. 1237–1242. DOI: 10.1126/science.1107981.

Rein, H. and S. -F. Liu (Jan. 2012). "REBOUND: an open-source multi-purpose N-body code for collisional dynamics". In: *A&A* 537, A128, A128. DOI: 10.1051/0004-6361/201118085. arXiv: 1110.4876 [astro-ph.EP].

Rufu, Raluca and Robin M. Canup (Nov. 2017). "Triton's Evolution with a Primordial Neptunian Satellite System". In: *The Astronomical Journal* 154.5, 208, p. 208. DOI: 10.3847/1538-3881/aa9184. arXiv: 1711.01581 [astro-ph.EP].

Schlichting, Hilke E. and Re'em Sari (Feb. 2011). "Runaway Growth During Planet Formation: Explaining the Size Distribution of Large Kuiper Belt Objects". In: *The Astrophysical Journal* 728.1, 68, p. 68. DOI: 10.1088/0004-637X/728/1/68. arXiv: 1011.0201 [astro-ph.EP].

Sharkey, Benjamin N. L. et al. (Aug. 2021). "Complex Water-ice Mixtures on NII Nereid: Constraints from NIR Reflectance". In: *PSJ* 2.4, 143, p. 143. DOI: 10.3847/PSJ/ac0bbe. arXiv: 2106.12084 [astro-ph.EP].

Thomas, Peter, Joseph Veverka, and Paul Helfenstein (Oct. 1991). "Voyager observations of Nereid". In: *Journal of Geophysical Research* 96, pp. 19253–19259. DOI: 10.1029/91JA01735.

Tsiganis, K. et al. (May 2005). "Origin of the orbital architecture of the giant planets of the Solar System". In: *Nature* 435.7041, pp. 459–461. DOI: 10.1038/nature03539.

Tsui, K. H. (Mar. 2002). "Satellite capture in a four-body system". In: *Planet. Space Sci.* 50.3, pp. 269–276. DOI: 10.1016/S0032-0633(01)00131-3.

Wong, Ian (Sept. 2025). *jwstspec*. Version v0.6, DOI: 10.5281/zenodo.17186395. URL: https://doi.org/10.5281/zenodo.17186395.

Wong, Ian et al. (Apr. 2024). "JWST Near-infrared Spectroscopy of the Lucy Jupiter Trojan Flyby Targets: Evidence for OH Absorption, Aliphatic Organics, and CO_2". In: *PSJ* 5.4, 87, p. 87. DOI: 10.3847/PSJ/ad2fc3. arXiv: 2311.11531 [astro-ph.EP].

Chapter 7

THE VOLATILE INVENTORY OF 3I/ATLAS AS SEEN WITH JWST/MIRI

Belyakov, Matthew et al. (Apr. 2026). "The Volatile Inventory of 3I/ATLAS as Seen with JWST/MIRI". In: *The Astrophysical Journal* 1001.1, L11, p. L11. DOI: 10.3847/2041-8213/ae5700. arXiv: 2601.22034 [astro-ph.EP].

We present the first spectroscopic characterization of an interstellar object at mid-infrared wavelengths. Post-perihelion observations of 3I/ATLAS using the JWST/MIRI medium-resolution spectrometer were obtained on 2025 December 15–16 and 27 when the object was at heliocentric distances of 2.20 and 2.54 au, respectively. Our 5–28 μmspectra exhibit fluorescence features from several gaseous species, including the ν_2 band of H_2O at 5.8–7.0 μm, CO_2 around 15 μm, and a forbidden transition of atomic nickel at 7.507 μm. We also report the first direct detection of CH_4 in an interstellar object. Comparison of volatile production rates between the two epochs indicates a significant reduction in overall outgassing over 12 days, with H_2O activity dropping more steeply than other species. 3I continues to display extended H_2O production from icy grains in the coma, and has a strongly enhanced CO_2:H_2O mixing ratio relative to typical solar system comets.

7.1 Introduction

Interstellar objects (ISOs) are planetesimals that formed around other stars and were later ejected from their birth systems through dynamical interactions (for a review, see Fitzsimmons et al., 2024; Jewitt, 2024). During their brief transit through our Solar System, ISOs offer discrete glimpses into extrasolar small body populations and provide a valuable point of comparison for assessing commonalities and differences in planetesimal formation processes throughout the galaxy (e.g., Gibson et al., 2025).

The interstellar comet 3I/ATLAS (hereafter, 3I) is the third confirmed ISO after 1I/'Oumuamua and 2I/Borisov (Denneau et al., 2025), with an estimated nucleus cross-section diameter of 2.6 km (Hui et al., 2026). In contrast to 1I, which had an inactive appearance (Meech et al., 2017; B. T. Bolin et al., 2018), 3I exhibits a significant extended coma (e.g., Bryce T. Bolin, Belyakov, et al., 2025; Chandler et al., 2025; Santana-Ros et al., 2025; Seligman et al., 2025). Its photometric evolution indicates that its coma consists of large, hundred-micron-sized dust grains (Jewitt and Luu, 2025). Ground-based observations (Belyakov et al., 2025; de la Fuente Marcos et al., 2025; Kareta et al., 2025; Opitom et al., 2025; Yang et al., 2025) revealed that 3I is redder than 2I (Jewitt and Luu, 2019; Bryce T. Bolin, Carey M. Lisse, et al., 2020) or typical cometary nuclei (Lamy et al., 2004). Modeling of galactic dynamics suggests that 3I's excess velocity is consistent with a dynamical age ranging from 3 to 11 Gyr (Hopkins et al., 2025; Taylor and Seligman, 2025).

A concerted effort has been undertaken to characterize the chemical makeup of 3I's coma. Ground-based spectroscopy at visible wavelengths yielded detections of gas-phase cyanogen and atomic nickel (Hoogendam et al., 2025; Rahatgaonkar et al., 2025; Salazar Manzano et al., 2025), while radio observations by ALMA added methanol and hydrogen cyanide to the molecular inventory (Roth et al., 2025; Coulson et al., 2026). Pre-perihelion space-based observations in the near-infrared with JWST and SPHEREx uncovered fluorescence signatures from H_2O, CO_2, and CO (M. A. Cordiner et al., 2025; Carey M. Lisse et al., 2025). Post-perihelion SPHEREx measurements indicated a significant increase in CO production and the emergence of an additional emission feature at 3.2–3.4 μm likely due to organics (C. M. Lisse, Bach, et al., 2026). Further evidence of 3I's evolving activity includes a bluing visible color (Zhang and Battams, 2026) and the apparent asymmetry between its pre- vs. post-perihelion H_2O production trends (Tan, Yan, and Li, 2026).

In this Letter, we present the first results from our JWST program targeting 3I at mid-infrared wavelengths during its outbound trajectory. Observations with the medium-resolution spectrometer (MRS; Wells et al. 2015; Argyriou et al. 2023) of the Mid-Infrared Instrument (MIRI) were obtained as part of Cycle 4 Director's Discretionary Time Program #9442 (PI: M. Belyakov). In this work, we focus on characterizing the gas-phase component of 3I's coma through spectral modeling of the fluorescence bands and mapping of their spatial distribution.

7.2 JWST/MIRI Observations

The JWST/MIRI MRS instrument consists of four integral field units (IFUs) that operate simultaneously and cover different portions of the MIRI wavelength range (referred to as channels). Three separate grating settings—short (A), medium (B), and long (C)—are needed to construct an uninterrupted spectrum from 5 to 28 μm. Two sets of A/B/C observations requiring six visits in total were included in the observing program to produce two complete mid-infrared spectra of 3I. All observations were executed on 2025 December 15–16. However, two of the observations (1 and 5) suffered from guide star acquisition failures and were repeated on 2025 December 27 with slightly reduced integration times as Observations 13 and 15. Table 7.1 summarizes the exposure details and viewing geometries for the six successful JWST/MIRI MRS observations of 3I collected as part of Program #9442. The apparent magnitude and target distance information are provided for the midpoint

Table 7.1: JWST/MIRI Observational Details for 3I/ATLAS

Obs.	UT Midpoint Time	Grating	Exp. (s)	V (mag)	Δ (au)	r_h (au)	α (deg)
2	2025 Dec 15 17:22:40	medium (B)	833	15.31	1.800	2.189	26.68
3	2025 Dec 15 12:49:14	long (C)	833	15.30	1.801	2.181	26.83
4	2025 Dec 16 00:49:25	short (A)	833	15.31	1.800	2.195	26.56
6	2025 Dec 16 06:22:11	long (C)	833	15.32	1.799	2.202	26.43
13	2025 Dec 27 11:20:29	short (A)	777	15.62	1.824	2.530	18.75
15	2025 Dec 27 20:20:30	medium (B)	777	15.63	1.826	2.541	18.46

The reported exposure time is the sum across the four dithered exposures. V, Δ, r_h, and α are the apparent V-band brightness, distance from JWST, heliocentric distance, and phase angle at the midpoint of the observation (JPL Horizons).

time of each set of dithered exposures.

Data reduction and spectral extraction were performed following standard procedures using the publicly-available JWST data analysis tool `jwstspec` (v0.9; Wong, 2025). This data processing framework has previously been applied to numerous JWST observations of small bodies, and detailed descriptions of the pipeline's functionality can be found in several published works (e.g., Rivkin et al., 2023; Emery et al., 2024; Wong et al., 2024). First, the uncalibrated stacks of nondestructive detector reads were downloaded from the Mikulski Archive for Space Telescopes and passed through all three stages of the official JWST calibration pipeline to produce dark-corrected, flat-fielded, flux-calibrated, spatially-rectified, background-subtracted, and dither-combined data cubes. Fully calibrated data cubes were also generated for each dithered exposure to aid in outlier removal and vet the various molecular signatures detected in the spectra. The pipeline products analyzed in this work were generated using Version 1.20.2 of the JWST calibration pipeline (Bushouse et al., 2025), with requisite reference files drawn from context `jwst_1471.pmap` of the JWST Calibration Reference Data System.

Several custom settings that are not part of the default processing workflow were applied to optimize performance: (1) the cosmic ray detection threshold in the `jump` step in Stage 1 of the calibration pipeline was raised to 10σ to prevent spurious flagging of points in light of the intrinsically variable nature of 3I and possible imperfect non-sidereal tracking of the object during each exposure due to ephemeris uncertainties; (2) the `clean_showers` routine was activated as part of the `straylight` step in Stage 2, which has been shown to greatly mitigate the dispersed flux (so-called showers) that arise from large cosmic ray impacts (Regan, 2024); (3) the `residual_fringe` step was performed in Stage 2 to improve the defringing of the flux-calibrated detector images prior to cube building; (4) the `outlier_detection` step was skipped in Stage 3 to prevent erroneous pixel masking during the dither combination process that can often occur with variable moving object targets.

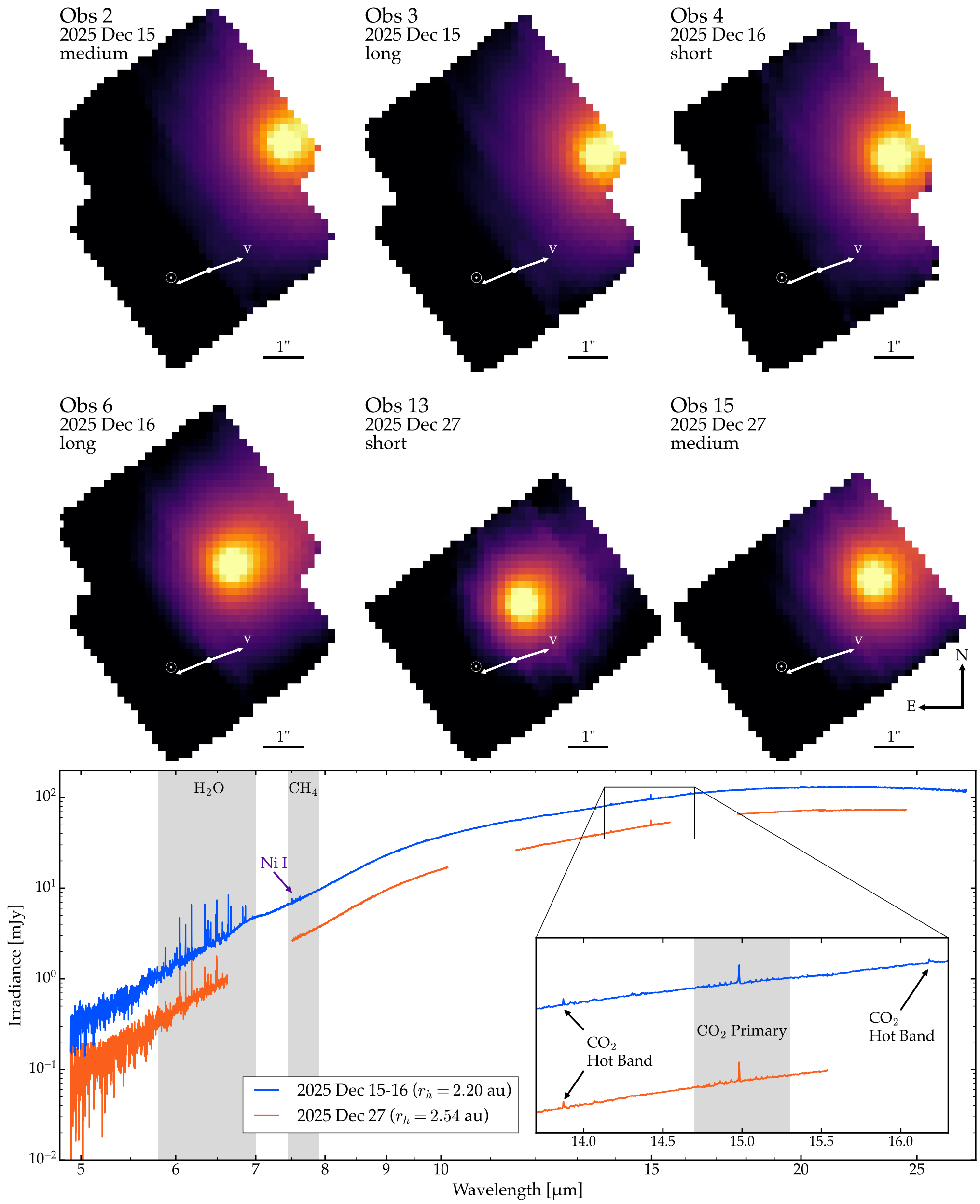

Figure 7.1: *Top panels*: Median-stacked images derived from the fully calibrated Channel 2 data cubes for the six successful JWST/MIRI observations of 3I. A logarithmic stretch has been applied to accentuate the extended coma. The sunward and target velocity directions are indicated. The panels are labeled with the corresponding date and spectral grating setting. The first three observations suffered from poor pointing due to uncertain ephemeris. Some striping persists due to numerical artifacts from the IFU data cube building process.

Bottom panel: Spectra of 3I extracted using a 1″-diameter circular aperture. Obs. 2, 4, and 6 (blue) are combined into a single spectrum by normalizing individual segments to align at overlapping wavelengths. The main H_2O, CO_2, CH_4, and Ni fluorescence features are marked. The inset panel provides a zoomed-in view of the CO_2 primary and hot bands.

Next, the target centroid was determined by median-averaging the data cube along the wavelength axis and fitting a 2D Gaussian to the flux values within a 5×5 cutout region centered on the brightest pixel in the field of view. Spectra were extracted using various circular and annular apertures centered on the centroid position, with the sizes and extents chosen to avoid optically-thick regions. The angular sizes were converted to pixel units using the corresponding pixel scale of each channel: $0.13''$ in Channel 1, $0.17''$ in Channel 2, $0.20''$ in Channel 3, and $0.35''$ in Channel 4.

The `jwstspec` tool enables the user to customize the level of outlier rejection in the data cubes prior to spectral extraction. Each pixel flux array within the spectral extraction region is smoothed using a cubic spline fit, and points that exceed a certain multiple of the flux uncertainty σ relative to the spline model are masked as outliers. Given the presence of narrow, large-amplitude emission features in the spectrum of 3I, the outlier rejection threshold was set to a very high value (100σ) to prevent unintentional removal of fluorescence peaks. Likewise, the post-extraction spectral outlier removal threshold, which is applied to a 21-pixel-wide moving median filter, was also set to 100σ to ensure that only extreme non-astrophysical outlier points were excluded.

Remaining outliers in the extracted spectra were manually trimmed in `jwstspec` through careful comparisons with coma fluorescence models (see section 7.3). PSG model spectra were generated for all common cometary volatile species with major emission bands in the mid-infrared, including H_2O, CO_2, and various aliphatic organic species (e.g., CH_4, C_2H_6). After identifying the locations of the molecular fluorescence lines, visible outliers were excised across the wavelength regions where no astrophysical spectral features are expected to occur. Lastly, as a final defringing step, the `ifu_rfcorr` routine contained within the `extract_1d` step of the JWST calibration pipeline was run on the outlier-removed spectra to fit and remove remaining periodic flux variations.

For the reanalysis of the UT 2025 August 6 JWST/NIRSpec IFU observations of 3I from Program #5094 (PI: M. Cordiner), the data processing workflow was largely identical to the one described above. The on-target exposures (Observation 1) were paired with a set of dedicated background exposures (Observation 2), and pixel-by-pixel background subtraction was carried out as part of Stage 2 of the calibration pipeline. Unlike MIRI, the NIRSpec detectors do not exhibit discernible fringing. Instead, readnoise artifacts, which manifest as vertical striping in the raw detector images, are present and were removed by activating the `nsclean` step during the pipeline processing. A 3-pixel-radius ($0.6''$ diameter) circular aperture was used to extract the spectrum.

7.3 Spectral Modeling

The PSG (G. L. Villanueva, Smith, et al., 2018) was used to retrieve the abundances (parametrized as either nuclear production rate or local column density) and rotational temperatures of the volatile molecular species in 3I's coma. The retrieval tool includes a Monte Carlo sampler to calculate the posterior distributions and corresponding 1σ uncertainties for all parameters, which are scaled to ensure a reduced χ^2 value of unity for the best-fit model. To generate the synthetic spectra, the PSG implements the Cometary Emission Model (Geronimo Luis Villanueva et al., 2022), which accounts for the expansion and evolution of gas molecules through the coma, relevant photodissociation lifetimes, and fluorescence pumping rates within a fully non-LTE (non-local thermal equilibrium) framework. The line lists for all modeled species were drawn from the GSFC Fluorescence Database (e.g., G. L. Villanueva, Mumma, et al., 2011). The coma expansion velocity at each epoch was set according to the scaling law of Ootsubo et al. (2012): $v = 0.8/\sqrt{r_h}$ km s^{-1}. The fluorescence modeling tool flagged instances where the optical depth within the modeled region exceeds $\tau = 0.1$, and those pixels were excluded from further analysis.

The viewing geometry (heliocentric distance, observer distance, phase angle) at the midpoint of each observation was queried from JPL Horizons. By default, the wavelength solution contained within the JWST/MIRI data cubes is adjusted to match the target's stationary frame, and so the radial velocity relative to the observer was set to zero. Imperfections in the wavelength calibration were addressed by allowing for small shifts to the wavelength grid in order to align the model spectra with the observed emission lines. The required shifts were less than 1–2 nm in all cases—comparable to or smaller than the spectral resolution element of the MRS gratings. The synthetic spectra were downsampled to match the local spectral resolution of the modeled data using a Gaussian convolution kernel with a full-width half-maximum (FWHM) scale set by the empirical laws of Pontoppidan et al. (2024) and Banzatti et al. (2025). In the case of the primary CO_2 band at 15 μm, the calculated FWHM of 0.0052 μm was found to be too large, resulting in a significant mismatch between the observed and modeled line shape of the Q-branch transition. A FWHM of 0.0045 μm provided a much better fit to the line profile.

As part of the fluorescence analysis of the JWST/MIRI observations, PSG retrievals were carried out on both aperture-extracted spectra and individual pixel spectra. To prepare the data for the retrievals, the spectra were trimmed to the fluorescence band regions and continuum-subtracted following a two-step process. First, a crude continuum removal was carried out by fitting a cubic polynomial to the aperture-extracted spectra. A preliminary set of retrieval runs was carried out on these spectra, and the corresponding best-fit coma fluorescence models were used to identify the locations of emission lines: all wavelengths with modeled emission amplitudes that exceed a certain fraction of the maximum value within a given band were masked. The masking threshold was set individually for different molecules and observations, pursuant to the characteristic line amplitude distribution and signal-to-noise ratio of the data. For H_2O, a threshold of 0.2% was applied to Observations 2 and 6, while a higher cutoff of 0.5% was used for the noisier Observation 15 spectrum. For CO_2 and CH_4, a limit of 1% was imposed across all observations.

The second, more refined continuum removal step involved an error-weighted cubic spline fit to the masked spectra. The `scipy.interpolate.UnivariateSpline` function includes a smoothing threshold $s = \chi^2$ that controls the performance of the spline fitting. For each modeled fluorescence band, s was adjusted via visual inspection to ensure that the continuum model adequately captures the large-scale modulations in flux without overfitting the point-to-point jitter. The optimal s values ranged from $2n$ to $5n$, where n is the number of continuum data points within the modeled spectral segment. The spline model was subtracted from the unmasked data to yield the continuum-corrected spectra shown in Figure 7.4. Figure 7.2 provides an illustrative example of the continuum modeling for the CO_2 primary band detected in the first epoch (Observation 2).

Due to the lower spectral resolution of the JWST/NIRSpec PRISM observations, with individual fluorescence lines fully blended, the continuum removal procedure was much simpler. The extracted spectrum was trimmed to 3.15–3.45 µm and the region containing the aliphatic emission features (3.25–3.40 µm) were masked prior to continuum modeling with a cubic spline; the smoothing threshold was set to $1.5n$. No wavelength shift was allowed when running the PSG retrievals on the NIRSpec spectrum.

7.4 Azimuthal Profiles

To quantify the spatial behavior of 3I's coma, azimuthal profiles of H_2O and CO_2 were obtained from Observations 6 and 15, respectively. For comparison, a dust profile was derived from the local continuum wavelengths within the CO_2 primary band in Observation 15. The profiles were computed from an annular aperture centered on the target centroid spanning radii from $0.8''$ to $1.5''$. This aperture was chosen to exclude both optically-thick pixels near the nucleus and regions outside of the combined field of view. The annulus was divided into 15°-wide sectors to produce the azimuthal profiles, which were then normalized to unity at their maximum values. The measured H_2O, CO_2, and dust continuum azimuthal profiles are shown in Figure 7.3. All three profiles are visibly asymmetric in the near-nucleus region, with the strongest emission roughly aligned with the anti-sunward direction. The H_2O and CO_2 profiles exhibit a slightly more muted asymmetry than the dust continuum.

To improve spatial sampling of the coma and guard against cosmic-ray and other detector

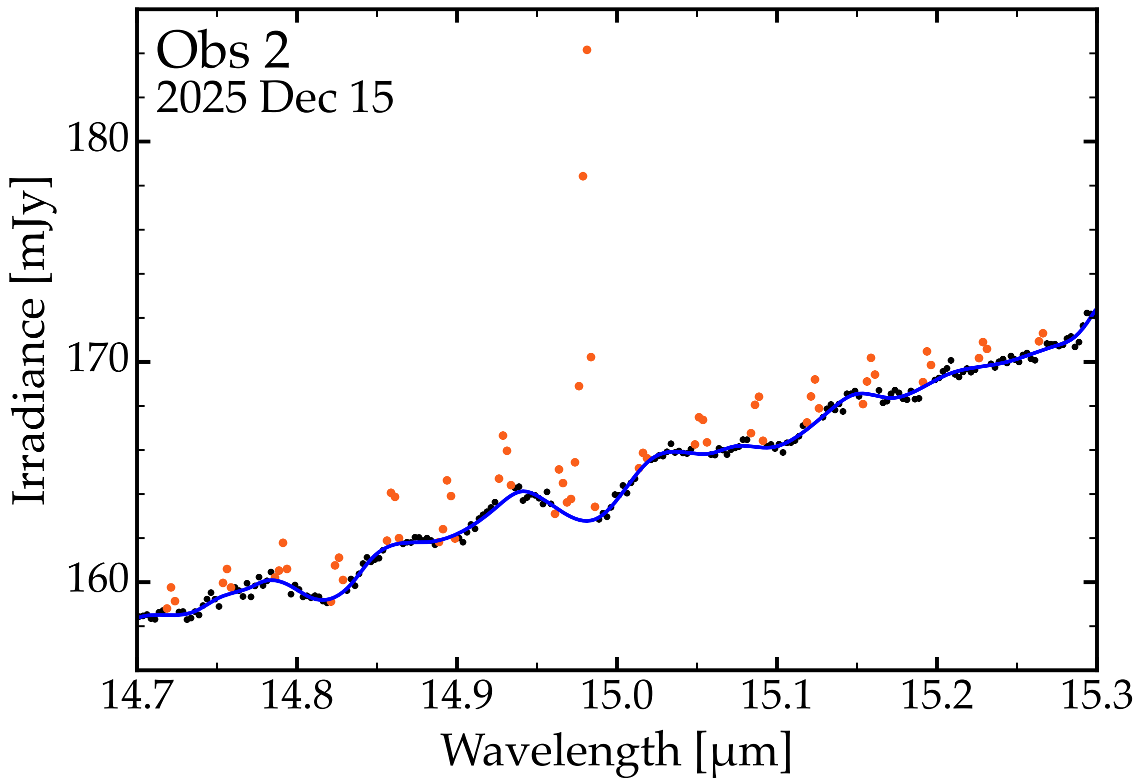

Figure 7.2: An example of the continuum modeling procedure applied to prepare the extracted JWST/MIRI spectra for retrieval analysis. The data points are the irradiance spectrum in sub-band 3B obtained from Observation 2 using a 2–3″ annular aperture. The orange points, which denote the wavelengths that contain CO_2 fluorescence emission, were masked prior to continuum modeling. The blue curve is the cubic spline fit to the continuum wavelengths, with the smoothing threshold set to $2.5n$, where n is the number of continuum data points. See text for more details.

artifacts, each 3I observation consisted of four dithered exposures. Observations of a nearby empty background field were acquired immediately following each on-target observation. To avoid possible contamination from 3I's extended coma, the background field was placed 5′ away from the target along a vector perpendicular to the sunward direction. The background observations employed a two-point dither pattern to optimize observing time usage, with the same per-dither integration time as the corresponding on-target observations.

Due to the relatively uncertain orbital ephemeris of 3I at the time, the initial set of observations used a wide dither pattern to maximize on-sky coverage. Subsequent astrometry reduced the uncertainty ellipse, and the rescheduled observations on 2025 December 27 used a smaller dither pattern designed for extended objects.

The uncalibrated data were processed using the `jwstspec` tool (Wong, 2025) to produce fully calibrated, background-subtracted, and dither-combined data cubes. Figure 7.1 shows

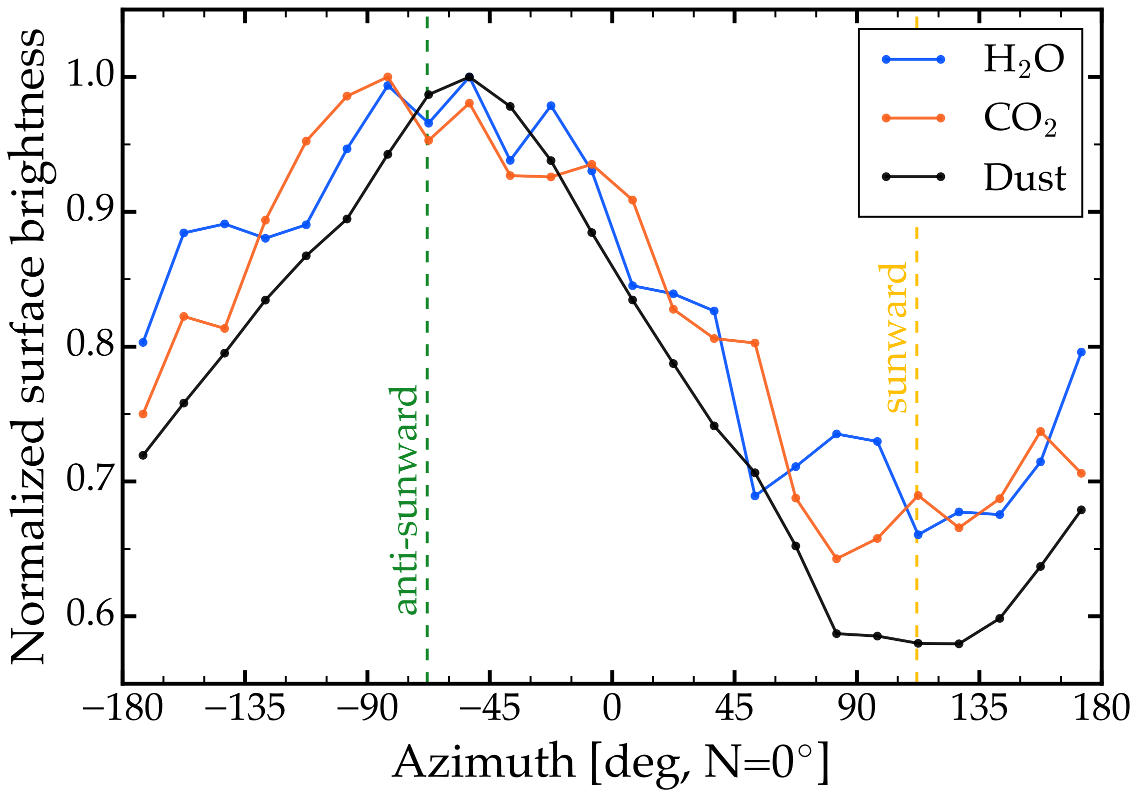

Figure 7.3: Azimuthal profiles of H_2O (blue) and CO_2 (orange) at 0.8″ − −1.5” from the optocenter, derived from Observations 6 and 15. The profile of the local dust continuum within the CO_2 primary band is also shown. The azimuth increases eastward with north at 0°. The sunward and anti-sunward directions are indicated by the yellow and green vertical dashed lines, respectively.

the wavelength-collapsed Channel 2 data cubes for the six successful observations of 3I. The target was situated close to the edge of the composite field of view in the first three observations. The off-center pointing proved to be problematic for Observation 3, where edge effects introduced significant correlated noise into the measured spectrum; as such, that observation was excluded from the analysis. The coma of 3I extends far beyond the spatial coverage of the MRS observations (C. M. Lisse, Bach, et al., 2026). In these close-in views of the near-nucleus region, the dust continuum follows a mostly isotropic spatial distribution, with a slight bias towards the anti-sunward direction, similar to the anti-solar coma direction of 2I/Borisov (Bryce T. Bolin and Carey M. Lisse, 2020; Kim et al., 2020). The extent of the coma's azimuthal asymmetry is quantified in section 7.4. Upon close inspection, some diagonal striping is evident in the images, which can be attributed to low-level numerical artifacts from the pixel resampling, dither combination, and spatial rectification processes required to construct the full IFU data cubes.

The bottom panel of Figure 7.1 shows the combined spectra of 3I from the two observing epochs: 2025 December 15–16 (blue; Observations 2, 4, 6) and 2025 December 27 (orange; Observations 13, 15). For these spectra, a fixed 1″-diameter circular aperture centered on the target's centroid position was chosen to ensure that the extraction region was fully within the field of view across all observations. Adjacent spectral segments from different observations showed small flux offsets, which may stem from short-term variability in the brightness and activity level of the target. To produce a continuous spectrum, each individual segment was rescaled to align the flux levels within the overlapping wavelength regions. The systematic difference in flux level between the two epochs reflects the rapid dimming of 3I during its outbound trajectory. Based on the change in heliocentric and geocentric distance between the two observing epochs, the thermal flux of 3I is expected to have fallen by ∼40%, which roughly matches the average decrease in the 8–25 μm irradiance between the spectra from the two epochs shown in Figure 7.1.

7.5 Fluorescence Modeling

The JWST/MIRI spectra of 3I reveal a rich collection of emission features from gas fluorescence within the coma. The Mid-infrared ro-vibrational bands of H_2O, CO_2, and CH_4, as well as the ground-state forbidden transition of monovalent atomic nickel (Ni I) can be seen above the thermal continuum (Figure 7.1). For each volatile species, gas production rates Q and rotational temperatures T_{rot} were derived from retrieval fits to continuum-subtracted spectra using the Planetary Spectrum Generator (PSG; G. L. Villanueva, Smith, et al. 2018; Geronimo Luis Villanueva et al. 2022). Model spectra were generated according to the aperture size, viewing geometry, and target ephemeris at the midpoint time of the observations. A full description of the continuum removal and spectral retrieval methodology is provided in section 7.3.

For each molecule, the first step in the analysis was a pixel-by-pixel retrieval of the column density (in units of m^{-2}) to check for regions with elevated optical depths ($\tau > 0.1$). Although PSG provides a first-order adjustment to the modeled fluorescence lines in such cases, this correction has only been benchmarked for small phase angles, while the JWST/MIRI observations were obtained at $\alpha > 18°$. In order to ensure that the reported Q and T_{rot} values are reliable, optically-thick regions near the nucleus were excluded from the analysis by using an annulus centered on the nucleus rather than a circular aperture.

The measured production rate depends on the assumed coma expansion velocity. For all models presented in this Letter, the expansion velocities were fixed to the values calculated from the scaling law of Ootsubo et al. (2012), which gives $v \sim 540$ and 500 m s^{-1} for the two JWST/MIRI observing epochs, respectively. Pre-perihelion observations of 3I at similar heliocentric distances provided direct measurements of the expansion velocity, with values ranging widely from 240 to 510 m s^{-1}(Roth et al., 2025; Coulson et al., 2026). Given that the production rate scales linearly with the expansion velocity, the roughly factor of two uncertainty in the expansion velocity at the time of the JWST/MIRI observations needs to be considered when interpreting the reported production rates. It is important to note, however, that the measured abundance ratios between the various gaseous molecular species are not affected by the assumed expansion velocity.

7.5.1 Water

The mid-infrared contains prominent emission lines between 5.8 and 7.0 μm from the ν_2 vibrational band of gas-phase H_2O. The ν_2 manifold of H_2O spans the transition region between grating/channel settings 1B and 1C, which were sampled by Observations 2 and 6 on 2025 December 15–16; only the medium grating was used on 2025 December 27 (Observation 15). From the pixel-by-pixel analysis of Observations 2 and 6, optical depths of $\tau > 0.1$ were measured throughout the innermost 1.0″–1.5″ circular region around the nucleus; in contrast, during the second epoch, the H_2O coma was optically thin throughout the field of view. Previous near-infrared observations found significant extended production of H_2O in the coma (e.g., M. A. Cordiner et al., 2025; C. M. Lisse, Bach, et al., 2026). To obtain estimates of the effective H_2O production rate that more closely approximate the total production, while simultaneously avoiding optical depth effects in the immediate near-nucleus region, an annular spectral extraction aperture spanning a 2–3″ diameter was selected. This aperture was not applicable to Observation 2, given that the target was close to the edge of the field of view; as such, the corresponding spectrum was excluded from the H_2O fluorescence analysis. The continuum-removed spectra in the H_2O fluorescence region from Observations 6 and 15 are shown in the top panels of Figure 7.4. More than 15 distinct emission peaks are clearly discernible above the noise level in the data.

At the spectral resolution of the MRS ($R \sim 3000$), the ro-vibrational lines of the ortho and para nuclear-spin isomers are easily distinguishable, with the two isomers distinguished in blue and green respectively in Figure 7.4. PSG provides separate molecular line lists for ortho- and para-H_2O, enabling direct measurement of the ortho-to-para ratio (OPR). As part of the pixel-by-pixel analysis, OPR values were obtained across the central region of the H_2O coma and were consistent with the equilibrium value of 3 when accounting for both measurement uncertainties and uncertainties stemming from the continuum removal process. When retrieving the overall H_2O production rates from the annulus-extracted spectra, the OPR was fixed to 3.

For Observation 6, the measured H_2O production rate was $Q_{H_2O} = (3.78 \pm 0.03) \times 10^{27}$ s^{-1},

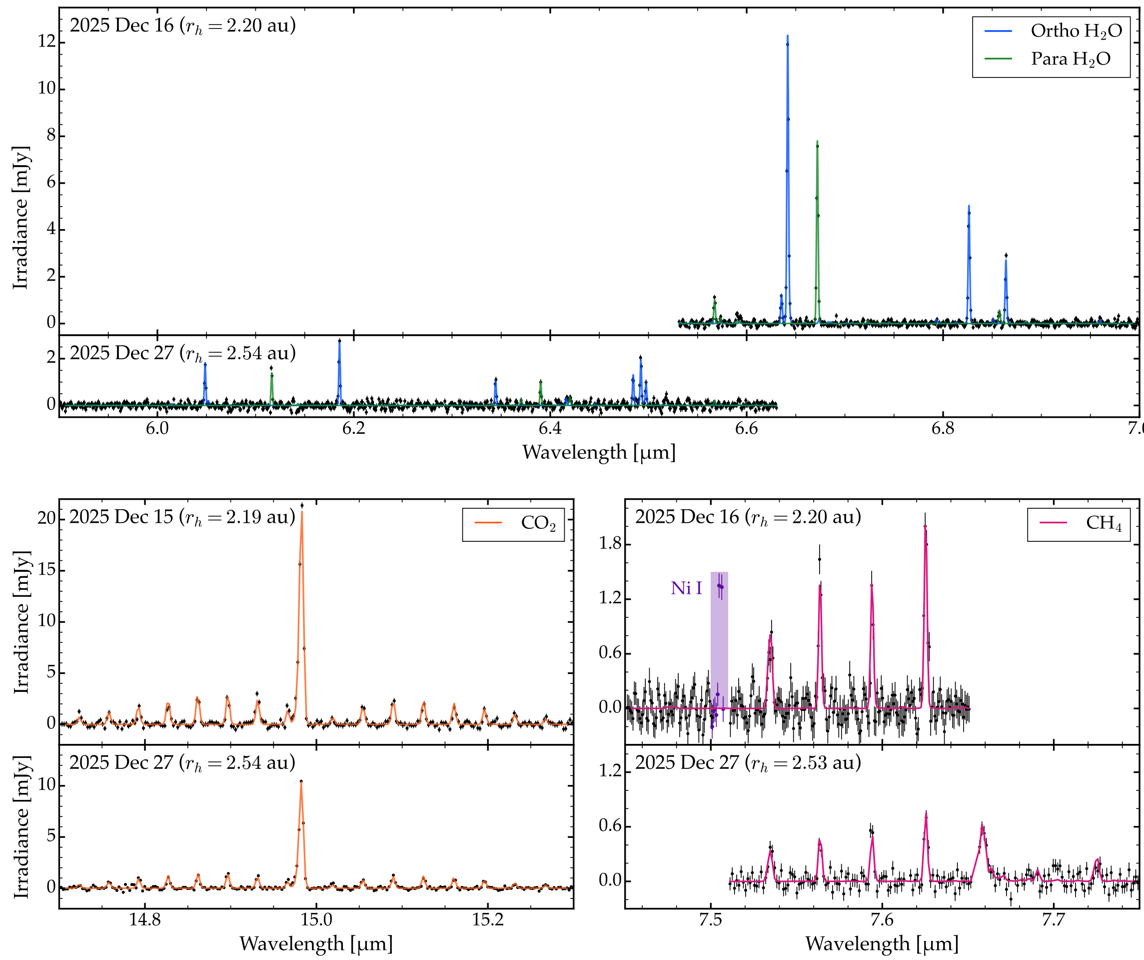

Figure 7.4: Top panels: continuum-subtracted JWST/MIRI spectra of 3I in the ν_2 band of H_2O from both epochs, with the best-fit PSG coma fluorescence models overlaid. For the H_2O and CO_2 analyses, spectra were extracted using a 2–3″ annular aperture to avoid optically-thick regions, while for CH_4, a circular 3″-diameter aperture was applied. The plotted error bars are based on the measured uncertainties from the spectral extractions and have been scaled to yield a reduced χ^2 of unity for the best-fit models. The contributions from ortho- and para-H_2O are shown separately in blue and green, respectively. The line intensities are significantly lower in the second epoch, corresponding to a sizable decrease in H_2O production. Bottom left panels: analogous fits to the ν_2 band of CO_2. Bottom right panels: CH_4 fluorescence model and data. The emission feature highlighted in purple at 7.5066 μm is from the ground-state forbidden transition of Ni I. To illustrate the systematic decrease in production between the two epochs, the vertical scale is identical within each set of panels.

with a rotational temperature of $T_{\rm rot} = 16.9 \pm 0.3$ K. A significant reduction in H_2O production is evident in the second epoch (Observation 15). The PSG retrievals yielded $Q_{H_2O} = (1.05 \pm 0.02) \times 10^{27}$ s^{-1}and $T_{\rm rot} = 10 \pm 1$ K. The best-fit coma fluorescence models are shown in Figure 7.4; the ortho- and para-H_2O contributions are plotted in different colors. The models provide an excellent match to the fluorescence peak amplitude distribution across the ν_2 manifold in both observing epochs.

Figure 7.5 shows the spatial distribution of H_2O abundance in 3I's coma for Observation 6, which produced the strongest detection of the molecule. The H_2O coma is mostly isotropic, with a discernible extension in the anti-sunward direction relative to the target centroid. The full azimuthal profile of the H_2O coma is shown in Figure 7.3. To facilitate examination of the relative extents of the dust and H_2O emission, the H_2O coma map is plotted alongside the continuum emission distribution within the H_2O fluorescence region. It is clear that the H_2O emission shows a significantly broader radial distribution than the dust, indicating that sublimation of H_2O ice from icy grains lofted into the coma by 3I's activity contributes significantly to the total gas-phase H_2O production (e.g., M. A. Cordiner et al., 2025; Tan, Yan, and Li, 2026).

7.5.2 Carbon Dioxide

JWST and SPHEREx observations of 3I have established CO_2 as the primary driver of its activity (M. A. Cordiner et al., 2025; Carey M. Lisse et al., 2025), explaining the reported onset of outgassing at distances beyond $r_h = 6$ au (Feinstein, Noonan, and Seligman, 2025; Martinez-Palomera et al., 2025). The new JWST/MIRI spectra present robust detections of the primary ν_2 bending mode of CO_2 centered at 15 μm, along with the associated hot bands near 13.89 and 16.18 μm (Figure 7.4). The continuum-subtracted spectra in the CO_2 primary band region, which were captured with the medium grating setting in Observations 2 and 15, are plotted in the bottom left panels of Figure 7.4. The central Q-branch peak at 14.98 μm is flanked by several lines from the ro-vibrational P- and R-branches. These spectra were extracted from the same 2–3″ diameter annular aperture that was used for H_2O fluorescence modeling. The pixel-by-pixel examination revealed optical depths above 0.1 throughout the innermost 2″-diameter region, rising as high as $\tau \sim 0.5$ at the centroid pixel.

Retrievals in the primary CO_2 band at 14.7–15.3 μm yielded $Q_{CO_2} = (8.70 \pm 0.09) \times 10^{27}$ s^{-1}and $T_{\rm rot} = 46 \pm 1$ K for the 2025 December 15 observation, and $Q_{CO_2} = (5.42 \pm 0.06) \times 10^{27}$ s^{-1}and $T_{\rm rot} = 49 \pm 1$ K on 2025 December 27. The measured $T_{\rm rot}$ values are consistent across the two epochs, while being significantly lower than the reported $T_{\rm rot}$ of ~90 K obtained from the previously published analysis of JWST/NIRSpec PRISM observations (M. A. Cordiner et al., 2025). At the low spectral resolution ($R \sim 100$) of

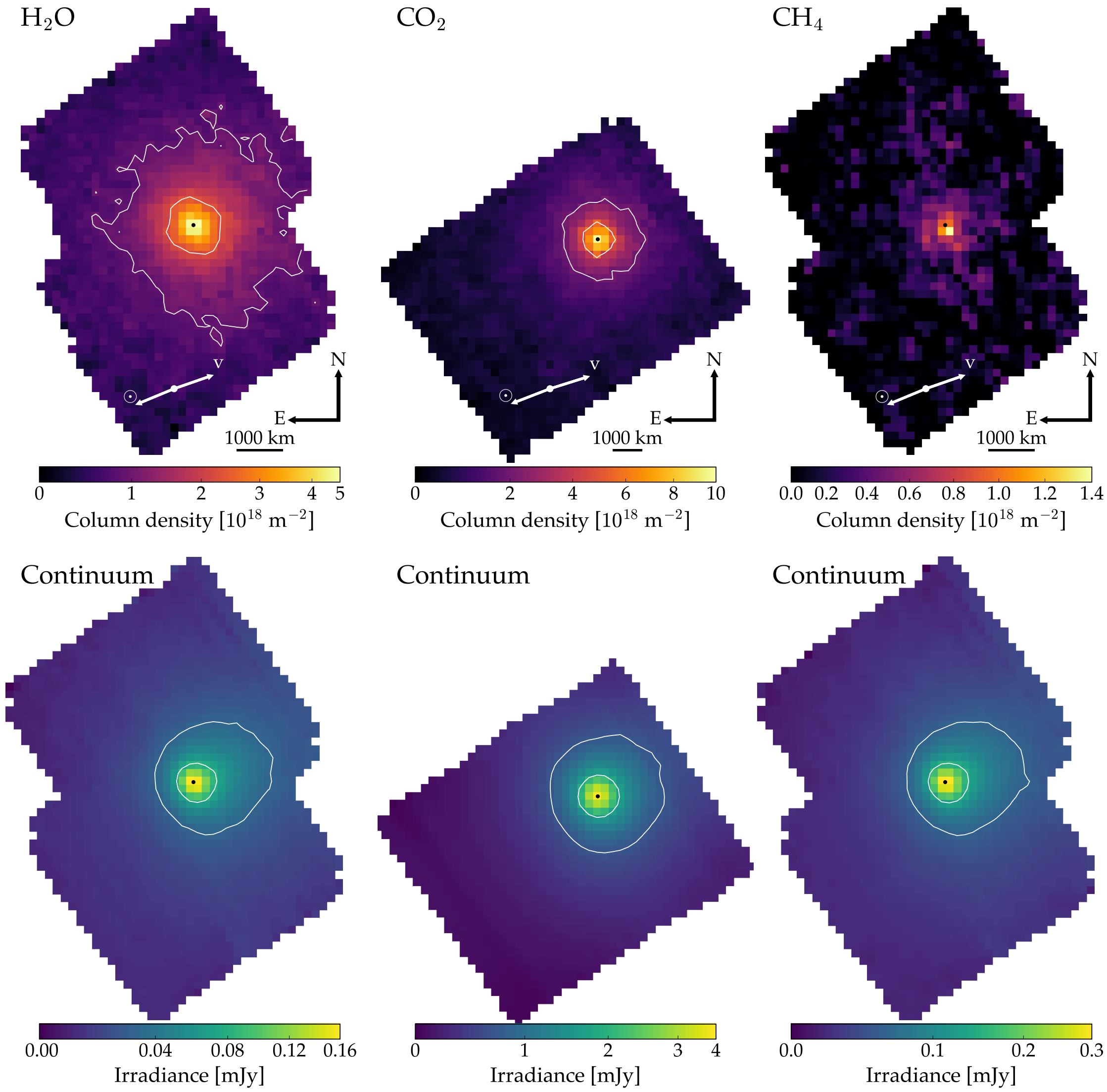

Figure 7.5: Top row: coma maps of H_2O, CO_2, and CH_4, computed as the molecular column density from a pixel-by-pixel retrieval analysis for Observations 6, 15, and 6, respectively. The sunward and target velocity directions are denoted by the white arrows. The target centroids, computed as the photocenter in the median-stacked images (Figure 7.1), are marked with the black points. For H_2O and CO_2, the white contours correspond to emission levels of 50% and 20% relative to the maximum value and illustrate the slight anti-sunward extension of the respective comae. The contours are omitted in the CH_4 panel due to the poorer signal-to-noise ratio of the data. Bottom row: corresponding median-stacked images across the continuum wavelengths within each fluorescence region. The H_2O coma map shows significant enhancement in emission level at large nucleocentric distances relative to the dust continuum, indicating extended H_2O production within the coma.

the JWST/NIRSpec PRISM spectrum, the individual transition lines within the P- and R-branches of the ν_3 asymmetric stretch band at ~4.3 μm are fully blended and cannot be isolated from the underlying continuum. The possible presence of an underlying CO_2 ice absorption band can greatly affect the continuum modeling across the fluorescence feature. Such an absorption band, if unaccounted for in the continuum subtraction, would artificially depress the band profile near the central Q-branch line, effectively broadening the distribution of emission strength across the P- and R-branches and yielding a positive bias in the T_{rot} estimate. Follow-up JWST/NIRSpec observations of 3I (Program #5094, PI: M. Cordiner) using a higher-resolution grating setting (G395H; $R \sim 2700$) were collected in 2025 December and will provide a more robust estimate of T_{rot} based on the ν_3 band.

While the hot bands of CO_2 have not been previously reported in the literature on comets, they have been detected in recent observations of gas-rich protoplanetary disks with the JWST/MIRI MRS. Modeling of the ν_2 CO_2 manifold observed in GW Lup by Grant et al., 2023 demonstrated that detailed radiative transfer modeling within an optically thick regime is necessary to self-consistently reproduce the amplitudes of the primary and hot bands. Currently, there is no model available for CO_2 that combines cometary non-LTE radiative transfer processes as presented in the PSG with optically-thick radiative transfer modeling for the near-nucleus region. In the context of 3I, the presence of hot bands suggests that collisionally-induced pumping of high-energy ro-vibrational levels may be occurring in the dense innermost region of the CO_2 coma, given that fluorescence modeling with PSG is unable to simultaneously provide a satisfactory fit to the primary and hot CO_2 bands.

The CO_2 column density map measured from the second epoch (Observation 15) is plotted in Figure 7.5. It is evident that CO_2 exhibits a much more compact coma than H_2O in the near-nucleus region. The radial profile of 3I at the CO_2 fluorescence wavelengths is slightly more compact than the dust across the full range of sampled nucleocentric distances, obviating the need to invoke a significant extended source within the coma. This dependence is in line with the findings of M. A. Cordiner et al. (2025). From the 2025 August SPHEREx observations (Carey M. Lisse et al., 2025), which probed regions far from the nucleus where optical depth is not a concern, the CO_2 coma is apparent at much farther distances (~3′) than the H_2O coma (~0.5′) due to the higher signal-to-noise ratio of the detected CO_2 feature, but follows a radial dependence that is steeper than the dust continuum's $1/\rho$ profile. As in the case of H_2O, the CO_2 coma shows a slight azimuthal asymmetry with higher abundance in the anti-sunward direction, though neither is as asymmetric as the dust, as shown in Figure 7.3.

7.5.3 Methane

Four fluorescence peaks of the ν_4 triply degenerate bending mode of CH_4 are evident between 7.50 and 7.65 μm in both the sub-band 1C and 2A spectra obtained in Observations 6 and 13, respectively (see the bottom right panels of Figure 7.4). This constitutes the first reported direct detection of CH_4 on any ISO. Near-infrared spectrophotometry of 3I collected by the SPHEREx spacecraft in 2025 December revealed a broad emission signature at 3.2–3.6 μm (C. M. Lisse, Bach, et al., 2026)—a range that contains the ν_1 symmetric stretching band of CH_4. However, SPHEREx lacks the requisite spectral resolving power to identify the specific hydrocarbon producing the spectral feature, as several other major cometary volatiles have fluorescence bands in that region (e.g., methanol, ethane, formaldehyde, and polycyclic aromatic hydrocarbons).

The pixel-by-pixel modeling analysis revealed that 3I's CH_4 coma is optically thin across the field of view. A 3″-diameter circular aperture was used to extract the spectra plotted in Figure 7.4 and estimate the CH_4 production rate and rotational temperature. The PSG retrievals yielded $Q_{CH_4} = (4.2 \pm 0.2) \times 10^{26}$ s^{-1}and $T_{rot} = 37 \pm 2$ K for the first epoch. By the time of the second epoch, CH_4 production had fallen by almost 50%, while the rotational temperature remained unchanged, following the same general trends seen for CO_2: $Q_{CH_4} = (2.3 \pm 0.1) \times 10^{26}$ s^{-1}and $T_{rot} = 37 \pm 3$ K. The best-fit fluorescence model spectra are plotted in the bottom right panels of Figure 7.4. Close inspection of the sub-band 2A spectrum reveals marginal detections of weaker emission features beyond 7.65 μm with amplitudes that are consistent with the model. Due to the low amplitude of the CH_4 fluorescence lines, which are at or below the level of noise in the individual pixel spectra, the corresponding coma abundance map from the first epoch (Observation 6) is noisy (Figure 7.5). The spatial pixel with the highest CH_4 column density is situated to the southwest of the target centroid, which contrasts with the slight anti-sunward bias in the H_2O and CO_2 coma maps. However, while it may be tempting to attribute this difference in spatial extent to a distinct production region and/or mechanism, the exact morphology of the column density distribution in the near-nucleus region is poorly constrained and varies strongly when adjusting the details of the pixel-by-pixel continuum modeling.

The detection of CH_4 in the JWST/MIRI observations raises the prospect of a previously unreported CH_4 fluorescence feature in the 2025 August 6 JWST/NIRSpec observations published by M. A. Cordiner et al. (2025). In the near-infrared, the ν_3 asymmetric stretching band of CH_4 is located near 3.3 μm. We reanalyzed the NIRSpec observations following a similar methodology to the MIRI data, and the irradiance spectrum was extracted using a 0.6″-diameter circular aperture. A notable feature in the dedicated background spectral images is the presence of a spatially uniform emission signature stemming from polycyclic

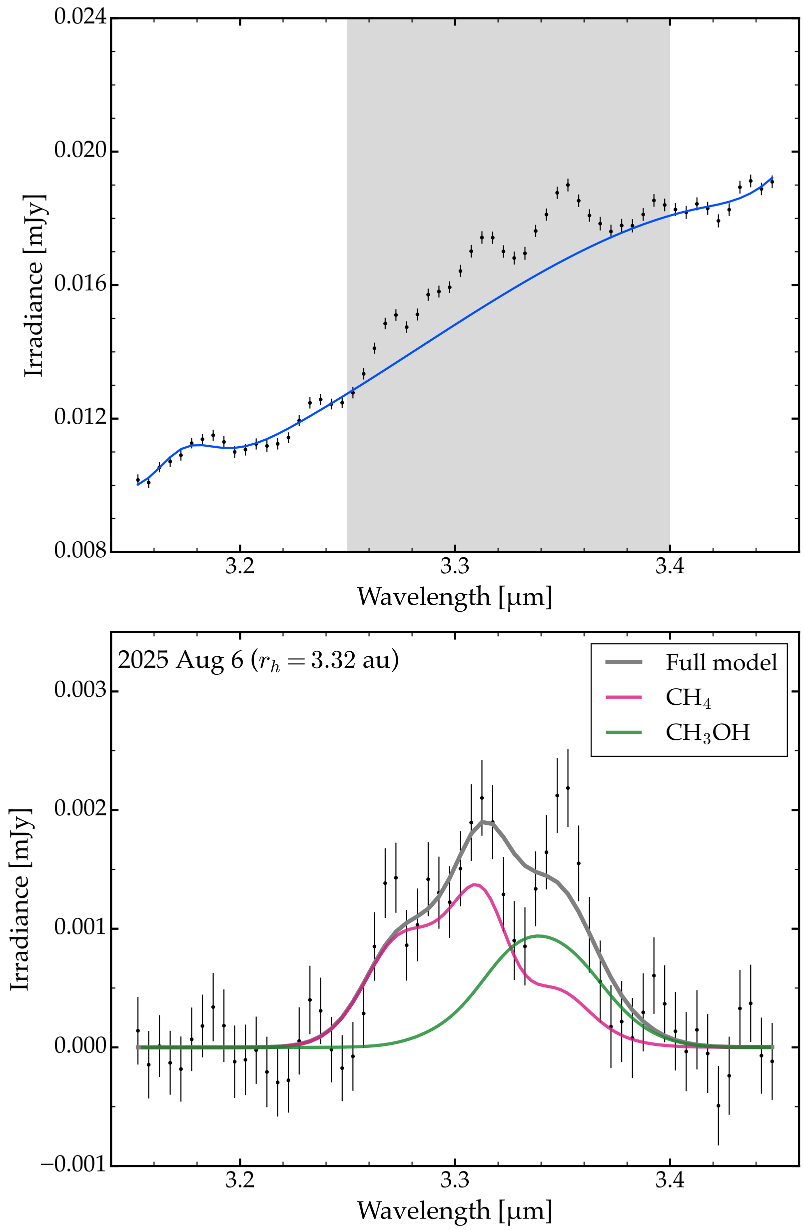

Figure 7.6: Top panel: the JWST/NIRSpec PRISM spectrum of 3I in the vicinity of the CH_4 ν_3 fluorescence band (black points). The shaded region denotes the wavelength range that includes the detected emission bands, which was masked prior to continuum fitting. The blue curve is the cubic spline fit to the continuum points. Bottom panel: the continuum-subtracted spectrum (black points), with the best-fit PSG model overplotted. The gray curve corresponds to the full model, with the individual contributions from CH_4 and CH_3OH plotted in magenta and green, respectively.

aromatic hydrocarbons (PAHs) in galactic dust near 3.3 μm (e.g., Tsumura et al., 2013), which coincides with the region of CH_4 fluorescence. Because the amplitude of this feature varies across the sky, the background field was placed close to 3I (3′ away) to provide a reliable contemporaneous measurement of the PAH emission strength. Continuum removal in the 3.15–3.45 μm region revealed three positive bumps in the residual spectrum (top panel of Figure 7.6). The first two features spanning 3.25–3.33 μm are well-matched by the combined profile of the P, Q, and R-branch fluorescence lines of CH_4, which are fully blended at the low resolution of the PRISM spectrum. The final band centered at ∼3.35 μm is broadly consistent with both methanol (CH_3OH) and ethane (C_2H_6). Each of these molecules possesses additional weaker fluorescence features beyond 3.4 μm; however, the signal-to-noise ratio of the JWST/NIRSpec spectrum and the presence of significant correlated noise do not permit a reliable detection.

Coma modeling of the near-infrared fluorescence feature was carried out using PSG (see section 7.3). Several compositions were considered, including CH_4 only, CH_4+CH_3OH, CH_4+C_2H_6, and CH_4+CH_3OH+C_2H_6. The latter three mixed configurations provided similar fit quality and comparable Q_{CH_4} values. Motivated by the previously reported detection of CH_3OH on 3I from radio observations (Roth et al., 2025), we present the results from the CH_4+CH_3OH retrieval. The bottom panel of Figure 7.6 shows the best-fit PSG model alongside the continuum-subtracted JWST/NIRSpec spectrum. The retrieved production rates are $Q_{CH_4} = 1.4\times10^{25}$ s^{-1}and $Q_{CH_3OH} = 1.6\times10^{25}$ s^{-1}. A systematic relative uncertainty of 30% is placed on the production rate measurements based on the variance in values when altering the modeled composition and continuum subtraction methodology. We caution that the possible presence of an underlying absorption feature from solid hydrocarbons (e.g., C_2H_6, CH_3OH, and/or tholins) in the ∼3.3–3.4 μm region may cause an underestimation of the true CH_4 production rate from the JWST/NIRSpec PRISM spectrum—perhaps by up to a factor of a few. Future analysis of the JWST/NIRSpec observations obtained with the G395H grating will enable a more detailed exploration of the near-infrared fluorescence band inventory.

7.5.4 Nickel

Previous detections of emission lines from electronic transitions from gaseous atomic nickel in distant cometary comae (Manfroid, D. Hutsemékers, and Jehin, 2021) and on 2I (Guzik and Drahus, 2021) have raised the question of how transition metal species can appear as atomic gases at temperatures as low as 150 K—well below the sublimation temperature of Ni-bearing minerals or Ni metal. The short parent lifetime and $1/\rho$ spatial distribution of gaseous Ni have been invoked to suggest that atomic Ni is produced from photodissociation of organometallic complexes, e.g. $Ni(CO)_4$ (Bromley et al., 2021; Guzik and Drahus, 2021; D. Hutsemékers et al., 2021; Manfroid, D. Hutsemékers, and Jehin, 2021).

In the case of 3I, fluorescence from Ni I at near-UV and visible wavelengths has been reported by Hoogendam et al. (2025), Damien Hutsemékers et al. (2026), and Rahatgaonkar et al. (2025). Interestingly, while the Ni/Fe ratio was initially found to be extremely elevated from early pre-perihelion measurements (Rahatgaonkar et al., 2025), it has since steeply declined to Sun-like levels (Damien Hutsemékers et al., 2026). However, the absolute production rates remain significantly higher than those observed on solar system comets.

The JWST/MIRI observations access ground-state transitions from the lowest-energy levels of atomic Ni. A query for forbidden electronic transitions of Ni I in the 5-28 μm range from the NIST Atomic Spectra Database (A. Kramida et al., 2024) returned six transitions. The 7.5066 μm $3d^8(^3F)4s^2(^3F_3) \rightarrow 3d^8(^3F)4s^2(^3F_4)$ line is a transition from a 0.165 eV upper state to the ground state and is clearly detected in the 2025 December 16 spectrum, as shown in Figure 7.4. The next brightest line, $3d^8(^3F)4s^2(^3F_2) \rightarrow 3d^8(^3F)4s^2(^3F_3)$ at 11.307 μm, cascades into the upper level of the 7.5066 μm transition from a higher energy level of 0.275 eV. The fluorescence efficiency of the 11.307 μm line is roughly three times weaker than that of the 7.5066 μm line. Close inspection of the JWST/MIRI spectra uncovers the 11.307 μm line at approximately the expected flux ratio relative to the stronger 7.5066 μm line, given our computed fluorescence efficiencies. A [Ni I] line at 3.119 μm has a comparable fluorescence efficiency to the 7.5066 μm line and should be easily detected by JWST/NIRSpec observations with the medium- or high-resolution spectral grating, which are part of Program #5094 (PI: M. Cordiner, M. Cordiner et al. 2026). Our observations do not provide a measurement of the Fe/Ni ratio, as there are no strong forbidden transitions from Fe I in the MRS wavelength range, except for the 24.04 μm line, which is in a region of the spectrum dominated by thermal emission and significant systematics that preclude its detection.

To compute Ni production rates from the two observed lines, fluorescence efficiencies (i.e., g-factors) were first calculated following the method described in Bromley et al., 2021. Next, the number of Ni atoms within the spectral extraction aperture is given as

$$N_{\mathrm{atom}} = 4\pi\Delta^2 \underbrace{\frac{F_\nu d\lambda}{g \cdot h \cdot \lambda}}_{\#\ \mathrm{Density}} \underbrace{\frac{1}{\pi\rho^2}}_{\mathrm{Aperture}}, \tag{7.1}$$

where $F_\nu d\lambda$ is the integrated line flux in Jy·μm, ρ is the corresponding extraction radius in distance units, and Δ is the observer distance. Finally, the Haser model provides the absolute production rate (Haser, Oset, and Bodewits, 2020):

$$Q_{\mathrm{Ni}} = 2\pi\rho v N_{\mathrm{atom}} \times \frac{(\gamma_p - \gamma_d)/\gamma_d}{\int_0^{\rho/\gamma_p} K_0(x)dx - \int_0^{\rho/\gamma_d} K_0(x)dx}, \tag{7.2}$$

where $\gamma_d = 9\times10^5$ km and $\gamma_p = 200$ km are the scale lengths of the daughter and parent in the hypothesized photodissociation reaction (i.e., Ni I and the putative nickel-bearing carbonyl molecule) taken from Bromley et al., 2021, K_0 is the modified zeroth-order Bessel function of the second kind, and $v = 0.8/\sqrt{r_h} = 0.54$ km s^{-1} is the coma expansion velocity (Ootsubo et al., 2012). The resulting production rate is $\log Q_{\mathrm{Ni}} = 23.72 \pm 0.12$ s^{-1}. Using a more straightforward $1/\rho$ fit without accounting for photodissociation of a parent species, which entails removing the final multiplicative factor containing the γ terms from Equation (7.2), yields a slightly higher production rate of $\log Q_{\mathrm{Ni}} = 23.89 \pm 0.15$ s^{-1}. The production rate estimated from the 11.307 μm line is slightly larger at $\log Q_{\mathrm{Ni}} = 24.0 \pm 0.2$ s^{-1}and 24.2 ± 0.2 s^{-1} for the two aforementioned models, respectively. The reported production rate uncertainties incorporate the spread in calculated band areas obtained from iterative Monte Carlo resampling of the data based on the measurement uncertainties line, as well as the uncertainty on the fluorescence efficiency (roughly 20%, based on information from the NIST Atomic Spectra Database; A. Kramida et al. 2024).

It is worth noting that all detections of atomic Ni in cometary nuclei to date have probed higher-energy transitions at near-UV wavelengths, in contrast with the low-energy transitions (0.11 and 0.165 eV) observed by JWST/MIRI. The population of the upper level of the two lines is likely to be primarily determined by fluorescence pumping of strong UV lines, which cascade down to the upper state of the 11.307 μm transition. Many of the Ni lines in the UV and visible region exhibit $\sim$ 20% uncertainties in their Einstein A coefficients and corresponding absorption rates, suggesting that the g-factor for both the 7.5066 μm and 11.307 μm lines may be subject to additional uncertainties. Contemporaneous ground-based spectroscopy targeting the nickel lines in the near-UV would help confirm the validity of production rates measured in the mid-infrared. Despite the issues inherent to a production rate derived from two lines, our results are highly consistent with pre-perihelion measurements (Rahatgaonkar et al., 2025; Damien Hutsemékers et al., 2026).

Within this context, we briefly examine the implications of the Ni detection on 3I. The common hypothesis is that Ni is trapped in organometallic complexes (either metal carbonyls, or metal-bonded polycyclic aromatic hydrocarbons; Bromley et al. 2021; Manfroid, D. Hutsemékers, and Jehin 2021), which produce bare Ni atoms upon photodissociation. Our production rate measurements are consistent with the pre-perihelion value obtained at roughly the same heliocentric distance: $\log Q_{\mathrm{Ni}} = 23.80 \pm 0.03$ s^{-1} at 2.19 au (Damien

Hutsemékers et al., 2026). If these measurements are taken to imply symmetric inbound and outbound production rates, it would appear that the steep heliocentric distance dependence of Ni production does not stem from the comet's long passage through the interstellar medium. An alteration-driven production (e.g., via irradiation by galactic cosmic rays) would result in a distinct nickel production rate, as the outer surface of the comet was shed during its perihelion approach. The symmetric pre- vs. post-perihelion behavior of the production rate, however, confirms that the metal's production mechanism and source are distinct from canonical volatile release in comets, as suggested by Rahatgaonkar et al., 2025. The JWST/MIRI production rates for CO_2 and H_2O suggest that 3I releases 2.5×10^{28} oxygen atoms from the gas, which can be roughly doubled to account for oxygen in the silicates. This crude estimate for the atomic abundance of oxygen yields a Ni/O ratio of 0.002%. Given that the solar abundance of nickel relative to oxygen is approximately 0.34% (Lodders, 2003), the observed Ni:H_2O and Ni:CO_2 ratios indicate that the measured gaseous Ni emission—as well as the hypothesized organometallic complexes from which it is sourced—represents only a fraction of a percent of 3I's total nickel reservoir.

7.6 Discussion

From a scientific standpoint, the rescheduling of Observations 13 and 15 proved fortuitous, as the 12-day baseline between the two epochs enables a self-consistent assessment of 3I's evolving gas production. Between 2025 December 15–16 and 27, 3I passed from 2.20 to 2.54 au (Table 7.1), providing two distinct views of the object's volatile production at heliocentric distances not sampled by previous observations. The H_2O, CO_2, and CH_4 production rates measured from the JWST/MIRI spectra are plotted in the left panel of Figure 7.7, where the marked decrease in activity between the two epochs is clearly seen. Notably, the Q_{H_2O} values exhibit a significantly steeper drop between $r_h = 2.20$ and 2.54 au than the other volatiles, which can be attributed to the lower volatility of H_2O compared to CO_2 and CH_4. The H_2O ice line in the Solar System is located around 2.5 au, and as 3I approached those heliocentric distances in 2025 December, H_2O production from the coldest regions of 3I's surface and coma was starting to shut down. Meanwhile, because of their much lower vapor pressures, CO_2 and CH_4 are expected to have remained fully activated.

Figure 7.7 shows a collection of published volatile production rates for 3I. The pre-perihelion data points include Q_{H_2O} and Q_{CO_2} values calculated from JWST/NIRSpec PRISM observations (M. A. Cordiner et al., 2025), Q_{H_2O} and Q_{CO_2} production rates obtained from SPHEREx spectrophotometry spanning $r_h = 3.01$–3.49 au (Carey M. Lisse et al., 2025), Q_{H_2O} measurements derived from observations by the Swift Observatory (Xing et al., 2025), and the Q_{CH_4} value estimated from our reanalysis of the JWST/NIRSpec observations

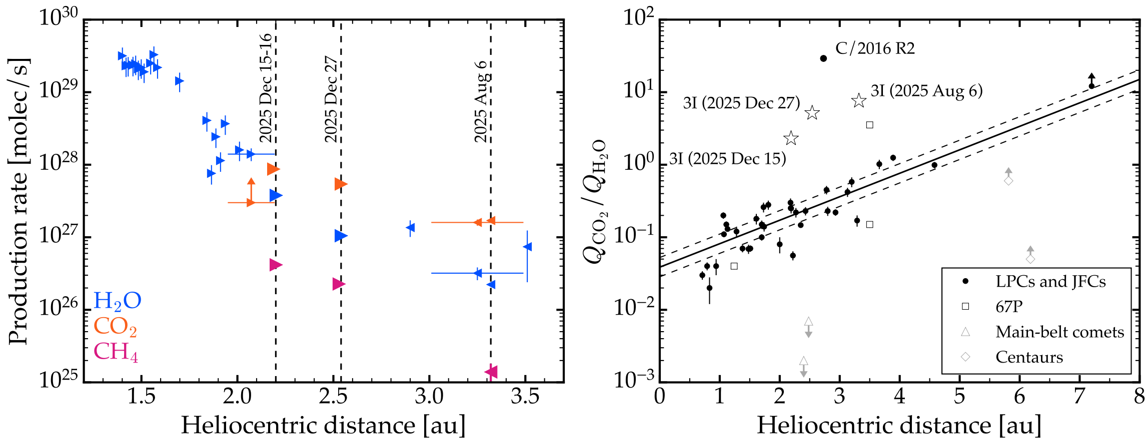

Figure 7.7: Left panel: a compilation of H_2O, CO_2, and CH_4 production rates for 3I published in Combi et al. (2026), M. A. Cordiner et al. (2025), Carey M. Lisse et al. (2025), Xing et al. (2025), C. M. Lisse, Bach, et al. (2026), and this work, plotted as a function of heliocentric distance. The JWST epochs (both NIRSpec and MIRI) are marked with vertical dashed lines. The MIRI measurements and the Q_{CH_4} value obtained from the reanalysis of the NIRSpec observations are shown with larger symbols. Left-facing triangles denote pre-perihelion measurements, and vice versa. Right panel: CO_2-to-H_2O production ratios versus heliocentric distance for various active objects, sorted by dynamical class, with 3I's measurements marked with the star symbols. This plot is a reproduction of Figure 6 in M. A. Cordiner et al. (2025) (see reference therein), with the new JWST/MIRI-derived values added. The solid and dashed black lines indicate the best-fit log-linear trend and associated 1σ bounds for the population of long-period comets (LPCs) and Jupiter-family comets (JFCs), excluding the exceptionally CO_2-rich object C/2016 R2. The measured CO_2:H_2O mixing ratios for 3I are significantly enriched relative to the trend, as is the case for C/2016 R2. See text for details.

(Section 7.5.3). Post-perihelion production rates include 18 Q_{H_2O} estimates derived from Lyman-α measurements by the Solar and Heliosphere Observatory (SOHO; Combi et al. 2026) and Q_{H_2O} and Q_{CO_2} values obtained from 2025 December SPHEREx observations spanning $r_h = 1.95$–2.19 au (C. M. Lisse, Bach, et al., 2026). Note that due to the optical thickness of the innermost CO_2 coma during the latest SPHEREx visit, which was not accounted for in the CO_2 activity measurement, the corresponding Q_{CO_2} value is a strict lower limit to the true production rate.

The JWST/MIRI-derived Q_{H_2O} values presented in this Letter continue the steep drop in H_2O production indicated by the other post-perihelion measurements. Notably, both the SOHO and SPHEREx Q_{H_2O} values were obtained using large apertures ($> 10^5$ km) that are well-suited to capture the full extent of distributed H_2O production within 3I's expansive coma. It follows that, given the smooth heliocentric distance trend traced by all post-perihelion H_2O production rates, there is no indication that the Q_{H_2O} values retrieved from the MRS spectra are significantly underestimating 3I's total H_2O production.

The previous JWST/NIRSpec observations obtained at $r_h = 3.32$ au found that 3I is unusually rich in CO_2 relative to H_2O, with a measured Q_{CO_2}/Q_{H_2O} ratio of 7.3 ± 0.6 (M. A. Cordiner et al., 2025). SPHEREx measurements from 2025 August likewise indicated an enhanced CO_2:H_2O ratio of 5.0 ± 1.3 (Carey M. Lisse et al., 2025). We report $Q_{CO_2}/Q_{H_2O} = 2.30 \pm 0.03$ and 5.16 ± 0.13 for the two epochs of JWST/MIRI spectroscopy, respectively. The right panel of Figure 7.7 shows an ensemble of published Q_{CO_2}/Q_{H_2O} measurements for active objects (after M. A. Cordiner et al. 2025, adding our new mixing ratio measurements). While the heliocentric dependence of Q_{CO_2}/Q_{H_2O} for 3I is roughly similar to that of typical long-period and Jupiter-family comets, 3I's mixing ratio measurements are enhanced by over an order of magnitude relative to most other published values obtained at similar heliocentric distances and approach the CO_2:H_2O mixing ratio of the exceptionally volatile-rich comet C/2016 R2.

The most notable finding from our mid-infrared spectroscopy of 3I is the robust detection of CH_4 production. As with CO_2:H_2O, the CH_4:H_2O mixing ratio of 3I may also be enhanced relative to typical solar system comets. However, previous measurements of the CH_4 production rate for solar system comets beyond $r_h = 2$ au are sparse. Excluding the exceptionally hypervolatile-rich comet C/2016 R2, which has a reported CH_4:H_2O mixing ratio of $181\% \pm 25\%$ (McKay et al., 2019), the handful of published Q_{CH_4}/Q_{H_2O} values spans 0.1–10% (Le Roy et al., 2015; Dello Russo et al., 2016; Bonev et al., 2017). The Q_{CH_4}/Q_{H_2O} values for 3I from the two JWST/MIRI epochs are $11.0\% \pm 0.5\%$ and $21.6\% \pm 1.3\%$, respectively, with the higher mixing ratio in the second epoch consistent with the aforementioned pronounced reduction in H_2O outgassing as 3I approached the H_2O sublimation line during its outbound track. Contemporaneous SPHEREx observations on 2025 December 7–15 yielded a CH_4:H_2O mixing ratio of $\sim 14\%$, assuming that the emission from organics at 3.2–3.5 μm is dominated by CH_4 (C. M. Lisse, Bach, et al., 2026). The SPHEREx measurement is interpreted as an upper limit for the mixing ratio, as the presence of CH_3OH, which was demonstrated from ALMA measurements (Roth et al., 2025), also contributes to the 3.4 μm excess. The agreement between the SPHEREx value, obtained from a large aperture, and the JWST/MIRI measurements suggests that any potential underestimation of Q_{H_2O} due to the limited MRS field of view does not have a substantial impact on the reported CH_4:H_2O mixing ratio.

A peculiar feature of 3I's CH_4 activity history is the pre-perihelion Q_{CH_4} value measured from the 2025 August 6 JWST/NIRSpec observation, which is almost an order of magnitude lower than the extrapolated trend line from the two post-perihelion measurements (Figure 7.7). Meanwhile, the production rate of CO_2 displays monotonic combined pre- and post-perihelion activity modulation. The distinctive behavior of CH_4 indicates that a significant enhancement in CH_4 production occurred sometime after the 2025 August 6 pre-perihelion JWST/NIRSpec observation and prior to the post-perihelion JWST/MIRI visits.

Solid-phase CH_4 is hypervolatile, with a significantly lower sublimation temperature than CO_2. Thermal modeling of airless bodies (e.g., Schaller and Brown, 2007; C. M. Lisse, Young, et al., 2021; C. M. Lisse, Gladstone, et al., 2022) has demonstrated that CH_4 ice at or near the surface of 3I would have been vigorously sublimating at the time of the first reports of cometary activity during 3I's pre-perihelion track ($r_h \sim 6$ au; Feinstein, Noonan, and Seligman 2025; Martinez-Palomera et al. 2025; Ye et al. 2025). However, the CH_4 production rate measurements indicate that the molecule was not fully activated when 3I was inbound at ~3.3 au. This could imply that 3I previously underwent a period of significant heating within its natal planetary system prior to its ejection into the cold interstellar medium (C. M. Lisse, Bach, et al., 2026) that depleted the CH_4 in the outermost layers. Consequently, the surviving reservoir of primordial CH_4 ice resides at depth and was only fully activated after the thermal wave induced by 3I's perihelion passage propagated into the interior. This behavior is mirrored by CO—even more volatile than CH_4—which displayed a roughly 40-fold increase in production relative to CO_2 in the 2025 December SPHEREx observations of 3I when compared to pre-perihelion measurements (C. M. Lisse, Bach, et al., 2026). An additional contributing factor to the increased production of these hypervolatile species could be the removal of the outermost layers of the surface through sublimation-driven mass loss during 3I's perihelion passage.

References

A. Kramida et al. (2024). NIST Atomic Spectra Database (ver. 5.12), [Online]. Available: https://physics.nist.gov/asd [2016, January 31]. National Institute of Standards and Technology, Gaithersburg, MD.

Argyriou, Ioannis et al. (July 2023). "JWST MIRI flight performance: The Medium-Resolution Spectrometer". In: *A&A* 675, A111, A111. DOI: 10.1051/0004-6361/202346489. arXiv: 2303.13469 [astro-ph.IM].

Banzatti, Andrea et al. (Mar. 2025). "Water in Protoplanetary Disks with JWST-MIRI: Spectral Excitation Atlas and Radial Distribution from Temperature Diagnostic Diagrams and Doppler Mapping". In: *AJ* 169.3, 165, p. 165. DOI: 10.3847/1538-3881/ada962. arXiv: 2409.16255 [astro-ph.EP].

Belyakov, Matthew et al. (July 2025). "Palomar and Apache Point Spectrophotometry of Interstellar Comet 3I/ATLAS". In: *RNAAS* 9.7, 194, p. 194. DOI: 10.3847/2515-5172/adf059. arXiv: 2507.11720 [astro-ph.EP].

Bolin, B. T. et al. (Jan. 2018). “APO Time-resolved Color Photometry of Highly Elongated Interstellar Object 1I’ Oumuamua”. In: *ApJL* 852, L2, p. L2. DOI: 10.3847/2041-8213/aaa0c9. arXiv: 1711.04927 [astro-ph.EP].

Bolin, Bryce T., Matthew Belyakov, et al. (Sept. 2025). “Interstellar comet 3I/ATLAS: discovery and physical description”. In: *MNRAS* 542.1, pp. L139–L143. DOI: 10.1093/mnrasl/slaf078. arXiv: 2507.05252 [astro-ph.EP].

Bolin, Bryce T. and Carey M. Lisse (Oct. 2020). “Constraints on the spin-pole orientation, jet morphology, and rotation of interstellar comet 2I/Borisov with deep HST imaging”. In: *MNRAS* 497.4, pp. 4031–4041. DOI: 10.1093/mnras/staa2192. arXiv: 1912.07386 [astro-ph.EP].

Bolin, Bryce T., Carey M. Lisse, et al. (July 2020). “Characterization of the Nucleus, Morphology, and Activity of Interstellar Comet 2I/Borisov by Optical and Near-infrared GROWTH, Apache Point, IRTF, ZTF, and Keck Observations”. In: *AJ* 160.1, 26, p. 26. DOI: 10.3847/1538-3881/ab9305. arXiv: 1910.14004 [astro-ph.EP].

Bonev, Boncho P. et al. (May 2017). “Beyond 3 au from the Sun: The Hypervolatiles CH_4, C_2H_6, and CO in the Distant Comet C/2006 W3 (Christensen)”. In: *AJ* 153.5, 241, p. 241. DOI: 10.3847/1538-3881/aa64dd.

Bromley, S. J. et al. (Dec. 2021). “Atomic Iron and Nickel in the Coma of C/1996 B2 (Hyakutake): Production Rates, Emission Mechanisms, and Possible Parents”. In: *PSJ* 2.6, 228, p. 228. DOI: 10.3847/PSJ/ac2dff. arXiv: 2106.04701 [astro-ph.EP].

Bushouse, Howard et al. (Nov. 2025). *JWST Calibration Pipeline*. Version v1.20.2. DOI: 10.5281/zenodo.17515973.

Chandler, Colin Orion et al. (July 2025). “NSF-DOE Vera C. Rubin Observatory Observations of Interstellar Comet 3I/ATLAS (C/2025 N1)”. In: *arXiv*, arXiv:2507.13409, arXiv:2507.13409. DOI: 10.48550/arXiv.2507.13409. arXiv: 2507.13409 [astro-ph.EP].

Combi, M. R. et al. (Feb. 2026). “Water Production of Interstellar Comet 3I/ATLAS from SOHO/SWAN Observations after Perihelion”. In: *ApJL* 998.1, L17, p. L17. DOI: 10.3847/2041-8213/ae3bd8.

Cordiner, Martin et al. (Mar. 2026). “JWST Spectroscopy of 3I/ATLAS: Isotopic Evidence for a Cold and Distant Origin”. In: DOI: 10.21203/rs.3.rs-8930056/v1. URL: http://dx.doi.org/10.21203/rs.3.rs-8930056/v1.

Cordiner, Martin A. et al. (Oct. 2025). “JWST Detection of a Carbon-dioxide-dominated Gas Coma Surrounding Interstellar Object 3I/ATLAS”. In: *ApJL* 991.2, L43, p. L43. DOI: 10.3847/2041-8213/ae0647. arXiv: 2508.18209 [astro-ph.EP].

Coulson, Iain M. et al. (Feb. 2026). “JCMT detection of HCN emission from 3I/ATLAS at 2.1 au”. In: *MNRAS* 546.2, stag063, stag063. DOI: 10.1093/mnras/stag063. arXiv: 2510.02817 [astro-ph.EP].

de la Fuente Marcos, R. et al. (Aug. 2025). "Assessing interstellar comet 3I/ATLAS with the 10.4 m Gran Telescopio Canarias and the Two-meter Twin Telescope". In: *A&A* 700, L9, p. L9. DOI: 10.1051/0004-6361/202556439. arXiv: 2507.12922 [astro-ph.EP].

Dello Russo, Neil et al. (Nov. 2016). "Emerging trends and a comet taxonomy based on the volatile chemistry measured in thirty comets with high-resolution infrared spectroscopy between 1997 and 2013". In: *Icarus* 278, pp. 301–332. DOI: 10.1016/j.icarus.2016.05.039.

Denneau, L. et al. (Jan. 2025). "3I/ATLAS = C/2025 n1 (atlas)". In: *MPEC* 2025-N12. DOI: 10.48377/MPEC/2025-N12.

Emery, J. P. et al. (May 2024). "A tale of 3 dwarf planets: Ices and organics on Sedna, Gonggong, and Quaoar from JWST spectroscopy". In: *Icarus* 414, 116017, p. 116017. DOI: 10.1016/j.icarus.2024.116017. arXiv: 2309.15230 [astro-ph.EP].

Feinstein, Adina D., John W. Noonan, and Darryl Z. Seligman (Sept. 2025). "Precovery Observations of 3I/ATLAS from TESS Suggest Possible Distant Activity". In: *ApJL* 991.1, L2, p. L2. DOI: 10.3847/2041-8213/adfd4d. arXiv: 2507.21967 [astro-ph.EP].

Fitzsimmons, Alan et al. (2024). "Interstellar Objects and Exocomets". In: *Comets III*. Ed. by Karen. J. Meech et al. Tucson, AZ: Univ. Arizona Press, pp. 731–766. DOI: 10.2458/azu_uapress_9780816553631-ch022.

Gibson, Adalyn et al. (Nov. 2025). "TESS Discovers a Second System of Transiting Exocomets in the Extreme Debris Disk of RZ Psc". In: *ApJL* 993.1, L29, p. L29. DOI: 10.3847/2041-8213/ae11a1. arXiv: 2510.09920 [astro-ph.EP].

Grant, Sierra L. et al. (Apr. 2023). "MINDS. The Detection of $^{13}CO_2$ with JWST-MIRI Indicates Abundant CO_2 in a Protoplanetary Disk". In: *ApJL* 947.1, L6, p. L6. DOI: 10.3847/2041-8213/acc44b. arXiv: 2212.08047 [astro-ph.SR].

Guzik, Piotr and Michał Drahus (May 2021). "Gaseous atomic nickel in the coma of interstellar comet 2I/Borisov". In: *Nature* 593.7859, pp. 375–378. DOI: 10.1038/s41586-021-03485-4. arXiv: 2105.09305 [astro-ph.EP].

Haser, L., Shawn Oset, and D. Bodewits (Dec. 2020). "Intensity Distribution in the Heads of Comets". In: *PSJ* 1.3, 83, p. 83. DOI: 10.3847/PSJ/abc17b.

Hoogendam, W. B. et al. (Oct. 2025). "Spatial Profiles of 3I/ATLAS CN and Ni Outgassing from Keck/KCWI Integral Field Spectroscopy". In: *arXiv*, arXiv:2510.11779, arXiv:2510.11779. DOI: 10.48550/arXiv.2510.11779. arXiv: 2510.11779 [astro-ph.EP].

Hopkins, Matthew J. et al. (Sept. 2025). "From a Different Star: 3I/ATLAS in the Context of the Ōtautahi–Oxford Interstellar Object Population Model". In: *ApJL* 990.2, L30, p. L30. DOI: 10.3847/2041-8213/adfbf4. arXiv: 2507.05318 [astro-ph.EP].

Hui, Man-To et al. (Jan. 2026). "Nucleus and Postperihelion Activity of Interstellar Object 3I/ATLAS Observed by Hubble Space Telescope". In: *arXiv*, arXiv:2601.21569, arXiv:2601.21569. DOI: 10.48550/arXiv.2601.21569. arXiv: 2601.21569 [astro-ph.EP].

Hutsemékers, D. et al. (Aug. 2021). “FeI and NiI in cometary atmospheres. Connections between the NiI/FeI abundance ratio and chemical characteristics of Jupiter-family and Oort-cloud comets”. In: *A&A* 652, L1, p. L1. DOI: 10.1051/0004-6361/202141554. arXiv: 2107.05932 [astro-ph.EP].

Hutsemékers, Damien et al. (Jan. 2026). “Pre-perihelion evolution of the NiI/FeI abundance ratio in the coma of the interstellar comet 3I/ATLAS: From extreme to normal”. In: *A&A* 706, A43, A43. DOI: 10.1051/0004-6361/202557484. arXiv: 2509.26053 [astro-ph.EP].

Jewitt, David (July 2024). “Interstellar Objects in the Solar System”. In: *arXiv e-prints*, arXiv:2407.06475, arXiv:2407.06475. DOI: 10.48550/arXiv.2407.06475. arXiv: 2407.06475 [astro-ph.EP].

Jewitt, David and Jane Luu (Dec. 2019). “Initial Characterization of Interstellar Comet 2I/2019 Q4 (Borisov)”. In: *ApJL* 886.2, L29, p. L29. DOI: 10.3847/2041-8213/ab530b. arXiv: 1910.02547 [astro-ph.EP].

— (Nov. 2025). “Preperihelion Development of Interstellar Comet 3I/ATLAS”. In: *ApJL* 994.1, L3, p. L3. DOI: 10.3847/2041-8213/ae1832.

Kareta, Theodore et al. (Sept. 2025). “Near-discovery Observations of Interstellar Comet 3I/ATLAS with the NASA Infrared Telescope Facility”. In: *ApJL* 990.2, L65, p. L65. DOI: 10.3847/2041-8213/adfbdf. arXiv: 2507.12234 [astro-ph.EP].

Kim, Yoonyoung et al. (June 2020). “Coma Anisotropy and the Rotation Pole of Interstellar Comet 2I/Borisov”. In: *ApJL* 895.2, L34, p. L34. DOI: 10.3847/2041-8213/ab9228. arXiv: 2005.02468 [astro-ph.EP].

Lamy, P. L. et al. (2004). “The sizes, shapes, albedos, and colors of cometary nuclei”. In: *Comets II*. Ed. by Michel C. Festou, H. Uwe Keller, and Harold A. Weaver. Tucson, AZ: Univ. Arizona Press, p. 223.

Le Roy, Léna et al. (Nov. 2015). “Inventory of the volatiles on comet 67P/Churyumov-Gerasimenko from Rosetta/ROSINA”. In: *A&A* 583, A1, A1. DOI: 10.1051/0004-6361/201526450.

Lisse, C. M., YP. Bach, et al. (Jan. 2026). “SPHEREx Re-Observation of Interstellar Object 3I/ATLAS in December 2025: Detection of Increased Post-Perihelion Activity, Refractory Coma Dust, and New Coma Gas Species”. In: *arXiv e-prints*, arXiv:2601.06759, arXiv:2601.06759. DOI: 10.48550/arXiv.2601.06759. arXiv: 2601.06759 [astro-ph.EP].

Lisse, C. M., G. R. Gladstone, et al. (May 2022). “A Predicted Dearth of Majority Hypervolatile Ices in Oort Cloud Comets”. In: *PSJ* 3.5, 112, p. 112. DOI: 10.3847/PSJ/ac6097.

Lisse, C. M., L. A. Young, et al. (Mar. 2021). “On the origin & thermal stability of Arrokoth’s and Pluto’s ices”. In: *Icarus* 356, 114072, p. 114072. DOI: 10.1016/j.icarus.2020.114072. arXiv: 2009.02277 [astro-ph.EP].

Lisse, Carey M. et al. (Dec. 2025). "SPHEREx Pre-Perihelion Mapping of H_2O, CO_2, and CO in Interstellar Object 3I/ATLAS". In: *arXiv*, arXiv:2512.07318, arXiv:2512.07318. DOI: 10.48550/arXiv.2512.07318. arXiv: 2512.07318 [astro-ph.EP].

Lodders, Katharina (July 2003). "Solar System Abundances and Condensation Temperatures of the Elements". In: *ApJ* 591.2, pp. 1220–1247. DOI: 10.1086/375492.

Manfroid, J., D. Hutsemékers, and E. Jehin (May 2021). "Iron and nickel atoms in cometary atmospheres even far from the Sun". In: *Natur* 593.7859, pp. 372–374. DOI: 10.1038/s41586-021-03435-0.

Martinez-Palomera, Jorge et al. (Dec. 2025). "Prediscovery TESS Observations of Interstellar Object 3I/ATLAS". In: *ApJL* 994.2, L51, p. L51. DOI: 10.3847/2041-8213/ae1f91. arXiv: 2508.02499 [astro-ph.EP].

McKay, Adam J. et al. (Sept. 2019). "The Peculiar Volatile Composition of CO-dominated Comet C/2016 R2 (PanSTARRS)". In: *AJ* 158.3, 128, p. 128. DOI: 10.3847/1538-3881/ab32e4. arXiv: 1907.07208 [astro-ph.EP].

Meech, Karen J. et al. (Dec. 2017). "A brief visit from a red and extremely elongated interstellar asteroid". In: *Natur* 552.7685, pp. 378–381. DOI: 10.1038/nature25020.

Ootsubo, Takafumi et al. (June 2012). "AKARI Near-infrared Spectroscopic Survey for CO_2 in 18 Comets". In: *ApJ* 752.1, 15, p. 15. DOI: 10.1088/0004-637X/752/1/15.

Opitom, Cyrielle et al. (Nov. 2025). "Snapshot of a new interstellar comet: 3I/ATLAS has a red and featureless spectrum". In: *MNRAS* 544.1, pp. L31–L36. DOI: 10.1093/mnrasl/slaf095. arXiv: 2507.05226 [astro-ph.EP].

Pontoppidan, Klaus M. et al. (Mar. 2024). "High-contrast JWST-MIRI Spectroscopy of Planet-forming Disks for the JDISC Survey". In: *ApJ* 963.2, 158, p. 158. DOI: 10.3847/1538-4357/ad20f0. arXiv: 2311.17020 [astro-ph.EP].

Rahatgaonkar, Rohan et al. (Dec. 2025). "Very Large Telescope Observations of Interstellar Comet 3I/ATLAS. II. From Quiescence to Glow: Dramatic Rise of Ni I Emission and Incipient CN Outgassing at Large Heliocentric Distances". In: *ApJL* 995.1, L34, p. L34. DOI: 10.3847/2041-8213/ae1cbc. arXiv: 2508.18382 [astro-ph.SR].

Regan, Michael (June 2024). *Detection and Flagging of Showers and Snowballs in JWST*. URL: https://www.stsci.edu/files/live/sites/www/files/home/jwst/documentation/technical-documents/_documents/JWST-STScI-008545.pdf.

Rivkin, Andrew S. et al. (Nov. 2023). "Near to Mid-infrared Spectroscopy of (65803) Didymos as Observed by JWST: Characterization Observations Supporting the Double Asteroid Redirection Test". In: *PSJ* 4.11, 214, p. 214. DOI: 10.3847/PSJ/ad04d8. arXiv: 2310.11168 [astro-ph.EP].

Roth, Nathan X. et al. (Nov. 2025). "CH_3OH and HCN in Interstellar Comet 3I/ATLAS Mapped with the ALMA Atacama Compact Array: Distinct Outgassing Behaviors and a Remarkably High CH_3OH/HCN Production Rate Ratio". In: *arXiv*, arXiv:2511.20845, arXiv:2511.20845. DOI: 10.48550/arXiv.2511.20845. arXiv: 2511.20845 [astro-ph.EP].

Salazar Manzano, Luis E. et al. (Nov. 2025). "Onset of CN Emission in 3I/ATLAS: Evidence for Strong Carbon-chain Depletion". In: *ApJL* 993.1, L23, p. L23. DOI: 10.3847/2041-8213/ae1232. arXiv: 2509.01647 [astro-ph.EP].

Santana-Ros, T. et al. (Oct. 2025). "Temporal evolution of the third interstellar comet 3I/ATLAS: Spin, color, spectra, and dust activity". In: *A&A* 702, L3, p. L3. DOI: 10.1051/0004-6361/202556717. arXiv: 2508.00808 [astro-ph.EP].

Schaller, E. L. and M. E. Brown (Apr. 2007). "Volatile Loss and Retention on Kuiper Belt Objects". In: *ApJL* 659.1, pp. L61–L64. DOI: 10.1086/516709.

Seligman, Darryl Z. et al. (Aug. 2025). "Discovery and Preliminary Characterization of a Third Interstellar Object: 3I/ATLAS". In: *ApJL* 989.2, L36, p. L36. DOI: 10.3847/2041-8213/adf49a. arXiv: 2507.02757 [astro-ph.EP].

Tan, Hanjie, Xiaoran Yan, and Jian-Yang Li (Jan. 2026). "Perihelion Asymmetry in the Water Production Rate of the Interstellar Object 3I/ATLAS". In: *arXiv e-prints*, arXiv:2601.15443, arXiv:2601.15443. DOI: 10.48550/arXiv.2601.15443. arXiv: 2601.15443 [astro-ph.EP].

Taylor, Aster G. and Darryl Z. Seligman (Sept. 2025). "The Kinematic Age of 3I/ATLAS and Its Implications for Early Planet Formation". In: *ApJL* 990.1, L14, p. L14. DOI: 10.3847/2041-8213/adfa28. arXiv: 2507.08111 [astro-ph.EP].

Tsumura, Kohji et al. (Dec. 2013). "Low-Resolution Spectrum of the Diffuse Galactic Light and 3.3μm PAH Emission with the AKARI InfraRed Camera". In: *PASJ* 65.6, 120, p. 120. DOI: 10.1093/pasj/65.6.120. arXiv: 1307.6736 [astro-ph.GA].

Villanueva, G. L., M. J. Mumma, et al. (Nov. 2011). "The molecular composition of Comet C/2007 W1 (Boattini): Evidence of a peculiar outgassing and a rich chemistry". In: *Icarus* 216.1, pp. 227–240. DOI: 10.1016/j.icarus.2011.08.024.

Villanueva, G. L., M. D. Smith, et al. (Sept. 2018). "Planetary Spectrum Generator: An Accurate Online Radiative Transfer Suite for Atmospheres, Comets, Small Bodies and Exoplanets". In: *JQSRT* 217, pp. 86–104. DOI: 10.1016/j.jqsrt.2018.05.023. arXiv: 1803.02008 [astro-ph.EP].

Villanueva, Geronimo Luis et al. (2022). *Fundamentals of the Planetary Spectrum Generator*.

Wells, Martyn et al. (July 2015). "The Mid-Infrared Instrument for the James Webb Space Telescope, VI: The Medium Resolution Spectrometer". In: *PASP* 127.953, p. 646. DOI: 10.1086/682281. arXiv: 1508.03070 [astro-ph.IM].

Wong, Ian (Sept. 2025). *jwstspec*. Version v0.6, DOI: 10.5281/zenodo.17186395. URL: https://doi.org/10.5281/zenodo.17186395.

Wong, Ian et al. (Apr. 2024). "JWST Near-infrared Spectroscopy of the Lucy Jupiter Trojan Flyby Targets: Evidence for OH Absorption, Aliphatic Organics, and CO_2". In: *PSJ* 5.4, 87, p. 87. DOI: 10.3847/PSJ/ad2fc3. arXiv: 2311.11531 [astro-ph.EP].

Xing, Zexi et al. (Oct. 2025). “Water Production Rates of the Interstellar Object 3I/ATLAS”. In: *ApJL* 991.2, L50, p. L50. DOI: 10.3847/2041-8213/ae08ab. arXiv: 2508.04675 [astro-ph.EP].

Yang, Bin et al. (Oct. 2025). “Spectroscopic Characterization of Interstellar Object 3I/ATLAS: Water Ice in the Coma”. In: *ApJL* 992.1, L9, p. L9. DOI: 10.3847/2041-8213/ae08a7. arXiv: 2507.14916 [astro-ph.EP].

Ye, Quanzhi et al. (Nov. 2025). “Prediscovery Activity of New Interstellar Object 3I/ATLAS: Rapid Brightening from 6 to 4 au”. In: *ApJL* 993.1, L31, p. L31. DOI: 10.3847/2041-8213/ae147b. arXiv: 2509.08792 [astro-ph.EP].

Zhang, Qicheng and Karl Battams (Jan. 2026). “Rapid Brightening of 3I/ATLAS Ahead of Perihelion”. In: *PASP* 138.1, 014403, p. 014403. DOI: 10.1088/1538-3873/ae2e88. arXiv: 2510.25035 [astro-ph.EP].

Chapter 8

CONCLUSION

I conclude this thesis with some discussion of my next steps and future outlook for research in small bodies. In essence, this chapter is a more well-formulated version of notes written down regarding proposals, upcoming events, and new directions to look into.

Loose Ends: **The story of the Uranian satellite system.** With the results on Nereid part of the thesis and published, and the results of my colleague Ryleigh Davis soon to be out on the inner part of the Neptunian system, my attention turns to the Uranian system. I plan, in the immediate future, to publish on the Uranian irregular satellites Sycorax and Caliban, commenting on their unique spectra and the capture of irregular satellites. The inner part of the system appears to have a simple story, with the moons appearing much like water-rich Kuiper belt objects. However, there are other lines of investigation into the system past the observations of my program. I hope to revisit the Neptunian system and Uranian system with future James Webb Observations. Given my reclassification of Nereid, it would be wise to observe some of the actual irregular satellites of Neptune. These are rather faint, with only 2 brighter than 25th magnitude, and 3 more brighter than 26th, and may prove challenging. Turning back to Nereid, our spectrum was not the best signal-to-noise ratio, with an 11 minute integration total. It is possible to obtain a medium-resolution spectrum to determine its CO_2 band center, measure the O-D stretch at 4.13 microns, and search for narrow spectral features that were missed in our spectrum. Turning to the Uranian system, public data can give a fascinating result. Past 15 microns, JWST MIRI/MRS observations of Uranus itself also clearly show the rings as well-separated pixels. These can be extracted to obtain the mid-infrared spectrum of the rings, and thus extract their silicate composition. Characterizing the mineralogy of the rings may give the necessary impetus to obtain a dedicated set of observations targeting the rings in the mid-infrared.

Looser Ends: **Bridging the gap between disks and Solar System planetesimals.** The 3I/ATLAS observations presented here are only half of the result – the other half of the mid-infrared spectroscopy lies in obtaining an emissivity spectrum of 3I/ATLAS by removing the blackbody continuum. Emissivity conveys key information about the mineralogy of the dust coming off the object. Work in progress will show that 3I/ATLAS is dominated by amorphous silicates, without a significant fraction of crystalline silicates as seen in

Solar System comets. The broader perspective here is that the field may be at the cusp of a revolution in the discovery of interstellar objects, with Vera Rubin Observatory/LSST primed to detect up to several a year. Some of these will, similarly to 3I, come close enough to Earth and will be at high enough temperatures to become bright in the mid-infrared. While the pitch to continue observing these objects with JWST is obvious, such observations come with significant challenges. 3I came at a significant velocity through our system, placing it at the limits of JWST's tracking capabilities. Our observations suffered from several failed visits, as a result, and we were only able to observe in December, while ground-based observers caught the comet starting early November, when it was closer to the sun. Ground-based low-resolution N-band spectroscopy (8–13 μm) can access the broad silicate emission feature in sufficiently bright comets. Telluric ozone absorption near 9.6 μmlimits coverage of the pyroxene shoulder, but the diagnostic 11.2 μmcrystalline olivine peak falls in a relatively clean portion of the atmospheric window. Measuring the 11.2 μm/10 μmratio as a proxy for the crystalline-to-amorphous silicate mass ratio during a comet's apparition would allow tracking the evolution of dust. Nearly all comets with mid-infrared spectra have been observed just once, with few studies examining change in observed crystallinity over time. These observations would address an open question: what is the rate of amorphization of crystalline dust in ISM-like conditions, such as those that Oort cloud comets experience outside the heliopause. The potentially upcoming PRIMA space telescope, which would observe at wavelengths between 25-250 microns, may also be a vital instrument for obtaining compositional information about interstellar objects. In service of interpreting these kinds of mid-infrared observations, I plan to investigate the latest JWST observations of debris disk and comets, seeking to develop the suite of tools (e.g. compositional models) necessary for future work.

In the next year — cras, cras, semper cras: **Retrograde Centaurs and their Origins** The high-inclination ($i > 60°$) and retrograde KBOs and Centaurs are a dynamically anomalous population in the outer Solar System – of the 3779 total q >5.2 au bodies with well-determined orbits, only 7 are high-i Centaurs ($5.2 < a, q < 30$ au) and 26 are high-i KBOs ($a > 30$, $q > 5.2$ au).

While many of these objects have semi-major axes well past 100 au and are probable Oort cloud-derived objects, the dynamical origin and evolution of the closer objects sets them apart from other Centaurs and low-perihelion KBOs. Their origin is still unresolved, but inner Oort cloud injection (whether from an undiscovered distant planet, stellar fly-bys, or self-gravity inclination instabilities) is frequently suggested as a possible origin for the retrograde objects, as excitation of KBOs onto high-i orbits is unlikely. Their recent and

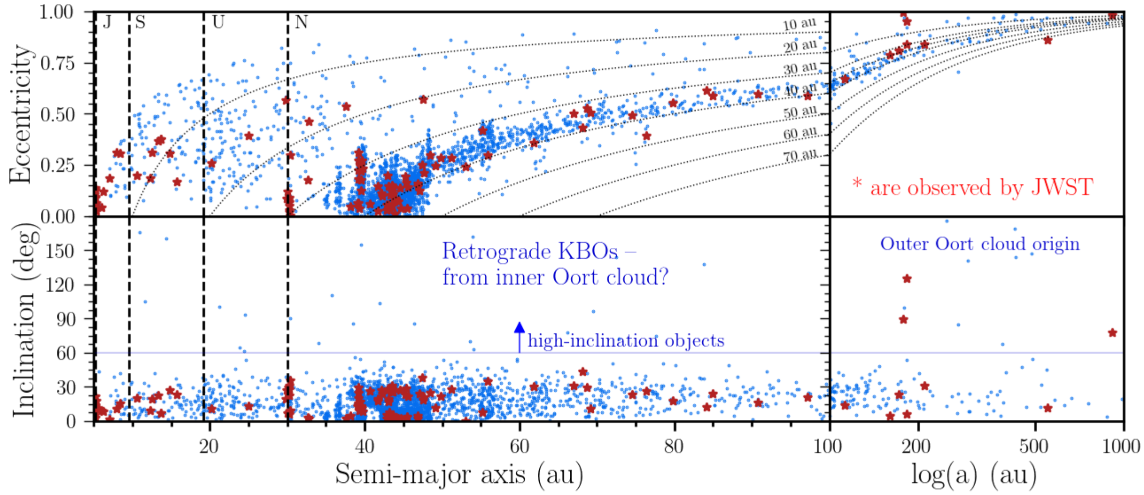

Figure 8.1: Orbital elements of known KBOs (those with more than 2 oppositions), with those that have been observed using JWST NIRSpec as red stars. The retrograde Centaurs stand out as a population not observed until my Cycle 4 JWST observations.

future dynamical evolution is no less interesting: orbital integrations of this population suggest average dynamical lifetimes significantly longer than those of the average Centaur. These significant lifetimes can be leveraged to study the long-term evolution of KBO surfaces at closer heliocentric distances. My accepted Cycle 4 JWST program sought to observe 6 such objects, with 5 observations completed by the time of the submission of this thesis. The results will require revamping the simulations discussed in Chapter 2 of the thesis with a significantly updated model of the Kuiper belt in order to determine the true rarity of retrograde orbits.

In the next half-decade: **Roman Space Telescope** Launching in May 2027, Roman Space Telescope offers a wide-angle imager from 0.6-2.2 microns, conducting a significant survey at incredible depth, likely 2-2.5 magnitudes deeper than LSST. However, it does not offer support for moving target observations, requiring custom work to obtain information about solar system small bodies. I am preparing to apply for dedicated observations of the giant planets to find new irregular satellites. Proposed observations would go deeper than the faintest-known irregular moon: 10 hours observing Uranus will yield r$\sim$1 km moons whereas the current smallest is $\sim$5 km. Discovering new moons will yield a high-fidelity irregular satellite size frequency distribution that can calibrate capture probability in models. Moreover, Roman will be able to get color information in the infrared for these objects, serving as a poor man's JWST.

***In the next half-decade: Lucy* and the Trojans** The *Lucy* mission will fly past 5 Jupiter Trojans between 2027 and 2033. Named after the *Australopithecus afarensis* (early hominin) skeleton that represents one of the early evolutionary steps between apes and humans, *Lucy* seeks to investigate the outer Solar System through the Trojans. As already discussed at length in the thesis, the likely connection between Trojans and the Kuiper belt is of vital interest to reconstructing the early Solar System's dynamical history. *Lucy* is equipped with a high-resolution imager, a multi-spectral imager and infrared spectrograph in another instrument, and a thermal emission spectrometer covering the range from 5-100 microns. With JWST observations having revealed the presence of CO_2 on Eurybates, it is likely new fascinating results await in the near future. Besides looking at the eventual mission data, there is work to be done looking at other sources of data for the Trojans. LSST will obtain colors and sparse lightcurves for tens of thousands of Trojans, allowing for detailed statistical analysis of the ensemble of objects down to the kilometer scale. Neptune's Trojans also are of great interest – their L5 cloud is steadily moving out of the galactic plane, and by 2032, should be readily observable by the LSST.

***In aere aedificare:* Habitable Worlds Observatory (HWO), PRIMA, other acronym-based observatories** Future space-based observatories hold promise to continue expanding the limits of possible observations. HWO is targeted towards, as the name implies, searching for habitable exoplanets. Hopefully, the observatory supports moving target observations, allowing for UV spectroscopy of small bodies in the outer solar system, which were simply too faint for Hubble to observe. Observations of incoming Oort Cloud comets such as C/2014 UN271 may prove an interesting case, obtaining production rates of volatiles in the UV. Surface colors of KBOs in the UV is also an unexplored frontier, one that HWO will uniquely unlock. PRIMA goes the other way in wavelength space, being the first observatory since Herschel and ISO to have significant capabilities in the far-infrared. This region contains important spectral features from carbonates, metal sulfides, metal oxides, and complex organics, which may otherwise be spectrally ambiguous. Few Solar System objects have been studied in this wavelength range, and only a handful have any spectra.

***Ad kalendas Graecas:* A Uranus Orbiter and Probe** The current (past, and future) political situation presents an unfavorable environment for developing, building, and launching a mission to the Uranian system. I hope that I have enough decades ahead of me to still be doing science by the time one does arrive. The Uranian system may present up to five past and present ocean worlds, along with the numerous moons with which I have become acquainted through JWST. Uranus is fascinating. Its significant obliquity (tilted on its side) presents a challenge regarding how its satellites formed. Whether through the re-accretion of a disrupted ancient system, a collision-generated disk, or some other mechanism – the answer remains unclear. Many details of the system also present interesting puzzles, such as why are the rings so narrow, how did Mab arrive at its orbit, coming off of Miranda as a fragment, and why are all but one of the known irregular satellites retrograde. A mission seems necessary to produce a dozen new, yet more interesting questions.

Habe nun, ach! Philosophie, Juristerey und Medicin, Und leider auch Theologie! **Some Concluding Thoughts** The many bodies in the outer Solar System, the dozens of observatories available to study them, and the numerous techniques and lines of inquiry, inexorably draw me back to the same underlying question of what the architecture of the early Solar System was and how exactly does dynamical instability bring us to the present day? This question, of course, is not one that can be answered in a single thesis, by a single person, or by a single future mission. I conclude with the suggestion that there are several questions which will lead to productive investigations, that is to say, any tentative answers will lead to new, more pointed questions.

- What is the role of nature and nurture in shaping the surfaces of outer Solar System objects? What spectral differences provide meaningful constraints on natal conditions?
- How do satellites form around the giant planets? What material was available for their formation?
- How and from what source are irregular satellites captured?
- What is the structure of the Kuiper belt past 50 au?

These questions, and several more, really seek to address the following, much broader question: when did the dynamical instability occur, what was its mechanism, and where were all the present-day actors when it occurred, and what was their state at the time?